MICRO-MACRO MODELING OF ADVANCED MATERIALS BY HYBRID FINITE ELEMENT METHOD

by

Changyong Cao

A thesis submitted for the degree of

Doctor of Philosophy

of The Australian National University

September 2013

Thesis Supervisors:

Prof. Qinghua Qin

Prof. Aibing Yu

Supervisory Panel:

Prof. Qinghua Qin, The Australian National University, Chair

Prof. Aibing Yu, The University of New South Wales

Prof. Xi-Qiao Feng, Tsinghua University, China

Prof. Xuanhe Zhao, Duke University, USA

Prof. Zbigniew H. Stachurski, The Australian National University

Declaration

I hereby declare that this submission is my own work at the Research School of Engineering of The Australian National University, Canberra, Australia. This thesis contains no material that has been previously accepted for the award of any other degree in any university, and contains no material previously published or written by another person, except where acknowledged in the customary manner.

I also declare that the intellectual content of this thesis is the product of my own work, except to the extent that assistance from others in the project's design and conception or in style, presentation and linguistic expression is acknowledged.

_____________________ (Signed)

Changyong Cao

September, 2013

Dedication

To my family

For their love and support

Acknowledgements

During the long journey of my PhD study over the past few years, many people have supported me in different ways. This is a right moment that I would like to give those people sincerely gratitude. First I would like to express my deepest gratitude to my thesis supervisors Professor Qinghua Qin and Professor Aibing Yu for their great support, inspiring guidance and kind encouragement to me during my study, especially in difficult moments. Their breadth of intellectual inquisition continually stimulates my analytical thinking skills. This work would not have been accomplished without their efforts. I am deeply indebted for their guidance and support in both my study and my daily life.

I sincerely thank my committee members for their continuous effort, valuable insights and kind willingness to serve in my supervisory committee. In particular, I would like to thank Professor Xi-Qiao Feng for his guidance on instability analysis and modeling of biomaterials during my stay at Tsinghua University. I am deeply impressed by his enthusiasm as to the various scientific researches. His dedication to science has inspired me to be a scholar in mechanics for which I owe much gratitude.

I would like to express my sincerely gratitude to Professor Xuanhe Zhao of Duke University for his kind guidance, strong support and fruitful discussion. I have benefited significantly from his teaching and mentorship on mechanics of soft active materials. He taught me many wonderful things about mechanics, offered me much sound advice, and helped me get through difficult times. I am grateful to Professor Zbigniew Stachurski for his discussion and guidance in the topic of composite materials. I would like to thank Professor Shaofan Li for his hosting, support and discussions during my research visit to the University of California at Berkeley.

I would like to thank Dr. Jiangfeng Zang and Dr. Sungmin Hong for helpful discussions and teaching me experimental skills. I also express my gratitude to Dr.

Hui Wang for his valuable suggestions and fruitful discussion during his visit to ANU. I would like to thank my colleagues Mr. Jin Tao, Mr. Zewei Zhang, Mr. Check Yu Lee and Mr. Song Chen for their help, discussion and company during my study at ANU. Special thanks are also due to my friends Mr. Wensheng Liang, Ms. Ting Cao, Mr. Zhuojia Fu, Dr. Yongling Ren and Mr. Yimao Wan from ANU for their help and the wonderful times we had together. I would like to thank Mr. Xiaoyu Sun for his great help during my stay at Tsinghua. Thanks also to Ms. Weihua Xie, Mr. Mangong Zhang, Mr. Cheng Ye, Dr. Yue Li, Mr. Liyuan Zhang, Ms. Xiangying Ji and many other friends from Tsinghua, and Mr. Honfai Chan, Mr. Stephene Ubnoske, Mr. Qiming Wang and Mr. Qing Tu from Duke. I sincerely thank our supporting staff at CECS, especially Mr. Jonathan Peters, Ms. Kylee Robinson and Ms. Suzy Andrew. I would like to extend my thanks to all the friends, colleagues and staff at ANU, Tsinghua, Duke and UC Berkeley for their help and for creating a pleasant working atmosphere.

I greatly acknowledge the International PhD Scholarship and HDR Merits Scholarship from ANU, and research funding from Laboratory for Simulation and Modeling of Particulate Systems at UNSW for providing financial support during my PhD study. My research visit overseas and conference attendance were also funded by Vice Chancellor’s Travel Grants and Dean’s Travel Grant from ANU.

Last, but certainly not least, I would like to thank my wife, Yuhui Fang, for all her understanding, encouragement and companionship. Her faithful and unconditional support has always been my main source of strength and happiness. I am greatly indebted to my parents for their tremendous care, endless support and constant encouragement during my lengthy study. They deserve more thanks than I can ever give.

Micro-macro Modeling of Advanced Materials by Hybrid Finite Element Method

by

Changyong Cao

Research School of Engineering, Australian National University, 2013

ABSTRACT

Advanced composite materials are increasingly used in a variety of fields due to their desirable properties. The use of these advanced materials in different applications requires a thorough understanding of the effect of their complex microstructures and the effect of the operating environment on the materials. This requires an efficient, robust and powerful tool that is able to predict the behavior of composites under a variety of loading conditions. This research addresses this problem and develops a new convenient numerical method and framework for users to perform such analyses of composites.

In this thesis, the hybrid fundamental solution based finite element method (HFS-FEM) is developed and applied to model composite materials across microscale and macroscale and from single field to multi-field. The basic idea and detailed formulations of the HFS-FEM for elasticity and potential problems are first presented. Then this method is extended to solve general three-dimensional (3D) elasticity problems with body forces and to model anisotropic materials encountered in composite analysis. Standard tests for proposed elements are carried out to assess their performance. Further, an efficient numerical homogenization method based on HFS-FEM is applied to predict the macroscopic elasticity properties and thermal conductivity of heterogeneous composites in micromechanical analysis. The effect of material parameters, such as fiber volume fractions, inclusion shapes and arrangements on the effective coefficients of composites are investigated by means of

the proposed micromechanical models. Meanwhile, special elements are also proposed for mesh reduction and efficiency improvement in the analyses.

Finally, the HFS-FEM method is developed for modeling two-dimensional (2D) and 3D thermoelastic problems. The particular solutions related to the body force and temperature change are approximated using the radial basis function interpolation. The new HFS-FEM is also developed for modeling plane piezoelectric materials in two different formulations: Lekhnitskii formalism and Stroh formalism. Numerical examples are provided for each kind of problems to demonstrate the accuracy, efficiency and versatility of the proposed method.

Table of Contents

List of Tables

List of Figures

Chapter 1. Introduction

1.1. BACKGROUND AND MOTIVATION

Advanced composite materials are being increasingly used in a variety of fields such as aerospace, automobile, defense, medical and sports due to their preferred mechanical behaviors and desired properties. Examples of their desirable properties are light weight, high stiffness or high flexibility, good thermal and mechanical durability, high yield strength under static or dynamic loading and good surface hardness. Some smart structures can energy transform among different forms such as piezoelectric sensors. Many of these materials, either human-designed or natural, are heterogeneous and have complex microstructures at a certain scale, features that increases the challenges involved in product design and analysis. The heterogeneous microstructure of composites has a significant impact on their observed macroscopic behavior. Indeed, the overall behavior of these materials depends strongly on the size, shape, spatial distribution and properties of the microstructural constituents and their respective interfaces (Wriggers and Hain 2007).

The use of these advanced materials in variety of applications requires thorough understanding of the effect of complex microstructures and the effect of operating environment on these materials. This requires an efficient, robust and powerful tool that can predict the behavior of composites under a variety of environmental and loading conditions. Numerical simulations can significantly reduce the number of time-consuming and expensive experiments with laboriously manufactured material samples. Such simulations would clearly improve the development and design of new materials for modern engineering applications. This research thus attempts to address this problem and sets in place a framework that makes it convenient for users to perform such analyses.

The main motivation of this research is to develop a new efficient methodology for modeling advanced composite materials and to assess the performance of the method in predicting behaviors of these materials at both micro and macro scales. The research also underscores the need for convenient performance of multiphysics analyses and for thorough understanding of the underlying mechanisms. The work presented lays the foundation for establishing a multiscale framework to facilitate the design and analysis of advanced materials such as the carbon nanotube reinforced composites and piezoelectric materials widely used in smart structures and materials.

1.2. MODELING OF ADVANCED MATERIALS

With the advances in computing power and simulation methodology, computational modeling has been increasingly employed in the design and development of advanced composites. During the past several decades, a few methods have been proposed and successfully applied to modeling composites from nanoscale to macroscale (Ghosh, Nowak et al. 1997; Yang and Qin 2003; Chawla, Ganesh et al. 2004; Yang and Qin 2004; Ghosh, Bai et al. 2009). In the following section of the chapter, a brief literature review on the modeling of composites is presented from the perspectives of macro-, micro- and multi-scale.

1.2.1. Macroscale modeling of composites

Composite materials were first used in aircraft engine rotor blades in the 1960s. Since then, a great deal of research has been conducted to improve the properties of composite materials; now numerous publications cover anisotropic elasticity, mechanics of composite materials, design, analysis, fabrication, and application of composite structures (Lekhnitskii 1968; Lekhnitskii 1981; Reddy 2004; Vasiliev and Morozov 2007).

A typical composite structure consists of a system of layers bonded together. The layers can be made of different isotropic or anisotropic materials, and have different structures, thicknesses, and mechanical properties. The laminate characteristics are usually calculated using information about the number of layers, their stacking sequence, geometric and mechanical properties (Vasiliev and Morozov 2007).

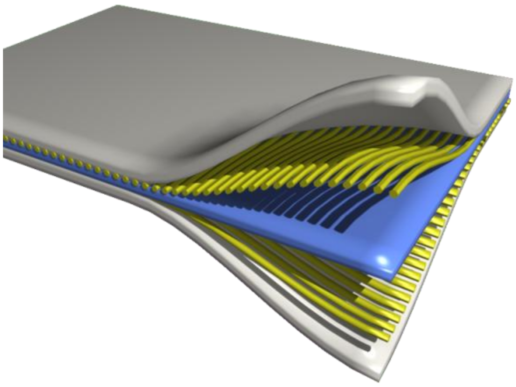

Figure 1.1 Schematic of a laminate composite plate with unidirectional ply.

The laminate composite plate (Figure 1.1), as one of the most widely used composites in engineering, has attracted most attention. Models developed for laminated composite plates are mainly based on classical laminate plate and first-order shear deformation theories (Reddy 2004). However, it has been demonstrated that these theories can lead to substantial errors in the prediction of stresses of highly anisotropic and/or moderately thick composite plates (Kant 1993). To overcome the limitations of analytical methods, numerical models based on finite element method (FEM) and boundary element method (BEM) have been increasingly employed in the last three decades (Ghosh, Nowak et al. 1997; Yang and Qin 2003; Chawla, Ganesh et al. 2004; Yang and Qin 2004; Ghosh, Bai et al. 2009; Sen and Aldas 2009; Ye and Chen 2011). BEM involves boundary integrals only, which makes it less computationally exhaustive than FEM, where integrals must be carried out throughout the volume (Huang, Hu et al. 1994; Qin 2004; Liu, Nishimura et al. 2008). However, the treatment of singular or near-singular boundary integrals is usually quite tedious and inefficient and an extra boundary integral equation is also required to evaluate the interior fields inside the domain; additionally, BEM is also difficult and tedious when dealing with multi-domain problems in applying compatibility and equilibrium conditions along the interfaces between subregions (Qin 2000; Qin 2004).

Extensive research has been performed on damage modeling of composites and a number of models have been proposed to predict damage accumulation (Shokrieh and Lessard 2000; Dvorak and Zhang 2001; Van Paepegem and Degrieck 2003). Among those, progressive damage models that use one or more damage variables related to measurable manifestations of damage (interface debonding, transverse matrix cracks, delamination size, etc.) are considered the most promising because they quantitatively account for the accumulation of damage in the composite structure. Kumar et al. studied the effect of impactor and laminate parameters on the impact response and impact-induced damages in graphite/epoxy laminated cylindrical shells using three-dimensional (3D) finite element formulation (Kumar, Rao et al. 2007). Ghosh and Sinha (2004) developed a finite element analysis procedure to predict the initiation and propagation of damages as well as to analyze laminated composite plates damaged under forced vibration and impact loads. Zhao and Cho (2004) investigated the impact-induced damage initiation and propagation in the laminated composite shell under low-velocity impact. In addition, Abrate (1994) presented an overview of the work carried out by different researchers in the field of the optimum design of composite laminated plates and shells subjected to constraints on strength, stiffness, buckling loads and fundamental natural frequencies.

1.2.2. Microscale modeling of composites

Micromechanics has gained significant attention and been extensively used to investigate heterogeneous composites on a finer scale so as to relate the properties of composite materials to their microstructures (Hill 1963; Hill 1965; Hashin 1979; Mura 1987; Ghosh, Nowak et al. 1997; Nemat-Nasser and Hori 1999; Chawla, Sidhu et al. 2006; Zohdi and Wriggers 2008; Ghosh, Bai et al. 2009; Zeng and Li 2010). The micromechanical approach can reveal some inherited characteristics of composites from the known properties of their constituents and can extract the macroscopic material properties required for a macroscale analysis. As a result, not only the global properties of the composites, but also various mechanisms such as damage initiation, crack growth and propagation can also be studied through microscale analysis.

In micromechanical analysis, the macroscopic properties are determined by a homogenization process that yields the effective stresses and strains acting on an effective, homogenized sample of material. Not long ago, homogenization and the determination of effective material parameters could only be done either by performing experiments or tests with an existing material sample or by applying semi-analytical methods with strong assumptions on the mechanical field variables or the microstructure of the material. There are several analytical micromechanical techniques extensively employed in practice such as the Eshelby approach, Mori-Tanaka method and Halpin-Tsai method (Eshelby 1957; Hill 1963; Mori and Tanaka 1973; Hashin 1983; Benveniste 1987; Aboudi 1991; Nemat-Nasser and Hori 1999). However, these semi-analytical methods do not lead to sufficiently accurate results, especially for complex morphologies, high contrast in phase properties material nonlinearities and more non-proportional load histories. This suggests the need to carry out direct numerical simulation of microstructures and to try to establish a realistic representation of the heterogeneous structure that appends and contains all the microscale details.

Some numerical methods, such as FEM and BEM have been widely used in micromechanical analysis for such a purpose (Ghosh, Nowak et al. 1997; Yang and Qin 2003; Chawla, Ganesh et al. 2004; Yang and Qin 2004; Seidel and Lagoudas 2006; Tyrus, Gosz et al. 2007; Ghosh, Bai et al. 2009). The BEM-based micromechanics model seems effective for handling materials with defects such as cracks and holes. It involves boundary integrals only, which makes BEM less computationally exhaustive than FEM, where integrals must be carried out throughout the volume (Huang, Hu et al. 1994; Qin 2004; Liu, Nishimura et al. 2008). However, the treatment of singular or near-singular boundary integrals is usually quite tedious and inefficient and an extra boundary integral equation is also required to evaluate the interior fields inside the domain; additionally, for solving multi-domain problems with BEM, each region is dealt with separately and then the whole body is linked together by applying compatibility and equilibrium conditions along the interfaces between the subregions. In consequence, implementation of the BEM becomes quite complex and the nonsymmetrical coefficient matrix of the resulting equations weakens the advantages of BEM (Qin 2000; Qin 2004). Nowadays sophisticated and efficient models to simulate realistic material behaviors continue to be developed in this active research area.

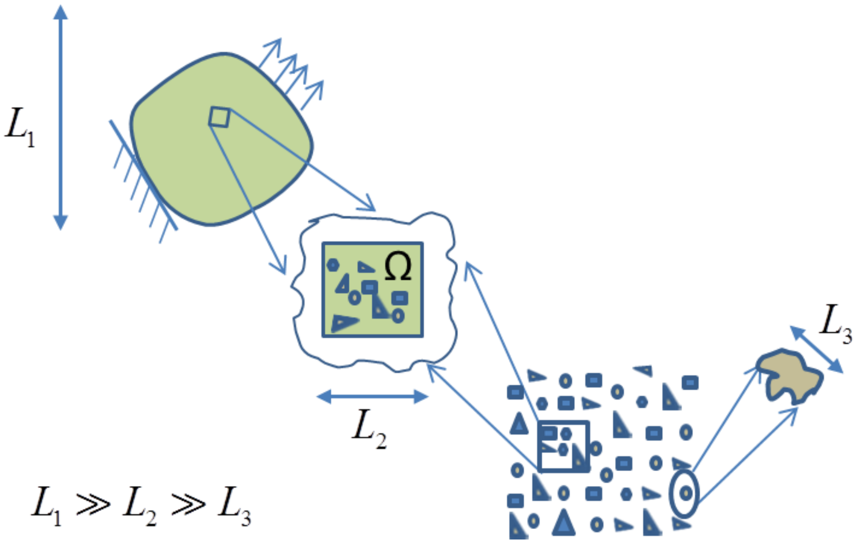

Figure 1.2 The size requirements of a representative volume element (RVE).

In micromechanical analysis, volume averaging takes place over a statistically representative volume element (RVE). The internal fields to be volumetrically averaged must be computed by solving a series of boundary value problems with test loadings (Zohdi and Wriggers 2008). It is noted that the RVE should satisfy the condition of that the characteristic size L_3 of heterogeneities is much smaller than the dimension L_2 of the RVE, which in turn is small compared to the wavelength L_1 of the macroscopic structure, as shown in Figure 1.2. As a result, the macro-stress and macro-strain are directly associated with the global analysis of the composite and on the macro-level, a RVE is regarded just as a point with a homogenized constitutive law.

The interface damage between fiber and matrix is also studied explicitly in the framework of a RVE of the composite (Caporale, Luciano et al. 2006; Aghdam, Falahatgar et al. 2008; Maligno, Warrior et al. 2009; Kushch, Shmegera et al. 2011). A RVE combined with proper boundary conditions to represent as closely as possible the real composite material macro-behavior would provide a tool to enhance practical understanding of the composite's material behavior based on its micro-constituents.

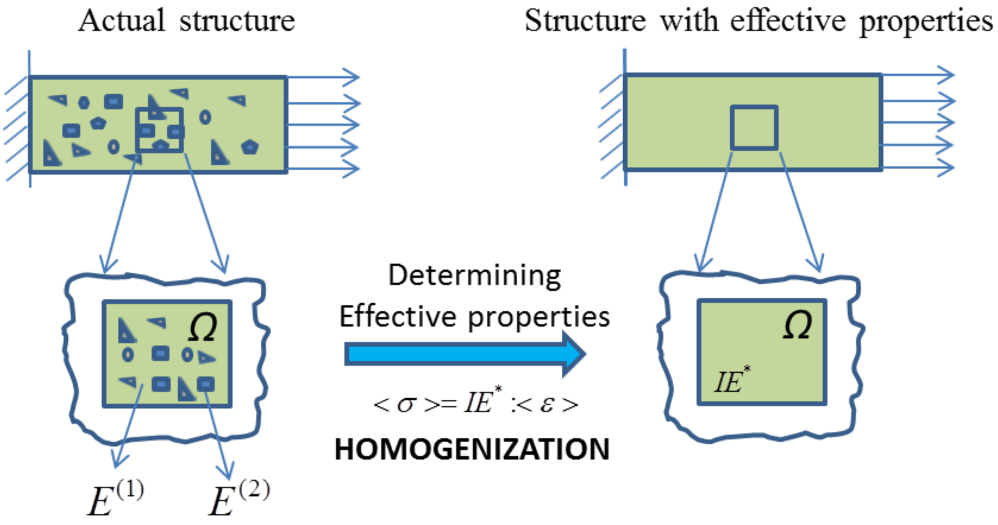

Figure 1.3 Effective material properties by homogenizing the heterogeneous microstructure.

The aim of computational micro-macro mechanics is to develop relationships between the microstructure and the macroscopic response of a composite material (Figure 1.3), using representative models on the microscale that are as simple as possible and provide an acceptable representation of the composite material under investigation (Zohdi and Wriggers 2008). However, it should be noted that in the foreseeable future it will be computationally prohibitive to conduct modeling and simulation of structures at the micro scale with explicit representation of heterogeneities. Similarly, it is possible to describe other effective quantities such as conductivity or diffusivity, in virtually the same manner, relating other volumetrically averaged field variables, as discussed in details in Chapter 7.

1.2.3. Multiscale modeling of composites

In the so-called multiscale modeling, macroscopic and microscopic models are coupled to take advantage of the efficiency of macroscopic models and the accuracy of the microscopic models. Multiscale modeling involves the design of combined macroscopic-microscopic computational methods that are more efficient than solving the full microscopic model and at the same time provides needed the information with desired accuracy. The asymptotic homogenization method is based on asymptotic expansion of the displacement, strain and stress fields and assumptions of spatial periodicity of microscopic RVEs (Bensoussan, Lions et al. 1978; Sánchez-Palencia 1980). Concurrent multiscale analyses are executed at macro- and micro-scales with information transfer between them (Fish, Yu et al. 1999; Kouznetsova, Brekelmans et al. 2001; Terada and Kikuchi 2001; Özdemir, Brekelmans et al. 2008; Yuan and Fish 2009). Ghosh and co-workers (Ghosh, Lee et al. 2001) combined the asymptotic homogenization method with the micro-mechanical Voronoi cell finite element method for multiscale analysis of deformation and damage in non-uniformly distributed microstructures.

Such homogenization studies have overcome the shortcomings of phenomenological and effective micromechanical theories through the introduction of simultaneous two-scale analysis at each load step. However, such approaches can be computationally very expensive since detailed micromechanical analyses must be conducted for every integration point of macroscopic elements. In recent work, a multiscale cohesive zone model have been proposed and implemented to relate mesoscale interface properties to atomistic potential (Zeng and Li 2010), which naturally takes into account material microstructures such as interface lattice orientation and rotation. In this method, there are two coarse graining models: one for the bulk medium and the other for the material interfaces, or defects. By constructing a finite width cohesive zone and extending the Cauchy-Born rule to coarse scale deformation field, the multiscale cohesive zone model can simulate the overall behaviors of non-uniform deformation caused by defects.

1.2.4. Modeling of multifield materials

Multifield materials have attracted much attention from researchers and scientists for their capability of interactively transferring energy from one type to another (Parton and Kudryavtsev 1988). These “smart materials” are responsive to multiphysical fields such as electric, magnetic or thermal fields in addition to the traditional mechanical field. Examples include piezoelectric ceramics, piezoelectric polymers and some biological tissues like bones. Piezoelectric materials are the most popular smart materials: they undergo deformation (strain) when an electric field is applied across them, and conversely produce voltage when a strain is applied, and thus can be used both as actuators and sensors. The coupling behaviors of these multifield materials are critical and unique for their applications in adaptive structures, actuators and sensors. It is of paramount important, therefore, to investigate the coupling behaviors of these materials for product design and analysis.

Meric and Saigal (1990) derived shape sensitivity expressions for linear piezoelectric structures with coupled mechanical and elastic field. Suleman and Venkayya (1995) presented a simple finite element formulation for laminated composite plates with piezoelectric layers. Chattopadhyay and Seeley (1997) used a finite element model based on a refined higher order theory to analyze piezoelectric materials surface bonded or embedded in composite laminates. Varelis and Saravanos (2008) presented a coupled multi-field mechanics framework for analyzing the non-linear response of shallow doubly curved adaptive laminated piezoelectric shells undergoing large displacements and rotations in thermal environments.

The Trefftz method such as the hybrid Trefftz FEM (HT-FEM), Trefftz BEM and Trefftz collocation method has also been successfully applied to problems of piezoelasticity. Qin (2003) derived the corresponding Trefftz finite element formulation for anti-plane problems of piezoelectric materials by constructing a pair of dual variational functional. Wang et.al (2006) analyzed singular electromechanical stress field in piezoelectric by combining the eigensolution approach and Trefftz finite element models. Qin (2003) presented a family of modified variational principles of piezoelectricity and succeeded in applying them to establish a Trefftz finite element formulation. Jin et al (2005) formulated the Trefftz collocation and the Trefftz Galerkin methods for plane piezoelectricity based on the solution sets derived by the complex variables method. Sheng et al (2006) developed a multi-domain Trefftz boundary collocation method for plane piezoelectricity with defects according to the plane piezoelectricity solution derived by Lekhnitskii's formalism. In addition, much work has been done on micromechanics modeling for designing a smart composite, e.g. piezoelectric composites, shape memory alloy (SMA) fiber composites, and piezoresistive composites, where smart materials with coupling behavior are used as reinforcement (Minoru 1999).

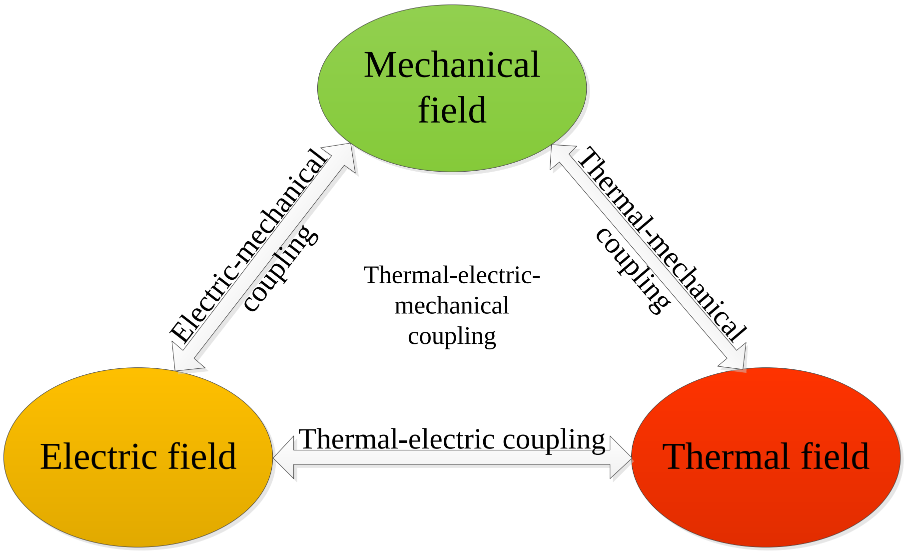

Figure 1.4 Coupling between the three considered physical fields.

In the present dissertation three physical fields are considered: mechanical, electrical and thermal field and their possible interactions (see Figure 1.4). The possible interactions are:

- One field problem: mechanical problem, thermal problem, electrical problem.
- Two fields problem: thermo-mechanical coupling, electro-mechanical coupling, and thermo-electrical coupling;

- Three fields problem: electro-thermo-mechanical coupling;

1.3. HYBRID FINITE ELEMENT METHOD

1.3.1. Hybrid Trefftz finite element method

The HT-FEM can be regarded as a variant of the conventional formulations of the FEM (Ritz-method-based FEM). The concept of Trefftz consists simply of using an approximation basis extracted from the solution set of the governing system of differential equations. When this concept is implemented in the framework of the FEM released from both node and local conformity concepts, the resulting finite element solving systems are sparse, free of spurious modes, and well-suited to adaptive refinement and parallel processing (Qin 2000; Toma 2007).

As Trefftz bases embody the physics of the problem, substantially higher levels of performance are observed in accuracy, stability and convergence (Jirousek and Wroblewski 1996; Qin 2000). Moreover, this basis leads to a solving system in which all coefficients are defined by boundary integral expressions. Hence, it leads to a formulation that combines the main features of the FEM and BEM, namely domain decomposition and boundary integral expressions, while dispensing with the use of (strongly singular) fundamental solutions and avoiding the major weaknesses of BEM, such as singularity and loss of symmetry and sparsity (Toma 2007).

In contrast to conventional FEM, the HT-FEM is based on a hybrid method which involves two novel independent fields: an independent auxiliary inter-element frame field defined on element boundary and an independent internal field chosen so as a priori satisfy the homogeneous governing differential equations by means of a suitable truncated T-complete function set of homogeneous solutions (Qin 2000; Qin and Wang 2008, Qin 2000). Inter-element continuity is enforced by employing a modified variational principle, which is used to construct a standard stiffness equation, and to establish the relationship between the frame field and the internal field of the element.

This approach involves only element boundary integrals, inherits the advantages of both conventional FEM and BEM, and has been successfully applied to various engineering problems (Qin 1994; Qin 1995; Qin 1996; Qin 2003; Qin and Wang 2008). The main advantages of HTFEM are: (a) it is only integral along element boundaries, enabling arbitrary polygonal or even curve-sided elements to be used; (b) no singular element boundary integral is involved; (c) it is likely to represent the optimal expansion bases for hybrid-type elements where inter-element continuity need not to be satisfied; (d) it can develop accurate crack-tip, singular corner or perforated elements by using appropriate known local solution functions as the trial functions of intra-element displacements (Qin 2003). However, the terms of truncated T-complete functions must be carefully selected to achieve the desired results, and it is difficult to generate T-complete functions for certain complex or new physical problems (Qin 2000; Qin and Wang 2008). Further, in the HT-FEM a coordinate transformation is required to keep the system matrix stable, and the necessary variational functional is somewhat complex for practical use.

The earliest applications of general purpose Trefftz elements can be dated back to 1977 when Jiroušek presented four formulations for solid mechanics problems (Jirousek and Leon 1977; Jirousek 1978), in which nonconforming elements are assumed to fulfill the governing equations a priori and the inter-element continuity and the boundary conditions are then enforced in some weighted residual or point-wise sense. Later Herrera (1980) introduced completeness and convergence criteria and Cheung et al. (Cheung, Jin et al. 1989; Jin and Cheung 1995) proposed the direct Trefftz boundary element method in opposition to the so-called indirect approach of Jiroušek by enforcing in a weak form of the governing differential equation, using a complete basis as weighting functions.

Since then, because of its generality and efficiency, this method has been quite successfully applied to plane elasticity (Jirousek and Teodorescu 1982), and Kirchhoff plates (Jirousek and N'Diaye 1990), moderately thick Reissner-Mindlin plates

(Jirousek, Wroblewski et al. 1995; Jirousek, Wróblewski et al. 1995), thick plates (Piltner 1992), thin shells (Voros 1991), general 3-D solid mechanics (Piltner 1987; Piltner 1992; de Freitas and Bussamra 2000), the Poisson equation (Zielinski and Zienkiewicz 1985), transient heat conduction analysis (Jirousek and Qin 1995), nonlinear problems (Qin 1996; Qin and Diao 1996; Qin 2005), and piezoelectric problems (Qin 2003; Qin 2003). Moreover, the h-version and the p-version of T-elements have been suggested, implemented and studied (Jirousek 1987; Jirousek and Venkatesh 1989; Qin and Diao 1996). Besides, special-purpose elements have been proposed to deal with various geometries or load-dependent singularities and local defects such as obtuse corners, cracks, holes, and concentrated load (Piltner 1985; Jirousek and Guex 1986; Dhanasekar, Han et al. 2006).

Extension into elastic and elastoplastic dynamic analyses in the time domain (Freitas 1999; Teixeira de Freitas and Wang 2001; Teixeira de Freitas and Wang 2002) was hindered by the fact that the commonly used time integration schemes destroy the parabolicity or hyperbolicity of the problem. This led to the subsequent development of special-purpose methods that rely on non-periodic spectral decomposition techniques (Teixeira de Freitas 2002; de Freitas 2003; de Freitas 2003) or on space-time approximations (Reutskiy 2004). The natural suitability of the Trefftz method to modeling solutions in the frequency domain has been reported in the literature in applications ranging from the solution of the Helmholtz equation (Cheung, Jin et al. 1991) to applications in acoustics and in fluid and solid mechanics (De Freitas 1997; Stojek 1998; Harari, Barai et al. 1999; Harari, Barai et al. 2001; Teixeira de Freitas and Cismaşiu 2003; Harari and Djellouli 2004), for both bounded and unbounded media. These results motivated the extension of the approach into coupled problems, as applied to structural acoustics, to poroelasticity, for saturated soils and soft tissues, and, in particular, to piezoelectricity (Sze, Wang et al. 2001; Qin 2003; Jin, Sheng et al. 2005; Wang, Sze et al. 2006; Moldovan and Freitas 2008; de Freitas and Toma 2009; de Freitas and Moldovan 2011).

1.3.2. Hybrid fundamental solution-based finite element method

Based on the framework of HT-FEM and the idea of the method of fundamental solution (MFS), a novel hybrid finite element formulation, called the Hybrid fundamental solution-based FEM (HFS-FEM), was recently developed for solving 2D linear heat conduction problems (Wang and Qin 2009; Wang and Qin 2010a), elastic problems (Wang and Qin 2010b; Cao, Qin et al. 2012a; Cao, Qin et al. 2013a), and piezoelectric problems (Cao, Qin et al. 2012b; Cao, Yu et al. 2013c). In HFS-FEM, fundamental solutions rather than T-complete functions are employed, which also exactly satisfy a priori the governing equations for the problem under consideration. In the approach, the intra-element field is approximated by the linear combination of the fundamental solutions analytically satisfying the related governing equation, and the domain integrals in the hybrid functional can be directly converted to boundary integrals without any appreciable increase in computational effort. It is also noticed that no singular integrals are involved in the HFS-FEM if the source point is located outside the element of interest and does not overlap with field point during computation (Wang and Qin 2010a). The resulting system of equations from the modified hybrid variational functional is expressed in terms of symmetric stiffness matrix and nodal displacements only, which is easy to implement into the standard FEM.

The proposed HFS-FEM inherits all the advantages of HT-FEM over the traditional FEM and the BEM, and obviates the difficulties that occur in HT-FEM. The HFS-FEM has simpler interpolation kernel expressions for intra-element fields (fundamental solutions) and avoids the coordinate transformation procedure required in the HT-FEM to keep the matrix inversion stable. Moreover, this approach also has the potential to achieve high accuracy using coarse meshes of high-degree elements, to enhance insensitivity to mesh distortion, to allow great liberty in element shape, and to accurately represent various local effects (such as hole, crack and inclusions) without troublesome mesh adjustment (Qin 2003; Gao, Wang et al. 2005; Dhanasekar, Han et al. 2006; Qin 2003; Dhanasekar, Han et al. 2006).

It should be noted that, however, the HFS-FEM approach differs from the BEM, although the same fundamental solution is employed. Using the reciprocal theorem, the BEM obtains the boundary integral equation, and usually encounters difficulty in dealing with singular or hyper-singular integrals in the analysis, while this weakness is removed using HFS-FEM. Moreover, HFS-FEM makes possible a more flexible element material definition which is important in dealing with multi-material problems, rather than the material definition being the same in the entire domain in BEM.

1.4. OBJECTIVES OF RESEARCH

HFS-FEM has been proposed for solving 2D elasticity and heat transfer problems. Considering the attractive merits of this method, it is of interest to further extend this method for wider applications in the modeling of advanced materials across micro and macro scales. Thus, the main objectives of this research can be defined as follows:

- To develop formulations of the method for both the 2D and 3D elasticity problems;
- To formulate an alternative formulations based on the Stroh formalism for modeling anisotropic composites and to assess its performance in simulation;
- To develop and assess the HFS-FEM in micromechanical modeling of heterogeneous composite materials based on the homogenization method and RVE concept, for both elasticity problem and heat conduction problem;
- To derive special-purposed elements to facilitate the modeling of composites with holes and inclusions for mesh reduction, and to assess their performance;

- To assess the performance of the elements used in HFS-FEM in terms of convergence and of their sensitivity to mesh distortion and materials incompressibility;
- To develop HFS-FEM formulations for modeling multifield materials such as thermal-mechanical and electric-mechanical problems.

1.5. SCOPE AND ORGANIZATION OF THESIS

The dissertation is organized in three main parts (i.e. macroscale modeling of elasticity and composites, microscale modeling of composites, and modeling of multifield problems) divided into nine chapters. In Chapter 1, the background and motivation of this research are firstly introduced, followed by a brief literature review of the topics discussed in this thesis. The research objectives are also stated. In Chapter 2, the basic ideas and the detailed formulations of the HFS-FEM for elasticity and potential problems are presented based on relevant previous research.

Chapter 3 proposes the formulations of the HFS-FEM for general 3D elasticity problems. The methods of particular solution and radial basis function approximation are proposed to deal with body force. Standard tests are carried out for a linear 8-node brick element and quadratic 20-node brick element. Several numerical examples are performed to investigate the method for modeling various problems including nearly incompressible materials.

Chapter 4 proposes a new formulation of HFS-FEM for 2D anisotropic composite materials based on the powerful Stroh formalism. The Stroh formalism and the derived fundamental solutions for generalized 2D anisotropic elastic problem are presented. Four numerical examples are presented to demonstrate the accuracy and efficiency of the proposed method.

Chapter 5 addresses applications of the HFS-FEM in micromechanical modeling of heterogeneous composites with isotropic fibers and orthotropic fibers. An efficient numerical homogenization method based on the newly developed method is applied to predict the macroscopic parameters of heterogeneous composites. The homogenization method and representative volume element (RVE) concepts are introduced in this context. For comparison, formulations of the HT-FEM are also presented in this chapter. The effect of fiber volume fractions, different inclusion shapes and arrangements on the effective stiffness coefficients of composites are investigated using the proposed micromechanical models.

Chapter 6 has basically the same structure as Chapter 5. In Chapter 6, formulations of the HFS-FEM for heat conduction problem are presented to model heterogeneous fiber-reinforced composites. Both the general element and special elements for circular hole and inclusion are proposed based on the relevant fundamental solutions to reduce the mesh refinement effort in modeling heterogeneous composites. A homogenization procedure for non-mechanical field variables is introduced for estimating the effective thermal properties of composites. Two examples are considered to assess the performance of the method and to investigate the influence of fiber volume fraction and fiber arrangement pattern on the effective thermal conductivity.

Chapter 7 extends the HFS-FEM to model 2D and 3D thermoelastic problems considering arbitrary body forces and temperature change. The method of particular solution is used to decompose the displacement solution into two parts: homogeneous solution and particular solution. The particular solution related to the body force and temperature change is approximated by using the radial basis function interpolation. Five different numerical examples are presented to demonstrate the accuracy and versatility of the proposed method.

In Chapter 8, the HFS-FEM is presented for modeling 2D piezoelectric material. Two different formulations are presented, the first based on Lekhnitskii formalism and the second on Stroh formalism. The foundational solution of transversely isotropic piezoelectric materials is employed to approximate the intra-element displacement and electrical potential field. A modified variational functional, satisfying the governing equation, boundary and continuity conditions, is proposed to derive the element stiffness matrix of the proposed method for piezoelectric materials. Numerical examples are presented to assess the accuracy and efficiency of the proposed formulations.

The dissertation closes in Chapter 9 with a brief assessment of the current research and some recommendations for future research.

Chapter 2. Framework of HFS-FEM for Plane Elasticity and Potential Problems

2.1. INTRODUCTION

During past decades, research into the development of efficient finite elements has mostly concentrated on the three variants of FEM. The first is the conventional (Ritz based) FEM (Zienkiewicz, Taylor et al. 2005), which is based on polynomial interpolations and has been increasingly used for analyzing most engineering problems. With this method, the domain of interest is divided into a number of smaller sub-domains or elements, and material properties are defined at the element level. The second variant, the natural-mode FEM (Argyris, Dunne et al. 1974), presents a significant alternative to conventional FEM with ramifications on all aspects of structural analysis. It makes a distinction between the constitutive and geometric parts of the element tangent stiffness, which can lead effortlessly to the non-linear effects associated with large displacements. When applied to composite structures, the physically clear and comprehensible theory with complete quadrature elimination and avoidance of modal (shape) functions can show distinctly the mechanical behavior of isotropic and composite shell structures (Tenek and Argyris 1997).

The third variant is the so-called HT-FEM (Qin 1995; Jirousek and Wroblewski 1996; Qin 2000). Unlike the other two methods, HT-FEM is based on a hybrid method that combines two independent assumed fields, an auxiliary inter-element frame field defined on each element boundary and an intra-element field chosen so as to a priori satisfy the homogeneous governing differential equations. Inter-element continuity is enforced by using a modified variational principle, which is used to construct the standard force-displacement relationship. The HT-FEM combines the advantages of FEM and BEM, as addressed in Chapter 1.

However, the terms of truncated T-complete functions must be carefully selected to achieve the desired results. Furthermore, they are difficult to develop for some physical problems. To eliminate this drawback of HT-FEM, a novel hybrid finite formulation based on fundamental solutions, HFS-FEM, was first developed to solve 2D heat conduction problems in single and multilayer-materials (Wang and Qin 2009). It was then developed and successfully applied to analyze plane elasticity problems under various loading conditions (Wang and Qin 2010b). The proposed HFS-FEM can be viewed as another variant of hybrid FEM which is different from the three aforementioned types. Sophisticated and efficient models for simulating realistic material behaviors still continue to be developed in this active research area.

In this chapter, the framework of the HFS-FEM for 2D elasticity and potential problems is presented in detail, with the intention of providing a general overview of the recently proposed method. The detailed procedures and implementation of the HFS-FEM are all described. The two independent fields assumed in this method are highlighted, and the modified variaitional function to assure the continuity between elements is addressed and proved. The numerical integral and its implementation are given and the rigid motion recovery is also presented for complementation. In summary, this can be regarded as a brief review of the relevant work by some members of the candidate's research group over the past three years. It also serves as the foundation of this dissertation which presents further development and application of this new method for modeling advanced composite materials, and is also a reference for the following chapters. Most of the materials presented in this chapter are organized and extended based on previous papers (Wang and Qin 2009; Wang and Qin 2010a; Wang and Qin 2010b) and a book (Qin and Wang 2008) published by Q.H. Qin and his co-worker.

2.2. FORMULATIONS OF HFS-FEM FOR ELASTICITY

2.2.1. Linear theory of plane elasticity

In linear elastic theory, linear strain-displacement relations can be used and equilibrium equations refer to the undeformed geometry (Timoshenko and Goodier

1970). In the rectangular Cartesian coordinates (X_1, X_2), the governing equations of plane elasticity can be expressed as

$$\sigma_{ij,j} = b_i, \qquad i, j = 1, 2 \tag{2.1}$$

If written in matrix form, it can be presented as

$$\mathbf{L}\boldsymbol{\sigma} = \mathbf{b} \tag{2.2}$$

where the stress vector $\boldsymbol{\sigma} = \left[\sigma_{11} \;\; \sigma_{22} \;\; \sigma_{12}\right]^{\mathrm{T}}$, the body force vector $\mathbf{b} = \left[b_1, b_2\right]^{\mathrm{T}}$ and the differential operator matrix $\mathbf{L}$ is given as

$$\mathbf{L} = \begin{bmatrix} \dfrac{\partial}{\partial X_1} & 0 & \dfrac{\partial}{\partial X_2} \\ 0 & \dfrac{\partial}{\partial X_2} & \dfrac{\partial}{\partial X_1} \end{bmatrix} \tag{2.3}$$

The strain-displacement relation is expressed in matrix form as

$$\boldsymbol{\varepsilon} = \mathbf{L}^{\mathbf{T}}\mathbf{u} \tag{2.4}$$

where the strain vector $\boldsymbol{\varepsilon} = \left[\varepsilon_{11} \;\; \varepsilon_{22} \;\; \varepsilon_{12}\right]^{\mathrm{T}}$, and the displacement vector $\mathbf{u} = \left[u_1, u_2\right]^{\mathrm{T}}$.

The constitutive equations for linear elasticity are given in matrix form as

$$\boldsymbol{\sigma} = \mathbf{D}\boldsymbol{\varepsilon} \tag{2.5}$$

where $\mathbf{D}$ is the material coefficient matrix with constant components for isotropic materials, which can be expressed as follows

$$\mathbf{D} = \begin{bmatrix} \tilde{\lambda} + 2G & \tilde{\lambda} & 0 \\ \tilde{\lambda} & \tilde{\lambda} + 2G & 0 \\ 0 & 0 & G \end{bmatrix} \tag{2.6}$$

where

$$\tilde{\lambda} = \frac{2\tilde{\nu}}{1 - 2\tilde{\nu}} G, \qquad G = \frac{E}{2(1+\nu)} \tag{2.7}$$

and

$$\tilde{\nu} = \begin{cases} \nu & \text{for plane strain} \\ \dfrac{\nu}{1+\nu} & \text{for plane stress} \end{cases} \tag{2.8}$$

where E is Young's module and ν Poisson's ratio. The two different kinds of boundary conditions can be expressed as

$$\begin{aligned} \mathbf{u} &= \bar{\mathbf{u}} && \text{on } \Gamma_u \\ \mathbf{t} = \mathbf{A}\boldsymbol{\sigma} &= \bar{\mathbf{t}} && \text{on } \Gamma_t \end{aligned} \tag{2.9}$$

where $\mathbf{t} = [t_1 \quad t_2]^T$ denotes the traction vector, $\bar{\mathbf{u}}$ are the prescribed boundary displacement vector and $\bar{\mathbf{t}}$ the prescribed traction vector, and $\mathbf{A}$ is a transformation matrix related to the direction cosine of the outward normal

$$\mathbf{A} = \begin{bmatrix} n_1 & 0 & n_2 \\ 0 & n_2 & n_1 \end{bmatrix} \tag{2.10}$$

where n_i is the unit outward normal to the boundary. Substituting Eqs. (2.4) and (2.5) into Eq. (2.2) yields the well-known Navier partial differential equations in terms of displacements

$$\mathbf{LDL}^{\mathrm{T}}\mathbf{u} = \mathbf{b} \tag{2.11}$$

2.2.2. Assumed fields

The main concept of the HFS-FEM approach is to establish a finite element formulation whereby intra-element continuity is enforced on a nonconforming internal displacement field by a functional (Wang and Qin 2010a). In this approach, the intra-element displacement fields are approximated by a linear combination of fundamental solutions of the problem of interest, as follows;

$$\mathbf{u}(\mathbf{x}) = \begin{bmatrix} u_1(\mathbf{x}) \\ u_2(\mathbf{x}) \end{bmatrix} = \sum_{j=1}^{n_s} \begin{bmatrix} u_{11}(\mathbf{x}, \mathbf{y}_{sj}) & u_{12}(\mathbf{x}, \mathbf{y}_{sj}) \\ u_{12}(\mathbf{x}, \mathbf{y}_{sj}) & u_{22}(\mathbf{x}, \mathbf{y}_{sj}) \end{bmatrix} \begin{Bmatrix} c_{1j} \\ c_{2j} \end{Bmatrix} = \mathbf{N_e c_e} \tag{2.12}$$

where n_s is the number of source points $\mathbf{y}_{sj} \, (j = 1, 2, \ldots, n_s)$ arranged outside the element to remove the singularity of the fundamental solution. In the analysis, the number of source points can be taken to be the same as the number of element nodes, which is free of spurious energy modes and can maintain the stiffness equations in full rank, as indicated in (Qin 2000). The matrix $\mathbf{N_e}$ and vector $\mathbf{c_e}$ can be written as

$$\mathbf{N_e} = \begin{bmatrix} u_{11}(\mathbf{x}, \mathbf{y}_{s1}) & u_{12}(\mathbf{x}, \mathbf{y}_{s1}) & \ldots\ldots & u_{11}(\mathbf{x}, \mathbf{y}_{sn_s}) & u_{12}(\mathbf{x}, \mathbf{y}_{sn_s}) \\ u_{12}(\mathbf{x}, \mathbf{y}_{s1}) & u_{22}(\mathbf{x}, \mathbf{y}_{s1}) & \ldots\ldots & u_{12}(\mathbf{x}, \mathbf{y}_{sn_s}) & u_{22}(\mathbf{x}, \mathbf{y}_{sn_s}) \end{bmatrix} \tag{2.13}$$

$$\mathbf{c_e} = [c_{11} \quad c_{21} \quad \ldots\ldots \quad c_{1n} \quad c_{2n}]^T \tag{2.14}$$

in which the components $u_{ij}(\mathbf{x}, \mathbf{y}_{sk})$ is the induced displacement component in the *i*-direction at the field point **x** due to a unit point load applied at the source point $\mathbf{y}_{sk}$ in the *j*-direction. The fundamental solution $u_{ij}(\mathbf{x}, \mathbf{y}_{sk})$ is given as

$$
\begin{aligned}
u_{11}(\mathbf{x},\mathbf{y}_\mathbf{s}) &= A[(3-4\nu)\ln r - \frac{r_1^2}{r^2}] \\
u_{21}(\mathbf{x},\mathbf{y}_\mathbf{s}) &= u_{12}(\mathbf{x},\mathbf{x}_\mathbf{s}) = -A\frac{r_1 r_2}{r^2} \\
u_{22}(\mathbf{x},\mathbf{y}_\mathbf{s}) &= A[(3-4\nu)\ln r - \frac{r_2^2}{r^2}]
\end{aligned}
\tag{2.15}
$$

where $r_i = x_i - x_{is}$, $r = \sqrt{r_1^2 + r_2^2}$, $A = -1/8G\pi(1-\nu)$ for isotropic materials (Sauter and Schwab 2010).

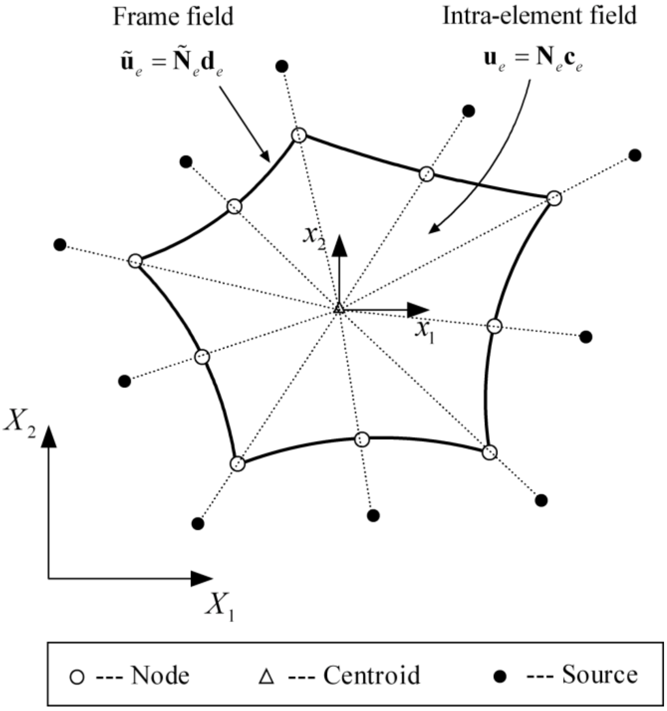

Figure 2.1 Intra-element field, frame field in a particular element in HFS-FEM, and the generation of source points for a particular element.

The source point $\mathbf{x}_{sj}\,(j = 1, 2, \ldots, n_s)$ can be generated by means of the following method employed in the MFS (Wang, Qin et al. 2006; Hui and Qinghua 2007; Wang and Qin 2010a)

$$\mathbf{y} = \mathbf{x}_b + \gamma\left(\mathbf{x}_b - \mathbf{x}_c\right) \tag{2.16}$$

where γ is a dimensionless coefficient, $\mathbf{x}_b$ is the elementary boundary point and $\mathbf{x}_c$ the geometrical centroid of the element. For a particular element as shown in Figure 2.1, the nodes of the element can be used to generate related source points for simplicity. Determination of γ must be discussed for different problems (Wang and Qin 2009; Wang and Qin 2010b).

Making use of the constitutive Eq. (2.5), the corresponding stress fields can be expressed as

$$\boldsymbol{\sigma}(\mathbf{x}) = \mathbf{T_e c_e} \tag{2.17}$$

where

$$\mathbf{T_e} = \begin{bmatrix} \sigma_{111}(\mathbf{x},\mathbf{y}_1) & \sigma_{211}(\mathbf{x},\mathbf{y}_1) & \ldots\ldots & \sigma_{111}(\mathbf{x},\mathbf{y}_{n_s}) & \sigma_{211}(\mathbf{x},\mathbf{y}_{n_s}) \\ \sigma_{122}(\mathbf{x},\mathbf{y}_1) & \sigma_{222}(\mathbf{x},\mathbf{y}_1) & \ldots\ldots & \sigma_{122}(\mathbf{x},\mathbf{y}_{n_s}) & \sigma_{222}(\mathbf{x},\mathbf{y}_{n_s}) \\ \sigma_{112}(\mathbf{x},\mathbf{y}_1) & \sigma_{212}(\mathbf{x},\mathbf{y}_1) & \ldots\ldots & \sigma_{112}(\mathbf{x},\mathbf{y}_{n_s}) & \sigma_{212}(\mathbf{x},\mathbf{y}_{n_s}) \end{bmatrix} \tag{2.18}$$

As a consequence, the traction is written as

$$\mathbf{t} = \begin{Bmatrix} t_1 \\ t_2 \end{Bmatrix} = \mathbf{n}\boldsymbol{\sigma} = \mathbf{Q_e c_e} \tag{2.19}$$

in which

$$\mathbf{Q_e} = \mathbf{n}\mathbf{T_e}, \ \mathbf{n} = \begin{bmatrix} n_1 & 0 & n_2 \\ 0 & n_2 & n_1 \end{bmatrix} \tag{2.20}$$

The corresponding stress components $\sigma_{ijk}(\mathbf{x},\mathbf{y})$ are expressed as

$$\begin{aligned} \sigma_{111} &= Ac_{11}\left(\frac{2r_1^3}{r^4} + \frac{(1-4\nu)r_1}{r^2}\right) + Ac_{12}\left(\frac{2r_1 r_2^2}{r^4} - \frac{r_1}{r^2}\right) \\ \sigma_{221} &= Ac_{12}\left(\frac{2r_1^3}{r^4} + \frac{(1-4\nu)r_1}{r^2}\right) + Ac_{22}\left(\frac{2r_1 r_2^2}{r^4} - \frac{r_1}{r^2}\right) \\ \sigma_{121} &= c_{66}A\left(\frac{4r_1^2 r_2}{r^4} + \frac{2(1-2\nu)r_2}{r^2}\right) \end{aligned} \tag{2.21}$$

$$\begin{aligned} \sigma_{112} &= \{Ac_{11}\left(\frac{2r_1^2 r_2}{r^4} - \frac{r_2}{r^2}\right) + Ac_{12}\left(\frac{(1-4\nu)r_2}{r^2} + \frac{2r_2^3}{r^4}\right)\} \\ \sigma_{222} &= \{Ac_{12}\left(\frac{2r_1^2 r_2}{r^4} - \frac{r_2}{r^2}\right) + Ac_{22}\left(\frac{(1-4\nu)r_2}{r^2} + \frac{2r_2^3}{r^4}\right)\} \\ \sigma_{122} &= Ac_{66}\left(\frac{2(1-2\nu)r_1}{r^2} + \frac{4r_1 r_2^2}{r^4}\right) \end{aligned} \tag{2.22}$$

The unknown $\mathbf{c_e}$ in Eq. (2.12) may be calculated by using a hybrid technique (Wang and Qin 2009), in which the elements are linked through an auxiliary conforming displacement frame which has the same form as in conventional FEM (see Figure 2.1). This means that in the HFS-FEM, a conforming displacement field should be independently defined on the element boundary to enforce the field continuity between elements and also to link the unknown $\mathbf{c_e}$ with nodal displacement $\mathbf{d_e}$. Thus, the frame is defined as

$$\tilde{\mathbf{u}}(\mathbf{x}) = \begin{Bmatrix} \tilde{u}_1 \\ \tilde{u}_2 \end{Bmatrix} = \begin{Bmatrix} \tilde{\mathbf{N}}_1 \\ \tilde{\mathbf{N}}_2 \end{Bmatrix} \mathbf{d}_e = \tilde{\mathbf{N}}_e \mathbf{d}_e, \qquad (\mathbf{x} \in \Gamma_e) \tag{2.23}$$

where the symbol "~" is used to specify that the field is defined on the element boundary only, $\tilde{\mathbf{N}}_e$ is the matrix of shape functions, $\mathbf{d}_e$ is the nodal displacements of elements. Taking side 1-2 of a particular 4-node element (see Figure 2.1) as an example, $\tilde{\mathbf{N}}_e$ and $\mathbf{d}_e$ can be expressed as

$$\tilde{\mathbf{N}}_e = \begin{bmatrix} 0 & 0 & \tilde{N}_1 & 0 & \tilde{N}_2 & 0 & 0 & 0 \\ 0 & 0 & 0 & \tilde{N}_1 & 0 & \tilde{N}_2 & 0 & 0 \end{bmatrix} \tag{2.24}$$

$$\mathbf{d}_e = \begin{bmatrix} u_{11} & u_{21} & u_{12} & u_{22} & u_{13} & u_{23} & u_{14} & u_{24} \end{bmatrix}^T \tag{2.25}$$

where $\tilde{N}_1$ and $\tilde{N}_2$ can be expressed by natural coordinate $\xi \in [-1,1]$

$$\tilde{N}_1 = \frac{1-\xi}{2}, \qquad \tilde{N}_2 = \frac{1+\xi}{2} \tag{2.26}$$

2.2.3. Modified functional for the hybrid FEM

The HFS-FEM equation for a plane elastic problem can be established by the variational approach (Wang and Qin 2010a). Compared to the functional employed in the conventional FEM, the present hybrid functional is constructed by adding a hybrid integral term related to the intra-element and element frame displacement fields to guarantee satisfaction of the displacement and traction continuity conditions on the common boundary of two adjacent elements. In the absence of body forces, the hybrid functional Π_{me} used for deriving the present HFS-FEM can be constructed as (Qin and Wang 2008)

$$\Pi_{me} = \frac{1}{2} \iint_{\Omega_e} \sigma_{ij} \varepsilon_{ij} d\Omega - \int_{\Gamma_t} \bar{t}_i \tilde{u}_i d\Gamma + \int_{\Gamma_e} t_i (\tilde{u}_i - u_i) d\Gamma \tag{2.27}$$

where $\tilde{u}_i$ and u_i are the intra-element displacement field defined within the element and the frame displacement field defined on the element boundary, respectively. Ω_e and Γ_e are the element domain and element boundary, respectively. Γ_t, Γ_u and Γ_I stands respectively for the specified traction boundary, specified displacement boundary and inter-element boundary ($\Gamma_e = \Gamma_t + \Gamma_u + \Gamma_I$).

By applying the Gaussian theorem, Eq. (2.27) can be simplified to

$$
\begin{aligned}
\Pi_{me} &= \frac{1}{2}\iint_{\Omega_e} \sigma_{ij}\varepsilon_{ij} d\Omega - \int_{\Gamma_t} \bar{t}_i \tilde{u}_i d\Gamma + \int_{\Gamma_e} t_i(\tilde{u}_i - u_i) d\Gamma \\
&= \frac{1}{2}(\int_{\Gamma_e} t_i u_i d\Gamma - \iint_{\Omega_e} \sigma_{ij,j} u_i d\Omega) - \int_{\Gamma_t} \bar{t}_i \tilde{u}_i d\Gamma + \int_{\Gamma_e} t_i(\tilde{u}_i - u_i) d\Gamma
\end{aligned}
\tag{2.28}
$$

Due to the satisfaction of the equilibrium equation with the constructed intra-element field, we have the following expression for HFS finite element model

$$
\begin{aligned}
\Pi_{me} &= \frac{1}{2}\int_{\Gamma_e} t_i u_i d\Gamma - \int_{\Gamma_t} \bar{t}_i \tilde{u}_i d\Gamma + \int_{\Gamma_e} t_i(\tilde{u}_i - u_i) d\Gamma \\
&= -\frac{1}{2}\int_{\Gamma_e} t_i u_i d\Gamma + \int_{\Gamma_e} t_i \tilde{u}_i d\Gamma - \int_{\Gamma_t} \bar{t}_i \tilde{u}_i d\Gamma
\end{aligned}
\tag{2.29}
$$

The functional in Eq. (2.29) contains boundary integrals only and will be used to derive the HFS-FEM formulation for the plane isotropic elastic problem.

2.2.4. Element stiffness equation

The element stiffness equation can be generated by setting $\delta\Pi_{me} = 0$. Substituting Eqs. (2.12), (2.23) and (2.19) into the functional of Eq. (2.29), we have

$$\Pi_{me} = -\frac{1}{2}\mathbf{c}_e{}^{\mathrm{T}}\mathbf{H}_e\mathbf{c}_e + \mathbf{c}_e{}^{\mathrm{T}}\mathbf{G}_e\mathbf{d}_e - \mathbf{d}_e{}^{\mathrm{T}}\mathbf{g}_e \tag{2.30}$$

where

$$\mathbf{H}_e = \int_{\Gamma_e} \mathbf{Q}_e^{\mathrm{T}}\mathbf{N}_e \mathrm{d}\Gamma, \quad \mathbf{G}_e = \int_{\Gamma_e} \mathbf{Q}_e^{\mathrm{T}}\tilde{\mathbf{N}}_e \mathrm{d}\Gamma, \quad \mathbf{g}_e = \int_{\Gamma_t} \tilde{\mathbf{N}}_e^{\mathrm{T}}\bar{\mathbf{t}} d\Gamma \tag{2.31}$$

To enforce inter-element continuity on the common element boundary, the unknown vector $\mathbf{c}_e$ should be expressed in terms of nodal degree of freedom (DOF) $\mathbf{d}_e$. The stationary condition of the functional Π_{me} with respect to $\mathbf{c}_e$ and $\mathbf{d}_e$ yields, respectively,

$$\frac{\partial\Pi_{me}}{\partial\mathbf{c}_e{}^{\mathrm{T}}} = -\mathbf{H}_e\mathbf{c}_e + \mathbf{G}_e\mathbf{d}_e = \mathbf{0} \tag{2.32}$$

$$\frac{\partial\Pi_{me}}{\partial\mathbf{d}_e{}^{\mathrm{T}}} = \mathbf{G}_e{}^{T}\mathbf{c}_e - \mathbf{g}_e = \mathbf{0} \tag{2.33}$$

Therefore, the relationship between $\mathbf{c}_e$ and $\mathbf{d}_e$, and the stiffness equation can be obtained as follows

$$\mathbf{c}_e = \mathbf{H}_e^{-1}\mathbf{G}_e\mathbf{d}_e \tag{2.34}$$

$$\mathbf{K}_e\mathbf{d}_e = \mathbf{g}_e \tag{2.35}$$

where $\mathbf{K}_e = \mathbf{G}_e{}^{\mathrm{T}}\mathbf{H}_e{}^{-1}\mathbf{G}_e$ is the element stiffness matrix.

2.2.5. Numerical integral for H and G matrix

It is generally difficult to obtain the analytical expression of the integral in Eq. (2.31) and numerical integration along the element boundary is required. In the calculation, the widely used Gaussian integration is employed.

The H matrix can be expressed as

$$\mathbf{H}_e = \int_{\Gamma_e} \mathbf{Q}_e^{\mathrm{T}} \mathbf{N}_e \mathrm{d}\Gamma = \int_{\Gamma_e} \mathbf{F}(\mathbf{x}) \mathrm{d}\Gamma \tag{2.36}$$

by introducing the matrix function

$$\mathbf{F}(\mathbf{x}) = \left[F_{ij}(\mathbf{x}) \right]_{m \times m} = \mathbf{Q}_e^{\mathrm{T}} \mathbf{N}_e \tag{2.37}$$

and further, it can be rewritten into the component form

$$H_{ij} = \int_{\Gamma_e} F_{ij}(\mathbf{x}) \mathrm{d}\Gamma = \sum_{l=1}^{n_e} \int_{\Gamma_{el}} F_{ij}(\mathbf{x}) \mathrm{d}\Gamma \tag{2.38}$$

where

$$\mathrm{d}\Gamma = \sqrt{(\mathrm{d}x_1)^2 + (\mathrm{d}x_2)^2} = \sqrt{\left(\frac{\mathrm{d}x_1}{\mathrm{d}\xi}\right)^2 + \left(\frac{\mathrm{d}x_2}{\mathrm{d}\xi}\right)^2} \mathrm{d}\xi = J \mathrm{d}\xi \tag{2.39}$$

and J is the Jacobian expressed as

$$J = \sqrt{\left(\frac{\mathrm{d}x_1}{\mathrm{d}\xi}\right)^2 + \left(\frac{\mathrm{d}x_2}{\mathrm{d}\xi}\right)^2}. \tag{2.40}$$

where

$$\left[\frac{\mathrm{d}x_1}{\mathrm{d}\xi}, \frac{\mathrm{d}x_2}{\mathrm{d}\xi} \right]^T = \sum_{i=1}^{n_o} \frac{\mathrm{d}N_i(\xi)}{\mathrm{d}\xi} \begin{Bmatrix} x_{1i} \\ x_{2i} \end{Bmatrix} \tag{2.41}$$

and n_0 is the number of nodes of each edge. Thus, the Gaussian numerical integration for the H matrix can be calculated by

$$H_{ij} = \sum_{l=1}^{n_e} \left[\int_{-1}^{+1} F_{ij}(\mathbf{x}(\xi)) J(\xi) \mathrm{d}\xi \right] \approx \sum_{l=1}^{n_e} \left[\sum_{k=1}^{n_p} w_k F_{ij}(\mathbf{x}(\xi_k)) J(\xi_k) \right] \tag{2.42}$$

where n_e is the number of edges of the element, n_p is the Gaussian sampling points employed in the Gaussian numerical integration and w_k is the weight of Gaussian integration for sampling point. Similarly, the $\mathbf{G}_e$ matrix can be calculated by

$$G_{ij} = \sum_{l=1}^{n_e} \left[\int_{-1}^{1} \tilde{F}_{ij} [\mathbf{x}(\xi)] \, J(\xi) d\xi \right] \approx \sum_{l=1}^{n_e} \left\{ \sum_{k=1}^{n_p} w_k \tilde{F}_{ij} [\mathbf{x}(\xi_k)] J(\xi_k) \right\} \tag{2.43}$$

The calculation of vector $\mathbf{g}_e$ in Eq. (2.31) is the same as that in the conventional FEM, so it is convenient to incorporate the proposed HFS-FEM into the standard FEM program. Besides, the flux is directly computed from Eqs. (2.56). The boundary DOF can be directly computed from Eq. (2.23) and the unknown variables at interior points of the element can be determined from Eq. (2.12) plus the recovered rigid-body modes in each element, which are introduced in the following section.

2.2.6. Recovery of rigid-body motion

Once the nodal displacement $\mathbf{d}_e$ of the element e has been determined, the internal parameters $\mathbf{c}_e$ can be found from Eq. (2.34). The internal displacements calculated by Eq. (2.12) may, however, be in error by three rigid-body motion modes, since such terms were discarded to prevent the element deformability matrix $\mathbf{H}_e$ from being singular. These missing terms can easily be recovered by setting for the augmented internal displacements

$$u_e = \mathbf{N}_e \mathbf{c}_e + \begin{bmatrix} 1 & 0 & x_2 \\ 0 & 1 & -x_1 \end{bmatrix} \mathbf{c_0} \tag{2.44}$$

where the undetermined rigid-body motion parameter $\mathbf{c}_0$ can be calculated using the least square matching of u_e and $\tilde{u}_e$ at element nodes

$$\sum_{i=1}^{n} \left[\left(u_{1i} - \tilde{u}_{1i}\right)^2 + \left(u_{2i} - \tilde{u}_{2i}\right)^2 \right] = \min \tag{2.45}$$

The above equation finally yields

$$\mathbf{c_0} = \mathbf{R}_e^{-1} \mathbf{r_e} \tag{2.46}$$

where

$$\mathbf{R_e} = \sum_{i=1}^{n} \begin{bmatrix} 1 & 0 & x_{2i} \\ 0 & 1 & -x_{1i} \\ x_{2i} & -x_{1i} & x_{1i}^2 + x_{2i}^2 \end{bmatrix} \tag{2.47}$$

$$\mathbf{r_e} = \sum_{i=1}^{n} \begin{Bmatrix} \Delta u_{e1i} \\ \Delta u_{e2i} \\ \Delta u_{e2i} x_{1i} - \Delta u_{e1i} x_{2i} \end{Bmatrix} \tag{2.48}$$

and $\Delta \mathbf{u}_{ei} = \left(\tilde{\mathbf{u}}_e - \mathbf{N}_e \mathbf{c}_e\right)\big|_{\text{node } i}$, and n is the number of nodes for the element under consideration.

2.3. FORMULATIONS OF HFS-FEM FOR POTENTIAL PROBLEMS

2.3.1. Basic equations of potential problems

The Laplace equation of a well-posed potential problem (e.g. heat conduction) in a general plane domain Ω can be expressed as

$$\nabla^2 u(\mathbf{x}) = 0 \qquad \forall \mathbf{x} \in \Omega \tag{2.49}$$

with the following boundary conditions:

—Dirichlet boundary condition related to the unknown potential field

$$u = \bar{u} \qquad \text{on } \Gamma_u \tag{2.50}$$

—Neumann boundary condition for the boundary normal flux

$$q = u_{,i} n_i = \bar{q} \qquad \text{on } \Gamma_q \tag{2.51}$$

where ∇^2 is the Lapalce operator, u is the unknown field variable and q represents the boundary flux, n_i is the i th component of outward normal vector to the boundary $\Gamma = \Gamma_u \cup \Gamma_q$, and $\bar{u}$ and $\bar{q}$ are specified functions on the related boundaries, respectively. The space derivatives are indicated by a comma, i.e. $u_{,i} = \partial u / \partial x_i$, and the subscript index i takes values 1 and 2 in the analysis. The repeated subscript indices stand for the summation convention.

For convenience, the equation (2.51) can be rewritten in matrix form as

$$q = \mathbf{A} \begin{bmatrix} u_{,1} \\ u_{,2} \end{bmatrix} = \bar{q} \tag{2.52}$$

with $\mathbf{A} = \begin{bmatrix} n_1 & n_2 \end{bmatrix}$.

2.3.2. Assumed fields

In the following section, the procedure for developing a hybrid finite element model with a fundamental solution as interior trial function is described based on the boundary value problem defined by Eqs. (2.49)-(2.51). As in the conventional FEM and HT-FEM, the domain under consideration is divided into a series of elements. For each element of the domain, two independent fields are assumed in the manner discussed in the next two subsections (Qin and Wang 2008).

For a particular element e which occupies sub-domain Ω_e, first assume that the field variable defined in the element domain is extracted from a linear combination of fundamental solutions centered at different source points (see Figure 2.1)

$$\mathbf{u}_e(\mathbf{x}) = \sum_{j=1}^{n_s} N_e(\mathbf{x}, \mathbf{y}_j) c_{ej} = \mathbf{N}_e(\mathbf{x}) \mathbf{c}_e \qquad \forall \mathbf{x} \in \Omega_e, \mathbf{y}_j \notin \Omega_e \tag{2.53}$$

where c_{ej} is undetermined coefficients and n_s is the number of virtual sources outside the element e. $N_e(\mathbf{x}, \mathbf{y}_j)$ is the fundamental solutions to the partial differential equation

$$\nabla^2 N_e(\mathbf{x}, \mathbf{y}) + \delta(\mathbf{x}, \mathbf{y}) = 0 \qquad \forall \mathbf{x}, \mathbf{y} \in \Re^2 \tag{2.54}$$

which gives

$$N_e(\mathbf{x}, \mathbf{y}) = -\frac{1}{2\pi} \ln r(\mathbf{x}, \mathbf{y}) \tag{2.55}$$

Clearly, Eq. (2.53) analytically satisfies Eq. (2.49) due to the solution property of $N_e(\mathbf{x}, \mathbf{y}_j)$. Virtual source points for potential problems are usually generated by the same means as in the elasticity problems addressed in Section 2.

The corresponding outward normal derivative of u_e on Γ_e is

$$\mathbf{q}_e = \frac{\partial u_e}{\partial n} = \mathbf{Q}_e \mathbf{c}_e \tag{2.56}$$

where

$$\mathbf{Q}_e = \frac{\partial \mathbf{N}_e}{\partial n} = \mathbf{A} \mathbf{T}_e \tag{2.57}$$

with

$$\mathbf{T}_e = \begin{bmatrix} \dfrac{\partial \mathbf{N}_e}{\partial x_1} \\ \dfrac{\partial \mathbf{N}_e}{\partial x_2} \end{bmatrix} \tag{2.58}$$

To enforce conformity on the field variable u, for instance, $u_e = u_f$ on $\Gamma_e \cap \Gamma_f$ of any two neighboring elements *e* and *f*, an auxiliary inter-element frame field $\tilde{u}$ is used and expressed in terms of the same DOF, $\mathbf{d}_e$, as used with conventional finite elements. In this case, $\tilde{u}$ is confined to the whole element boundary, that is

$$\tilde{\mathbf{u}}_e(\mathbf{x}) = \tilde{\mathbf{N}}_e(\mathbf{x}) \mathbf{d}_e \tag{2.59}$$

which is independently assumed along the element boundary in terms of nodal DOF $\mathbf{d}_e$, where $\tilde{\mathbf{N}}_e(\mathbf{x})$ represents the conventional finite element interpolating functions. For example, a simple interpolation of the frame field on the side with three nodes of a particular element can be given in the form

$$\tilde{u} = \tilde{N}_1 u_1 + \tilde{N}_2 u_2 + \tilde{N}_3 u_3 \tag{2.60}$$

where $\tilde{N}_i$ ($i = 1, 2, 3$) stands for shape functions in terms of natural coordinate ξ defined in Figure 2.2 .

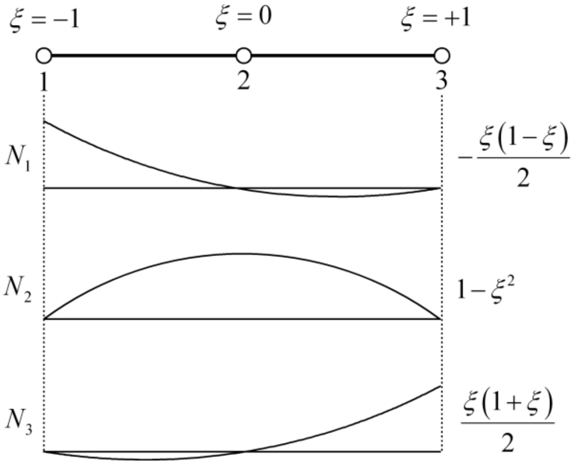

Figure 2.2 Typical quadratic interpolation for the frame field.

2.3.3. Modified variational principle

For the boundary value problem defined in Eqs. (2.49)-(2.50) and (2.51), since the stationary conditions of the traditional potential or complementary variational functional cannot guarantee the inter-element continuity condition required in the proposed HFS FE model, as done in the HT-FEM, a variational functional corresponding to the new trial functions should be modified to assure additional continuity across the common boundaries Γ_{Ief} between intra-element fields of element '*e*' and element '*f*' (see Figure 2.3):

$$\left.\begin{aligned} u_e &= u_f \quad \text{(conformity)} \\ q_e + q_f &= 0 \quad \text{(reciprocity)} \end{aligned}\right\} \text{ on } \Gamma_{Ief} = \Gamma_e \cap \Gamma_f \tag{2.61}$$

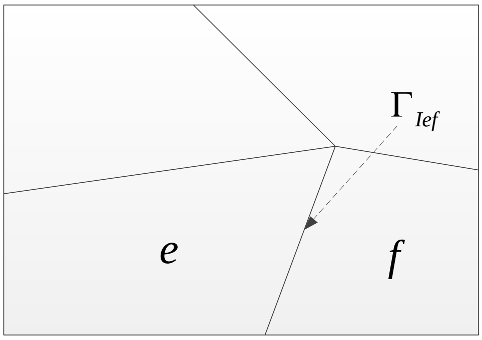

Figure 2.3 Illustration of continuity between two adjacent elements '*e*' and '*f*'.

A modified potential functional is developed as follows

$$\Pi_m = \sum_e \Pi_{me} = \sum_e \left\{ \Pi_e + \int_{\Gamma_e} (\tilde{u} - u) q \mathrm{d}\Gamma \right\} \tag{2.62}$$

where

$$\Pi_e = \frac{1}{2} \int_{\Omega_e} u_{,i} u_{,i} \mathrm{d}\Omega - \int_{\Gamma_{qe}} \bar{q} \tilde{u} \mathrm{d}\Gamma \tag{2.63}$$

in which the governing equation (2.49) is assumed to be satisfied, a *priori*, for deriving the HFS-FE model. It should be mentioned that the functional (2.62) is different from that used in (Qin 2000). The boundary Γ_e of a particular element consists of the following parts

$$\Gamma_e = \Gamma_{ue} \cup \Gamma_{qe} \cup \Gamma_{Ie} \tag{2.64}$$

where Γ_{Ie} represents the inter-element boundary of the element '*e*' shown in Figure 2.1.

Next we show that the stationary condition of the functional (2.62) leads to the governing equation (Euler equation), boundary conditions and continuity conditions. To this end, invoking (2.63) and (2.62) gives the following functional for the problem domain

$$\Pi_{me} = \frac{1}{2} \int_{\Omega_e} u_{,i} u_{,i} \mathrm{d}\Omega - \int_{\Gamma_{qe}} \bar{q} \tilde{u} \mathrm{d}\Gamma + \int_{\Gamma_e} q (\tilde{u} - u) \mathrm{d}\Gamma \tag{2.65}$$

of which the first-order variational yields

$$\delta\Pi_{me} = \int_{\Omega_e} u_{,i} \delta u_{,i} \mathrm{d}\Omega - \int_{\Gamma_{qe}} \bar{q} \delta\tilde{u} \mathrm{d}\Gamma + \int_{\Gamma_e} (\delta\tilde{u} - \delta u) q \mathrm{d}\Gamma + \int_{\Gamma_e} (\tilde{u} - u) \delta q \mathrm{d}\Gamma \tag{2.66}$$

Using divergence theorem

$$\int_\Omega f_{,i} h_{,i} \mathrm{d}\Omega = \int_\Gamma h f_{,i} n_i \mathrm{d}\Gamma - \int_\Omega h \nabla^2 f \mathrm{d}\Omega \tag{2.67}$$

we can obtain

$$\delta\Pi_{me} = \int_{\Omega_e} u_{,ii}\delta u \mathrm{d}\Omega - \int_{\Gamma_{qe}} \left(\bar{q}-q\right)\delta\tilde{u}\mathrm{d}\Gamma + \int_{\Gamma_{ue}} q\delta\tilde{u}\mathrm{d}\Gamma + \int_{\Gamma_{Ie}} q\delta\tilde{u}\mathrm{d}\Gamma + \int_{\Gamma_e} \left(\tilde{u}-u\right)\delta q\mathrm{d}\Gamma \tag{2.68}$$

For the displacement-based method, the potential conformity should be satisfied in advance, that is,

$$\begin{aligned} &\delta\tilde{u} = 0 && \text{on } \Gamma_{ue} && (\because \tilde{u} = \bar{u}) \\ &\delta\tilde{u}^e = \delta\tilde{u}^f && \text{on } \Gamma_{Ief} && (\because \tilde{u}^e = \tilde{u}^f) \end{aligned} \tag{2.69}$$

then, Eq. (2.68) can be rewritten as

$$\delta\Pi_{me} = \int_{\Omega_e} u_{,ii}\delta u \mathrm{d}\Omega - \int_{\Gamma_{qe}} \left(\bar{q}-q\right)\delta\tilde{u}\mathrm{d}\Gamma + \int_{\Gamma_{Ie}} q\delta\tilde{u}\mathrm{d}\Gamma + \int_{\Gamma_e} \left(\tilde{u}-u\right)\delta q\mathrm{d}\Gamma \tag{2.70}$$

from which the Euler equation in the domain Ω_e and boundary conditions and Γ_q can be obtained as

$$\begin{aligned} &u_{,ii} = 0 && \text{in } \Omega_e \\ &q = \bar{q} && \text{on } \Gamma_{qe} \\ &\tilde{u} = u && \text{on } \Gamma_e \end{aligned} \tag{2.71}$$

using the stationary condition $\delta\Pi_{me} = 0$.

The continuity requirement between two adjacent elements '*e*' and '*f*' given in Eq. (2.61), can be satisfied in the following way. When assembling elements '*e*' and '*f*', we have

$$\begin{aligned} \delta\Pi_{m(e+f)} = &\int_{\Omega_{e+f}} u_{,ii}\delta u \mathrm{d}\Omega - \int_{\Gamma_{qe}+\Gamma_{qf}} \left(\bar{q}-q\right)\delta\tilde{u}\mathrm{d}\Gamma + \int_{\Gamma_e} \left(\tilde{u}-u\right)\delta q\mathrm{d}\Gamma \\ &+ \int_{\Gamma_f} \left(\tilde{u}-u\right)\delta q\mathrm{d}\Gamma + \int_{\Gamma_{Ief}} \left(q^e + q^f\right)\delta\tilde{u}^{ef}\mathrm{d}\Gamma + \ldots \end{aligned} \tag{2.72}$$

from which the vanishing variation of $\Pi_{m(e+f)}$ leads to the reciprocity condition $q_e + q_f = 0$ on the inter-element boundary Γ_{Ief}.

If the following expression

$$\int_{\Gamma_q} \delta q\delta\tilde{u}ds - \sum_e \left[\int_{\Gamma_{Ie}} \delta q_e \delta\tilde{u}_e ds + \int_{\Gamma_e} \delta q_e \delta(\tilde{u}_e - u_e) ds \right] \tag{2.73}$$

is uniformly positive (or negative) in the neighborhood of $\{u\}_0$, where the displacement $\{u\}_0$ has such a value that $\Pi_m(\{u\}_0) = (\Pi_m)_0$, and where $(\Pi_m)_0$ stands for the stationary value of Π_m, we have

$$\Pi_m \geq (\Pi_m)_0 \quad \text{or} \quad \Pi_m \leq (\Pi_m)_0 \tag{2.74}$$

in which the relation that $\{\tilde{u}\}_e = \{\tilde{u}\}_f$ is identical on $\Gamma_e \cap \Gamma_f$ has been used. This is due to the definition in Eq. (2.61) in Section 2.3.3.

PROOF: The proof of the theorem on the existence of extremum, may be completed by way of the so-called "second variational approach" (Simpson and Spector 1987; Hui and Qinghua 2007). In doing this, performing variation of $\delta\Pi_m$ and using the constrained conditions (2.73), we find

$$\delta^2\Pi_m = \int_{\Gamma_q} \delta q\delta\tilde{u}ds - \sum_e\left[\int_{\Gamma_{Ie}} \delta q_e\delta\tilde{u}_e ds + \int_{\Gamma_e} \delta q_e\delta(\tilde{u}_e - u_e)ds\right] \tag{2.75}$$

Therefore the theorem has been proved from the sufficient condition of the existence of a local extreme of a functional (Simpson and Spector 1987).

2.3.4. Element stiffness equation

Having independently defined the intra-element field and frame field in a particular element (see Figure 2.1), it is then possible to generate the element stiffness equation by the variational derived in the previous section. The variational functional Π_e corresponding to a particular element e of the present problem can be written as

$$\Pi_{me} = \frac{1}{2}\int_{\Omega_e} u_{,i}u_{,i}\mathrm{d}\Omega - \int_{\Gamma_{qe}} \bar{q}\tilde{u}\mathrm{d}\Gamma + \int_{\Gamma_e} q\left(\tilde{u} - u\right)\mathrm{d}\Gamma \tag{2.76}$$

Appling the divergence theorem (2.67) to the above functional (2.76), we have the final functional for the HFS-FE model

$$\begin{aligned}\Pi_{me} &= \frac{1}{2}\left[\int_{\Gamma_e} qu\mathrm{d}\Gamma + \int_{\Omega_e} uk\nabla^2 u\mathrm{d}\Omega\right] - \int_{\Gamma_{qe}} \bar{q}\tilde{u}\mathrm{d}\Gamma + \int_{\Gamma_e} q\left(\tilde{u} - u\right)\mathrm{d}\Gamma \\ &= -\frac{1}{2}\int_{\Gamma_e} qu\mathrm{d}\Gamma - \int_{\Gamma_{qe}} \bar{q}\tilde{u}\mathrm{d}\Gamma + \int_{\Gamma_e} q\tilde{u}\mathrm{d}\Gamma\end{aligned} \tag{2.77}$$

Then, substituting Eqs. (2.53), (2.56) and (2.59) into the functional (2.77) finally produces

$$\Pi_e = -\frac{1}{2}\mathbf{c}_e^{\mathrm{T}}\mathbf{H}_e\mathbf{c}_e - \mathbf{d}_e^{\mathrm{T}}\mathbf{g}_e + \mathbf{c}_e^{\mathrm{T}}\mathbf{G}_e\mathbf{d}_e \tag{2.78}$$

in which

$$\mathbf{H}_e = \int_{\Gamma_e} \mathbf{Q}_e^{\mathrm{T}}\mathbf{N}_e\mathrm{d}\Gamma = \int_{\Gamma_e} \mathbf{N}_e^{\mathrm{T}}\mathbf{Q}_e\mathrm{d}\Gamma,\ \ \mathbf{G}_e = \int_{\Gamma_e} \mathbf{Q}_e^{\mathrm{T}}\tilde{\mathbf{N}}_e\mathrm{d}\Gamma,\ \ \mathbf{g}_e = \int_{\Gamma_{qe}} \tilde{\mathbf{N}}_e^{\mathrm{T}}\bar{q}\mathrm{d}\Gamma \tag{2.79}$$

The symmetry of $\mathbf{H}_e$ is obvious from the scale definition (2.79) of the variational functional Π_e.

To enforce inter-element continuity on the common element boundary, the unknown vector $\mathbf{c}_e$ should be expressed in terms of nodal DOF $\mathbf{d}_e$. Minimization of the functional Π_e with respect to $\mathbf{c}_e$ and $\mathbf{d}_e$, respectively, yields

$$\begin{aligned}
\frac{\partial \Pi_e}{\partial \mathbf{c}_e{}^{\mathrm{T}}} &= -\mathbf{H}_e\mathbf{c}_e + \mathbf{G}_e\mathbf{d}_e = \mathbf{0} \\
\frac{\partial \Pi_e}{\partial \mathbf{d}_e{}^{\mathrm{T}}} &= \mathbf{G}_e^{\mathrm{T}}\mathbf{c}_e - \mathbf{g}_e = \mathbf{0}
\end{aligned} \tag{2.80}$$

from which the optional relationship between $\mathbf{c}_e$ and $\mathbf{d}_e$, and the stiffness equation can be produced

$$\mathbf{c}_e = \mathbf{H}_e^{-1}\mathbf{G}_e\mathbf{d}_e \qquad \text{and} \qquad \mathbf{K}_e\mathbf{d}_e = \mathbf{g}_e \tag{2.81}$$

where $\mathbf{K}_e = \mathbf{G}_e^{\mathrm{T}}\mathbf{H}_e^{-1}\mathbf{G}_e$ stands for the element stiffness matrix.

2.3.5. Numerical integral for H and G matrix

It is generally difficult to obtain the analytical expression of the integral in Eq. (2.79) and numerical integration along the element boundary is required. In the calculation, the widely used Gaussian integration is employed.

The H matrix can be expressed as

$$\mathbf{H}_e = \int_{\Gamma_e} \mathbf{Q}_e^{\mathrm{T}}\mathbf{N}_e \mathrm{d}\Gamma = \int_{\Gamma_e} \mathbf{F}(\mathbf{x})\mathrm{d}\Gamma \tag{2.82}$$

by introducing the matrix function

$$\mathbf{F}(\mathbf{x}) = \left[F_{ij}(\mathbf{x})\right]_{m\times m} = \mathbf{Q}_e^{\mathrm{T}}\mathbf{N}_e \tag{2.83}$$

and further we can rewrite it into the component form

$$H_{ij} = \int_{\Gamma_e} F_{ij}(\mathbf{x})\mathrm{d}\Gamma = \sum_{l=1}^{n_e}\int_{\Gamma_{el}} F_{ij}(\mathbf{x})\mathrm{d}\Gamma \tag{2.84}$$

where

$$\mathrm{d}\Gamma = \sqrt{(\mathrm{d}x_1)^2 + (\mathrm{d}x_2)^2} = \sqrt{\left(\frac{\mathrm{d}x_1}{\mathrm{d}\xi}\right)^2 + \left(\frac{\mathrm{d}x_2}{\mathrm{d}\xi}\right)^2}\,\mathrm{d}\xi = J\mathrm{d}\xi \tag{2.85}$$

and J is the Jacobian expressed as

$$J = \sqrt{\left(\frac{\mathrm{d}x_1}{\mathrm{d}\xi}\right)^2 + \left(\frac{\mathrm{d}x_2}{\mathrm{d}\xi}\right)^2}\,. \tag{2.86}$$

where

$$\left[\frac{\mathrm{d}x_1}{\mathrm{d}\xi}, \frac{\mathrm{d}x_2}{\mathrm{d}\xi}\right]^T = \sum_{i=1}^{n_o}\frac{\mathrm{d}N_i(\xi)}{\mathrm{d}\xi}\begin{Bmatrix} x_{1i} \\ x_{2i} \end{Bmatrix} \tag{2.87}$$

and n_0 is the number of nodes of each edge. Thus, the Gaussian numerical integration for H matrix can be calculated by

$$H_{ij}=\sum_{l=1}^{n_e}\left[\int_{-1}^{+1}F_{ij}\left(\mathbf{x}(\xi)\right)J\left(\xi\right)\mathrm{d}\xi\right]\approx\sum_{l=1}^{n_e}\left[\sum_{k=1}^{n_p}w_kF_{ij}\left(\mathbf{x}(\xi_k)\right)J\left(\xi_k\right)\right] \tag{2.88}$$

where n_e is the number of edges of the element, n_p is the Gaussian sampling points employed in the Gaussian numerical integration and w_k is the weight of Gaussian integration for sampling point. Similarly, the $\mathbf{G}_e$ matrix can be calculated by

$$G_{ij}=\sum_{l=1}^{n_e}\left[\int_{-1}^{1}\tilde{F}_{ij}\left[\mathbf{x}(\xi)\right]J(\xi)d\xi\right]\approx\sum_{l=1}^{n_e}\left\{\sum_{k=1}^{n_p}w_k\tilde{F}_{ij}\left[\mathbf{x}(\xi_k)\right]J(\xi_k)\right\} \tag{2.89}$$

The calculation of vector $\mathbf{g}_e$ in Eq. (2.79) is the same as that in the conventional FEM, so it is convenient to incorporate the proposed HFS-FEM into the standard FEM program. Besides, the flux is directly computed from Eqs. (2.56). The boundary DOF can be directly computed from Eq. (2.59) and the unknown variable at interior points of the element can be determined from Eq. (2.53) plus the recovered rigid-body modes in each element, which are introduced in the following section.

2.3.6. Recovery of rigid-body motion

For the physical definition of the fundamental solution, it is necessary to recover the missing rigid-body motion modes from the above results. Following the method presented in (Qin 2000), the missing rigid-body motion can be recovered by writing the internal potential field of a particular element *e* as

$$u_e=\mathbf{N}_e\mathbf{c}_e+c_0 \tag{2.90}$$

where the undetermined rigid-body motion parameter c_0 can be calculated using the least square matching of u_e and $\tilde{u}_e$ at element nodes

$$\sum_{i=1}^{n}\left(\mathbf{N}_e\mathbf{c}_e+c_0-\tilde{u}_e\right)^2\Big|_{\text{node }i}=\min \tag{2.91}$$

which finally yields

$$c_0=\frac{1}{n}\sum_{i=1}^{n}\Delta u_{ei} \tag{2.92}$$

in which $\Delta u_{ei}=\left(\tilde{u}_e-\mathbf{N}_e\mathbf{c}_e\right)\big|_{\text{node }i}$ and n is the number of element nodes. Once the nodal field is determined by solving the final stiffness equation, the coefficient vector

$\mathbf{c}_e$ can be evaluated from Eq. (2.81), and then c_0 is evaluated from Eq. (2.92). Finally, the potential field u at any internal point in an element can be obtained by means of Eq. (2.53).

2.4. SUMMARY

In this chapter, the framework of the HFS-FEM for 2D elasticity and potential problems is presented, giving a general overview of the newly proposed method. Detailed procedures and implementations of the HFS-FEM are provided. The two independent fields assumed, as well as the modified variational function to assure the continuity between elements are addressed and proved. The numerical integral and the rigid-body motion recovery are also presented in detail. This chapter serves as the foundation for further development of this method for modeling advanced materials in both microscale and macroscale.

Chapter 3. HFS-FEM for Three-Dimensional Elastic Problems

3.1. INTRODUCTION

The HT-FEM, as a significant alternative to the conventional FEM, has become popular and is increasingly used to analyze various engineering problems (Patterson and Sheikh 1982; Jirousek and Guex 1986; Piltner 1992; Qin 1994; Jirousek and Qin 1995; Qin 2003; Fam and Rashed 2005; Qin 2005; Wang, Qin et al. 2007; Li, Lu et al. 2008; de Freitas and Toma 2009; Sze and Liu 2010; de Freitas and Moldovan 2011). In contrast to conventional FEM, HT-FEM is based on a hybrid method which includes the use of an independent auxiliary inter-element frame field defined on an element boundary and an independent internal field chosen so as a priori to satisfy the homogeneous governing differential equations by means of a suitable truncated T-complete function set of homogeneous solutions (Qin 2000). Inter-element continuity is enforced by employing a modified variational principle, which is used to construct standard stiffness equation, and to establish the relationship between the frame field and the internal field of the element. The property of nonsingular element boundary integral appearing in HT-FEM enables to the convenient construction of an arbitrarily shaped element; however, the terms of the truncated T-complete functions must be carefully selected to achieve the desired results and the T-complete functions for some physical problems are difficult to generate (Qin and Wang 2008).

To overcome the drawback of HT-FEM, a novel hybrid FE formulation based on the fundamental solutions, called the HFS-FEM, was first developed for solving 2D heat conduction problems in single and multi-materials (Wang and Qin 2009; Wang and Qin 2010a). In this approach, the intra-element field is approximated by a linear combination of fundamental functions analytically satisfying the related governing equations, an independent frame field defined along the element boundary and the newly developed variational functional are employed to guarantee the inter-element continuity, generate the final stiffness equation, and establish the relationship between the boundary frame field and the internal field of the element under consideration.

In the HFS-FEM, the domain integrals in the hybrid functional can be directly converted into boundary integrals without any appreciable increase in computational effort. Locating the source point outside the element of interest and not overlapping with the field point during computation ensures that no singular integrals are involved (Wang and Qin 2010a). Moreover, by virtue of the features of two independent interpolation fields and element boundary integral in HFS-FEM, the algorithm has potential applications in the aspect of mesh reduction by constructing special purpose elements such as functionally graded elements, hole elements, crack elements etc. (Qin 2003; Gao, Wang et al. 2005; Dhanasekar, Han et al. 2006).

In this chapter, a new solution procedure based on the HFS-FEM approach is proposed to solve 3D elastic problems with or without body forces. The detailed 3D formulations of HFS-FEM are first derived for elastic problems by ignoring body forces, then a procedure based on the method of particular solution and radial basis function approximation is presented to deal with the body force. In consequence the homogeneous solution is obtained by using the HFS-FEM, and the particular solution associated with body force is approximated by using the strong form basis function interpolation. The solution procedure for 3D elastostatic problem is then programmed by means of MATLAB. Several standard tests and numerical examples are investigated and their results are compared with the existing closed-form solutions or ABAQUS results. The results show that the proposed method has higher accuracy and efficiency than ABAQUS when using the same element meshes. It is also found that this method is not sensitive to mesh distortion and has the capacity to deal with nearly incompressible materials. The majority of this chapter has been published in a paper (Cao, Qin et al. 2012a) co-authored by the candidate.

3.2. FORMULATIONS FOR 3D ELASTICITY WITHOUT THE BODY FORCE

3.2.1. Governing equations and boundary conditions

In this subsection, basic equations commonly used in the literatures are briefly reviewed to provide notations for the subsequent sections. Let (X_1, X_2, X_3) denote the coordinates in the Cartesian coordinate system and consider a finite isotropic body occupying the domain Ω, as shown in Figure 3.1.

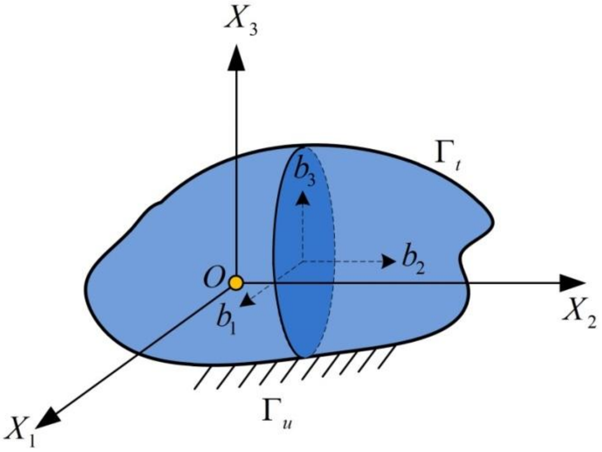

Figure 3.1 Geometrical definitions and boundary conditions for a general 3D solid.

The equilibrium equation for this finite body in the absence of body force can be expressed as

$$\sigma_{ij,j} = 0, \qquad i, j = 1, 2, 3 \tag{3.1}$$

The constitutive equations for linear elasticity and the kinematical relation are given as

$$\sigma_{ij} = \frac{2Gv}{1-2v}\delta_{ij}e_{kk} + 2Ge_{ij} \tag{3.2}$$

$$e_{ij} = \frac{1}{2}(u_{i,j} + u_{j,i}) \tag{3.3}$$

where σ_{ij} is the stress tensor, e_{ij} the strain tensor, u_i the displacement vector, δ_{ij} the Kronecker delta, G the shear modulus, and v Poisson's ratio. Substituting Eqs. (3.2) and (3.3) into Eq. (3.1), the equilibrium equations may be rewritten in terms of displacements as

$$Gu_{i,jj} + \frac{G}{1-2v}u_{j,ji} = 0 \tag{3.4}$$

For a well-posed boundary value problem, the following boundary conditions, either displacement or traction boundary condition, are prescribed as

$$u_i = \bar{u}_i \ \text{ on } \Gamma_u, \tag{3.5}$$

$$t_i = \bar{t}_i \ \text{ on } \Gamma_t, \tag{3.6}$$

where $\Gamma_u \bigcup \Gamma_t = \Gamma$ is the boundary of the solution domain Ω, $\bar{u}_i$ and $\bar{t}_i$ are the prescribed boundary values.

3.2.2. Assumed fields

To solve the problem governed by Eqs.(3.4)-(3.6) using the HFS-FEM approach, the solution domain Ω is divided into a series of elements as in conventional FEM. For each element, two independent fields, i.e. an intra-element field and a frame field, are assumed in the manner as that presented in (Wang and Qin 2010a; Wang and Qin 2010b). The main idea of the HFS-FEM is to establish a FE formulation whereby intra-element continuity is enforced on a nonconforming internal displacement field chosen as the fundamental solution of the problem under consideration (Wang and Qin 2010b). In this approach, the intra-element displacement fields is approximated in terms of a linear combination of fundamental solutions of the problem as

$$\mathbf{u(x)} = \begin{Bmatrix} u_1(\mathbf{x}) \\ u_2(\mathbf{x}) \\ u_3(\mathbf{x}) \end{Bmatrix} = \mathbf{N_e c_e} \quad (\mathbf{x} \in \Omega_e, \mathbf{y}_{sj} \notin \Omega_e) \tag{3.7}$$

where the matrix $\mathbf{N_e}$ and unknown vector $\mathbf{c_e}$ can be further written as

$$\mathbf{N_e} = \begin{bmatrix} u_{11}^*(\mathbf{x},\mathbf{y}_{s1}) & u_{12}^*(\mathbf{x},\mathbf{y}_{s1}) & u_{13}^*(\mathbf{x},\mathbf{y}_{s1}) & \cdots & u_{11}^*(\mathbf{x},\mathbf{y}_{sn_s}) & u_{12}^*(\mathbf{x},\mathbf{y}_{sn_s}) & u_{13}^*(\mathbf{x},\mathbf{y}_{sn_s}) \\ u_{12}^*(\mathbf{x},\mathbf{y}_{s1}) & u_{22}^*(\mathbf{x},\mathbf{y}_{s1}) & u_{23}^*(\mathbf{x},\mathbf{y}_{s1}) & \cdots & u_{12}^*(\mathbf{x},\mathbf{y}_{sn_s}) & u_{22}^*(\mathbf{x},\mathbf{y}_{sn_s}) & u_{23}^*(\mathbf{x},\mathbf{y}_{sn_s}) \\ u_{13}^*(\mathbf{x},\mathbf{y}_{s1}) & u_{32}^*(\mathbf{x},\mathbf{y}_{s1}) & u_{33}^*(\mathbf{x},\mathbf{y}_{s1}) & \cdots & u_{13}^*(\mathbf{x},\mathbf{y}_{sn_s}) & u_{32}^*(\mathbf{x},\mathbf{y}_{sn_s}) & u_{33}^*(\mathbf{x},\mathbf{y}_{sn_s}) \end{bmatrix} \tag{3.8}$$

$$\mathbf{c_e} = [c_{11} \quad c_{21} \quad c_{31} \quad \cdots \quad c_{1n} \quad c_{2n} \quad c_{3n}]^T \tag{3.9}$$

in which $\mathbf{x}$ and $\mathbf{y}_{sj}$ are respectively the field point and source point in the local coordinate system (X1, X2). The components $u_{ij}^*(\mathbf{x},\mathbf{y}_{sj})$ are the fundamental solution, i.e. the induced displacement component in the *i*-direction at the field point **x** due to a unit point load applied in the *j*-direction at the source point $\mathbf{y}_{sj}$ placed outside the element, as given by (Sauter and Schwab 2010)

$$u^*_{ij}(\mathbf{x},\mathbf{y}_{sj}) = \frac{1}{16\pi(1-\nu)Gr}\left\{(3-4\nu)\delta_{ij} + r_{,i}r_{,j}\right\} \tag{3.10}$$

where $r_i = x_i - x_{is}$, $r = \sqrt{r_1^2 + r_2^2 + r_3^2}$, n_s is the number of source points.

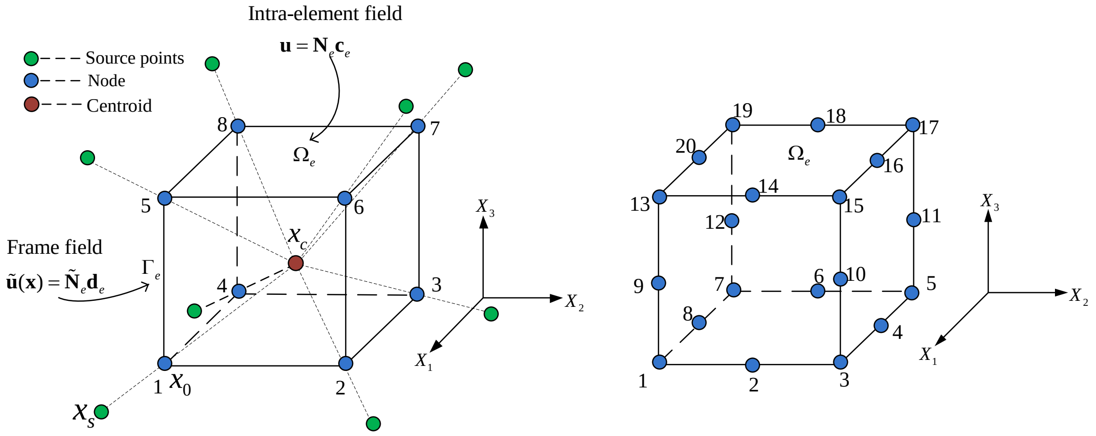

8-node 3D element

20-node 3D element

Figure 3.2 Intra-element field and frame field of a hexahedron HFS-FEM element for 3D elastic problem. (The source points and centroid of the 20-node element are omitted in the figure for clarity and clear view, and are similar to those of the 8-node element.)

In the analysis, the number of source points is taken to be the same as the number of element nodes, which are free of spurious energy modes and maintain the stiffness equations in full rank, as indicated in (Qin 2000). The source point $\mathbf{y}_{sj}\,(j = 1,2,\ldots,n_s)$ can be generated by means of the following method (Wang and Qin 2010b)

$$\mathbf{y}_s = \mathbf{x}_0 + \gamma(\mathbf{x}_0 - \mathbf{x}_c) \tag{3.11}$$

where γ is a dimensionless coefficient, $\mathbf{x}_0$ is a point on the element boundary (the nodal point in this work) and $\mathbf{x}_c$ the geometrical centroid of the element (see Figure 3.2). Determination of γ was discussed by (Wang and Qin 2009; Wang and Qin 2010b), and γ=8 is used in the following analysis.

According to Eqs. (3.2) and (3.3), the corresponding stress fields can be expressed as

$$\boldsymbol{\sigma}(\mathbf{x}) = \begin{bmatrix}\sigma_{11} & \sigma_{22} & \sigma_{33} & \sigma_{23} & \sigma_{31} & \sigma_{12}\end{bmatrix}^T = \mathbf{T_e c_e} \tag{3.12}$$

where

$$\mathbf{T_e} = \begin{bmatrix} \sigma^*_{111}(\mathbf{x},\mathbf{y}_1) & \sigma^*_{211}(\mathbf{x},\mathbf{y}_1) & \sigma^*_{311}(\mathbf{x},\mathbf{y}_1) & \cdots & \sigma^*_{111}(\mathbf{x},\mathbf{y}_{n_s}) & \sigma^*_{211}(\mathbf{x},\mathbf{y}_{n_s}) & \sigma^*_{311}(\mathbf{x},\mathbf{y}_{n_s}) \\ \sigma^*_{122}(\mathbf{x},\mathbf{y}_1) & \sigma^*_{222}(\mathbf{x},\mathbf{y}_1) & \sigma^*_{322}(\mathbf{x},\mathbf{y}_1) & \cdots & \sigma^*_{122}(\mathbf{x},\mathbf{y}_{n_s}) & \sigma^*_{222}(\mathbf{x},\mathbf{y}_{n_s}) & \sigma^*_{322}(\mathbf{x},\mathbf{y}_{n_s}) \\ \sigma^*_{133}(\mathbf{x},\mathbf{y}_1) & \sigma^*_{233}(\mathbf{x},\mathbf{y}_1) & \sigma^*_{333}(\mathbf{x},\mathbf{y}_1) & \cdots & \sigma^*_{133}(\mathbf{x},\mathbf{y}_{n_s}) & \sigma^*_{233}(\mathbf{x},\mathbf{y}_{n_s}) & \sigma^*_{333}(\mathbf{x},\mathbf{y}_{n_s}) \\ \sigma^*_{123}(\mathbf{x},\mathbf{y}_1) & \sigma^*_{223}(\mathbf{x},\mathbf{y}_1) & \sigma^*_{323}(\mathbf{x},\mathbf{y}_1) & \cdots & \sigma^*_{123}(\mathbf{x},\mathbf{y}_{n_s}) & \sigma^*_{223}(\mathbf{x},\mathbf{y}_{n_s}) & \sigma^*_{323}(\mathbf{x},\mathbf{y}_{n_s}) \\ \sigma^*_{131}(\mathbf{x},\mathbf{y}_1) & \sigma^*_{231}(\mathbf{x},\mathbf{y}_1) & \sigma^*_{331}(\mathbf{x},\mathbf{y}_1) & \cdots & \sigma^*_{131}(\mathbf{x},\mathbf{y}_{n_s}) & \sigma^*_{231}(\mathbf{x},\mathbf{y}_{n_s}) & \sigma^*_{331}(\mathbf{x},\mathbf{y}_{n_s}) \\ \sigma^*_{112}(\mathbf{x},\mathbf{y}_1) & \sigma^*_{212}(\mathbf{x},\mathbf{y}_1) & \sigma^*_{312}(\mathbf{x},\mathbf{y}_1) & \cdots & \sigma^*_{112}(\mathbf{x},\mathbf{y}_{n_s}) & \sigma^*_{212}(\mathbf{x},\mathbf{y}_{n_s}) & \sigma^*_{312}(\mathbf{x},\mathbf{y}_{n_s}) \end{bmatrix} \tag{3.13}$$

The components $\sigma^*_{ijk}(\mathbf{x},\mathbf{y})$ are given by

$$\sigma^*_{ijk}(\mathbf{x},\mathbf{y}) = \frac{-1}{8\pi(1-\nu)r^2}\left\{(1-2\nu)(r_{,k}\delta_{ij} + r_{,j}\delta_{ki} - r_{,i}\delta_{jk}) + 3r_{,i}r_{,j}r_{,k}\right\} \tag{3.14}$$

As a consequence, the traction can be written in the form

$$\begin{Bmatrix} t_1 \\ t_2 \\ t_3 \end{Bmatrix} = \mathbf{n\sigma} = \mathbf{Q_e c_e} \tag{3.15}$$

in which

$$\mathbf{Q_e} = \mathbf{nT_e}, \quad \mathbf{n} = \begin{bmatrix} n_1 & 0 & 0 & 0 & n_3 & n_2 \\ 0 & n_2 & 0 & n_3 & 0 & n_1 \\ 0 & 0 & n_3 & n_2 & n_1 & 0 \end{bmatrix} \tag{3.16}$$

The unknown $\mathbf{c}_e$ in Eqs. (3.7) and (3.12) may be calculated using a hybrid technique (Wang and Qin 2009), in which the elements are linked through an auxiliary conforming displacement frame which has the same form as in conventional FEM (see Figure 3.2). This means that in the HFS-FEM, a conforming displacement field should be independently defined on the element boundary to enforce the field continuity between elements and also to link the unknown $\mathbf{c}_e$ and the nodal displacement $\mathbf{d}_e$. Thus, the frame is defined as

$$\tilde{\mathbf{u}}(\mathbf{x}) = \begin{Bmatrix} \tilde{u}_1 \\ \tilde{u}_2 \\ \tilde{u}_3 \end{Bmatrix} = \begin{Bmatrix} \tilde{\mathbf{N}}_1 \\ \tilde{\mathbf{N}}_2 \\ \tilde{\mathbf{N}}_3 \end{Bmatrix} \mathbf{d}_e = \tilde{\mathbf{N}}_e \mathbf{d}_e, \qquad (\mathbf{x} \in \Gamma_e) \tag{3.17}$$

where the symbol "~" is used to specify that the field is defined on the element boundary only, $\tilde{\mathbf{N}}_e$ is the matrix of shape functions, $\mathbf{d}_e$ is the nodal displacements of elements. Taking the surface 2-3-7-6 of a particular 8-node brick element (see Figure 3.2) as an example, matrix $\tilde{\mathbf{N}}_e$ and vector $\mathbf{d}_e$ can be expressed as

$$\tilde{\mathbf{N}}_e = \begin{bmatrix} \mathbf{0} & \bar{\mathbf{N}}_1 & \bar{\mathbf{N}}_2 & \mathbf{0} & \mathbf{0} & \bar{\mathbf{N}}_4 & \bar{\mathbf{N}}_3 & \mathbf{0} \end{bmatrix} \tag{3.18}$$

$$\mathbf{d}_e = \begin{bmatrix} u_{11} & u_{21} & u_{31} & u_{12} & u_{22} & u_{32} & \cdots & u_{18} & u_{28} & u_{38} \end{bmatrix}^T \tag{3.19}$$

where the shape functions are expressed as

$$\bar{\mathbf{N}}_i = \begin{bmatrix} \tilde{N}_i & 0 & 0 \\ 0 & \tilde{N}_i & 0 \\ 0 & 0 & \tilde{N}_i \end{bmatrix}, \quad \mathbf{0} = \begin{bmatrix} 0 & 0 & 0 \\ 0 & 0 & 0 \\ 0 & 0 & 0 \end{bmatrix} \tag{3.20}$$

where $\tilde{N}_i$ (i=1-4) can be expressed by natural coordinate $\xi, \eta \in [-1,1]$

$$\begin{aligned} \tilde{N}_1 &= \frac{(1+\xi)(1+\eta)}{4}, & \tilde{N}_2 &= \frac{(1-\xi)(1+\eta)}{4} \\ \tilde{N}_3 &= \frac{(1-\xi)(1-\eta)}{4}, & \tilde{N}_4 &= \frac{(1+\xi)(1-\eta)}{4} \end{aligned} \tag{3.21}$$

and (ξ_i, η_i) is the natural coordinate of the i-node of the element (Figure 3.3).

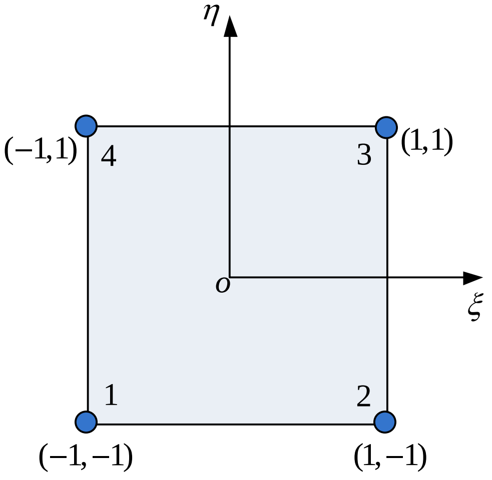

Figure 3.3 Typical linear interpolation for the frame fields.

3.2.3. Modified functional for hybrid FEM

The HFS-FEM formulation for 3D elastic problems can be established by the variational approach (Wang and Qin 2010b). In the absence of body forces, the hybrid functional Π_{me} used for deriving the present HFS-FEM can be constructed as (Qin and Wang 2008)

$$\Pi_{me} = \frac{1}{2}\iint_{\Omega_e} \sigma_{ij}\varepsilon_{ij} d\Omega - \int_{\Gamma_t} \bar{t}_i \tilde{u}_i d\Gamma + \int_{\Gamma_e} t_i (\tilde{u}_i - u_i) d\Gamma \tag{3.22}$$

where $\tilde{u}_i$ and u_i are the intra-element displacement field defined within the element and the frame displacement field defined on the element boundary, respectively. Ω_e and Γ_e are the element domain and element boundary, respectively. Γ_t, Γ_u and Γ_I

stand respectively for the specified traction boundary, specified the displacement boundary and the inter-element boundary ($\Gamma_e = \Gamma_t + \Gamma_u + \Gamma_I$).

Compared to the functional employed in the conventional FEM, the present hybrid functional is constructed by adding a hybrid integral term related to the intra-element and element frame displacement fields to guarantee satisfaction of the displacement and traction continuity conditions on the common boundary of two adjacent elements. By applying the Gaussian theorem, Eq. (3. 22) can be simplified as

$$\Pi_{me} = \frac{1}{2}\left(\int_{\Gamma_e} t_i u_i d\Gamma - \iint_{\Omega_e} \sigma_{ij,j} u_i d\Omega\right) - \int_{\Gamma_t} \bar{t}_i \tilde{u}_i d\Gamma + \int_{\Gamma_e} t_i (\tilde{u}_i - u_i) d\Gamma \tag{3.23}$$

Due to the satisfaction of the equilibrium equation by the constructed intra-element fields, we have the following expression for the HFS-FEM

$$\begin{aligned} \Pi_{me} &= \frac{1}{2}\int_{\Gamma_e} t_i u_i d\Gamma - \int_{\Gamma_t} \bar{t}_i \tilde{u}_i d\Gamma + \int_{\Gamma_e} t_i (\tilde{u}_i - u_i) d\Gamma \\ &= -\frac{1}{2}\int_{\Gamma_e} t_i u_i d\Gamma + \int_{\Gamma_e} t_i \tilde{u}_i d\Gamma - \int_{\Gamma_t} \bar{t}_i \tilde{u}_i d\Gamma \end{aligned} \tag{3.24}$$

The functional (3.24) contains only boundary integrals of the element and is used to derive the HFS-FEM formulation for the 3D elastic problem in the following section.

3.2.4. Element stiffness equation

The element stiffness equation can be generated by setting $\delta\Pi_{me} = 0$. Substituting Eqs. (3.7), (3.15) and (3.17) into the functional (3.24), we have

$$\Pi_{me} = -\frac{1}{2}\mathbf{c}_e^{\mathrm{T}}\mathbf{H}_e\mathbf{c}_e + \mathbf{c}_e^{\mathrm{T}}\mathbf{G}_e\mathbf{d}_e - \mathbf{d}_e^{\mathrm{T}}\mathbf{g}_e \tag{3.25}$$

where

$$\mathbf{H}_e = \int_{\Gamma_e} \mathbf{Q}_e^{\mathrm{T}}\mathbf{N}_e \mathrm{d}\Gamma, \quad \mathbf{G}_e = \int_{\Gamma_e} \mathbf{Q}_e^{\mathrm{T}}\tilde{\mathbf{N}}_e \mathrm{d}\Gamma, \quad \mathbf{g}_e = \int_{\Gamma_t} \tilde{\mathbf{N}}_e^{\mathrm{T}}\bar{\mathbf{t}} d\Gamma \tag{3.26}$$

To enforce inter-element continuity on the common element boundary, the unknown vector $\mathbf{c}_e$ should be expressed in terms of nodal DOF $\mathbf{d}_e$. The stationary condition of the functional Π_{me} with respect to $\mathbf{c}_e$ and $\mathbf{d}_e$ yields, respectively,

$$\frac{\partial\Pi_{me}}{\partial\mathbf{c}_e^{\mathrm{T}}} = -\mathbf{H}_e\mathbf{c}_e + \mathbf{G}_e\mathbf{d}_e = \mathbf{0} \tag{3.27}$$

$$\frac{\partial\Pi_{me}}{\partial\mathbf{d}_e^{\mathrm{T}}} = \mathbf{G}_e^{T}\mathbf{c}_e - \mathbf{g}_e = \mathbf{0} \tag{3.28}$$

Therefore, the relationship between $\mathbf{c}_e$ and $\mathbf{d}_e$, and the stiffness equation can be obtained as follows

$$\mathbf{c}_e = \mathbf{H}_e^{-1}\mathbf{G}_e\mathbf{d}_e \tag{3.29}$$

$$\mathbf{K}_e\mathbf{d}_e = \mathbf{g}_e \tag{3.30}$$

where $\mathbf{K}_e = \mathbf{G}_e^{\mathrm{T}}\mathbf{H}_e^{-1}\mathbf{G}_e$ is the element stiffness matrix. It should be mentioned that the condition number of matrix $\mathbf{H}_e$ may become very large if the positions of source points are not chosen appropriately. This issue can be determined by numerical experiments for the parameter γ in Eq. (3.11). According to our experience, the suitable range for γ is between 2 and 10 to assure a better condition number for matrix $\mathbf{H}_e$ in order to improve the accuracy.

3.2.5. Numerical integral over element

It is generally difficult to obtain the analytical expression of the integral in Eq.(3.26) and numerical integration over the element is required. In this calculation the widely used Gaussian integration is employed. For a surface of the 3D hexahedron element, as shown in Figure 3.3, the vector normal to the surface can be obtained by

$$v_n = v_\xi \times v_\eta = \begin{Bmatrix} v_{nx} \\ v_{ny} \\ v_{nz} \end{Bmatrix} = \begin{Bmatrix} \dfrac{dx}{d\xi} \\ \dfrac{dy}{d\xi} \\ \dfrac{dz}{d\xi} \end{Bmatrix} \times \begin{Bmatrix} \dfrac{dx}{d\eta} \\ \dfrac{dy}{d\eta} \\ \dfrac{dz}{d\eta} \end{Bmatrix} = \begin{Bmatrix} \dfrac{dy}{d\xi}\dfrac{dz}{d\eta} - \dfrac{dy}{d\eta}\dfrac{dz}{d\xi} \\ \dfrac{dz}{d\xi}\dfrac{dx}{d\eta} - \dfrac{dz}{d\eta}\dfrac{dx}{d\xi} \\ \dfrac{dx}{d\xi}\dfrac{dy}{d\eta} - \dfrac{dx}{d\eta}\dfrac{dy}{d\xi} \end{Bmatrix} \tag{3.31}$$

where v_ξ and v_η are the tangential vectors in the ξ-direction and η-direction, respectively, calculated by

$$v_\xi = \begin{Bmatrix} \dfrac{dx}{d\xi} \\ \dfrac{dy}{d\xi} \\ \dfrac{dz}{d\xi} \end{Bmatrix} = \sum_{i=1}^{n_d} \frac{\partial N_i(\xi,\eta)}{\partial \xi} \begin{Bmatrix} x_i \\ y_i \\ z_i \end{Bmatrix}, v_\eta = \begin{Bmatrix} \dfrac{dx}{d\eta} \\ \dfrac{dy}{d\eta} \\ \dfrac{dz}{d\eta} \end{Bmatrix} = \sum_{i=1}^{n_d} \frac{\partial N_i(\xi,\eta)}{\partial \eta} \begin{Bmatrix} x_i \\ y_i \\ z_i \end{Bmatrix} \tag{3.32}$$

where n_d is the number of nodes of the surface, (x_i, y_i, z_i) are the nodal coordinates. Thus the unit normal vector is given by

$$n = \frac{v_n}{|v_n|} \tag{3.33}$$

where

$$J(\xi,\eta) = |v_n| = \sqrt{v_{nx}^2 + v_{ny}^2 + v_{nz}^2} \tag{3.34}$$

is the Jacobian of the transformation from Cartesian coordinates (x, y) to natural coordinates (ξ, η).

For the H matrix, we introduce the matrix function

$$\mathbf{F(x,y)} = \left[F_{ij}(x,y)\right]_{m\times m} = \mathbf{Q}_e^{\mathrm{T}}\mathbf{N}_e \tag{3.35}$$

Then we can obtain

$$\mathbf{H}_e = \int_{\Gamma_e} \mathbf{Q}_e^{\mathrm{T}}\mathbf{N}_e \mathrm{d}\Gamma = \int_{\Gamma_e} \mathbf{F(x,y)}\mathrm{d}\Gamma \tag{3.36}$$

and rewrite it to the component form as

$$H_{ij} = \int_{\Gamma_e} F_{ij}(x,y)\mathrm{dS} = \sum_{l=1}^{n_f}\int_{\Gamma_{el}} F_{ij}(x,y)\mathrm{dS} \tag{3.37}$$

Using the relationship

$$\mathrm{dS}{=}J(\xi,\eta)d\xi d\eta \tag{3.38}$$

and the Gaussian numerical integration, we can obtain

$$\begin{aligned} H_{ij} &= \sum_{l=1}^{n_f}\int_{-1}^{1} F_{ij}\left[x(\xi,\eta),y(\xi,\eta)\right] J(\xi,\eta)d\xi d\eta \\ &\approx \sum_{l=1}^{n_f}\left\{\sum_{s=1}^{n_p}\sum_{t=1}^{n_p} w_s w_t F_{ij}\left[x(\xi_s,\eta_t),y(\xi_s,\eta_t)\right] J(\xi_s,\eta_t)\right\} \end{aligned} \tag{3.39}$$

where n_f and n_p are respectively the number of surface of the 3D element and the number of Gaussian integral points in each direction of the element surface. Similarly, the $\mathbf{G}_e$ matrix can be calculated by

$$\begin{aligned} G_{ij} &= \sum_{l=1}^{n_f}\int_{-1}^{1} \tilde{F}_{ij}\left[x(\xi,\eta),y(\xi,\eta)\right] J(\xi,\eta)d\xi d\eta \\ &\approx \sum_{l=1}^{n_f}\left\{\sum_{s=1}^{n_p}\sum_{t=1}^{n_p} w_s w_t \tilde{F}_{ij}\left[x(\xi_s,\eta_t),y(\xi_s,\eta_t)\right] J(\xi_s,\eta_t)\right\} \end{aligned} \tag{3.40}$$

The calculation of vector $\mathbf{g}_e$ in Eq.(3.30) is the same as that in conventional FEM, making it convenient to incorporate the proposed HFS-FEM into the standard FEM program. Besides, the stress and traction estimations are directly computed from Eqs.(3.12) and (3.13), respectively. The boundary displacements can be directly computed from Eq.(3.17) and the displacements at interior points of the element can be determined from Eq.(3.7) plus the recovered rigid-body modes in each element, a procedure that is introduced in the following section.

3.2.6. Recovery of rigid-body motion terms

From the above procedures, it is evident that the solution will fail if any of the functions u_{ij}^* is in a rigid-body motion mode, due to the fact that the matrix $\mathbf{H}_e$ is not in full rank and becomes singular for inversion (Qin 2000). Therefore, special care should be taken to discard all rigid-body motion terms from $\mathbf{u}_e$ to prevent the element deformability matrix $\mathbf{H}_e$ from being singular. However, it is necessary to reintroduce the discarded rigid-body motion terms when calculating the internal field $\mathbf{u}_e$ of an element. For this purpose the least squares method can be employed. The missing terms can easily be recovered by setting for the augmented internal field

$$\mathbf{u}_e = \mathbf{N}_e \mathbf{c}_e + \begin{bmatrix} 1 & 0 & 0 & 0 & x_3 & -x_2 \\ 0 & 1 & 0 & -x_3 & 0 & x_1 \\ 0 & 0 & 1 & x_2 & -x_1 & 0 \end{bmatrix} \mathbf{c}_0 \tag{3.41}$$

and using a least-square procedure to match u_{eh} and $\tilde{u}_{eh}$ at the nodes of the element boundary

$$\min = \sum_{i=1}^{n} \left[\left(u_{1i} - \tilde{u}_{1i}\right)^2 + \left(u_{2i} - \tilde{u}_{2i}\right)^2 + \left(u_{3i} - \tilde{u}_{3i}\right)^2 \right] \tag{3.42}$$

where n is the number of nodes for the element under consideration. The above equation finally yields

$$\mathbf{c_0} = \mathbf{R}_e^{-1} \mathbf{r_e} \tag{3.43}$$

where

$$\mathbf{R_e} = \sum_{i=1}^{n} \begin{bmatrix} 1 & 0 & 0 & 0 & x_{3i} & -x_{2i} \\ 0 & 1 & 0 & -x_{3i} & 0 & x_{1i} \\ 0 & 0 & 1 & x_{2i} & -x_{1i} & 0 \\ 0 & -x_{3i} & x_{2i} & x_{2i}^2 + x_{3i}^2 & -x_{1i}x_{2i} & -x_{1i}x_{3i} \\ x_{3i} & 0 & -x_{1i} & -x_{1i}x_{2i} & x_{1i}^2 + x_{3i}^2 & -x_{2i}x_{3i} \\ -x_{2i} & x_{1i} & 0 & -x_{1i}x_{3i} & -x_{2i}x_{3i} & x_{1i}^2 + x_{2i}^2 \end{bmatrix} \tag{3.44}$$

$$\mathbf{r_e} = \sum_{i=1}^{n} \begin{bmatrix} \Delta u_{e1i} \\ \Delta u_{e2i} \\ \Delta u_{e3i} \\ \Delta u_{e3i} x_{2i} - \Delta u_{e2i} x_{3i} \\ \Delta u_{e1i} x_{3i} - \Delta u_{e3i} x_{1i} \\ \Delta u_{e2i} x_{1i} - \Delta u_{e1i} x_{2i} \end{bmatrix} \tag{3.45}$$

and $\Delta \mathbf{u}_{ei} = \left(\tilde{\mathbf{u}}_e - \mathbf{N}_e \mathbf{c}_e \right)\Big|_{\text{node } i}$.

3.3. FORMULATIONS FOR 3D ELASTICITY WITH BODY FORCE

3.3.1. Governing equations

For the 3D isotropic body occupying the domain Ω, as shown in Figure 3.1, the equilibrium equation for the body with body force b_i can be expressed as

$$\sigma_{ij,j} = -b_i \quad i, j = 1, 2, 3 \tag{3.46}$$

The constitutive equations and the generalized kinematical relation are the same as those in Eqs. (3.2) and (3.3). Therefore, the equilibrium equations (3.46) can be rewritten in terms of displacements as

$$G u_{i,jj} + \frac{G}{1-2v} u_{j,ji} = -b_i \tag{3.47}$$

For a well-posed boundary value problem, boundary conditions are also defined by Eqs. (3.5) and (3.6). The following subsections present the procedure for handling the body force occurring in Eq. (3.47).

3.3.2. The method of particular solution

The inhomogeneous term b_i associated with the body force in Eq. (3.47) can be effectively handled by means of the method of particular solution (Chen and Brebbia 1998; Qin and Wang 2008). In this approach, the displacement u_i is decomposed into two parts, a homogeneous solution u_i^h and a particular solution u_i^p

$$u_i = u_i^c + u_i^p \tag{3.48}$$

where the particular solution u_i^p should satisfy the governing equation

$$G u_{i,jj}^p + \frac{G}{1-2v} u_{j,ji}^p = -b_i \tag{3.49}$$

without any restriction of boundary condition. However, the homogeneous solution should satisfy

$$Gu_{i,jj}^h + \frac{G}{1-2\nu} u_{j,ji}^h = 0 \tag{3.50}$$

with the modified boundary conditions

$$u_i^h = \bar{u}_i - u_i^p \quad \text{on } \Gamma_u \tag{3.51}$$

$$t_i^h = \bar{t}_i - t_i^p \quad \text{on } \Gamma_t \tag{3.52}$$

From the above equations it can be seen that once the particular solution u_i^p is known, the homogeneous solution u_i^h in Eqs. (3.50)-(3.52) can be obtained using the HFS-FEM. The final solution can then be given by Eq.(3.48). In the next section, radial basis function approximation is introduced to obtain the particular solution, and the HFS-FEM is given for solving Eqs. (3.50)-(3.52).

3.4. RADIAL BASIS FUNCTION APPROXIMATION

For the body force b_i, it is generally impossible to find an analytical solution that converts the domain integral into a boundary one. So it must be approximated by a combination of basis (trial) functions or other methods. The radial basis function (RBF), which has been found to be most suitable for this purpose (Golberg, Chen et al. 1999; Cheng, Chen et al. 2001), is used for interpolation of body forces in this paper. Hence, we assume

$$b_i \approx \sum_{j=1}^{N} \alpha_i^j \varphi^j \tag{3.53}$$

where N is the number of interpolation points, φ^j are the RBFs and α_i^j are the coefficients to be determined. Then, the particular solution can be approximated by

$$u_i^p = \sum_{j=1}^{N} \alpha_i^j \Phi_{ik}^j \tag{3.54}$$

where Φ_{ik}^j is the approximated particular solution kernel of displacement. Once the basis functions are selected, the problem of finding a particular solution is reduced to solving the following equation

$$G\Phi_{il,kk} + \frac{G}{1-2\nu} \Phi_{kl,ki} = -\delta_{il}\varphi \tag{3.55}$$

To solve this equation, the displacement is expressed in terms of the Galerkin -Papkovich vectors

$$\Phi_{ik} = \frac{1-\nu}{G} F_{ik,mm} - \frac{1}{2G} F_{mk,mi} \tag{3.56}$$

Substituting Eq. (3.56) into Eq. (3.55), we can obtain the following bi-harmonic equation is obtained

$$\nabla^4 F_{il} = -\frac{1}{1-\nu} \delta_{il} \varphi \tag{3.57}$$

Taking the Spline Type RBF $\varphi = r^{2n-1}$ as an example, we have the following solutions

$$F_{li} = -\frac{\delta_{li}}{1-\nu} \frac{r^{2n+3}}{(2n+1)(2n+2)(2n+3)(2n+4)} \tag{3.58}$$

$$\Phi_{li} = A_0 \left(A_1 \delta_{li} + A_2 r_{,i} r_{,l} \right) \tag{3.59}$$

where

$$\begin{aligned} A_0 &= -\frac{1}{8G(1-\nu)} \frac{r^{2n+1}}{(n+1)(n+2)(2n+1)} \\ A_1 &= 7 + 4n - 4\nu(n+2) \\ A_2 &= -(2n+1) \end{aligned} \tag{3.60}$$

and r_j represents the Euclidean distance between a field point (x, y, z) and a given point (x_j, y_j, z_j) in the domain of interest. The corresponding particular solution of stresses can be obtained by

$$S_{lij} = G(\Phi_{li,j} + \Phi_{lj,i}) + \lambda \delta_{ij} \Phi_{lk,k} \tag{3.61}$$

where $\lambda = \frac{2\nu}{1-2\nu} G$. Substituting Eq.(3.59) into Eq.(3.61) yields

$$S_{lij} = B_0 \left\{ B_1 \left(r_{,j} \delta_{li} + r_{,i} \delta_{jl} \right) + B_2 \delta_{ij} r_{,l} + B_3 r_{,i} r_{,j} r_{,l} \right\} \tag{3.62}$$

where

$$\begin{aligned} B_0 &= -\frac{1}{4(1-\nu)} \frac{r^{2n}}{(n+1)(n+2)} \\ B_1 &= 3 + 2n - 2\nu(n+2) \\ B_2 &= 2\nu(n+2) - 1 \\ B_3 &= 1 - 2n \end{aligned} \tag{3.63}$$

3.5. HFS-FEM FOR HOMOGENEOUS SOLUTION

After obtaining the particular solution, the next step is to modify the boundary conditions using Eqs. (3.51) and (3.52), after which the 3D problem can be treated as a homogeneous problem governed by Eqs. (3.50)-(3.52) by using the HFS-FEM presented in Section 3.2. It is clear that once the particular and homogeneous solutions for displacement and stress components at nodal points are determined, the distribution of displacement and stress fields at any point in the domain can be calculated using the element interpolation function.

3.6. NUMERICAL EXAMPLES

The performance of the proposed 3D HFS-FEM is now evaluated with a number of challenging problems from the literature. First, the 3D patch test presented by (Macneal and Harder 1985) is conducted for the proposed element and is passed. Then the standard two-element distortion test and straight beam tests (with rectangular, trapezoid and parallelogram shape elements) are conducted. An irregularly meshed biomaterial beam is also investigated and the element performance of different elements is compared. After that, a cube under uniform loading and body force is presented to demonstrate the performance of the method for solving problems involving body forces. Then a perforated thick plate is considered to assess the handling of stress concentration. Finally, nearly incompressible materials are used to investigate the applicability of the method to volumetric locking problems.

3.6.1. 3D Patch test

A standard 3D patch test presented by Macneal and Harder (Macneal and Harder 1985) is carried out in this example. A unit cube is discretized by seven irregular 8-node hexahedral elements, as shown in Figure 3.4. The material is linear elastic with Young's module E $=10^6$ Pa and Poisson ratio v=0.25. The eight exterior nodes are given a prescribed linear displacement as shown in Eq.(3.64) to reproduce a uniform strain/stress state for the irregular elements.

$$u=0.5\times10^{-3}(2x+y+z),\ v=0.5\times10^{-3}(x+2y+z),\ w=0.5\times10^{-3}(x+y+2z) \tag{3.64}$$

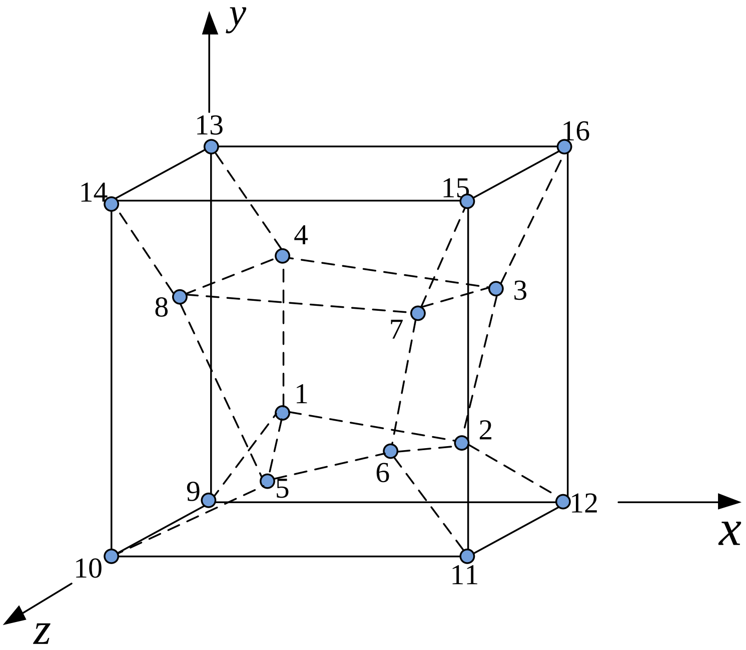

Figure 3.4 3D patch test with wrap element (unit cube: $E = 10^6$, $v = 0.25$).

Table 3.1 gives the nodal coordinates of the elements and the boundary condition for the eight external nodes, and the interior nodes are free of any external load. It is found that both the 8-node and a 20-node brick element can successfully pass the patch test. It is demonstrated that the linear field can be approximated by the superposition of a finite number of the fundamental solutions with relatively high accuracy.

3.6.2. Beam bending: sensitivity to mesh distortion

To demonstrate the sensibility of the proposed model to mesh distortion, the well-known two-element distortion test is examined (Weissman and Taylor 1992; Andelfinger and Ramm 1993; Weissman 1996; Korelc and Wriggers 1997), as shown in Figure 3.5. The surface separating the two elements is gradually rotated to skew the mesh. The tip deflection at point A of the beam under pure bending is presented in Figure 3.6. From this figure, it can be seen that the error of deflection from HFS-FEM (HFS-HEX8) increases from 10% to about 40% when the distortion parameter Δ increases from 1 to 4. However, the present element is not as sensitive to the distortion as the elements by Pian and Tong (Pian and Tong 1986) and Weissman (Weissman

1996). Compared with the results obtained by Pian and Tong (Pian and Tong 1986) and Weissman, it is obvious that the present results are much better when the element is distorted.

Table 3.1 Node coordinates and displacement boundary condition for external nodes of the 3D patch test.

Node	Coordinates			Displacement Boundary Condition		
	x_1	x_2	x_3	u_1	u_2	u_3
1	0.249	0.342	0.342	-	-	-
2	0.826	0.288	0.288	-	-	-
3	0.850	0.649	0.263	-	-	-
4	0.273	0.750	0.230	-	-	-
5	0.320	0.186	0.643	-	-	-
6	0.677	0.305	0.683	-	-	-
7	0.788	0.693	0.644	-	-	-
8	0.165	0.745	0.702	-	-	-
9	0.0	0.0	0.0	0.0	0.0	0.0
10	1.0	0.0	0.0	1.0	0.5	0.5
11	1.0	1.0	0.0	1.5	1.5	1.0
12	0.0	1.0	0.0	0.5	1.0	0.5
13	0.0	0.0	0.0	0.5	0.5	1.0
14	1.0	0.0	1.0	1.5	1.0	1.5
15	1.0	1.0	1.0	2.0	2.0	2.0
16	0.0	1.0	1.0	1.0	1.5	1.5

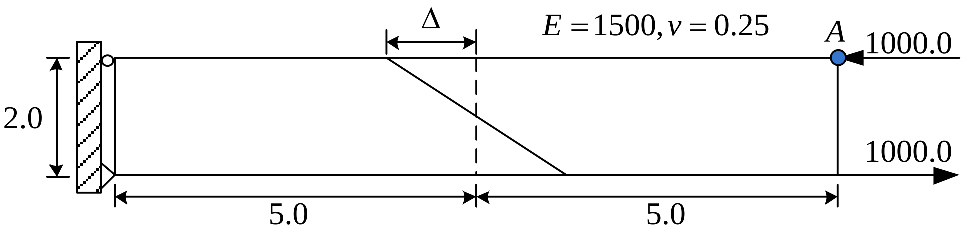

Figure 3.5 Perspective view of a cantilever beam under end moment: sensitivity to mesh distortion.

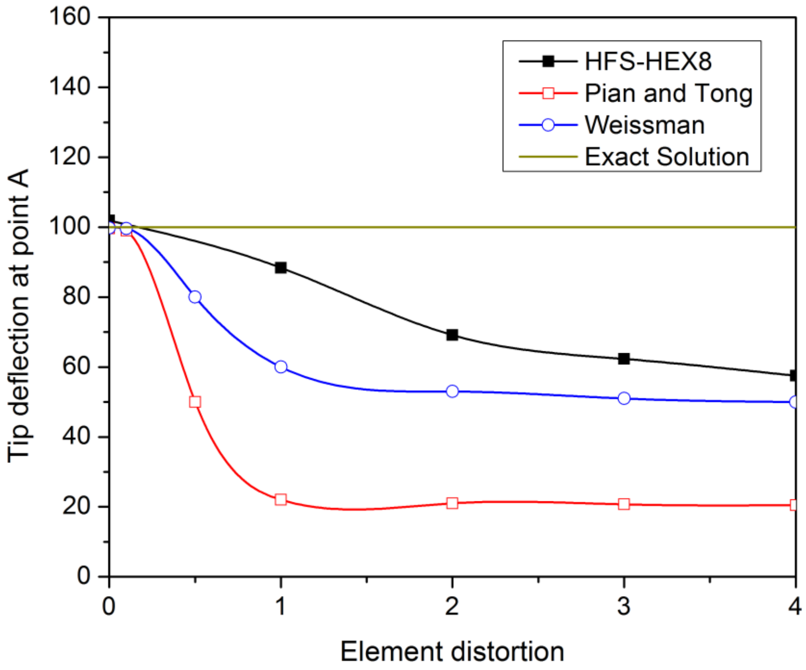

Figure 3.6 Comparison of deflection at point A for a cantilever beam (deflection at point A from a cantilever beam under end moment).

3.6.3. Cantilever beam under shear loading

A set of beams with rectangular, trapezoidal and parallelogram shapes (Macneal and Harder 1985; Cao, Hu et al. 2002) as shown in Figure 3.7 are investigated. The materials constants are $E = 1.0 \times 10^7$ and $v = 0.3$. One end of the beam is fixed and at the other end of the beam a concentrated load of $P = 1$ is applied. The length, width and thickness of the beams are 6.0, 0.2 and 0.1, respectively. The results obtained are normalized by the theoretical solution, 0.1081, which is obtained from beam theory (Macneal and Harder 1985).

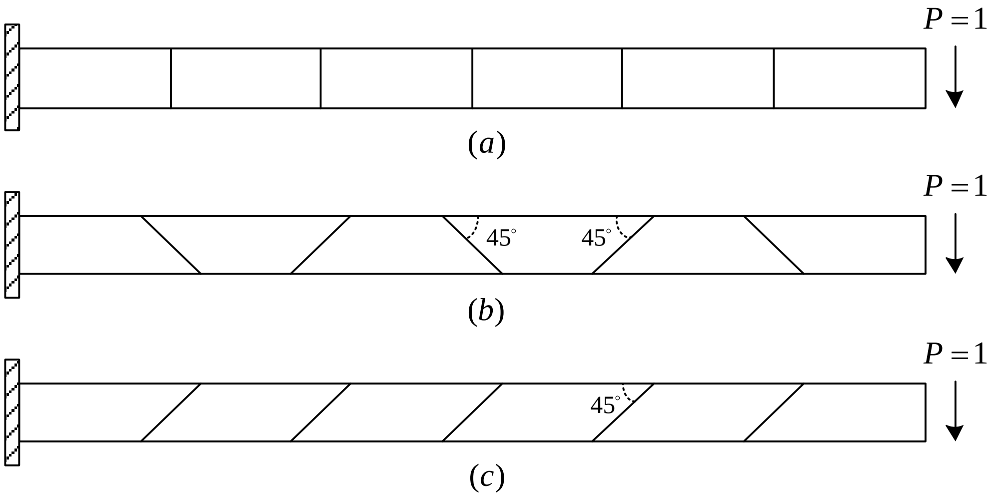

Figure 3.7 Perspective views of straight cantilever beams: (a) Regular shape beam; (b) Trapezoid shape elements; (c) Parallelogram shape element.

The normalized results are shown in Table 3.2. It is evident that the HFS-HEX8 element cannot overcome the locking phenomenon for the trapezoidal and parallelogram cases. It exhibits severe locking in the trapezoidal case, which is only 0.281 times the exact value. However, its performance is still better than that of the elements of Pian and Tong. For the parallelogram case, the accuracy of the HFS-HEX8 element is similar to that reported by Cao et.al (Cao, Hu et al. 2002) and Pian and Tong (Pian and Tong 1986).

Table 3.2 Comparison of normalized tip deflections of straight beam in load direction.

Mesh type	Pian and Tong (Pian and Tong 1986)	Cao et.al (Cao, Hu et al. 2002)	HFS-HEX-8
Rectangular	0.981	0.981	0.962
Trapezoidal	0.047	0.980	0.281
Parallelogram	0.625	0.653	0.657

3.6.4. Irregularly meshed beam with two materials

In the fourth example, a long beam composed of two materials as shown in Figure 3.8 is investigated. The beam is 4m long with a constant squared cross-section of 0.5×0.5m^2. The material parameters are respectively E_1=200 MPa, v_1=0.3 and E_2=400 MPa, v_2=0.3 (Ribeiro and Paiva 2009). The interface between the two materials is considered perfectly bonded. The displacements are restrained at one end of the beam and a transverse force of 2kN is uniformly applied on the cross-section of the other end, as shown in Figure 3.8.

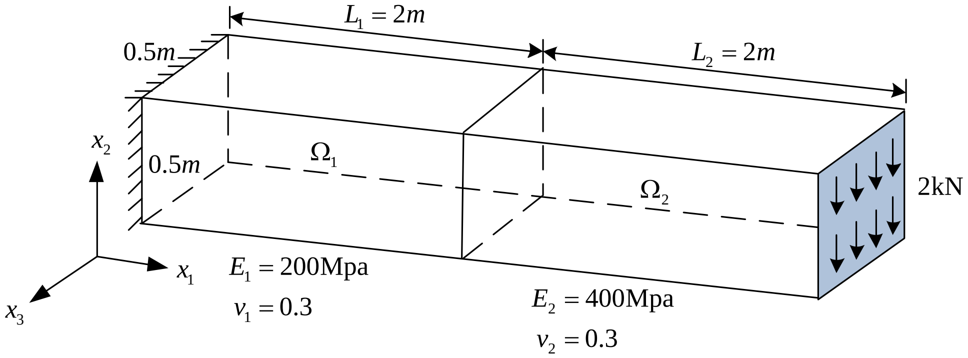

Figure 3.8 Irregularly meshed bimaterial beam: geometry, materials and boundary conditions.

The response of the beam is computed using the 3D HFS-FEM for three irregular meshes, as shown in Figure 3.9, i.e. Mesh 1 (2×2×10 elements with 99 nodes), Mesh 2 (4×4×20 elements with 525 nodes) and Mesh 3 (8×8×40 elements with 3321 nodes). The transverse displacements u_2 along the force direction at the central tip point of the cross-section are used for comparison. Table 3.3 gives the transverse displacement u_2 obtained by the HFS-FEM using HFS-HEX8 and HFS-HEX20 elements as well as the results by ABAQUS C3D8 elements and enhanced strain elements (EAS) (Simo and Rifai 1990). For Mesh 1 it is found that the C3D8 element is severely locked, as expected. EAS elements produce better results than the original C3D8 elements. The HFS-HEX8 element also displays a locking problem for Mesh 1 but significantly improves on the results of C3D8, which has similar performance to EAS element. The quadratic element HFS-HEX20 has the best performance of the listed elements. However, it can be expected that all the elements both from HFS-FEM and ABAQUS will converge to the benchmark value of 3.8388 cm (obtained by ABAQUS using 20×20×100 elements with 71001 nodes shown in Figure 3.10) with increase of the mesh density.

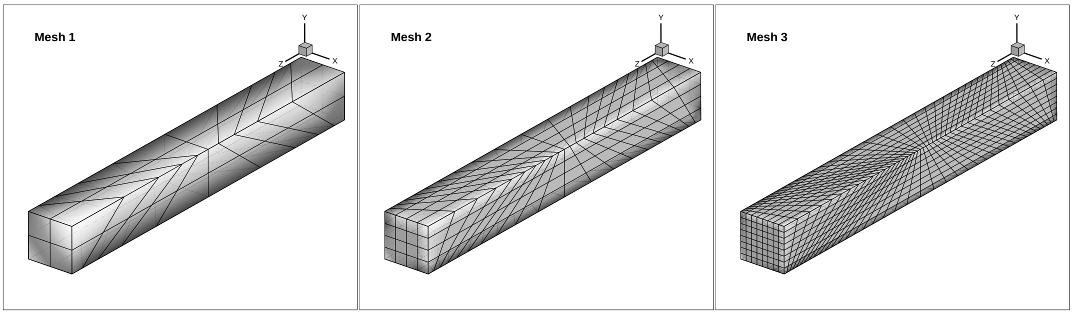

Figure 3.9 Irregularly meshed bimaterial beam: Mesh 1 (2×2×10 elements), Mesh 2 (4×4×20 elements) and Mesh 3 (8×8×40 elements).

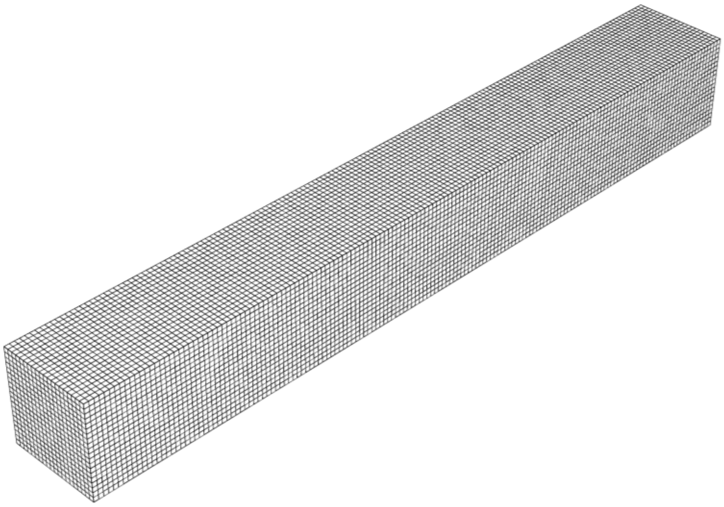

Figure 3.10 Regularly meshed bimaterial beam: fine mesh used by ABAQUS for benchmark reference (20×20×100 elements).

In comparison with the solution of ABAQUS using several tens of thousands of nodes, it is interesting that similar results of nearly the same accuracy can be obtained by HFS-FEM using much coarser meshes. It is expected that by using non-uniform mesh density for the interface and ends, similar results would be obtainable with an even smaller number of elements. It can be concluded from Table 3.3 that the

HFS-FEM with linear or quadratic elements is not sensitive to element distortion as shown in Example 3.6.2, and the shear locking problems is not as severe with the HFS-FEM as with C3D8, and the performance of the HFS-FEM is competitive with that of the EAS.

Table 3.3 Transverse displacement and relative errors of irregularly meshed beam calculated by HFS-FEM and ABAQUS using different elements.

Mesh	HFS-FEM		ABAQUS	
	HEX8	HEX20	EAS	C3D8
Mesh 1 (2×2×10)	3.0842 (19.65%)	3.7890 (1.30%)	3.2541 (15.23%)	2.1612 (43.70%)
Mesh 2 (4×4×20)	3.6188 (5.73%)	3.8305 (0.22%)	3.6982 (3.66%)	3.2769 (14.64%)
Mesh 3 (8×8×40)	3.7650 (1.92%)	3.8382 (0.01%)	3.7993 (1.03%)	3.6878 (3.93%)

Note: Displacement unit: cm; Values in parentheses are the relative error.

3.6.5. Cubic block under uniform tension and body force

To investigate the performance of the proposed method for problems involving body forces, an isotropic cubic block subject to uniform tension is considered in this example. The dimension of the block is 10×10×10mm and its geometry and boundary conditions are shown in Figure 3.11. A constant body force of 10 MPa and uniform distributed tension of 100 MPa are applied to the cube. To investigate the convergence of the method, three different meshes are employed with distorted 8-node brick elements: Mesh 1 (4×4×4), Mesh 2 (6×6×6) and Mesh 3 (10×10×10) as shown in Figure 3.12. The displacement and stress at Point *A* calculated by ABAQUS with a very fine mesh (shown in Figure 3.13, 40×40×40 C3D8 elements with 68921 nodes), which can be viewed as the exact solution are given as a reference benchmark for comparison.

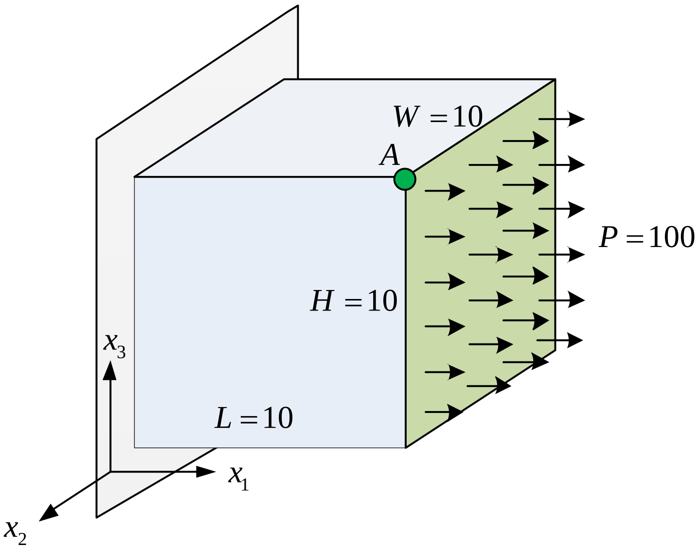

Figure 3.11 Cubic block under uniform tension and body force: geometry, boundary condition, and loading (Length unit: mm, force unit: MPa).

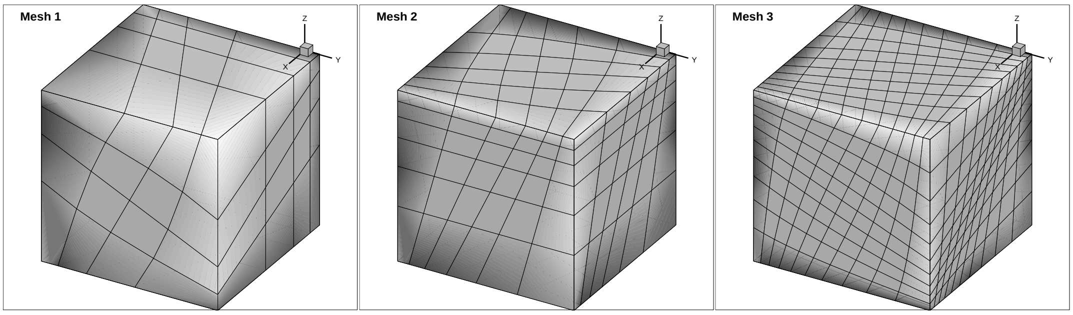

Figure 3.12 Cubic block under uniform tension and body force: Mesh 1 (4×4×4 elements), Mesh 2 (6×6×6 elements), and Mesh 3 (10×10×10 elements).

Figure 3.14 and Figure 3.15 present the displacement component u_1 and the stress component σ_{11} at Point *A* of the block, calculated by the HFS-FEM on the three meshes shown in Figure 3.12. The results from C3D8 and EAS elements are also presented for comparison. It can be seen from these figures that the results obtained from both the HFS-FEM and ABAQUS converge to the benchmark value with an increase in the number of DOF. For Mesh 1, the hybrid EAS element has the best performance whereas for Mesh 2 and Mesh 3 the HFS-FEM with HEX8 elements exhibits better accuracy for both displacement and stresses compared with EAS in traditional FEM. From the results it can be seen that the C3D8 has the poorest performance of the three types of elements presented. Contour plots of u_1 and σ_{11} obtained by HFS-FEM on Mesh 3 are also presented in Figure 3.16.

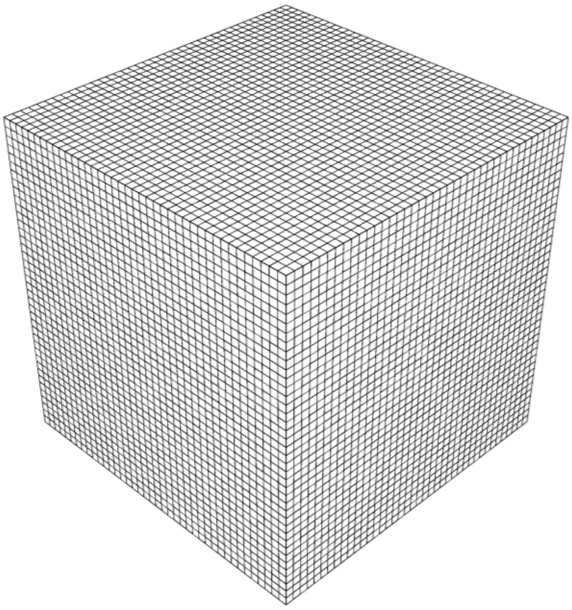

Figure 3.13 Cubic block under uniform tension and body force: fine mesh used by ABAQUS for benchmark reference (40×40×40 elements).

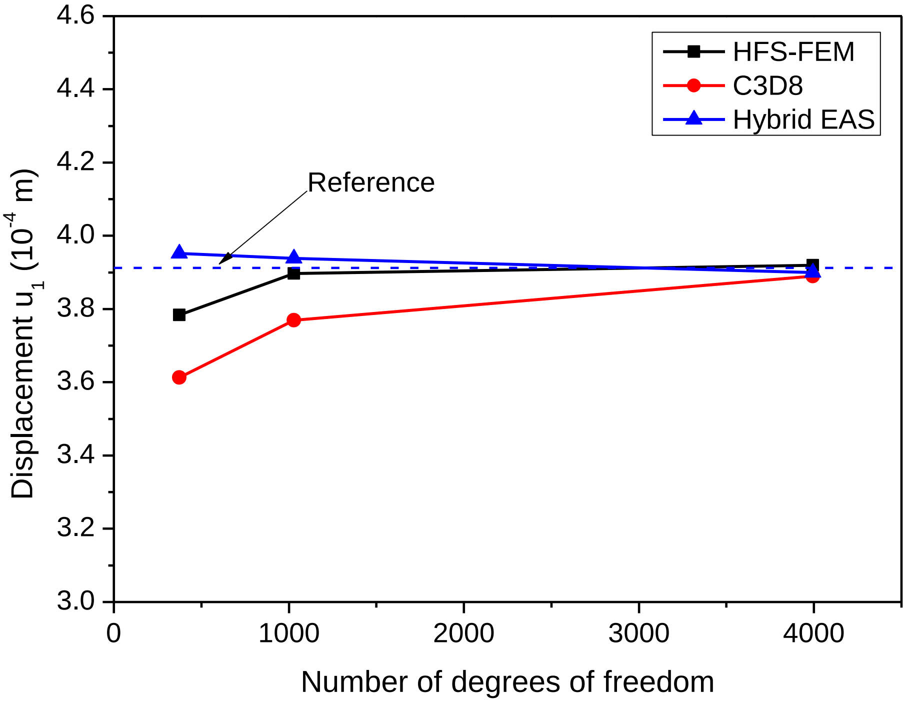

Figure 3.14 Cubic block with body force under uniform distributed load: Convergent study of displacements.

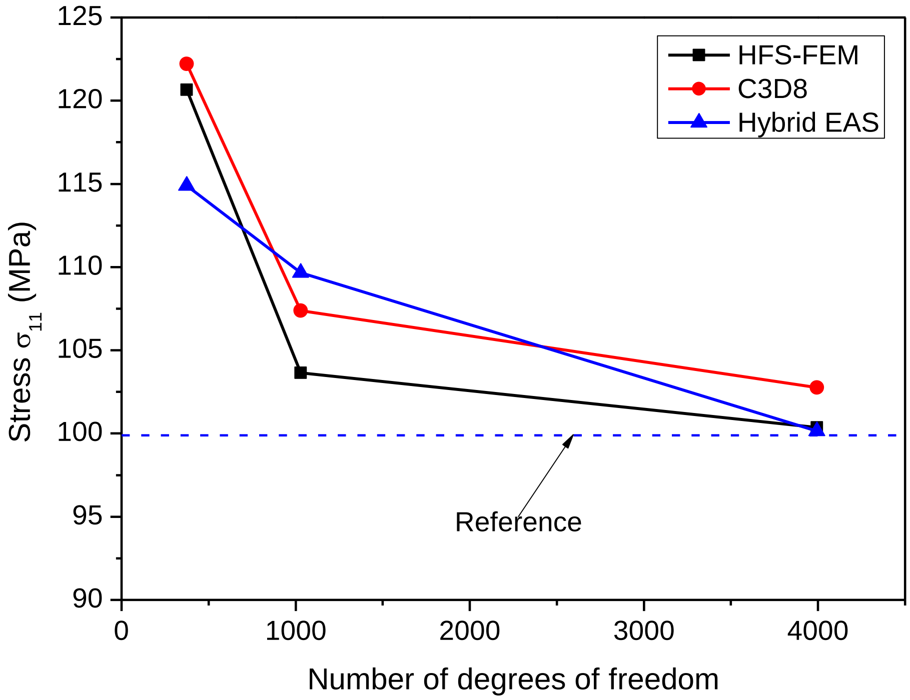

Figure 3.15 Cubic block with body force under uniform distributed load: Convergent study of stresses.

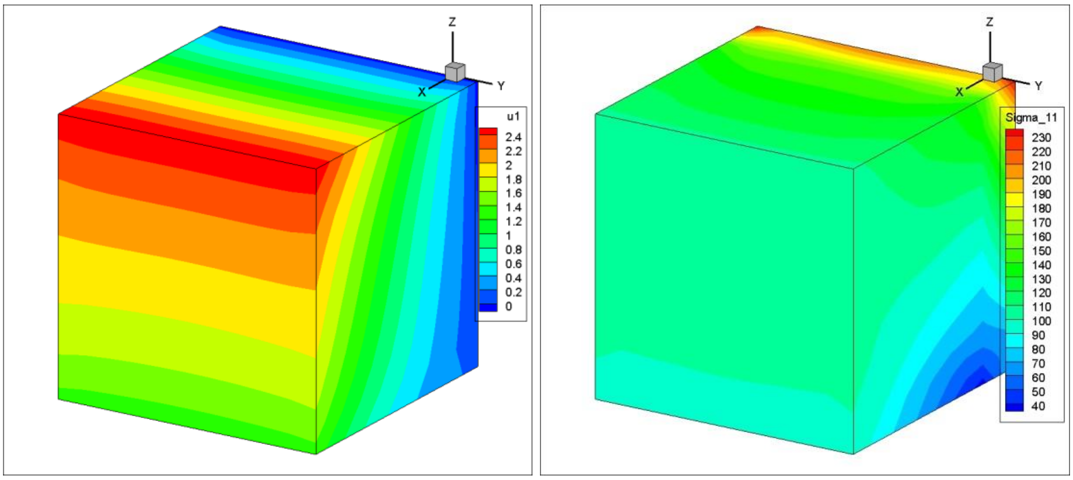

Figure 3.16 Contour plots of displacement u_1 and stress σ_{11} of the cube.

It should be noted that for problems involving body forces the accuracy of the RBF interpolation must be considered for a satisfactory solution. With the current method for producing interpolation points, i.e. the interpolation points are the same as the element nodes, increasing the nodes of the domain will improve the accuracy for body force approximation, and then the results of displacement and stress are improved. Thus, to improve the accuracy of HFS-FEM for problems involving body force, it would be expected to increase the number of nodes so as to increase the interpolation points. Details of the RBF interpolation can be found in previous literatures (Cheng, Chen et al. 2001).

3.6.6. Thick plate with a central hole

The influence of holes on the distribution of stresses in structural elements has been investigated for a long time (Savin 1961; Folias and Wang 1990; Golecki 1995). To demonstrate the capability of the new method to handle complex geometry and stress concentration, a thick plate with a circle hole at its center is investigated in this example. Uniform displacement $u_1 = 1$ mm is applied on one face of the plate along the *x* axis as shown in Figure 3.17. The reference results are obtained by ABAQUS using 138,866 C3D8R elements with 151,725 nodes, as illustrated in Figure 3.13. Three different meshes used in this example, Mesh 1 (660 elements with 985 nodes), Mesh 2 (1392 elements with 1876 nodes) and Mesh 3 (5274 elements with 6657 nodes), are shown in Figure 3.18.

Figure 3.20 presents the results calculated by the HFS-FEM and ABAQUS for the stress at point M (as shown in Figure 3.17). It is obvious that the results from HFS-FEM are much better than those given by ABAQUS. The error of HFS-FEM is less than 3% whereas the error of ABAQUS is greater than 20% when using the finer Mesh 3. The von Mises stress of the thick plates is also given in Figure 3.21, in which the von Mises stress is given by

$$\sigma_{vm} = \sqrt{\frac{3}{2}\sigma'_{ij}\sigma'_{ji}} \tag{3.65}$$

where σ_{vm} is the von Mises stress, σ_{ij} is the stress tensor and σ'_{ij} is the deviatory stress defined by

$$\sigma'_{ij} = \sigma_{ij} - \frac{1}{3}\sigma_{kk}\delta_{ij} \tag{3.66}$$

It can be seen from Figure 3.21 that the HFS-FEM demonstrates promising performance with a far smaller error than that obtained from ABAQUS in the stress concentration problems.

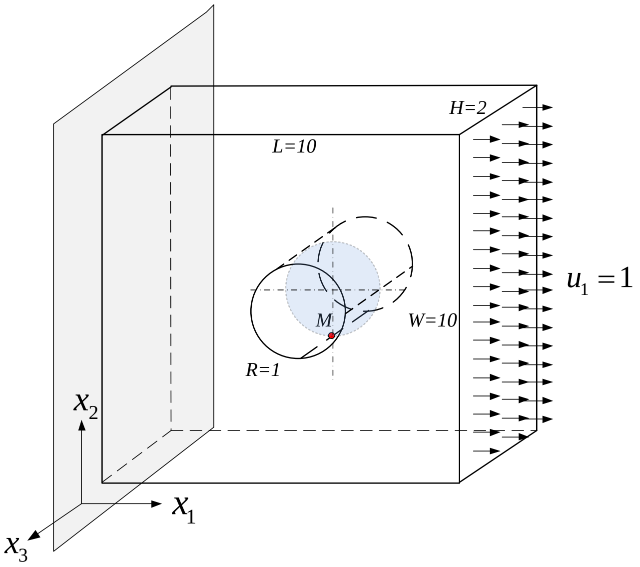

Figure 3.17 Thick plate with central hole: geometry, material and boundary conditions.

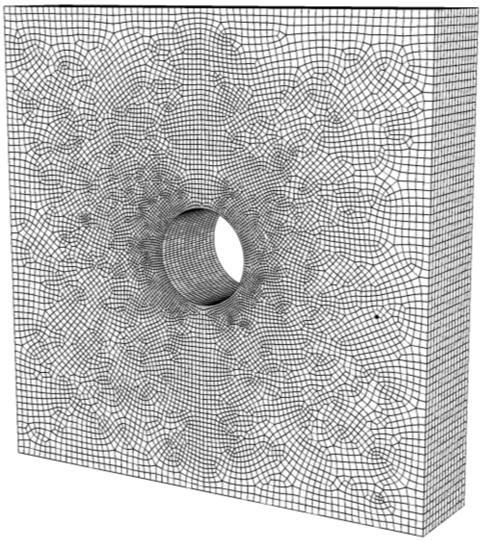

Figure 3.18 Thick plate with central hole: fine mesh used by ABAQUS for benchmark reference (138866 elements with 151725 nodes).

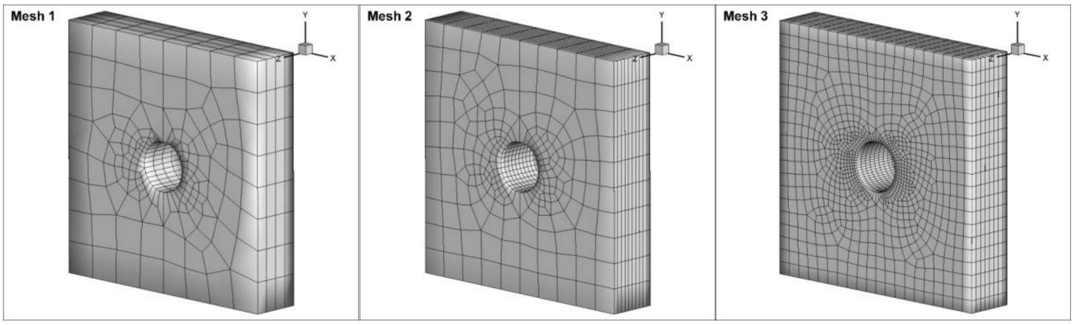

Figure 3.19 Perforated thick plate: Mesh 1 (660 elements with 985 nodes), Mesh 2 (1392 elements with 1876 nodes) and Mesh 3 (5274 elements with 6657 nodes).

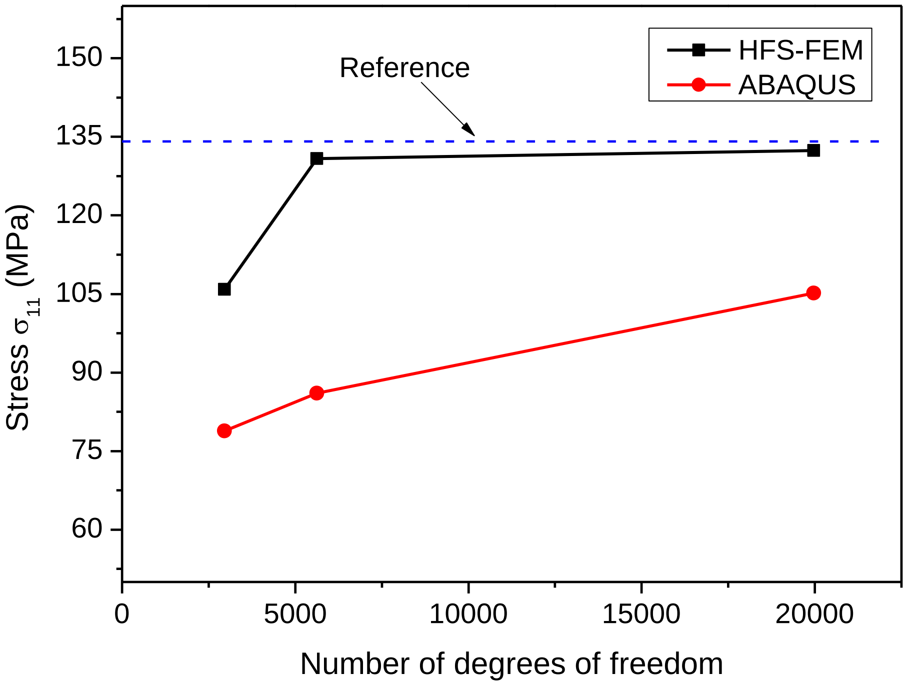

Figure 3.20 Perforated thick plate under uniform distributed load: Convergent study of stresses.

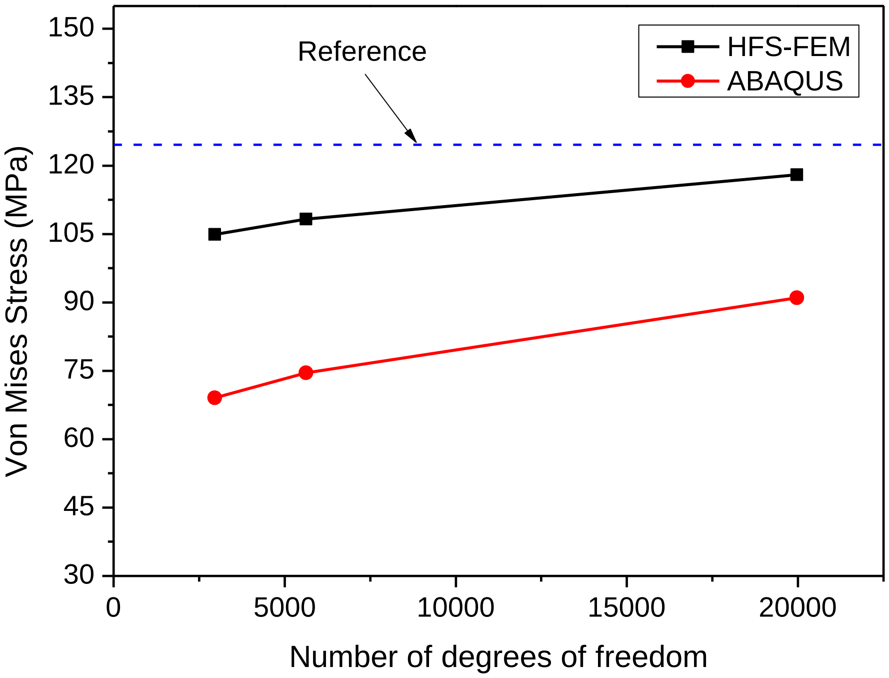

Figure 3.21 Perforated thick plate under uniformly distributed load: Convergent study of von Mises stress.

3.6.7. Nearly incompressible block

As shown in Figure 3.22, a nearly incompressible block with dimensions 100×100×50 m is considered (Andelfinger and Ramm 1993; Mueller-Hoeppe, Loehnert et al. 2009). The block is fixed at the bottom and loaded at the top by a uniform pressure of q=250 Pa, acting on an area of 20×20 at the center. Due to symmetry of the problem, only a quarter of the block is discretized with a uniform 5×5×5 mesh. The bottom face of the block is fixed in the x_3-direction, and the symmetry boundary conditions are applied to the symmetry surface of the block. The geometry and the material properties as well as the load applied and the boundary conditions are given in Figure 3.22.

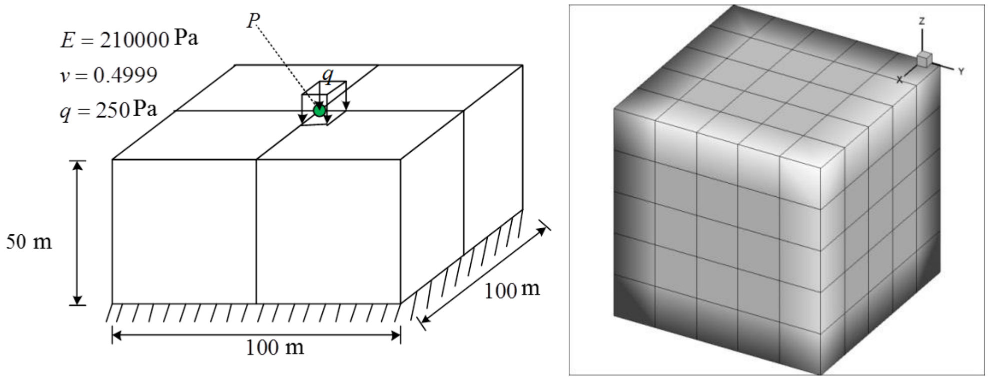

Figure 3.22 Nearly incompressible block: geometry, boundary conditions and the tested mesh (1/4 model).

The vertical displacement at the top center *P* of the block is listed for the HFS-HEX8 element, HIS element (Areias, César de Sá et al. 2003) as well as the 3D.EAS-30 (Andelfinger and Ramm 1993) and QM1/E12 (Korelc and Wriggers 1996) element in Table 3.4. It is found that HFS-HEX8 is free of volumetric locking and shows a significantly softer response compared with the QM1/E12 element. The enhanced strain element 3D.EAS-30 exhibits a little more stiffness than HFS-HEX-8 and HIS proposed by Areias et al.(Areias, César de Sá et al. 2003). The contour plot of the vertical displacement of the block using the HFS-HEX-8 element with 5×5×5 meshes is shown in Figure 3.23. With the QM1/E12 element, however, it is noted that solutions can be obtained for the two coarsest meshes only. With finer mesh resolutions, the QM1/E12 element shows unphysical hourglass instabilities (Mueller-Hoeppe, Loehnert et al. 2009).

Table 3.4 Near-incompressible regular block, displacement at the center *P* of the block.

Element	Displacement (m)	Error
HFS-HEX8	0.02132	10.98%
HIS (Areias, César de Sá et al. 2003)	0.01921	0.00%
3D.EAS-30 (Andelfinger and Ramm 1993)	0.01905	0.83%
QM1/E12 (Korelc and Wriggers 1996)	0.01892	1.51%

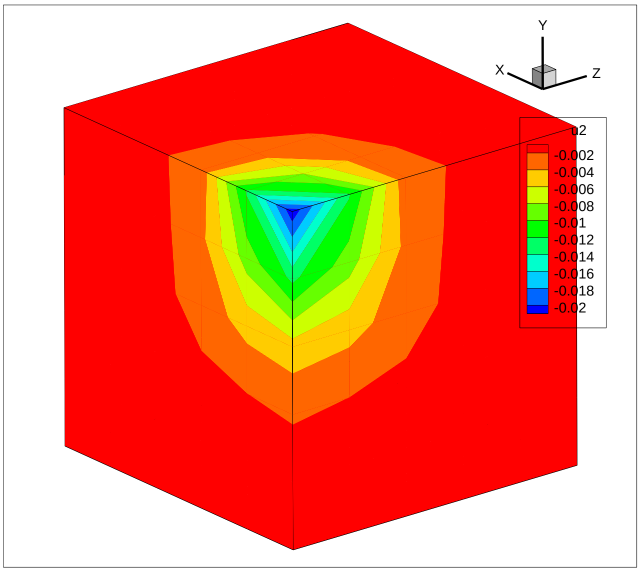

Figure 3.23 Contour plot of the vertical displacements (m) of the near-incompressible regular block under central uniform loading.

3.7. SUMMARY

In this work a new HFS-FEM approach is proposed for analyzing 3D elastic problems. Detailed formulations for the 3D HFS-FEM are first derived for elastic problems by ignoring body force terms and then the method of particular solution and the RBF approximation are integrated into the HFS-FEM model to solve elastic problems with body forces. The homogeneous solution is obtained by the HFS-FEM and the particular solution by the RBF approach. Several standard tests and numerical examples are presented to demonstrate the capability and accuracy of the method. It is found that the new method with linear 8-node and quadratic 20-node brick elements can successfully pass the patch test. It is also found that HFS-HEX8 element exhibits the shear locking phenomenon and cannot pass the trapezoidal and parallelogram beam test, although it is not very sensitive to mesh distortion and performance is superior to that of the Pian and Tong element. It is also demonstrated that the new method usually converges better than the traditional FEM and it can be used in problems with nearly incompressible materials without volumetric locking. This new method seems promising for dealing with problems involving complex geometry, stress concentration and multi-materials. It is possible to extend the current method to nonlinear problems by treating nonlinear terms as a generalized body force and developing a convergent iterative algorithm.

Chapter 4. HFS-FEM for Anisotropic Composites

4.1. INTRODUCTION

In materials science, composite laminates are usually assemblies of layers of fibrous composite materials which can be joined together to provide required engineering properties, such as specified in-plane stiffness, bending stiffness, strength, and coefficient of thermal expansion (see Figure 4.1) (Vasiliev and Morozov 2007). Individual layers (or laminas) of the laminates consist of high-modulus, high-strength fibers in a polymeric, metallic, or ceramic matrix material. On one hand, the fiber and matrix in each lamina can be treated as inclusion and matrix, respectively, from the viewpoint of micromechanics. On the other hand, each lamina and the whole laminate can also be viewed as a general anisotropic body in classical lamination theory, from the viewpoint of macromechanics. Hence, the analysis of anisotropic bodies is important for understanding of the micro- or macro-mechanical behavior of composites (Hwu and Yen 1991; Vasiliev and Morozov 2007).

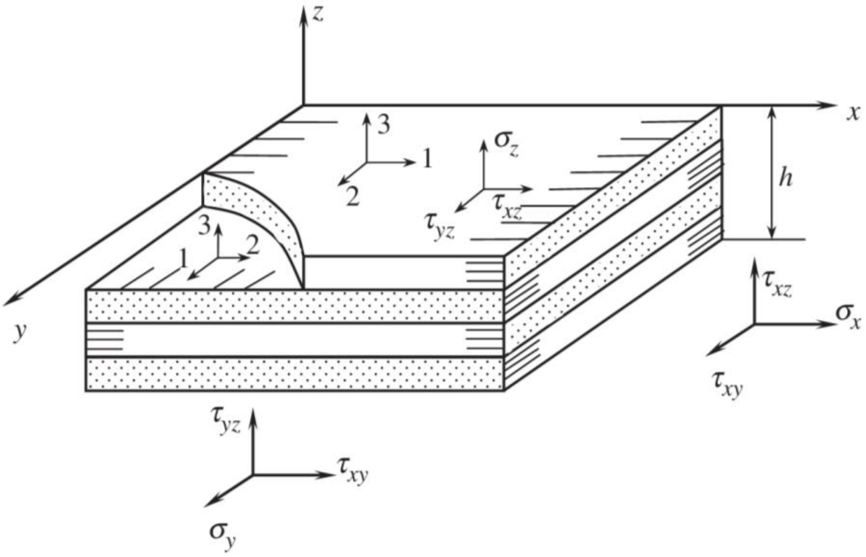

Figure 4.1 Schematic of a composite laminate (Vasiliev and Morozov 2007).

There are two main approaches in the literature, dealing with generalized two-dimensional anisotropic elastic problems. The first is Lekhnitskii formalism (Lekhnitskii 1981), which begins with the stresses as basic variables and the other is Stroh formalism (Stroh 1958; Ting 1996) , which starts with the displacements as basic variables. Both of these approaches are formulated in terms of complex variable functions. Stroh formalism, which has been shown to be elegant and powerful, is used to find analytical solutions for corresponding infinite bodies (Ting 1996). The basic assumption of Stroh formalism is that all components of stresses and displacements in an elastic body depend on x_1 and x_2 only, which is the condition for generalized plane deformation. Stroh formalism can be reduced directly to plane strain problems when out-of-plane displacement is zero. Moreover, it can also be applied to the generalized plane stress problems by considering displacements and stress as the average values through the thickness of the plates (Hwu and Yen 1991). In general, Stroh formalism is suitable for anisotropic material with distinct material eigenvalues. For degenerate materials with repeated eigenvalues such as isotropic materials, the results should be modified in analytical sense (Ting and Hwu 1988). However, a small perturbation of the material constants can usually lead to the eigenvalues be distinct and the results can be conveniently applied to isotropic materials. This formalism is also widely employed in the derivation of inclusion or crack problems of anisotropic materials (Ting 1996).

Because of the limitations of analytical solutions which are available only for certain problems with simple geometry and boundary conditions (Lekhnitskii 1981; Ting 1996), numerical methods such as FEM, BEM, mesh free method (MFM), and HT-FEM are usually resorted to solve more complex problems with complicated boundary constraints and loading conditions (Hwu and Yen 1991; Denda and Kosaka 1997; Ting, Chen et al. 1999; Qin 2000; Wang, Mogilevskaya et al. 2003; Rajesh and Rao 2010). As an alternative to the HT-FEM, a hybrid finite element formulation based on the fundamental solutions, called the HFS-FEM, has recently been developed for solving 2D elastic and thermal problems for isotropic (Wang and Qin 2010a; Wang and Qin 2011), orthotropic (Wang and Qin 2010b) and piezoelectric materials (Cao, Qin et al. 2012b). The HFS-FEM retains the advantages of the HT-FEM over the traditional FEM and the BEM, such as the possibility of high accuracy using coarse meshes of high-degree elements, enhanced insensitivity to mesh distortion, great liberty in element shape, and accurately representation of various local effects without troublesome mesh adjustment (Qin 2003; Dhanasekar, Han et al. 2006). Compared to the HT-FEM, HFS-FEM has simpler interpolation kernel expressions for intra-element fields (fundamental solutions) and avoids the coordinate transformation procedure required in the HT-FEM to keep the matrix inversion stable.

In this chapter, the new hybrid finite element model (HFS-FEM) for analyzing anisotropic composite materials is developed based on the associated fundamental solutions in terms of Stroh formalism. The foundational solutions of anisotropic materials are employed to approximate the intra-element displacement field of general elements. Four numerical examples are presented to demonstrate the accuracy and efficiency of the proposed method. The chapter is organized as follows: a brief review of the basic equations, Stroh formalism, and the related fundamental solutions for a generalized 2D anisotropic elastic problem is presented in Section 4.2. Then the detailed HFS-FE formulations for composite materials are presented in Section 4.3. Several numerical examples are presented in Section 4.4 to verify and demonstrate the performance of the proposed method and finally some concluding remarks are provided in Section 4.5. The majority of this chapter has been presented in a paper (Cao, Qin et al. 2013a) co-authored by the candidate.

4.2. LINEAR ANISOTROPIC ELASTICITY

4.2.1. Basic equations and Stroh formalism

In the Cartesian coordinate system (x_1, x_2, x_3), if we neglect the body force b_i , then the equilibrium equations, stress-strain laws and strain-displacement equations for anisotropic elasticity are (Ting 1996)

$$\sigma_{ij,j} = 0 \qquad (4.1)$$

$$\sigma_{ij} = C_{ijkl} e_{kl} \qquad (4.2)$$

$$e_{ij} = \frac{1}{2}(u_{i,j} + u_{j,i}) \qquad (4.3)$$

where $i, j = 1, 2, 3$, σ_{ij} is the stress tensor, e_{kl} the strain tensor, C_{ijkl} the fourth-rank anisotropic elasticity tensor, and u_i the displacement vector. For convenience, matrices are here represented by bold-face letters and a comma followed by an index implies differentiation with respect to that index. The summation convention is invoked over repeated indices. The equilibrium equations can be rewritten in terms of displacements by substituting Eqs. (4.2) and (4.3) into Eq. (4.1) as

$$C_{ijkl} u_{k,jl} = 0 \qquad (4.4)$$

The boundary conditions of the boundary value problem (4.2)-(4.4) are

$$u_i = \bar{u}_i \qquad \text{on } \Gamma_u \qquad (4.5)$$

$$t_i = \sigma_{ij} n_j = \bar{t}_i \qquad \text{on } \Gamma_t \qquad (4.6)$$

where $\bar{u}_i$ and $\bar{t}_i$ are the prescribed boundary displacement vector and the traction vector, respectively. In addition, n_i is the unit outward normal to the boundary and $\Gamma = \Gamma_u + \Gamma_t$ is the boundary of the solution domain Ω.

For the generalized 2D deformation of anisotropic elasticity u_i is assumed to depend on x_1 and x_2 only. With this assumption, the general solution to (4.4) can be written as (Stroh 1958; Ting 1996)

$$\mathbf{u} = 2\,\mathrm{Re}\{\mathbf{Af}(z)\}, \boldsymbol{\varphi} = 2\,\mathrm{Re}\{\mathbf{Bf}(z)\} \qquad (4.7)$$

where $\mathbf{u} = (u_1, u_2, u_3)^T$ is the displacement vector, $\boldsymbol{\varphi} = (\varphi_1, \varphi_2, \varphi_3)^T$ is the stress function vector, $\mathbf{f}(z) = [f_1(z_1), f_2(z_2), f_3(z_3)]^T$ is a function vector composed of three holomorphic complex functions $f_\alpha(z_\alpha)$, $\alpha = 1, 2, 3$, which are arbitrary functions with the arguments $z_\alpha = x_1 + p_\alpha x_2$ and will be determined by satisfying the boundary and loading conditions of a given problem. In Eq. (4.7), Re stands for the real part of a complex number, p_α are the material eigenvalues with a positive imaginary part, $\mathbf{A} = [\mathbf{a}_1, \mathbf{a}_2, \mathbf{a}_3]$ and $\mathbf{B} = [\mathbf{b}_1, \mathbf{b}_2, \mathbf{b}_3]$ are 3×3 complex matrices formed by the material eigenvector associated with p_α, which can be obtained by the following eigenrelations (Ting 1996)

$$\mathbf{N}\boldsymbol{\xi} = p\boldsymbol{\xi} \tag{4.8}$$

where $\mathbf{N}$ is a 6×6 foundational elasticity matrix and $\boldsymbol{\xi}$ is a 6×1 column vector defined by

$$\mathbf{N} = \begin{bmatrix} \mathbf{N_1} & \mathbf{N_2} \\ \mathbf{N_3} & \mathbf{N_1^T} \end{bmatrix}, \; \boldsymbol{\xi} = \begin{Bmatrix} \mathbf{a} \\ \mathbf{b} \end{Bmatrix} \tag{4.9}$$

where $\mathbf{N_1} = \mathbf{-T^{-1}R^T}, \mathbf{N_2} = \mathbf{T^{-1}}, \mathbf{N_3} = \mathbf{RT^{-1}R^T} - \mathbf{Q}$ and the matrices $\mathbf{Q}$, $\mathbf{R}$ and $\mathbf{T}$ are 3×3 matrices extracted from C_{ijkl} as follows

$$Q_{ik} = C_{i1k1}, R_{ik} = C_{i1k2}, T_{ik} = C_{i2k2} \tag{4.10}$$

The stresses can be obtained from the derivation of stress functions $\boldsymbol{\varphi}$ as follows

$$\{\sigma_{i1}\} = 2\,\mathrm{Re}\{\mathbf{Lf}'(z)\}, \{\sigma_{i2}\} = 2\,\mathrm{Re}\{\mathbf{Bf}'(z)\} \tag{4.11}$$

where

$$L = \left[-p_1\mathbf{b_1}, -p_2\mathbf{b_2}, -p_3\mathbf{b_3}, -p_4\mathbf{b_4}\right] \tag{4.12}$$

4.2.2. Foundational solutions

To find the fundamental solution needed in this analysis, we must first derive the Green's function of the problem: an infinite homogeneous anisotropic elastic medium loaded by a concentrated point force (or line force for 2D problems) $\hat{\mathbf{p}} = (\hat{p}_1, \hat{p}_2, \hat{p}_3)$ applied at an internal point $\hat{\mathbf{x}} = (\hat{x}_1, \hat{x}_2)$ distant from the boundary. The boundary conditions of this problem can be written as

$$\begin{aligned} &\int_C d\boldsymbol{\phi} = \hat{\mathbf{p}} \quad \text{for any closed curve } C \text{ enclosing } \hat{\mathbf{x}} \\ &\int_C d\mathbf{u} = \hat{\mathbf{p}} \quad \text{for any closed curve } C \\ &\lim_{\mathbf{x}\to\infty} \sigma_{ij} = 0 \end{aligned} \tag{4.13}$$

Thus, the Green's function satisfying the above boundary conditions is found to be (Ting 1996)

$$f(z) = \frac{1}{2\pi i}\langle \ln(z_\alpha - \hat{z}_\alpha)\rangle \mathbf{A}^T\hat{\mathbf{p}} \tag{4.14}$$

Therefore, the fundamental solutions of the problem can be expressed as

$$\begin{aligned} \mathbf{u} &= \frac{1}{\pi}\mathrm{Im}\left\{\mathbf{A}\left\langle \ln\left(z_\alpha - \hat{z}_\alpha\right)\right\rangle \mathbf{A^T}\right\}\hat{\mathbf{p}} \\ \phi &= \frac{1}{\pi}\mathrm{Im}\left\{\mathbf{B}\left\langle \ln\left(z_\alpha - \hat{z}_\alpha\right)\right\rangle \mathbf{A^T}\right\}\hat{\mathbf{p}} \end{aligned} \tag{4.15}$$

The corresponding stress components can be obtained from stress function ϕ

$$\begin{aligned}\sigma_{i1}^{*} &= -\phi_{,2} = -\frac{1}{\pi}\operatorname{Im}\left\{\mathbf{B}\left\langle p_\alpha / \left(z_\alpha - \hat{z}_\alpha\right)\right\rangle \mathbf{A}^{\mathrm{T}}\right\}\hat{\mathbf{p}} \\ \sigma_{i2}^{*} &= \phi_{,1} = \frac{1}{\pi}\operatorname{Im}\left\{\mathbf{B}\left\langle 1/\left(z_\alpha - \hat{z}_\alpha\right)\right\rangle \mathbf{A}^{\mathrm{T}}\right\}\hat{\mathbf{p}}\end{aligned} \tag{4.16}$$

where $\hat{\mathbf{p}}$ are chosen to be $(1,0,0)^T, (0,1,0)^T, (0,0,1)^T$, respectively, $<\cdot>$ stands for the diagonal matrix corresponding to subscript α, Im denotes the imaginary part of a complex number, and superscript T denotes the matrix transpose.

4.2.3. Coordinate transformation

A typical composite laminate consists of individual layers (see Figure 4.1) which are usually made of unidirectional plies with the same or regularly alternating orientation. A layer is generally referred to the global coordinate frame *x*, *y*, and *z* of the structural element rather than to the coordinates 1, 2, and 3 associated with the ply orientation. It is therefore necessary to transform the constitutive relationship of each layer from the material coordinate frame 1, 2, and 3 to the uniform global coordinate frame *x*, *y*, and *z*.

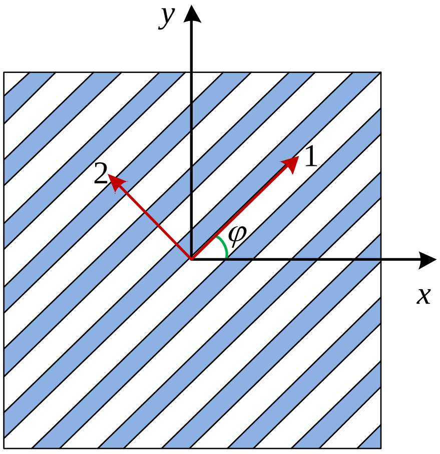

Figure 4.2 Schematic of the relationship between global coordinate system and local material coordinate system (1, 2).

For the two coordinate systems mentioned above (see Figure 4.2), the angle between axis-1 and axis-*x* is denoted by φ, which is positive in the anti-clockwise direction, and the relationship for transformation of stress and strain components between the local material coordinates and the global coordinates is given by

$$\left[\sigma_{xx},\sigma_{yy},\sigma_{yz},\sigma_{zx},\sigma_{xy}\right]^T=\mathbf{T}^{-1}\left[\sigma_{11},\sigma_{22},\sigma_{23},\sigma_{31},\sigma_{12}\right]^T \tag{4.17}$$

and

$$\left[\varepsilon_{11},\varepsilon_{22},\varepsilon_{23},\varepsilon_{31},\varepsilon_{12}\right]^T=\left(\mathbf{T}^{-1}\right)^T\left[\varepsilon_{xx},\varepsilon_{yy},\varepsilon_{yz},\varepsilon_{zx},\varepsilon_{xy}\right]^T \tag{4.18}$$

where the transformation matrix $\mathbf{T}$ and its inverse matrix are defined as

$$\mathbf{T}=\begin{bmatrix} c^2 & s^2 & 0 & 0 & 2cs \\ s^2 & c^2 & 0 & 0 & -2cs \\ 0 & 0 & c & -s & 0 \\ 0 & 0 & s & c & 0 \\ -cs & cs & 0 & 0 & c^2-s^2 \end{bmatrix}, \quad \mathbf{T}^{-1}=\begin{bmatrix} c^2 & s^2 & 0 & 0 & -2cs \\ s^2 & c^2 & 0 & 0 & 2cs \\ 0 & 0 & c & s & 0 \\ 0 & 0 & -s & c & 0 \\ cs & -cs & 0 & 0 & c^2-s^2 \end{bmatrix} \tag{4.19}$$

with $c=\cos(\varphi),\ \ s=\sin(\varphi)$. Subsequently, the constitutive relationship in the global coordinate system is given by

$$\left[\sigma_{xx},\sigma_{yy},\sigma_{yz},\sigma_{zx},\sigma_{xy}\right]^T=\mathbf{T}^{-1}\mathbf{C}\left(\mathbf{T}^{-1}\right)^T\left[\varepsilon_{xx},\varepsilon_{yy},\varepsilon_{yz},\varepsilon_{zx},\varepsilon_{xy}\right]^T \tag{4.20}$$

4.3. FORMULATIONS OF HFS-FEM

4.3.1. Assumed fields

To solve the anisotropic problem governed by Eqs. (4.4)-(4.6) using HFS-FEM approach, the solution domain Ω must be divided into a series of elements as done in conventional FEM. For each element, two independent fields, i.e. the intra-element field and the frame field, are assumed in the manner presented by (Wang and Qin 2010a; Wang and Qin 2010b). In this approach, the intra-element displacement fields for a particular element *e* are approximated in terms of a linear combination of fundamental solutions of the problem as

$$\mathbf{u}(\mathbf{x})=\begin{Bmatrix} u_1(\mathbf{x}) \\ u_2(\mathbf{x}) \\ u_3(\mathbf{x}) \end{Bmatrix}=\mathbf{N_e}\mathbf{c_e} \quad (\mathbf{x}\in\Omega_e,\mathbf{y}_{sj}\notin\Omega_e) \tag{4.21}$$

where the matrix $\mathbf{N_e}$ and unknown vector $\mathbf{c_e}$ can be further written as

$$\mathbf{N_e}=\begin{bmatrix} u_{11}^*(\mathbf{x},\mathbf{y}_{s1}) & u_{12}^*(\mathbf{x},\mathbf{y}_{s1}) & u_{13}^*(\mathbf{x},\mathbf{y}_{s1}) & \cdots & u_{11}^*(\mathbf{x},\mathbf{y}_{sn_s}) & u_{12}^*(\mathbf{x},\mathbf{y}_{sn_s}) & u_{13}^*(\mathbf{x},\mathbf{y}_{sn_s}) \\ u_{12}^*(\mathbf{x},\mathbf{y}_{s1}) & u_{22}^*(\mathbf{x},\mathbf{y}_{s1}) & u_{23}^*(\mathbf{x},\mathbf{y}_{s1}) & \cdots & u_{12}^*(\mathbf{x},\mathbf{y}_{sn_s}) & u_{22}^*(\mathbf{x},\mathbf{y}_{sn_s}) & u_{23}^*(\mathbf{x},\mathbf{y}_{sn_s}) \\ u_{13}^*(\mathbf{x},\mathbf{y}_{s1}) & u_{32}^*(\mathbf{x},\mathbf{y}_{s1}) & u_{33}^*(\mathbf{x},\mathbf{y}_{s1}) & \cdots & u_{13}^*(\mathbf{x},\mathbf{y}_{sn_s}) & u_{32}^*(\mathbf{x},\mathbf{y}_{sn_s}) & u_{33}^*(\mathbf{x},\mathbf{y}_{sn_s}) \end{bmatrix} \tag{4.22}$$

$$\mathbf{c_e}=[c_{11} \quad c_{21} \quad c_{31} \quad \cdots \quad c_{1n} \quad c_{2n} \quad c_{3n}]^T \tag{4.23}$$

in which n_s is the number of source points, $\mathbf{x}$ and $\mathbf{y}_{sj}$ are respectively the field point and the source point in the coordinate system (X_1, X_2) local to the element under consideration. The components $u_{ij}^{*}(\mathbf{x},\mathbf{y}_{sj})$ represent the fundamental solution, i.e. the induced displacement component in the *i*-direction at the field point $\mathbf{x}$ due to a unit point load applied in the *j*-direction at the source point $\mathbf{y}_{sj}$ placed outside the element, as given by Eq.(4.15) for general elements.

In the analysis, the number of source points is taken to be same as the number of element nodes, which is free of spurious energy modes and retain the stiffness equations in full rank, as indicated by (Qin 2000). The source point $\mathbf{y}_{sj}\,(j=1,2,\ldots,n_s)$ can be generated through the following method (Wang and Qin 2010b)

$$\mathbf{y}_s=\mathbf{x}_0+\gamma(\mathbf{x}_0-\mathbf{x}_c) \tag{4.24}$$

where γ is a dimensionless coefficient, $\mathbf{x}_0$ is a point on the element boundary (the nodal point in this work) and $\mathbf{x}_c$ the geometrical centroid of the element. Determination of γ has been discussed in literatures (Wang and Qin 2009; Wang and Qin 2010b) and γ=8 is used in the following analysis.

The corresponding stress fields can be expressed as

$$\boldsymbol{\sigma}(\mathbf{x})=\begin{bmatrix}\sigma_{11} & \sigma_{22} & \sigma_{23} & \sigma_{31} & \sigma_{12}\end{bmatrix}^T=\mathbf{T_e}\mathbf{c_e} \tag{4.25}$$

where

$$\mathbf{T_e}=\begin{bmatrix}
\sigma_{111}^{*}(\mathbf{x},\mathbf{y}_1) & \sigma_{211}^{*}(\mathbf{x},\mathbf{y}_1) & \sigma_{311}^{*}(\mathbf{x},\mathbf{y}_1) & \cdots & \sigma_{111}^{*}(\mathbf{x},\mathbf{y}_{n_s}) & \sigma_{211}^{*}(\mathbf{x},\mathbf{y}_{n_s}) & \sigma_{311}^{*}(\mathbf{x},\mathbf{y}_{n_s}) \\
\sigma_{122}^{*}(\mathbf{x},\mathbf{y}_1) & \sigma_{222}^{*}(\mathbf{x},\mathbf{y}_1) & \sigma_{322}^{*}(\mathbf{x},\mathbf{y}_1) & \cdots & \sigma_{122}^{*}(\mathbf{x},\mathbf{y}_{n_s}) & \sigma_{222}^{*}(\mathbf{x},\mathbf{y}_{n_s}) & \sigma_{322}^{*}(\mathbf{x},\mathbf{y}_{n_s}) \\
\sigma_{123}^{*}(\mathbf{x},\mathbf{y}_1) & \sigma_{223}^{*}(\mathbf{x},\mathbf{y}_1) & \sigma_{323}^{*}(\mathbf{x},\mathbf{y}_1) & \cdots & \sigma_{123}^{*}(\mathbf{x},\mathbf{y}_{n_s}) & \sigma_{223}^{*}(\mathbf{x},\mathbf{y}_{n_s}) & \sigma_{323}^{*}(\mathbf{x},\mathbf{y}_{n_s}) \\
\sigma_{131}^{*}(\mathbf{x},\mathbf{y}_1) & \sigma_{231}^{*}(\mathbf{x},\mathbf{y}_1) & \sigma_{331}^{*}(\mathbf{x},\mathbf{y}_1) & \cdots & \sigma_{131}^{*}(\mathbf{x},\mathbf{y}_{n_s}) & \sigma_{231}^{*}(\mathbf{x},\mathbf{y}_{n_s}) & \sigma_{331}^{*}(\mathbf{x},\mathbf{y}_{n_s}) \\
\sigma_{112}^{*}(\mathbf{x},\mathbf{y}_1) & \sigma_{231}^{*}(\mathbf{x},\mathbf{y}_1) & \sigma_{312}^{*}(\mathbf{x},\mathbf{y}_1) & \cdots & \sigma_{112}^{*}(\mathbf{x},\mathbf{y}_{n_s}) & \sigma_{212}^{*}(\mathbf{x},\mathbf{y}_{n_s}) & \sigma_{312}^{*}(\mathbf{x},\mathbf{y}_{n_s})
\end{bmatrix} \tag{4.26}$$

The components $\sigma_{ijk}^{*}(\mathbf{x},\mathbf{y})$ are given by Eq.(4.16) when $\hat{\mathbf{p}}_i$ is selected to be $(1,0,0)^T$, $(0,1,0)^T$ and $(0,0,1)^T$, respectively. As a consequence, the traction can be written as

$$\begin{Bmatrix}t_1\\ t_2\\ t_3\end{Bmatrix}=\mathbf{n}\boldsymbol{\sigma}=\mathbf{Q_e}\mathbf{c_e} \tag{4.27}$$

in which

$$\mathbf{Q_e}=\mathbf{n}\mathbf{T_e} \tag{4.28}$$

$$\mathbf{n}=\begin{bmatrix} n_1 & 0 & 0 & n_3 & n_2 \\ 0 & n_2 & n_3 & 0 & n_1 \\ 0 & 0 & n_2 & n_1 & 0 \end{bmatrix} \tag{4.29}$$

The unknown $\mathbf{c}_e$ in Eq.(4.21) and Eq.(4.25) may be calculated using a hybrid technique (Wang and Qin 2009), in which the elements are linked through an auxiliary conforming displacement frame which has the same form as in conventional FEM. This means that in the HFS-FEM, a conforming displacement field should be independently defined on the element boundary to enforce the field continuity between elements and also to link the unknown $\mathbf{c}_e$ and the nodal displacements $\mathbf{d}_e$. Thus, the frame field is defined as

$$\tilde{\mathbf{u}}(\mathbf{x})=\begin{Bmatrix} \tilde{u}_1 \\ \tilde{u}_2 \\ \tilde{u}_3 \end{Bmatrix}=\begin{Bmatrix} \tilde{\mathbf{N}}_1 \\ \tilde{\mathbf{N}}_2 \\ \tilde{\mathbf{N}}_3 \end{Bmatrix}\mathbf{d}_e=\tilde{\mathbf{N}}_e\mathbf{d}_e, \qquad (\mathbf{x}\in\Gamma_e) \tag{4.30}$$

where the symbol "~" is used to specify that the field is defined on the element boundary only, $\tilde{\mathbf{N}}_e$ is the matrix of shape functions, $\mathbf{d}_e$ is the nodal displacements of elements. Taking the side 3-4-5 of a particular 8-node quadrilateral element as an example, $\tilde{\mathbf{N}}_e$ and $\mathbf{d}_e$ can be expressed as

$$\tilde{\mathbf{N}}_e=\begin{bmatrix} \mathbf{0} & \mathbf{0} & \bar{\mathbf{N}}_1 & \bar{\mathbf{N}}_2 & \bar{\mathbf{N}}_3 & \mathbf{0} & \mathbf{0} & \mathbf{0} \end{bmatrix} \tag{4.31}$$

$$\mathbf{d}_e=\begin{bmatrix} u_{11} & u_{21} & u_{31} & u_{12} & u_{22} & u_{32} & \cdots & u_{18} & u_{28} & u_{38} \end{bmatrix}^T \tag{4.32}$$

where the shape functions are expressed as

$$\bar{\mathbf{N}}_\mathbf{i}=\begin{bmatrix} \tilde{N}_i & 0 & 0 \\ 0 & \tilde{N}_i & 0 \\ 0 & 0 & \tilde{N}_i \end{bmatrix}, \mathbf{0}=\begin{bmatrix} 0 & 0 & 0 \\ 0 & 0 & 0 \\ 0 & 0 & 0 \end{bmatrix} \tag{4.33}$$

and $\tilde{N}_1$, $\tilde{N}_2$ and $\tilde{N}_3$ are expressed by natural coordinate $\xi\in[-1,1]$

$$\tilde{N}_1=-\frac{\xi(1-\xi)}{2},\ \tilde{N}_2=1-\xi^2,\ \tilde{N}_3=\frac{\xi(1+\xi)}{2} \quad (\xi\in[-1,1]) \tag{4.34}$$

4.3.2. Modified functional for HFS-FEM

With the assumption of a distinct intra-element field and frame field for elements, the modified variational principle can be established based on Eqs. (4.4)-(4.6) for the hybrid finite element method of anisotropic materials (Qin 2000; Qin

2003). In the absence of the body forces, the hybrid variational functional Π_{me} for a particular element *e* is constructed as

$$\Pi_{me} = \frac{1}{2}\iint_{\Omega_e} \sigma_{ij}\varepsilon_{ij} d\Omega - \int_{\Gamma_t} \bar{t}_i \tilde{u}_i d\Gamma + \int_{\Gamma_e} t_i(\tilde{u}_i - u_i) d\Gamma \tag{4.35}$$

where the boundary Γ_e of the element *e* is

$$\Gamma_e = \Gamma_{eu} \cup \Gamma_{et} \cup \Gamma_{eI} \tag{4.36}$$

and

$$\Gamma_{eu} = \Gamma_e \cap \Gamma_u, \Gamma_{et} = \Gamma_e \cap \Gamma_t \tag{4.37}$$

and Γ_{eI} is the inter-element boundary of element *e*. Compared to the functional employed in the conventional FEM, the present variational functional is constructed by adding two integral terms related to the intra-element and element frame fields to guarantee the satisfaction of the displacement continuity condition on the common boundary of two adjacent elements. To this end, performing a variation of Π_m, yields

$$\delta\Pi_{me} = \iint_{\Omega_e} \sigma_{ij}\delta u_{i,j} d\Omega - \int_{\Gamma_{et}} \bar{t}_i \delta\tilde{u}_i d\Gamma + \int_{\Gamma_e} [(\tilde{u}_i - u_i)\delta t_i + t_i(\delta\tilde{u}_i - \delta u_i)] d\Gamma \tag{4.38}$$

Applying Gaussian theorem

$$\iint_{\Omega_e} f_{,i} d\Omega = \int_{\Gamma_e} f \cdot n_i d\Gamma \tag{4.39}$$

and the definitions of traction force

$$t_i = \sigma_{ij} n_j \tag{4.40}$$

we obtain

$$\delta\Pi_e = -\iint_{\Omega_e} \sigma_{ij,j}\delta u_i d\Omega + \int_{\Gamma_e} t_i \delta u_i d\Gamma - \int_{\Gamma_{et}} \bar{t}_i \delta\tilde{u}_i d\Gamma \tag{4.41}$$

Then, substituting Eq.(4.41) into Eq. (4.38) gives

$$\delta\Pi_{me} = -\iint_{\Omega_e} \sigma_{ij,j}\delta u_i d\Omega - \int_{\Gamma_{et}} \bar{t}_i \delta\tilde{u}_i d\Gamma + \int_{\Gamma_e} [(\tilde{u}_i - u_i)\delta t_i + t_i \delta\tilde{u}_i] d\Gamma \tag{4.42}$$

Considering the fact that

$$\int_{\Gamma_{eu}} t_i \delta\tilde{u}_i d\Gamma = 0 \tag{4.43}$$

the following form is finally obtained

$$\delta\Pi_{me} = -\iint_{\Omega_e} \sigma_{ij,j}\delta u_i d\Omega + \int_{\Gamma_{et}} (t_i - \bar{t}_i)\delta\tilde{u}_i d\Gamma + \int_{\Gamma_e} (\tilde{u}_i - u_i)\delta t_i d\Gamma + \int_{\Gamma_I} t_i \delta\tilde{u}_i d\Gamma \tag{4.44}$$

Therefore, the Euler equations for Eq. (4.35) result in Eqs. (4.4)-(4.6) because the quantities δu_i, δt_i and $\delta\tilde{u}_i$ may be arbitrary. The continuity condition between elements can easily be seen from the following variational of two adjacent elements such as *e* and *f*

$$\delta\Pi_{m(e\cup f)} = -\iint\limits_{\Omega_e\cup\Omega_f} \sigma_{ij,j}\delta u_i d\Omega + \int\limits_{\Gamma_{et}+\Gamma_{et}} (t_i-\bar{t}_i)\delta\tilde{u}_i d\Gamma + \int\limits_{\Gamma_e+\Gamma_f} (\tilde{u}_i-u_i)\delta t_i d\Gamma + \int_{\Gamma_{efI}} \left(t_{ie}+t_{if}\right)\delta\tilde{u}_i \tag{4.45}$$

This indicates that the stationary condition of the functional satisfies both the required boundary and inter-element continuity equations. In addition, the existence of extremum of functional (4.35) can be easily proved by the so-called "second variational approach", which indicates that functional (4.35) has a local extreme. Therefore, it is concluded that the variational functional (4.35) can be used for deriving hybrid finite element formulations.

4.3.3. Element stiffness equation

Using Gaussian theorem and equilibrium equations, all domain integrals in Eq. (4.35) can be converted into boundary integrals as follows

$$\Pi_{me} = -\frac{1}{2}\int_{\Gamma_e} t_i u_i d\Gamma + \int_{\Gamma_e} t_i\tilde{u}_i d\Gamma - \int_{\Gamma_t} \bar{t}_i\tilde{u}_i d\Gamma \tag{4.46}$$

Substituting Eqs. (4.21), (4.27) and (4.30) into the functional (4.46) yields the formulation

$$\Pi_{me} = -\frac{1}{2}\mathbf{c}_e{}^T\mathbf{H}_e\mathbf{c}_e + \mathbf{c}_e{}^T\mathbf{G}_e\mathbf{d}_e - \mathbf{d}_e{}^T\mathbf{g}_e \tag{4.47}$$

where

$$\mathbf{H}_e = \int_{\Gamma_e}\mathbf{Q}_e^{\mathrm{T}}\mathbf{N}_e \mathrm{d}\Gamma, \quad \mathbf{G}_e = \int_{\Gamma_e}\mathbf{Q}_e^{\mathrm{T}}\tilde{\mathbf{N}}_e \mathrm{d}\Gamma, \quad \mathbf{g}_e = \int_{\Gamma_t}\tilde{\mathbf{N}}_e^{\mathrm{T}}\bar{\mathbf{t}} d\Gamma \tag{4.48}$$

To enforce inter-element continuity on the common element boundary, the unknown vector $\mathbf{c}_e$ should be expressed in terms of nodal DOF $\mathbf{d}_e$. The stationary condition of the functional Π_{me} with respect to $\mathbf{c}_e$ and $\mathbf{d}_e$, respectively, yields

$$\frac{\partial\Pi_{me}}{\partial\mathbf{c}_e{}^{\mathrm{T}}} = -\mathbf{H}_e\mathbf{c}_e + \mathbf{G}_e\mathbf{d}_e = \mathbf{0} \tag{4.49}$$

$$\frac{\partial\Pi_{me}}{\partial\mathbf{d}_e{}^{\mathrm{T}}} = \mathbf{G}_e{}^T\mathbf{c}_e - \mathbf{g}_e = \mathbf{0} \tag{4.50}$$

from which the relationship between $\mathbf{c}_e$ and $\mathbf{d}_e$, and the stiffness equation can be obtained as

$$\mathbf{c}_e = \mathbf{H}_e^{-1}\mathbf{G}_e\mathbf{d}_e \tag{4.51}$$

$$\mathbf{K}_e\mathbf{d}_e = \mathbf{g}_e \tag{4.52}$$

where $\mathbf{K}_e = \mathbf{G}_e{}^{\mathbf{T}}\mathbf{H}_e{}^{-1}\mathbf{G}_e$ is the element stiffness matrix with symmetric properties. The numerical calculations for $\mathbf{H}_e$, $\mathbf{G}_e$,and $\mathbf{g}_e$ can utilize the popular Gauss integration as used in FEM and BEM.

4.3.4. Recovery of rigid-body motion terms

It is necessary to reintroduce the discarded rigid-body motion terms when calculating the internal field u_{eh} of an element (Qin 2000). The least squares method can be employed for this purpose (Wang and Qin 2011). The missing terms can easily be recovered by setting for the augmented internal field

$$\mathbf{u}_e = \mathbf{N}_e\mathbf{c}_e + \begin{bmatrix} 1 & 0 & 0 & 0 & x_3 & -x_2 \\ 0 & 1 & 0 & -x_3 & 0 & x_1 \\ 0 & 0 & 1 & x_2 & -x_1 & 0 \end{bmatrix}\mathbf{c}_0 \tag{4.53}$$

where the undetermined rigid-body motion parameter $\mathbf{c}_0$ can be calculated using the least square matching of $\mathbf{u_e}$ and $\tilde{\mathbf{u}}_\mathbf{e}$ at element nodes, and using a least-square procedure to match u_{eh} and $\tilde{u}_{eh}$ at the nodes of the element boundary

$$\min = \sum_{i=1}^{n}\left[\left(u_{1i}-\tilde{u}_{1i}\right)^2 + \left(u_{2i}-\tilde{u}_{2i}\right)^2 + \left(u_{3i}-\tilde{u}_{3i}\right)^2\right] \tag{4.54}$$

where n is the number of nodes for the element under consideration. The above equation finally yields

$$\mathbf{c_0} = \mathbf{R}_e^{-1}\mathbf{r_e} \tag{4.55}$$

where

$$\mathbf{R_e} = \sum_{i=1}^{n}\begin{bmatrix} 1 & 0 & 0 & 0 & x_{3i} & -x_{2i} \\ 0 & 1 & 0 & -x_{3i} & 0 & x_{1i} \\ 0 & 0 & 1 & x_{2i} & -x_{1i} & 0 \\ 0 & -x_{3i} & x_{2i} & x_{2i}^2 + x_{3i}^2 & -x_{1i}x_{2i} & -x_{1i}x_{3i} \\ x_{3i} & 0 & -x_{1i} & -x_{1i}x_{2i} & x_{1i}^2 + x_{3i}^2 & -x_{2i}x_{3i} \\ -x_{2i} & x_{1i} & 0 & -x_{1i}x_{3i} & -x_{2i}x_{3i} & x_{1i}^2 + x_{2i}^2 \end{bmatrix} \tag{4.56}$$

$$\mathbf{r_e} = \sum_{i=1}^{n} \begin{bmatrix} \Delta u_{e1i} \\ \Delta u_{e2i} \\ \Delta u_{e3i} \\ \Delta u_{e3i} x_{2i} - \Delta u_{e2i} x_{3i} \\ \Delta u_{e1i} x_{3i} - \Delta u_{e3i} x_{1i} \\ \Delta u_{e2i} x_{1i} - \Delta u_{e1i} x_{2i} \end{bmatrix} \tag{4.57}$$

and $\mathbf{\Delta u}_{ei} = \left(\tilde{\mathbf{u}}_e - \hat{\mathbf{u}}_e\right)\Big|_{\text{node i}}$. Consequently, once the nodal displacement fields $\mathbf{d}_e$ and the interpolation coefficients $\mathbf{c}_e$ are respectively determined by Eqs. (4.52) and (4.51), $\mathbf{c}_0$ can be calculated by Eq. (4.55). Then the complete displacement fields $\mathbf{u}_e$ can be obtained from Eq. (4.53).

4.4. NUMERICAL EXAMPLES

In this section, the accuracy, efficiency and versatility of the present element model are shown by some examples which have been solved analytically or numerically. The 8-node quadratic element is employed for the HFS-FEM in all the examples, in which a plane stress condition is involved in the first three examples and a plane strain condition in the fourth example. Numerical results calculated by HFS-FEM are compared to analytical solutions or those obtained from traditional FEM (ABAQUS).

4.4.1. Finite orthotropic composite plate under tension

A finite composite lamina with length *L*=100 mm and width *W*=100 mm is considered in this example. As shown in Figure 4.3, one side of the composite plate is fixed and a uniform tension of σ_0=10 GPa along the x_1 direction is applied to its opposite side. The material parameters of the orthotropic lamina are taken as E_1=11.8 GPa, E_2=5.9 GPa, G_{12}=0.69 GPa, v_{12}= 0.071 (Hwu and Yen 1991). The lamina angle φ is measured from the x_1 axis to the fiber direction, and the fiber direction is denoted by 1 as shown in Figure 4.2. Regular meshes are employed in this analysis and two of the mesh configurations with 16 and 100 8-node hybrid elements are shown in Figure 4.4.

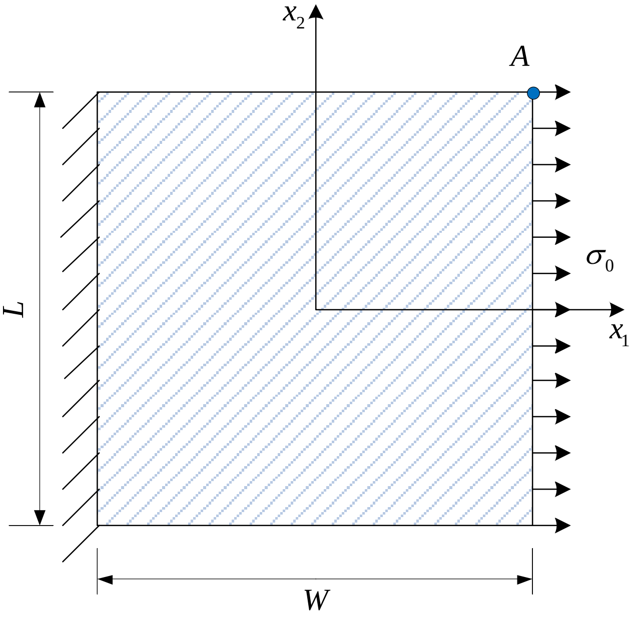

Figure 4.3 Schematic of an orthotropic composite plate under tension.

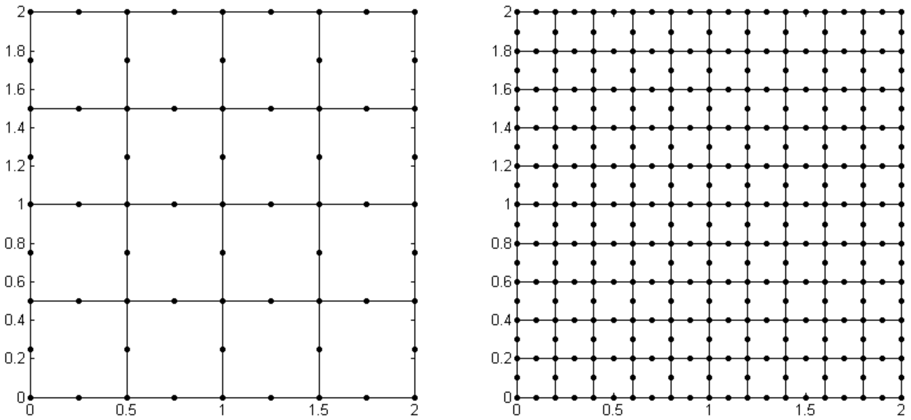

Figure 4.4 Two mesh configurations (left: 4×4 elements, right: 10×10 elements) for the orthotropic composite plate.

The effects of the locations of source points on the convergence and accuracy of stress and displacements have been investigated in previous work (Wang and Qin 2009), and are omitted in this chapter. Thus, $\gamma = 8$ is chosen in the following computations. The displacement u_1 and stress σ_{11} at point *A* of the plate calculated by HFS-FEM on four different meshes (2×2 elements, 4×4 elements, 8×8 elements and 10×10 elements) are shown in Table 4.1. It can be seen that the results obtained from

HFS-FEM converges to the reference values calculated by ABAQUS using a much finer mesh (50×50 quadratic elements). The stress and displacement for the composite lamina has a satisfactory accuracy for the analysis, in which the maximum relative error is 0.12% only when using 2×2 elements.

Table 4.1 Convergence of the displacement and stress at point A of the composite plate.

Method and Mesh Size	HFS-FEM (2×2)	HFS-FEM (4×4)	HFS-FEM (8×8)	HFS-FEM (10×10)	ABAQUS (50×50)
Disp. u_1 (mm)	1.6969	1.6968	1.6967	1.6967	1.6949
Stress σ_{11} (GPa)	10.016	10.013	10.007	10.005	10.000

Table 4.2 Displacement (mm) of point A of the composite plate for various fiber orientations.

Fiber angle θ	0°	30°	45°	60°	90°
HFS-FEM	1.6967	6.5545	8.4564	7.4003	3.3904
ABAQUS	1.6949	6.5549	8.4574	7.4024	3.3898
Relative error	0.106%	0.006%	0.012%	0.028%	0.018%

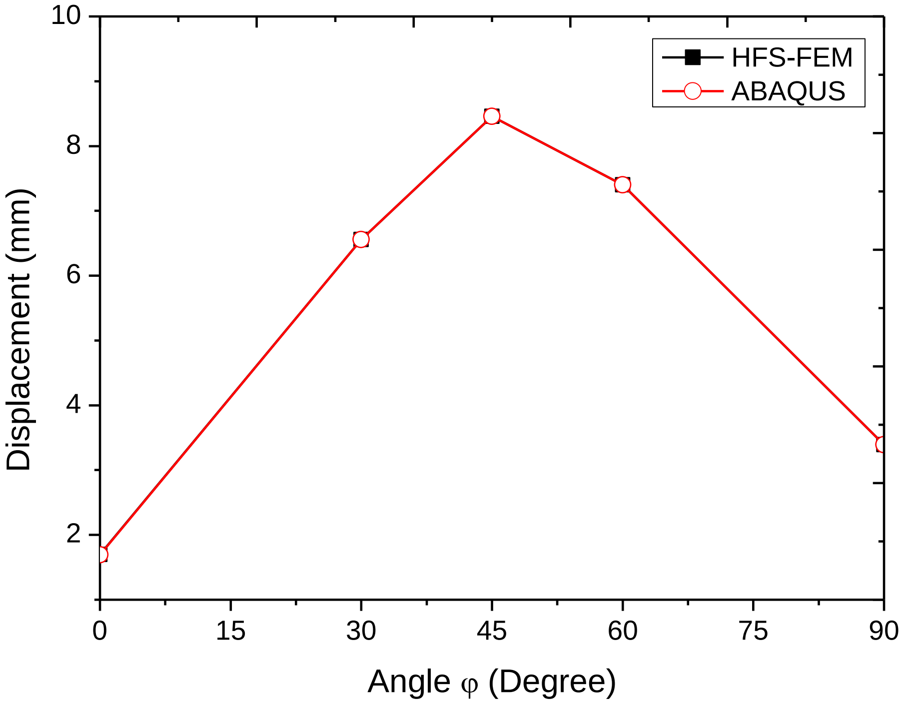

Figure 4.5 Variation of the displacements at point A of orthotropic plate with fiber orientation.

Table 4.2 gives the displacements at point *A* of the composite plate when the material orientation, i.e. the orientation of fibers, varies from 0° to 90°. The variation curves are shown in Figure 4.5, from which it is noticed that the orientation of orthotropic lamina has a significant influence on the mechanical behavior of the composite plate, and the largest displacement at φ=45° is up to five times that at φ =0°. Figure 4.5 also demonstrates that the proposed method has good performance for various material orientations.

4.4.2. Orthotropic composite plate with an elliptic hole under tension

A finite composite plate containing an elliptical hole, as shown in Figure 4.6, is investigated in this example. A uniform tension of σ_0=1 GPa is applied in the x_2 direction. The material parameters of the orthotropic plate are taken as E_1=113 GPa, E_2=52.7 GPa, G_{12}=28.5 GPa, v_{12}= 0.45. The length and width of the plate are *L=20* mm and *W=20* mm; the major and minor lengths of the ellipse *a* and *b* are respectively 2 mm and 1 mm. In the computation, the plane stress condition is used.

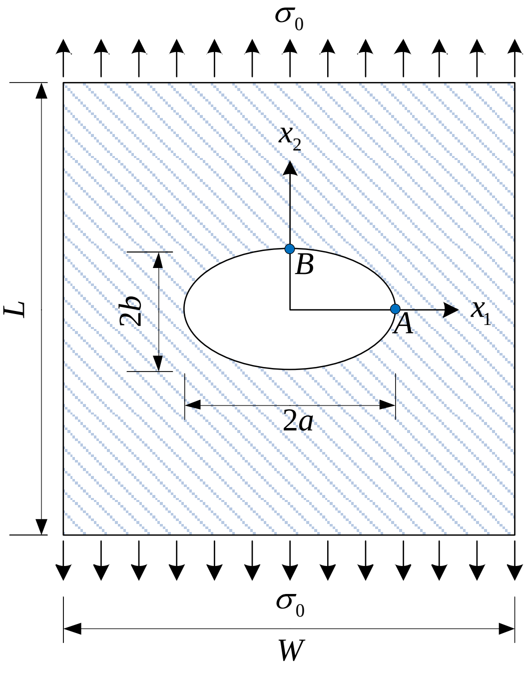

Figure 4.6 Schematic of an orthotropic composite plate with an elliptic hole under uniform tension.

The mesh configuration used in the HFS-FEM analysis for the composite plate is given in Figure 4.7, which employs 1515 quadratic hybrid elements with 4665 nodes. For comparison, the numerical results from ABAQUS, based on a very fine mesh (9498 quadratic elements with 28854 nodes) as shown in Figure 4.7, are also given.

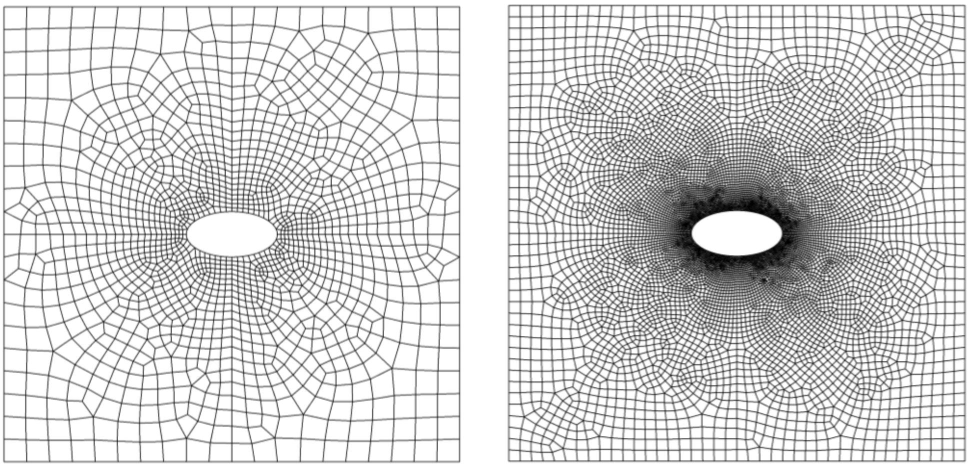

Figure 4.7 Mesh configurations for the orthotropic composite plate with an elliptic hole: (a) for HFS-FEM; (b) for ABAQUS.

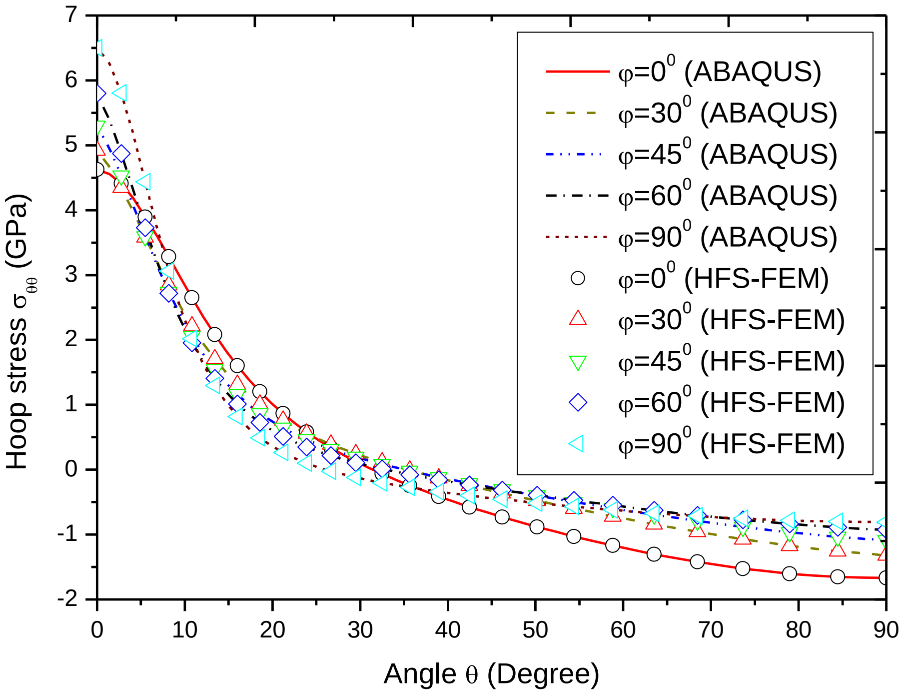

Figure 4.8 Variation of hoop stresses along the rim of the elliptical hole for different fiber orientation φ.

Figure 4.8 shows the corresponding variation of the hoop stress along the rim of the elliptical hole when the orientation angle φ of reinforced fibers is equal to 0°, 30° 45°, 60°, and 90°. From Figure 4.8, the results from HFS-FEM are in good agreement with the reference solutions from ABAQUS. This indicates that the proposed method is able to capture the dramatic variations of the hoop stress induced by the elliptical hole in the plate. The contour plots of stress components σ_{11}, σ_{22}, σ_{12} around the elliptic hole in the composite plate for several different fiber angles are shown in Figure 4.9.

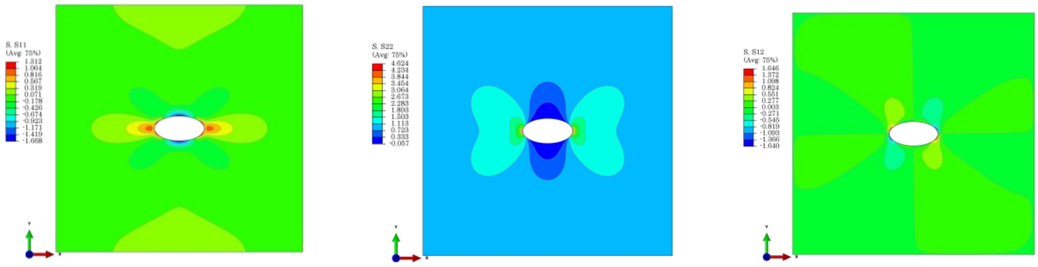

(a) $\varphi = 0^0$

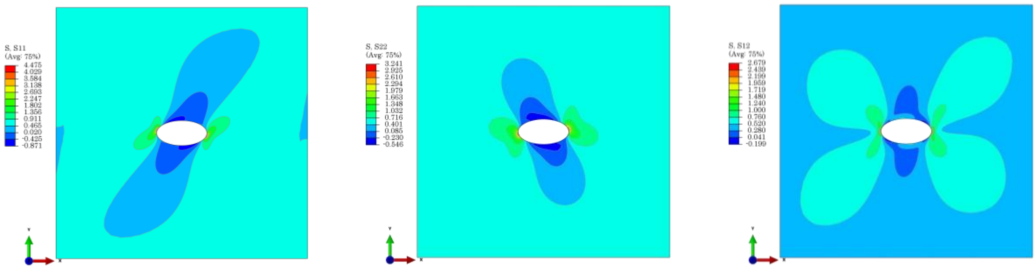

(b) $\varphi = 45^0$

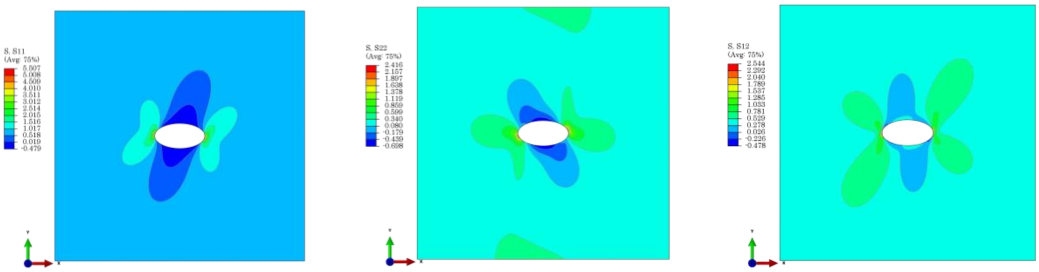

(c) $\varphi = 60^0$

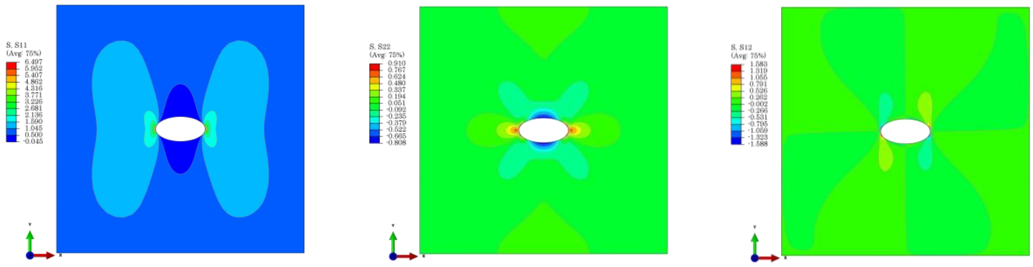

(d) $\varphi = 90^0$

Figure 4.9 Contour plots of stress components around the elliptic hole in the composite plate.

The stress concentration factor (SCF) induced by the hole in the plate, which is defined by $\sigma_{\theta\theta} / \sigma_0$ at point *A*, are of particular interest in practical engineering. As shown in Figure 4.8, the corresponding variation of hoop stress along the rim of the elliptical hole calculated by the HFS-FEM exhibits good agreement with the solutions from ABAQUS. The relationship between the SCF and the inclined angle φ of the reinforced fibers is shown in Figure 4.10. It is obvious that the SCF of the punched plate rises with an increase in fiber angle φ. From Figure 4.10, the largest SCF occurs at $\varphi = 90^0$ and the smallest appears at $\varphi = 0^o$. There is good agreement between the numerical solution from ABAQUS and the corresponding results from HFS-FEM. Figure 4.10 also indicates the effectiveness of the proposed method in predicting the SCF for anisotropic composites.

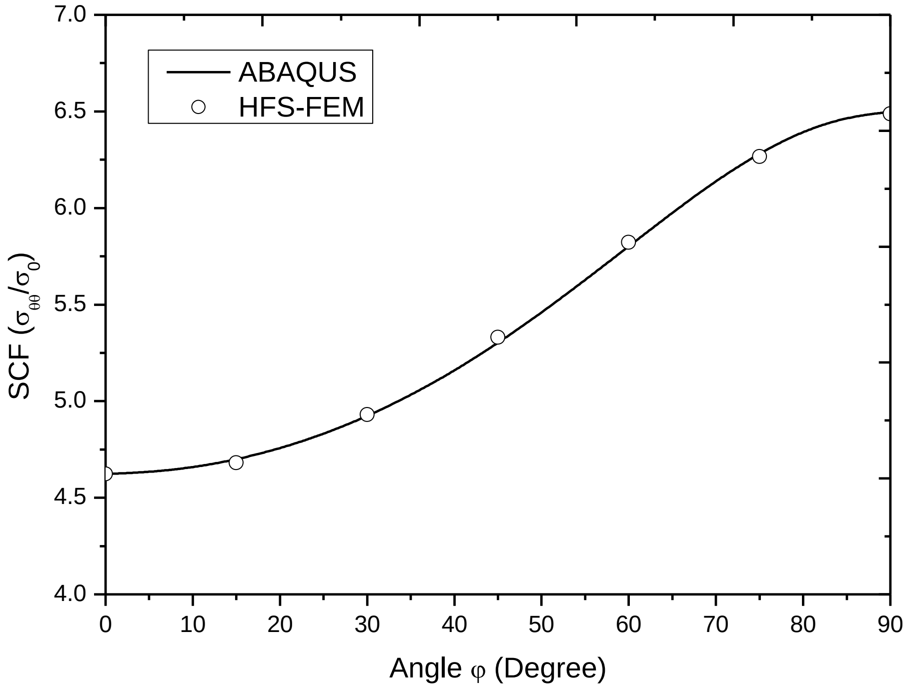

Figure 4.10 Variation of SCF with the lamina angle φ.

4.4.3. Cantilever composite beam under bending

A cantilever composite beam with a rectangular cross-section is fixed at one end and is bent by a normal load q=2 N/mm (per unit length) uniformly distributed along one of the long sides (Figure 4.11). The geometrical parameters of the beam are h=1 mm, b=50 mm, and l=300 mm. The material constants of the composite beam are taken as E_1=113 GPa, E_2=52.7 GPa, G_{12}=28.5 GPa, v_{12}=0.45 (Chern and Tuttle 2000). The angle between the reinforcing fiber direction *1* and the x axis is denoted by φ.

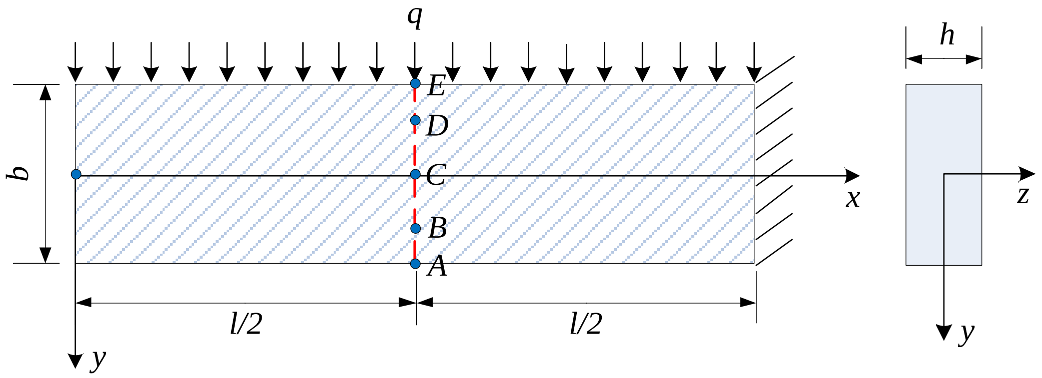

Figure 4.11 Schematic of a cantilever composite beam under bending.

In verification of the accuracy of the method, the analytical stress solution for this problems was given by Lekhnitskii (Lekhnitskii 1968) as

$$\begin{aligned}
\sigma_x &= -\frac{qx^2y}{2I} + \frac{q}{h}\left[\frac{s_{16}}{s_{11}}\cdot\frac{x}{b}\left(1-12\frac{y^2}{b^2}\right) + 2\left(\frac{2s_{12}+s_{66}}{4s_{11}} - \frac{s_{16}^2}{s_{11}^2}\right)\left(\frac{4y^3}{b^3} - \frac{3y}{5b}\right)\right] \\
\sigma_y &= \frac{q}{2h}\left(-1+3\frac{y}{b}-4\frac{y^3}{b^3}\right) \\
\tau_{xy} &= -\frac{qx}{2I}\left(\frac{b^2}{4}-y^2\right) - \frac{q}{h}\frac{s_{16}}{s_{11}}\left(\frac{y}{b}-4\frac{y^3}{b^3}\right)
\end{aligned} \tag{4.58}$$

where $I=\frac{hb^3}{12}$, and $s_{11}, s_{16}, s_{12}, s_{66}$ are the compliance parameters of the orthotropic composites defined in (Lekhnitskii 1968; Chern and Tuttle 2000). The deflection of the axis of the beam can be given as follows by using the corresponding governing equations and boundary conditions:

$$\begin{aligned}
\eta &= \frac{qs_{11}}{24I}\left(x^4-4l^3x+3l^4\right) + \frac{qs_{26}}{2h}\left(l-x\right) - \frac{qb^2}{80I} \\
&\left[\left(3s_{12}+4s_{66}-\frac{8s_{16}^2}{3s_{11}}\right)x^2 - \left(6s_{12}-2s_{66}+\frac{4s_{16}^2}{3s_{11}}\right)l + \left(3s_{12}-6s_{66}+4\frac{s_{16}^2}{s_{11}}\right)l^2x\right]
\end{aligned} \tag{4.59}$$

Table 4.3 lists the deflection at the free end (i.e. x=0, y=0) of the composite beam for various material orientations: 0°, 30°, 45°, 60° and 90°. It is obvious that the present HFS-FEM method has good accuracy for the composite beam analysis. The errors of the results, compared with the analytical solutions from Lekhnitskii (Lekhnitskii 1968), are all less than 1% using only 100 8-node elements, a result that is competitive with the ABAQUS using 50×500 quadratic elements (CPS8R).

Table 4.3 Deflection (mm) at the free end of the composite beam for various fiber angles.

Orientation angle θ	0°	30°	45°	60°	90°
HFS-FEM (5×20)	13.50	17.15	20.74	24.58	28.62
ABAQUS (50×500)	13.47	17.00	20.71	24.59	28.65
Analytical solution	13.61	17.20	20.93	24.80	28.80
Relative Error	0.81%	0.29%	0.91%	0.89%	0.63%

(HFS-FEM)

Table 4.4 presents the stress σ_x at points: *A* (250, 25), *B* (250, 15), *C* (250, 0), *D* (250, -15) and *E* (250, -25) along the cross-section of the composite beam for various fiber angles φ. It can be seen from Table 4.4 that the tensile stress in the *x*-direction obtained by the HFS-FEM is slightly lower than the analytical solutions whereas the compressive stress in the *x*-direction of the beam by HFS-FEM (5×20 8-node elements) is slightly higher than in the analytical solutions. However, all the results from ABAQUS (50×500 8-node CPS8R elements) are lower than the corresponding analytical solutions except for the points *B* and *D*, and the difference becomes larger when approaching to the upper and lower surface of the beam. It is also noted that the results from the HFS-FEM are usually more accurate than those from ABAQUS (50×500 CPS8R elements), especially for the maximum or minimum stresses on the upper and lower surfaces of the beam, which are more important in design and analysis.

Table 4.4 Stress σ_x (GPa) along the cross section of composite beam for different fiber angles.

Fiber angle φ	Method	Stress σ_x at different points				
		A (250,25)	B (250,15)	C (250,0)	D (250,-15)	E (250,-25)
0°	HFS-FEM (5×20)	-149.510	-90.221	0.000	90.221	149.510
	ABAQUS (50×500)	-146.518	-90.2558	0.000	90.2558	146.518
	Analytical	-149.387	-90.221	0.000	90.221	149.387
30°	HFS-FEM (5×20)	-142.394	-90.177	-3.873	90.096	156.846
	ABAQUS (50×500)	-139.638	-89.866	-3.758	90.481	153.803
	Analytical	-142.092	-89.837	-3.763	90.439	157.142
45°	HFS-FEM (5×20)	-142.537	-90.170	-3.891	90.010	156.676
	ABAQUS (50×500)	-139.856	-89.844	-3.681	90.445	153.731
	Analytical	-	-89.814	-3.686	90.403	157.070

		142.327				
60°	HFS-FEM (5×20)	-143.735	-90.239	-2.998	89.920	154.578
	ABAQUS (50×500)	-141.577	-89.910	-2.778	90.364	152.047
	Analytical	-144.158	-89.878	-2.781	90.323	155.282
90°	HFS-FEM (5×20)	-152.822	-90.078	0.000	90.078	152.822
	ABAQUS (50×500)	-146.807	-90.1388	0.000	90.1388	146.807
	Analytical	-149.714	-90.103	0.000	90.103	149.714

4.4.4. Isotropic plate with multi-anisotropic inclusions

This example investigates the capability of the new method to deal with both isotropic and anisotropic materials in a unified way, through a multi-inclusion problem. As shown in Figure 4.12, an isotropic plate containing multi-anisotropic inclusions of square geometry (edge length a=2 mm) are considered. The distance between any two inclusions is assumed to be b=3 mm. The material parameters for the inclusions are chosen as E_1=134.45 GPa, E_2= E_3=11.03 GPa, G_{23}=2.98 GPa, G_{31}= G_{12}=28.5 GPa, v_{23}=0.49, v_{31}= v_{12}=0.301. The material parameters for the isotropic matrix are elastic modules E=2.8 GPa and Poisson's ratio v=0.3. Figure 4.13(a) shows the mesh configuration of the plate for HFS-FEM, which uses 272 quadratic general elements. The results from the ABAQUS with 30471 CPS8R elements as shown in Figure 4.13(b) are also presented for comparison.

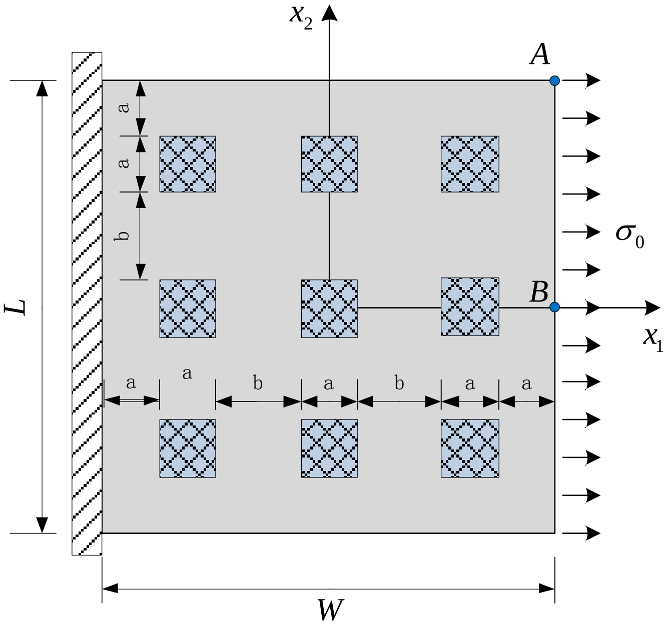

Figure 4.12 Schematic of an isotropic plate with multi-anisotropic inclusions.

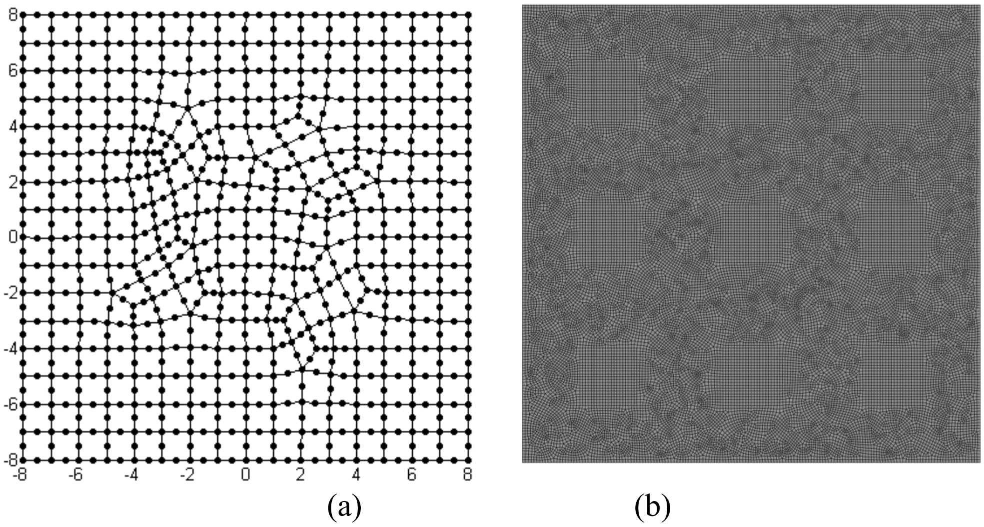

(a) (b)

Figure 4.13 Mesh configuration of an isotropic plate with multi-anisotropic inclusions: (a) for HFS-FEM, (b) for ABAQUS.

In general, Stroh formalism used in our method is suitable for anisotropic material with distinct material eigenvalues, but it fails for degenerated materials such as isotropic material with repeated eigenvalues $p_\alpha = i, (\alpha = 1, 2, 3)$ (Lekhnitskii, 1968). However, a small perturbation of the material constants, such as p_1= (1-0.004)i,

$p_2=i$, $p_3=(1+0.004)i$, can be applied to render the eigenvalues be distinct and the results can be applied conveniently.

Table 4.5 shows the displacement and stresses at points *A* and *B* as indicated in Figure 4.12. For the HFS-FEM only the coarse mesh in Figure 4.13(a) is used, whereas for ABAQUS both the coarse mesh in Figure 4.13(a) and the fine mesh in Figure 4.13(b) are employed. It is observed that there is a good agreement between the results from the HFS-FEM and those from ABAQUS a using very fine mesh, in which the maximum relative error for displacement and stress by HFS-FEM occur at point *B* (i.e. $x_2=0$) and are 0.7% and 1.3%, respectively. Further, accuracy of the results from the HFS-FEM is superior to those from ABAQUS using the same mesh. The variations of displacement components u_1 and u_2 along the right edge ($x=8$) from the HFS-FEM are shown in Figure 4.14 and Figure 4.15 respectively with the results from ABAQUS with fine mesh for comparison, in which good agreement can also be observed. Figure 4.16 shows the contour plots for displacements u_1, u_2 and stress σ_{11} for the composite plate.

Table 4.5 Comparison of displacement and stress at points *A* and *B*.

Items	*Points*	*HFS-FEM (Coarse mesh)*	*ABAQUS (Coarse mesh)*	*ABAQUS (Fine mesh)*
Disp. u_1 (mm)	A	0.04322	0.04318	0.04335
	B	0.03719	0.03721	0.03744
Stress σ_{11} (GPa)	A	10.0446	9.9219	9.9992
	B	9.8585	9.8304	9.9976

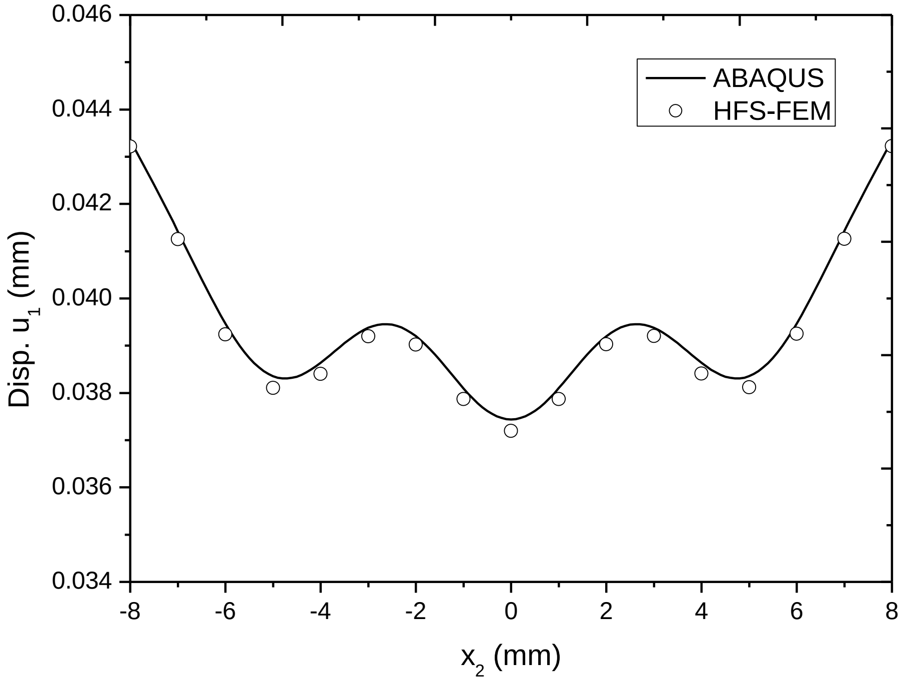

Figure 4.14 Variation of displacement component u_1 along the right edge of the plate (x=8) by HFS-FEM and ABAQUS.

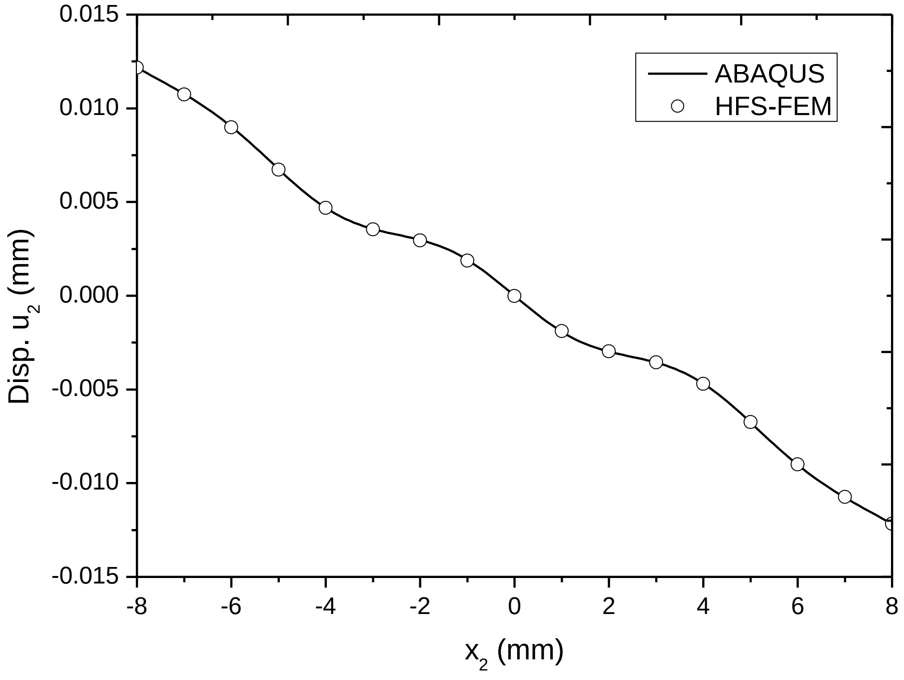

Figure 4.15 The variation of displacement component u_2 along the right edge of the plate (x=8) by HFS-FEM and ABAQUS.

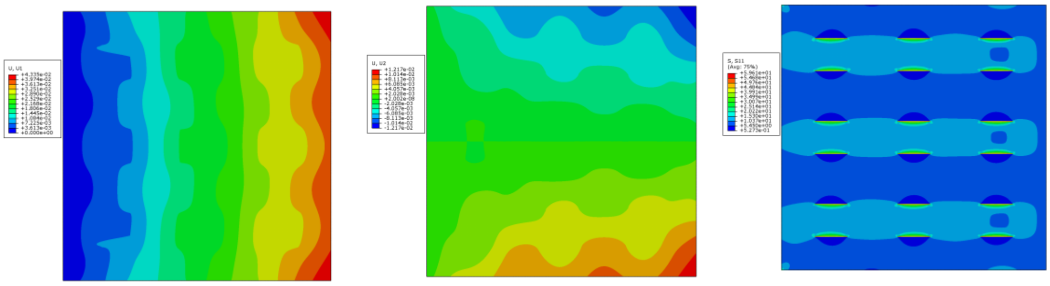

Figure 4.16 Contour plots of displacement u_1, u_2 and stress σ_{11} for the composite plate.

4.5. SUMMARY

In this chapter a hybrid finite element formulation based on fundamental solutions is developed to provide a simple but accurate approach for analyzing general anisotropic composite materials. In this approach, the foundational solutions of anisotropic materials in terms of Stroh formalism are employed to approximate the intra-element displacement field of the elements, and the polynomial shape functions used in traditional FEM are utilized to interpolate the frame field.

Several numerical examples involving isotropic and anisotropic composite with various loadings were provided to demonstrate the performance of the proposed method. Accuracy and convergence were verified through comparison with the exact or numerical solutions given in the literature or by ABAQUS. The numerical results show that the proposed method is accurate and efficient in modeling anisotropic composites and can easily be further extended to analyze composite laminates.

Chapter 5. Micromechanical Modeling of 2D Heterogeneous Composites

5.1. INTRODUCTION

Due to their excellent physical properties, fiber-reinforced composites have been widely used in practical engineering for the past several decades. Such materials usually present heterogeneous microstructures, often a complex ensemble of defects and multiple phases, which directly affect their macroscopic properties and thereby the usability of these materials. Consequently, quantitative characterization and modeling of the microstructures of these composites are becoming increasingly important with strong demands for accurate predictions of their behaviors under external stimuli and for designs of new materials with desired properties.

In the past decades, micromechanics analysis has gained significant attention and has been extensively used to solve problems on a finer scale (Hill 1963; Mura 1987; S. Nemat-Nasser 1999; Feng, Mai et al. 2003; Fu, Feng et al. 2008). Micromechanical approaches can determine the overall behavior of composites from the properties and distributions of their constituents by means of the analysis of a RVE model. Therefore, not only the global properties of the composites, but also various mechanisms such as damage initiation, evolution, and microcrack growth can be studied through micromechanical analysis. In the literatures, many methods, both analytical and numerical, have been proposed for predicting the physical behaviors of composites and some of those methods have been widely used in recent years. Closed-form solutions for pioneering micromechanical models, based on simplifying assumptions such as the shape, the size, and the spatial distribution of inclusions, were first obtained for practical applications (Eshelby 1957; Qin and Swain 2004; Qu and Cherkaoui 2006). Well-known analytical micromechanical methods employed in material analysis includes the Mori-Tanaka method, the self-consistent method, the differential approach, and the Halpin-Tsai method (Hill 1965; Mori and Tanaka 1973;

Benveniste 1987; Aboudi 1991; Qin, Mai et al. 1998; Qin and Yu 1998). These methods, however, are applicable only to problems with simple geometry and loading conditions. For example, Eshelby's tensor widely used in the above methods is size independent due to the assumption of prescribed uniform eigenstrains inside the inclusion. This limitation makes it valid only when the size of the inclusion is relatively small compared to the dimensions of the RVE (Eshelby 1957; Benveniste 1987; Feng, Mai et al. 2003; Wang, Li et al. 2005).

To overcome such limitations, numerical micromechanical models based on the FEM and BEM have been increasingly employed (Ghosh, Nowak et al. 1997; Yang and Qin 2003; Chawla, Ganesh et al. 2004; Yang and Qin 2004; Ghosh, Bai et al. 2009). These methods are widely used for simulating the mechanical properties of micro-structured and nano-structured composites (Yang and Qin 2004; Seidel and Lagoudas 2006; Tyrus, Gosz et al. 2007). The BEM-based micromechanical model seems to be effective for handling materials with defects such as cracks and holes. The BEM involves boundary integrals only, which makes it less computationally exhaustive than FEM (Huang, Hu et al. 1994; Qin 2004; Liu, Nishimura et al. 2008). However, the treatment of singular or near-singular boundary integrals is usually quite tedious and inefficient and an extra boundary integral equation is also required to evaluate the fields inside the domain; moreover, when solving multi-domain problems, the compatibility and equilibrium conditions along the interfaces between subregions must be involved. As a consequence, implementation of the BEM becomes quite complex and the nonsymmetrical coefficient matrix of the resulting equations detracts from the advantages of the BEM (Qin 2000; Qin 2004). Currently, sophisticated and efficient models to simulate realistic material behaviors continue to be developed in this active research area.

The HT-FEM has recently become a highly efficient computational tool for solving complex boundary value problems. The HT-FEM is based on a hybrid method by employing an auxiliary inter-element displacement or traction frame to link the internal displacement fields of the elements. Such internal fields, chosen so as to a priori satisfy the governing differential equations, have conveniently been represented as the sum of a particular integral of non-homogeneous equations and a suitably truncated T-complete set of regular homogeneous solutions multiplied by undetermined coefficients (Qin 2000; Qin and Wang 2008). The main advantages of HT-FEM are: (a) being integral along element boundaries only, which enables arbitrary polygonal or even curve-sided elements to be used; (b) being likely to represent the optimal expansion bases for hybrid-type elements where inter-element continuity need not be satisfied; and (c) being able to develop accurate crack-tip, singular corner or perforated elements by using appropriate known local solution functions as the trial functions of intra-element displacements (Qin 2003; Dhanasekar, Han et al. 2006).

In the last two years, another recently developed method - HFS-FEM has demonstrated good performance in heat transfer problem and elastic problem by employing fundamental solutions (Green's function) to substitute for the T-complete functions in HT-FEM as a trial function (Wang and Qin 2009; Wang and Qin 2010a; Wang and Qin 2010b). The intra-element field is approximated by a linear combination of the foundational solutions, which analytically satisfies the related governing equations. The domain integrals in the hybrid functional can be directly converted into boundary integrals without any appreciable increase in computational effort, and by locating the source point outside the element of interest, no singular integrals are involved in the HFS-FEM. Moreover, the features of two independent interpolation fields and the element boundary integral in HFS-FEM give the algorithm potential applications in mesh reduction by constructing special-purpose elements such as functionally graded elements, hole elements, crack elements, and so on (Wang and Qin 2011).

In this chapter, an efficient numerical homogenization method is proposed to predict the macroscopic parameters of heterogeneous composites, which is based on the newly developed HT-FEM and HFS-FEM methods. In particular, firstly a HFS-FEM is constructed for 2D elastic materials. Then, two numerical examples of composites containing isotropic and orthotropic fibers are studied to demonstrate the efficiency and accuracy of these two methods in predicting the effective stiffness parameters of composites. The effect of fiber volume fractions, and the shapes and patterns of reinforced fibers on the effective stiffness coefficients of composites are investigated by using the proposed micromechanical models. The majority of this chapter has been presented in a paper (Cao, Qin et al. 2013b) co-authored by the candidate.

5.2. GOVERNING EQUATIONS AND HOMOGENIZATION

5.2.1. Governing equations of linear elasticity

In the Cartesian coordinate system (x_1, x_2), without considering the body force b_i, the equilibrium equations, stress-strain laws and strain-displacement equations for elasticity are

$$\sigma_{ij,j} = 0, \qquad i, j = 1, 2 \tag{5.1}$$

$$\sigma_{ij} = C_{ijkl} e_{kl} \tag{5.2}$$

$$e_{ij} = \frac{1}{2}(u_{i,j} + u_{j,i}) \tag{5.3}$$

where σ_{ij} is the stress tensor, e_{kl} the strain tensor, C_{ijkl} the fourth-rank elasticity tensor, and u_i the displacement vector. The boundary conditions of the boundary value problem (5.1)-(5.3) are

$$u_i = \bar{u}_i \qquad \text{on } \Gamma_\text{u} \tag{5.4}$$

$$t_i = \sigma_{ij} n_j = \bar{t}_i \qquad \text{on } \Gamma_\text{t} \tag{5.5}$$

where $\bar{u}_i$ and $\bar{t}_i$ are the prescribed boundary displacement and traction vector, respectively, n_i is the unit outward normal to the boundary and $\Gamma = \Gamma_u \cup \Gamma_t$ is the boundary of the solution domain Ω. For convenience, in the present work, matrices are represented by bold-face letters and a comma followed by an index implies differentiation with respect to that index. The summation convention is invoked over repeated indices.

5.2.2. Representative volume elements

The concept of the RVE has been intensively employed in micromechanical analysis (Miehe 2003; Zohdi and Wriggers 2008). It serves as a "specimen" for specified tests to extract desired effective material properties in an averaged or homogenized method. The success of homogenization is based on the identification of such a "specimen" under appropriate boundary conditions. It should be noted that for a RVE to be statistically representative, it must contain a large number of heterogeneities. The characteristic size of the heterogeneities should be much smaller than the dimension of the RVE, which in turn is should be small compared to the characteristic length of the macroscopic structure (Figure 5.1). As a result, a RVE is regarded on the macro-level as just a point with a homogenized constitutive law.

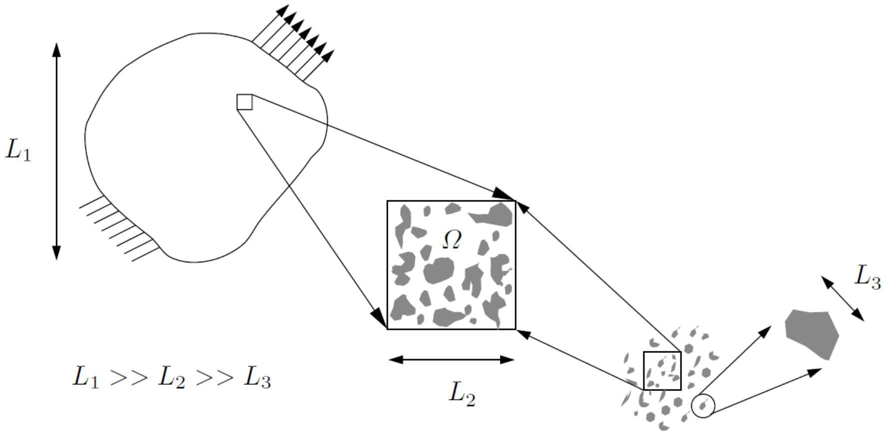

Figure 5.1 Schematic of representative volume elements (RVE).

In the present analysis, a RVE consisting of matrix material and inclusion phase, as shown in Figure 5.1, is chosen to be statistically representative of a two-phase composite. Because the RVE is comprised of two different materials, the micro-constitutive law that governs each material or phase is given by the standard elastic constitutive law. For a periodic composite, it is usually sufficient to draw conclusions for the whole structure by considering only a unit periodic RVE (Zohdi and Wriggers 2008).

5.2.3. Boundary conditions for RVE

The macroscopic properties of composites are determined by specified tests on RVEs with appropriate boundary conditions. Three types of boundary conditions are usually employed to evaluate the overall effective material properties: (a) uniform traction boundary conditions (UT-BCs), (b) linear displacement boundary conditions (LD-BCs) and (c) periodic boundary conditions (PR-BCs). Previous investigations have found that the periodic boundary conditions are much more accurate than the other two boundary conditions in micromechanical analysis of composite materials for both periodic materials and random materials (Huet 1990; Hazanov and Huet 1994). Consequently, PR-BCs are applied to the RVE models in the present research. This implies that each RVE of the composite has the same deformation profile and there is no separation or overlap between neighboring RVEs (Miehe and Koch 2002; Qin and Yang 2008).

For a 2D square RVE of periodic fiber-reinforced composites, as shown in Figure 5.2, the PR-BCs of RVE requires a periodic displacement boundary condition and an anti-periodic traction boundary condition, which can be expressed as follows:

$$\begin{aligned} u_i(x_1^0, x_2) &= u_i(x_1^0 + L, x_2) \\ \sigma_{1i}(x_1^0, x_2) &= -\sigma_{1i}(x_1^0 + L, x_2) \end{aligned} \tag{5.6}$$

for the left and right sides, and

$$\begin{aligned} u_i(x_1, x_2^0) &= u_1(x_1, x_2^0 + L) \\ \sigma_{2i}(x_1, x_2^0) &= -\sigma_{2i}(x_1, x_2^0 + L) \end{aligned} \tag{5.7}$$

for the upper and lower sides, where L is the periodicity of RVE. The PR-BCs can be implemented in the code by the penalty function method as done in the traditional FEM (Miehe and Koch 2002; Temizer and Wriggers 2007; Zohdi and Wriggers 2008). After defining the specified PR-BC, the boundary-value problem of a RVE can be solved to obtain the distributions of stresses and strains within the RVE. Then the remaining necessary procedures are (a) homogenizing/averaging the stresses and strains over the volume, and (b) calculating the effective material properties according to the formulations given in the following section.

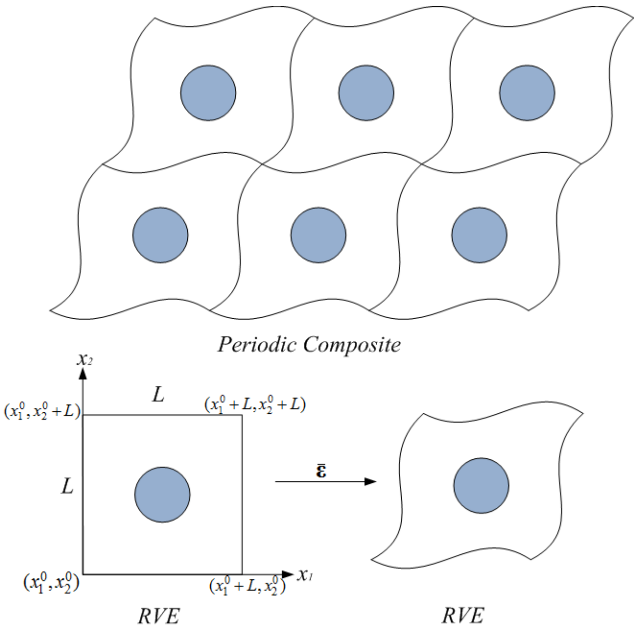

Figure 5.2 Schematic of periodic boundary conditions of RVE.

5.2.4. Homogenization for Representative Volume Element

To determine the properties of an equivalent homogeneous medium which at the macroscopic level accurately represents the response of a microscopically heterogeneous material, the effective macroscopic stress σ_{ij}^* and strain ε_{ij}^* are defined as the corresponding mean values of the stresses $\bar{\sigma}_{ij}$ and strains $\bar{\varepsilon}_{ij}$ over the RVE

$$\sigma_{ij}^* = \bar{\sigma}_{ij} = \left\langle \sigma_{ij} \right\rangle_\Omega = \frac{1}{\Omega}\int_\Omega \sigma_{ij} d\Omega \tag{5.8}$$

$$\varepsilon_{ij}^* = \bar{\varepsilon}_{ij} = \left\langle \varepsilon_{ij} \right\rangle_\Omega = \frac{1}{\Omega}\int_\Omega \varepsilon_{ij} d\Omega \tag{5.9}$$

where σ_{ij} and ε_{ij} are the stress and strain tensors, respectively, Ω is the volume of the RVE. The effective elastic constants of the equivalent homogeneous material can then be defined by the linear constitutive equation

$$\bar{\sigma}_{ij} = C_{ijkl}^* \bar{\varepsilon}_{kl} \tag{5.10}$$

Using Voigt-notation following the rules 11→1, 22→2, 33→3, 23→4, 13→5, 12→6 and written in matrix form, Eq. (5.10) can be expressed as

$$\bar{\boldsymbol{\sigma}} = \mathbf{C}^* \bar{\boldsymbol{\varepsilon}} \tag{5.11}$$

where the stress vector is expressed as $\bar{\boldsymbol{\sigma}} = \left[\bar{\sigma}_{11} \;\; \bar{\sigma}_{22} \;\; \bar{\sigma}_{12}\right]^{\mathrm{T}}$, the strain vector as $\bar{\boldsymbol{\varepsilon}} = \left[\bar{\varepsilon}_{11} \;\; \bar{\varepsilon}_{22} \;\; 2\bar{\varepsilon}_{12}\right]^{\mathrm{T}}$ and

$$\mathbf{C}^* = \begin{bmatrix} c_{11}^* & c_{12}^* & c_{16}^* \\ c_{12}^* & c_{22}^* & c_{26}^* \\ c_{16}^* & c_{26}^* & c_{66}^* \end{bmatrix} \tag{5.12}$$

The heterogeneous stresses and strains in Eqs. (5.8) and (5.9) are calculated using the formulations presented in Section 5.3.

5.3. FORMULATIONS OF THE HFS-FEM

5.3.1. Two assumed independent fields

The main idea of the HFS-FEM approach is to establish a finite element formulation whereby intra-element continuity is enforced on a nonconforming internal displacement field chosen so as to a priori the fundamental solution of the problem under consideration (Wang and Qin 2010b). In this approach, for a particular element *e*, the intra-element displacement field is approximated in terms of a linear combination of fundamental solutions of the problem of interest

$$\mathbf{u}(\mathbf{x}) = \begin{bmatrix} u_1(\mathbf{x}) \\ u_2(\mathbf{x}) \end{bmatrix} = \sum_{j=1}^{n_s} \begin{bmatrix} u_{11}(\mathbf{x},\mathbf{x}_{sj}) & u_{12}(\mathbf{x},\mathbf{x}_{sj}) \\ u_{12}(\mathbf{x},\mathbf{x}_{sj}) & u_{22}(\mathbf{x},\mathbf{x}_{sj}) \end{bmatrix} \begin{Bmatrix} c_{1j} \\ c_{2j} \end{Bmatrix} = \mathbf{N}_e \mathbf{c}_e \tag{5.13}$$

where n_s is the number of source points $\mathbf{x}_{sj}\,(j=1,2,\ldots,n_s)$ located outside the element. The matrix $\mathbf{N}_e$ and vector $\mathbf{c}_e$ can be written as

$$\mathbf{N}_e = \begin{bmatrix} u_{11}(\mathbf{x},\mathbf{x}_{s1}) & u_{12}(\mathbf{x},\mathbf{x}_{s1}) & \ldots\ldots & u_{11}(\mathbf{x},\mathbf{x}_{sn_s}) & u_{12}(\mathbf{x},\mathbf{x}_{sn_s}) \\ u_{12}(\mathbf{x},\mathbf{x}_{s1}) & u_{22}(\mathbf{x},\mathbf{x}_{s1}) & \ldots\ldots & u_{12}(\mathbf{x},\mathbf{x}_{sn_s}) & u_{22}(\mathbf{x},\mathbf{x}_{sn_s}) \end{bmatrix} \tag{5.14}$$

$$\mathbf{c}_e = [c_{11} \quad c_{21} \quad \ldots\ldots \quad c_{1n} \quad c_{2n}]^T \tag{5.15}$$

in which the component $u_{ij}(\mathbf{x},\mathbf{x}_{sk})$ is the fundamental solution, i.e. the induced displacement component in the *i*-direction at the field point **x** due to a unit point load applied at the source point $\mathbf{x}_{sk}$ in the *j*-direction. The detailed expressions of $u_{ij}(\mathbf{x},\mathbf{x}_{sk})$ are given as

$$\begin{aligned} u_{11}(\mathbf{x},\mathbf{x}_s) &= A[(3-4\nu)\ln r - \frac{r_1^2}{r^2}] \\ u_{21}(\mathbf{x},\mathbf{x}_s) &= u_{12}(\mathbf{x},\mathbf{x}_s) = -A\frac{r_1 r_2}{r^2} \\ u_{22}(\mathbf{x},\mathbf{x}_s) &= A[(3-4\nu)\ln r - \frac{r_2^2}{r^2}] \end{aligned} \tag{5.16}$$

where $r_i = x_i - x_{is}$, $r = \sqrt{r_1^2 + r_2^2}$, $A = -1/8G\pi(1-\nu)$, for isotropic materials (Sauter and Schwab 2010), and

$$\begin{aligned} u_{11}(\mathbf{x},\mathbf{x}_s) &= D(\sqrt{\lambda_1} A_2^2 \ln \rho_1 - \sqrt{\lambda_2} A_1^2 \ln \rho_2) \\ u_{22}(\mathbf{x},\mathbf{x}_s) &= -D(\frac{A_1^2}{\sqrt{\lambda_1}} \ln \rho_1 - \frac{A_2^2}{\sqrt{\lambda_2}} \ln \rho_2) \\ u_{12}(\mathbf{x},\mathbf{x}_s) &= u_{21}(\mathbf{x},\mathbf{x}_s) = DA_1A_2\left(\arctan\frac{r_2}{r_1\sqrt{\lambda_2}} - \arctan\frac{r_2}{r_1\sqrt{\lambda_1}}\right) \end{aligned} \tag{5.17}$$

where

$$D = \frac{1}{2\pi(\lambda_1 - \lambda_2)s_{22}}, \lambda_1 + \lambda_2 = \frac{2s_{12} + s_{66}}{s_{22}}$$

$$\lambda_1\lambda_2 = \frac{s_{11}}{s_{22}}, A_i = s_{12} - \lambda_i s_{22},$$

$$\rho_i = \sqrt{\lambda_i r_1^2 + r_2^2}, r_i = x_i - x_{si}$$

for orthotropic elastic materials (Rizzo and Shippy 1970).

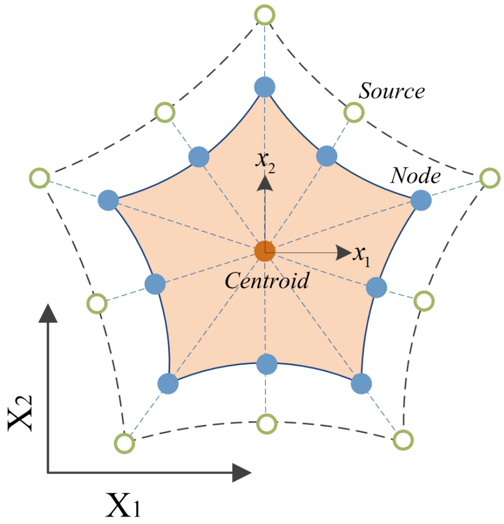

Figure 5.3 Intra-element field and frame field in a particular element of a HFS-FEM element for plane elastic problems.

In the present work, the number of source points is taken to be the same as the number of element nodes, which are free of spurious energy modes and can maintain the stiffness equations in full rank, as indicated by (Qin 2000). In practice, the source point $\mathbf{x}_{sj}\,(j=1,2,\ldots,n_s)$ can be generated by means of the following method (Wang and Qin 2010b)

$$x_s = x_0 + \gamma(x_0 - x_c) \tag{5.18}$$

where γ is a dimensionless coefficient, x_0 is the element boundary point, and x_c the geometrical centroid of the element (see Figure 5.3). It should be noted that the parameter γ must be determined by numerical tests. Thus, γ=8 is used in our analysis.

Using the constitutive Eq.(4.2), the corresponding stress fields can be expressed as

$$\boldsymbol{\sigma}(\mathbf{x}) = \mathbf{T}_e \mathbf{c}_e \tag{5.19}$$

where

$$\mathbf{T}_e = \begin{bmatrix} \sigma_{111}(\mathbf{x},\mathbf{y}_1) & \sigma_{211}(\mathbf{x},\mathbf{y}_1) & \ldots\ldots & \sigma_{111}(\mathbf{x},\mathbf{y}_{n_s}) & \sigma_{211}(\mathbf{x},\mathbf{y}_{n_s}) \\ \sigma_{122}(\mathbf{x},\mathbf{y}_1) & \sigma_{222}(\mathbf{x},\mathbf{y}_1) & \ldots\ldots & \sigma_{122}(\mathbf{x},\mathbf{y}_{n_s}) & \sigma_{222}(\mathbf{x},\mathbf{y}_{n_s}) \\ \sigma_{112}(\mathbf{x},\mathbf{y}_1) & \sigma_{212}(\mathbf{x},\mathbf{y}_1) & \ldots\ldots & \sigma_{112}(\mathbf{x},\mathbf{y}_{n_s}) & \sigma_{212}(\mathbf{x},\mathbf{y}_{n_s}) \end{bmatrix} \tag{5.20}$$

As a consequence, the traction is written as

$$\mathbf{t} = \begin{Bmatrix} t_1 \\ t_2 \end{Bmatrix} = \mathbf{n}\boldsymbol{\sigma} = \mathbf{Q}_e \mathbf{c}_e \tag{5.21}$$

in which

$$\mathbf{Q}_e = \mathbf{n}\mathbf{T}_e,\; \mathbf{n} = \begin{bmatrix} n_1 & 0 & n_2 \\ 0 & n_2 & n_1 \end{bmatrix} \tag{5.22}$$

The corresponding stress components $\sigma_{ijk}(\mathbf{x},\mathbf{y})$ are as follows:

(1) Isotropic elastic materials

$$\begin{aligned} \sigma_{111} &= Ac_{11}\left(\frac{2r_1^3}{r^4} + \frac{(1-4\nu)r_1}{r^2}\right) + Ac_{12}\left(\frac{2r_1r_2^2}{r^4} - \frac{r_1}{r^2}\right) \\ \sigma_{221} &= Ac_{12}\left(\frac{2r_1^3}{r^4} + \frac{(1-4\nu)r_1}{r^2}\right) + Ac_{22}\left(\frac{2r_1r_2^2}{r^4} - \frac{r_1}{r^2}\right) \\ \sigma_{121} &= c_{66}A\left(\frac{4r_1^2r_2}{r^4} + \frac{2(1-2\nu)r_2}{r^2}\right) \end{aligned} \tag{5.23}$$

$$\begin{aligned} \sigma_{112} &= \{Ac_{11}\left(\frac{2r_1^2r_2}{r^4} - \frac{r_2}{r^2}\right) + Ac_{12}\left(\frac{(1-4\nu)r_2}{r^2} + \frac{2r_2^3}{r^4}\right)\} \\ \sigma_{222} &= \{Ac_{12}\left(\frac{2r_1^2r_2}{r^4} - \frac{r_2}{r^2}\right) + Ac_{22}\left(\frac{(1-4\nu)r_2}{r^2} + \frac{2r_2^3}{r^4}\right)\} \\ \sigma_{122} &= Ac_{66}\left(\frac{2(1-2\nu)r_1}{r^2} + \frac{4r_1r_2^2}{r^4}\right) \end{aligned} \tag{5.24}$$

(2) Orthotropic materials (Rizzo and Shippy 1970)

$$\begin{aligned}
\sigma_{111} &= \left(c_{11}B_1 - c_{12}B_3\right)r_1 & \sigma_{112} &= \left(c_{11}B_3 + c_{12}B_5\right)r_2 \\
\sigma_{221} &= \left(c_{12}B_1 - c_{22}B_3\right)r_1 & \sigma_{222} &= \left(c_{12}B_3 + c_{22}B_5\right)r_2 \\
\sigma_{121} &= c_{66}\left(B_3 + B_2\right)r_2 & \sigma_{122} &= c_{66}\left(-B_3 + B_4\right)r_1
\end{aligned} \tag{5.25}$$

where

$$\begin{aligned}
B_1 &= D(\sqrt{\lambda_1}A_2^2\frac{\lambda_1}{\rho_1^2} - \sqrt{\lambda_2}A_1^2\frac{\lambda_2}{\rho_2^2}) \\
B_2 &= D(\sqrt{\lambda_1}A_2^2\frac{1}{\rho_1^2} - \sqrt{\lambda_2}A_1^2\frac{1}{\rho_2^2}) \\
B_3 &= DA_1A_2\frac{\left(\sqrt{\lambda_1} - \sqrt{\lambda_2}\right)\left(r_2^2 - \sqrt{\lambda_1\lambda_2}r_1^2\right)}{\left(r_2^2 + \sqrt{\lambda_1\lambda_2}r_1^2\right) + \left(\sqrt{\lambda_1} - \sqrt{\lambda_2}\right)^2 r_1^2 r_2^2} \\
B_4 &= -D(\frac{A_1^2}{\rho_1^2}\sqrt{\lambda_1} - \frac{A_2^2}{\rho_2^2}\sqrt{\lambda_2}) \\
B_5 &= -D(\frac{A_1^2}{\rho_1^2}\frac{1}{\sqrt{\lambda_1}} - \frac{A_2^2}{\rho_2^2}\frac{1}{\sqrt{\lambda_2}})
\end{aligned} \tag{5.26}$$

The unknown $\mathbf{c}_e$ in Eq. (5.13) can be calculated using a hybrid technique (Wang and Qin 2009), in which the elements are linked through an auxiliary conforming displacement frame which has the same form as in conventional FEM (see Figure 5.3). This means that in the HFS-FEM, a conforming displacement field should be independently defined on the element boundary to enforce the field continuity between elements and also to establish the relationship between the unknown $\mathbf{c}$ and the nodal displacement $\mathbf{d}_e$. The frame is defined as

$$\tilde{\mathbf{u}}(\mathbf{x}) = \begin{Bmatrix} \tilde{u}_1 \\ \tilde{u}_2 \end{Bmatrix} = \begin{Bmatrix} \tilde{\mathbf{N}}_1 \\ \tilde{\mathbf{N}}_2 \end{Bmatrix}\mathbf{d}_e = \tilde{\mathbf{N}}_e\mathbf{d}_e, \qquad (\mathbf{x} \in \Gamma_e) \tag{5.27}$$

where the symbol "~" is used to specify that the field is defined on the element boundary only, $\tilde{\mathbf{N}}_e$ is the matrix of shape functions, $\mathbf{d}_e$ is the nodal displacements of elements. Taking the side 1-2 of a particular 4-node element (see Figure 5.4) as an example, $\tilde{\mathbf{N}}_e$ and $\mathbf{d}_e$ can be expressed as

$$\tilde{\mathbf{N}}_e = \begin{bmatrix} 0 & 0 & \tilde{N}_1 & 0 & \tilde{N}_2 & 0 & 0 & 0 \\ 0 & 0 & 0 & \tilde{N}_1 & 0 & \tilde{N}_2 & 0 & 0 \end{bmatrix} \tag{5.28}$$

$$\mathbf{d}_e = \begin{bmatrix} u_{11} & u_{21} & u_{12} & u_{22} & u_{13} & u_{23} & u_{14} & u_{24} \end{bmatrix} \tag{5.29}$$

where $\tilde{N}_1$ and $\tilde{N}_2$ can be expressed by natural coordinate $\xi \in [-1,1]$

$$\tilde{N}_1 = \frac{1-\xi}{2}, \qquad \tilde{N}_2 = \frac{1+\xi}{2} \tag{5.30}$$

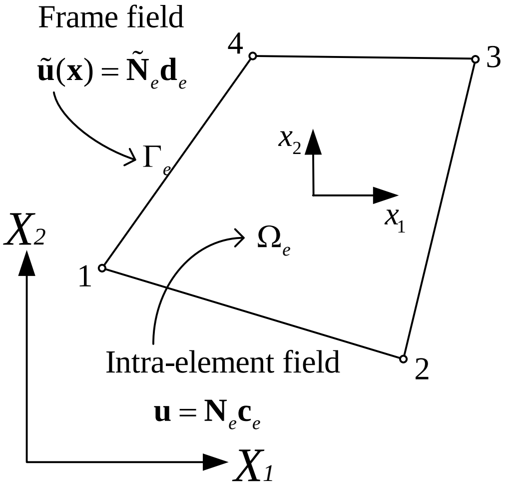

Figure 5.4 Intra-element field and frame field of a HT-FEM element for plane elastic problems.

5.3.2. Modified functional for hybrid FEM

The HFS-FEM equations for plane elastic problems can be established by the variational approach (Wang and Qin 2010b). Compared to the functional employed in the conventional FEM, the present hybrid functional for HFS-FEM is constructed by adding a hybrid integral term related to the intra-element and element frame displacement fields to guarantee the satisfaction of displacement and traction continuity conditions on the common boundary of two adjacent elements. In the absence of body forces, the hybrid functional Π_{me} for deriving HFS-FEM stiffness equations can be constructed as (Qin and Wang 2008)

$$\Pi_{me} = \frac{1}{2}\iint_{\Omega_e} \sigma_{ij}\varepsilon_{ij} d\Omega - \int_{\Gamma_t} \bar{t}_i \tilde{u}_i d\Gamma + \int_{\Gamma_e} t_i(\tilde{u}_i - u_i) d\Gamma \tag{5.31}$$

where $\tilde{u}_i$ and u_i are the intra-element displacement field defined within the element and the frame displacement field defined on the element boundary, respectively. Ω_e and Γ_e are the element domain and element boundary, respectively. Γ_t, Γ_u, and Γ_I stand for the specified traction boundary, specified displacement boundary, and inter-element boundary, respectively ($\Gamma_e = \Gamma_t + \Gamma_u + \Gamma_I$).

Appling the Gaussian theorem, Eq.(5.31) can be simplified to

$$\Pi_{me} = \frac{1}{2}\left(\int_{\Gamma_e} t_i u_i d\Gamma - \iint_{\Omega_e} \sigma_{ij,j} u_i d\Omega\right) - \int_{\Gamma_t} \bar{t}_i \tilde{u}_i d\Gamma + \int_{\Gamma_e} t_i(\tilde{u}_i - u_i) d\Gamma \tag{5.32}$$

Due to satisfaction of the equilibrium equation with the constructed intra-element fields, we have the following expression for the HFS-FE model

$$\Pi_{me} = -\frac{1}{2}\int_{\Gamma_e} t_i u_i d\Gamma + \int_{\Gamma_e} t_i \tilde{u}_i d\Gamma - \int_{\Gamma_t} \bar{t}_i \tilde{u}_i d\Gamma \tag{5.33}$$

The functional (5.33) contains boundary integrals only and is used to derive HFS-FE formulation for the plane elastic problem.

5.3.3. Element stiffness matrix

The element stiffness equation can be generated by setting $\delta\Pi_{me} = 0$. Substituting Eqs. (5.13), (5.21) and (5.27) into the functional (5.33) produces

$$\Pi_{me} = -\frac{1}{2}\mathbf{c}_e{}^{\mathrm{T}}\mathbf{H}_e\mathbf{c}_e + \mathbf{c}_e{}^{\mathrm{T}}\mathbf{G}_e\mathbf{d}_e - \mathbf{d}_e{}^{\mathrm{T}}\mathbf{g}_e \tag{5.34}$$

where

$$\mathbf{H}_e = \int_{\Gamma_e} \mathbf{Q}_e^{\mathrm{T}}\mathbf{N}_e \mathrm{d}\Gamma, \quad \mathbf{G}_e = \int_{\Gamma_e} \mathbf{Q}_e^{\mathrm{T}}\tilde{\mathbf{N}}_e \mathrm{d}\Gamma, \quad \mathbf{g}_e = \int_{\Gamma_t} \tilde{\mathbf{N}}_e^{\mathrm{T}}\bar{\mathbf{t}} d\Gamma \tag{5.35}$$

To enforce inter-element continuity on the common element boundary, the unknown vector $\mathbf{c}_e$ should be expressed in terms of nodal DOF $\mathbf{d}_e$. The stationary condition of the functional Π_{me} with respect to $\mathbf{c}_e$ and $\mathbf{d}_e$ yields, respectively,

$$\frac{\partial\Pi_{me}}{\partial\mathbf{c}_e{}^{\mathrm{T}}} = -\mathbf{H}_e\mathbf{c}_e + \mathbf{G}_e\mathbf{d}_e = \mathbf{0} \tag{5.36}$$

$$\frac{\partial\Pi_{me}}{\partial\mathbf{d}_e{}^{\mathrm{T}}} = \mathbf{G}_e{}^{T}\mathbf{c}_e - \mathbf{g}_e = \mathbf{0} \tag{5.37}$$

Therefore, the relationship between $\mathbf{c}_e$ and $\mathbf{d}_e$, and the stiffness equation can be obtained as follows

$$\mathbf{c}_e = \mathbf{H}_e^{-1}\mathbf{G}_e\mathbf{d}_e \tag{5.38}$$

$$\mathbf{K}_e\mathbf{d}_e = \mathbf{g}_e \tag{5.39}$$

where $\mathbf{K}_e = \mathbf{G}_e{}^{\mathrm{T}}\mathbf{H}_e{}^{-1}\mathbf{G}_e$ is the element stiffness matrix. The matrix $\mathbf{H}_e$, matrix $\mathbf{G}_e$ and vector $\mathbf{g}_e$ can be integrated numerically by the common Gaussian integral method.

5.3.4. Recovery of rigid-body motion

Considering the physical definition of the fundamental solution, it is necessary to recover the missing rigid-body motion modes from the above results. Following the method presented in (Qin 2000; Wang and Qin 2010b), the missing rigid-body motion can be recovered by writing the internal potential field of a particular element *e* as

$$\mathbf{u}_e = \mathbf{N}_e \mathbf{c}_e + \mathbf{c}_0 \tag{5.40}$$

where the undetermined rigid-body motion parameter c_0 can be calculated using the least square matching of $\mathbf{u}_e$ and $\tilde{\mathbf{u}}_e$ at element nodes

$$\sum_{i=1}^{n} \left(\mathbf{N}_e \mathbf{c}_e + \mathbf{c}_0 - \tilde{\mathbf{u}}_e \right)^2 \Big|_{\text{node } i} = \min \tag{5.41}$$

which finally gives

$$\mathbf{c}_0 = \frac{1}{n} \sum_{i=1}^{n} \Delta \mathbf{u}_{ei} \tag{5.42}$$

in which $\Delta \mathbf{u}_{ei} = \left(\tilde{\mathbf{u}}_e - \mathbf{N}_e \mathbf{c}_e \right)\Big|_{\text{node } i}$ and n is the number of element nodes. Once the nodal field is determined by solving the final stiffness equation, the coefficient vector $\mathbf{c}_e$ can be evaluated from Eq. (5.38), and then $\mathbf{c}_0$ is evaluated from Eq. (5.42). Finally, the potential field $\mathbf{u}$ at any internal point in an element can be obtained by means of Eq. (5.13).

5.4. FORMULATIONS OF THE HT-FEM

The formulations of HT-FEM have the same forms as those of HFS-FEM, except for the intra-element displacement field (5.13), which must be replaced by

$$\mathbf{u} = \begin{Bmatrix} u_1 \\ u_2 \end{Bmatrix} = \begin{Bmatrix} \mathbf{N}_1 \\ \mathbf{N}_2 \end{Bmatrix} \mathbf{c}_e = \mathbf{N}_e \mathbf{c}_e \qquad (\mathbf{x} \in \Omega_e) \tag{5.43}$$

where

$$\mathbf{N}_e = \begin{bmatrix} N_1^1 & N_2^1 & \cdots & N_m^1 \\ N_1^2 & N_2^2 & \cdots & N_m^2 \end{bmatrix} \tag{5.44}$$

and N_m are the truncated T-complete functions satisfying the homogeneous Navier equations in terms of displacements. The T-complete functions of elastostatics can be generated in a systematic way from Muskhelishvili's complex variable formulation (Qin and Wang 2008), which is given as

$$N_{1k} = \frac{1}{2G}\begin{Bmatrix} \mathrm{Re}(i\kappa z^k + ikz\bar{z}^{k-1}) \\ \mathrm{Im}(i\kappa z^k + ikz\bar{z}^{k-1}) \end{Bmatrix} \tag{5.45}$$

$$N_{2k} = \frac{1}{2G}\begin{Bmatrix} \mathrm{Re}(\kappa z^k - kz\bar{z}^{k-1}) \\ \mathrm{Im}(\kappa z^k - kz\bar{z}^{k-1}) \end{Bmatrix} \tag{5.46}$$

$$N_{1k} = \frac{1}{2G}\begin{Bmatrix} \mathrm{Re}(i\bar{z}^k) \\ \mathrm{Im}(i\bar{z}^k) \end{Bmatrix} \tag{5.47}$$

$$N_{2k} = \frac{1}{2G}\begin{Bmatrix} \mathrm{Re}(-\bar{z}^k) \\ \mathrm{Im}(-\bar{z}^k) \end{Bmatrix} \tag{5.48}$$

Note that it is essential to discard all rigid-body motion terms from u_e to form the vector $N_e = [N_1\ N_2\ \ldots\ N_m]$ as a set of linearly independent functions N_j associated with non-vanishing strains. As well, to ensure that the resulting stiffness matrix has full rank, the number of independent solutions N_j should be higher than (N_{dof}-3), i.e. $m > N_{dof} - 3$, where N_{dof} is the number of nodal DOF of the element. As an example, the terms of the T-complete function of a 4-node linear quadrilateral element shown in Figure 5.4, should be greater than 2×4-3=5.

The corresponding components of the $\mathbf{T_e}$ matrix in Eq. (5.19) should be changed as follows (Qin 2000)

$$T_{1k} = \begin{Bmatrix} \mathrm{Re}(2ikz^{k-1} - ik(k-1)\bar{z}z^{k-2}) \\ \mathrm{Re}(2ikz^{k-1} + ik(k-1)\bar{z}z^{k-2}) \\ \mathrm{Im}(ik(k-1)\bar{z}z^{k-2}) \end{Bmatrix} \tag{5.49}$$

$$T_{2k} = \begin{Bmatrix} \mathrm{Re}(2kz^{k-1} - k(k-1)\bar{z}z^{k-2}) \\ \mathrm{Re}(2kz^{k-1} + k(k-1)\bar{z}z^{k-2}) \\ \mathrm{Im}(k(k-1)\bar{z}z^{k-2}) \end{Bmatrix} \tag{5.50}$$

$$T_{3k} = \begin{Bmatrix} -\mathrm{Re}(ikz^{k-1}) \\ \mathrm{Re}(ikz^{k-1}) \\ \mathrm{Im}(ikz^{k-1}) \end{Bmatrix} \tag{5.51}$$

$$T_{4k} = \begin{Bmatrix} -\mathrm{Re}(kz^{k-1}) \\ \mathrm{Re}(kz^{k-1}) \\ \mathrm{Im}(kz^{k-1}) \end{Bmatrix} \tag{5.52}$$

5.5. NUMERICAL EXAMPLES AND DISCUSSION

Determination of the equivalent homogeneous material properties implies a homogenization procedure that requires the application of several independent loading conditions on the RVE under consideration (Zohdi and Wriggers 2008). Each loading case consists of specifying displacement fields that render null all but one of the three independent components of the strain tensor. In the present investigation, the strain controlled method is employed to conduct the necessary tests. Resolving the stress field in the heterogeneous material through a static equilibrium analysis allows calculation of the average stress field $\bar{\boldsymbol{\sigma}}$. Since the average strain $\bar{\boldsymbol{\varepsilon}}$ is imposed, the stiffness tensor components for the equivalent material $\bar{C}_{ij}$ can be directly calculated from Eq. (5.11).

In the following two examples, the effective properties of two-phase composites are investigated by means of the HT-FEM and HFS-FEM. It is assumed that both fiber and matrix are linear elastic and that they are perfectly bonded at their interface. It is also assumed that the reinforced fibers are infinite in the third direction so that it can be treated as plane strain problem. Two different cases (isotropic reinforced fiber embedded in isotropic matrix, and orthotropic reinforced fiber embedded in isotropic matrix) are studied to demonstrate the efficiency and accuracy of the two hybrid finite element methods.

5.5.1. Composite with isotropic fiber

A composite with embedded periodic isotropic fibers is investigated in this section. The material parameters of the matrix and fiber are as follows

Matrix: Young's modulus $E_m = 3$ GPa, Poisson's ratio $v_m = 0.35$;

Fiber: Young's modulus $E_f = 70$ GPa, Poisson's ratio $v_f = 0.2$.

5.5.1.1. Effect of mesh density

For finite element method, it is of interest and paramount importance to investigate the convergence and distortion sensitivity of the elements before conducting the analysis. In this section, three different meshes, as shown in Figure 5.5, are employed to investigate the convergent performance of the HT-FEM and the HFS-FEM in predicting the effective elastic parameters of the heterogeneous composite. The meshing of the model is obtained using ABAQUS's built-in free meshing algorithm. Figure 5.5(a) contains irregular geometry, non-uniform elements. The number of elements for the coarse mesh, medium mesh, and fine mesh are 28, 135, and 522, respectively.

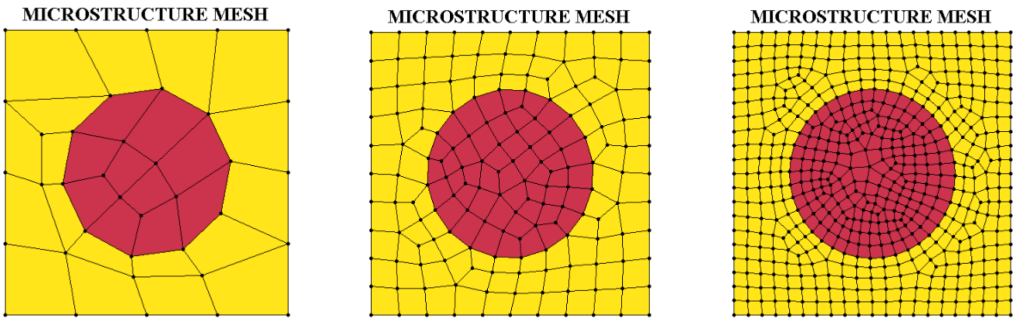

(a) Coarse mesh (b) Medium mesh (c) Fine mesh

Figure 5.5 Three different mesh densities (red: fiber, yellow: matrix).

Table 5.1 presents the predicted effective stiffness parameters, effective transversal Young's modulus and effective Poisson's ratios calculated by the HT-FEM with linear quadrilateral elements based on three different mesh densities. The effective engineering constants (transversal Young's modulus E_T, Poisson's ratios ν_T and shear modulus G_T) are calculated by C_{11}, C_{12}, and C_{66} based on the following equations (Yang and Qin 2004):

$$\nu_T = C_{12} / (C_{11} + C_{12}) \tag{5.53}$$

$$E_T = \frac{C_{11}(1+\nu_T)(1-2\nu_T)}{(1-\nu_T)} \tag{5.54}$$

$$G_T = C_{66} \tag{5.55}$$

For comparison and verification, the corresponding effective parameters calculated using ABAQUS with the same meshes are also presented in Table 5.1. It can be seen that, compared with the ABAQUS, good accuracy can be achieved by the HTFEM when using the coarse mesh.

Table 5.1 Effective parameters calculated by HT-FEM and ABAQUS based on different meshing with linear elements.

Mesh Density	Coarse Mesh (28)		Medium Mesh (135)		Fine Mesh (522)	
Method	HT-FEM	ABAQUS	HT-FEM	ABAQUS	HT-FEM	ABAQUS
C_{11}	7226.608	7095.709	7289.793	7263.611	7318.937	7276.700
C_{12}	3271.800	2909.319	3361.714	3296.600	3378.242	3314.374
C_{66}	1671.889	1630.440	1640.908	1633.470	1639.296	1635.974
E_T	5187.313	5403.733	5167.818	5205.400	5185.194	5202.297
υ_T	0.312	0.291	0.316	0.312	0.316	0.313

Table 5.2 shows the effective parameters calculated by the HT-FEM and HFS-FEM with quadratic quadrilateral elements (8-node quadrilateral elements) for the three different meshes in Figure 5.5. The results obtained by ABAQUS are also presented for comparison. It can be found that for the HT-FEM and HFS-FEM, the error of the engineering constant v_T between linear element and quadratic element is less than 1.3% for the coarse mesh and 0.1% for the fine mesh, whereas the error of v_T calculated by ABAQUS can be up to 8% for the same coarse mesh and 1.3% for the same fine mesh.

Table 5.2 Effective parameters calculated by HT-FEM, HFS-FEM and ABAQUS using different meshing and quadratic elements.

Mesh Density	Coarse Mesh (28)			Medium Mesh (135)			Fine Mesh (522)		
	HT-FEM	HFS-FEM	ABAQUS	HT-FEM	HFS-FEM	ABAQUS	HT-FEM	HFS-FEM	ABAQUS
C_{11}	7327.519	7321.741	7103.658	7328.007	7327.285	7268.491	7328.055	7326.448	7309.561
C_{12}	3383.973	3374.516	3278.802	3384.733	3384.911	3358.074	3384.723	3385.245	3373.518
C_{66}	1639.981	1641.007	1601.484	1639.629	1639.998	1627.928	1639.575	1640.025	1636.495
E_T	5189.390	5192.517	5032.753	5189.168	5188.112	5146.138	5189.235	5186.751	5178.972
υ_T	0.316	0.315	0.316	0.316	0.316	0.316	0.316	0.316	0.316

Moreover, it can be seen from Table 5.1 and Table 5.2 that there is little difference in the results calculated by HT-FEM and HFS-FEM when the number of elements is increased. In contrast, an obvious difference is found in the results calculated by ABAQUS although the ABAQUS results approach those calculated by HT-FEM and HFS-FEM when using the finest meshes. It is well known that by increasing mesh density and employing higher order elements, ABAQUS results can be improved and tend to converge to the exact solutions. Consequently, it is believed that the difference between the results of HT-FEM and ABAQUS decreases along with an increase in the mesh density or/and the order of element.

From Table 5.1 and Table 5.2, it can be seen that the results with lower-order coarse meshes in HT-FEM and HFS-FEM are similar to those given by ABAQUS with a higher-order fine mesh. The results also indicate that the HT-FEM and the HFS-FEM are not sensitive to mesh density and element distortion. This can also be observed from Figure 5.6, in which the contour plots of the stress fields of a RVE with a fiber volume fraction (FVF) of 28.27% are shown when the RVE is subjected to controlled shear strains (10^{-4}). The results shown in Figure 5.6 (a) are calculated using HT-FEM with the fine mesh shown in Figure 5.5 (c), and the results shown in Figure 5.6 (b) are obtained using HFS-FEM. For a clear view, all the deformations of the RVE in Figure 5.6 have magnified 1000 times. It can be seen that the stress distributions and profile of RVE obtained from HT-FEM and HFS-FEM are the same. It should be pointed out that the number of terms of the Trefftz function has no obvious influence on the results of effective material parameters as long as the requirements are satisfied of a minimum number of terms of T-complete functions (Qin 2000).

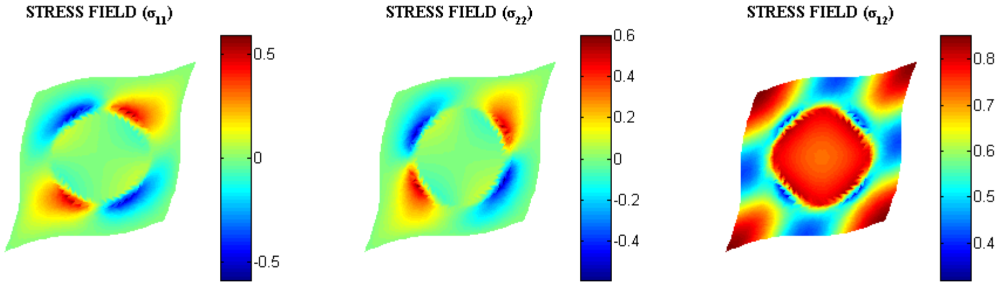

(a) HT-FEM

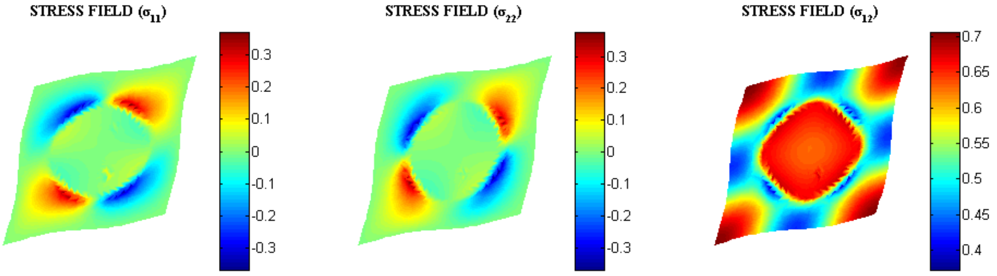

(b) HFS-FEM

Figure 5.6 Stress fields of the RVE of composites with isotropic fiber on deformed configuration under pure shear strain using (a) HT-FEM and (b) HFS-FEM (FVF: 28.27%).

5.5.1.2. Effect of fiber volume fraction

It has been found that the FVF has a significant influence on the effective mechanical properties of composites. In this section, six different FVFs, varying from 12.57% to 63.62%, are used to study the macroscopic effective parameters of composites. The FVF is changed by varying the radius of the fiber in the analysis. The fiber radius is assumed to be r=4, r=5, r=6, r=7, r=8 and r=9, respectively. The predicted effective stiffness parameters from HT-FEM are listed in Table 5.3 and Table 5.4. Compared with the results in Table 5.3 and Table 5.4, it is found that there is little difference (<2%) for C11, C12 and C66 when elements of different orders are employed. That indicates that linear elements can be employed to improve the calculation efficiency of large-scale simulations without the decrease in accuracy incurred by ABAQUS.

Table 5.3 Predicted effective stiffness parameters for different FVFs using HT-FEM with linear element.

FVF	12.57%	19.63%	28.27%	38.48%	50.27%	63.62%
C_{11}	5695.083	6329.452	7289.793	8839.901	11503.063	16860.629
C_{12}	2927.021	3120.798	3361.714	3651.620	3927.328	4488.681
C_{66}	1329.382	1460.801	1640.908	1900.043	2329.915	3254.094
E_T	3707.760	4268.260	5167.818	6704.960	9503.904	14973.143
v_T	0.340	0.331	0.316	0.292	0.256	0.210

Table 5.4 Predicted effective stiffness parameters for different FVFs using HT-FEM with quadratic element.

FVF	12.57%	19.63%	28.27%	38.48%	50.27%	63.62%
C_{11}	5703.923	6346.791	7328.007	8881.711	11538.307	16902.291
C_{12}	2936.343	3136.764	3384.733	3676.311	4011.769	4543.670
C_{66}	1328.242	1459.639	1639.629	1901.206	2333.549	3261.974
E_T	3708.126	4271.770	5189.168	6729.260	9468.312	14976.993
v_T	0.340	0.331	0.316	0.293	0.258	0.212

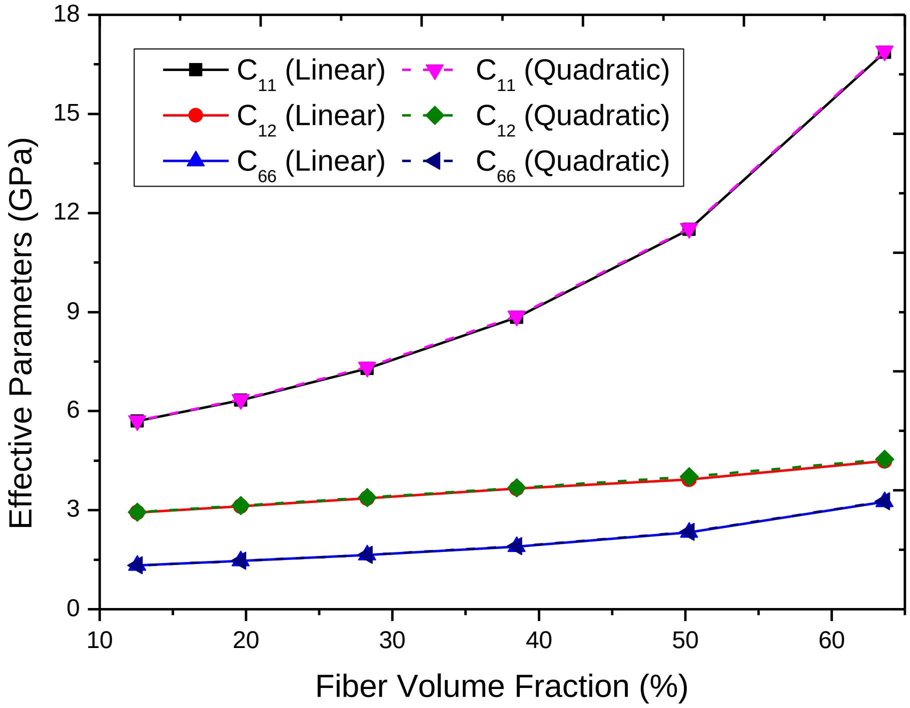

Figure 5.7 Variation of the composite effective parameters with increasing FVF using HT-FEM (linear and quadratic elements).

Figure 5.7 graphically illustrates the variation of the composite effective parameters with an increase in FVF by the HT-FEM using linear elements and quadratic elements. As expected, all three effective stiffness parameters C_{11}, C_{12}, and C_{22} increase along with the increase in FVF. However, the rates of increase for these three parameters are not the same which C_{11} experiences a dramatic increase whereas C_{12} increases only slightly. The rate of increase becomes greater as the FVF increases.

It is obvious that for all the cases investigated in this analysis, good accuracy can be achieved by both linear and quadratic elements as mentioned in previous section.

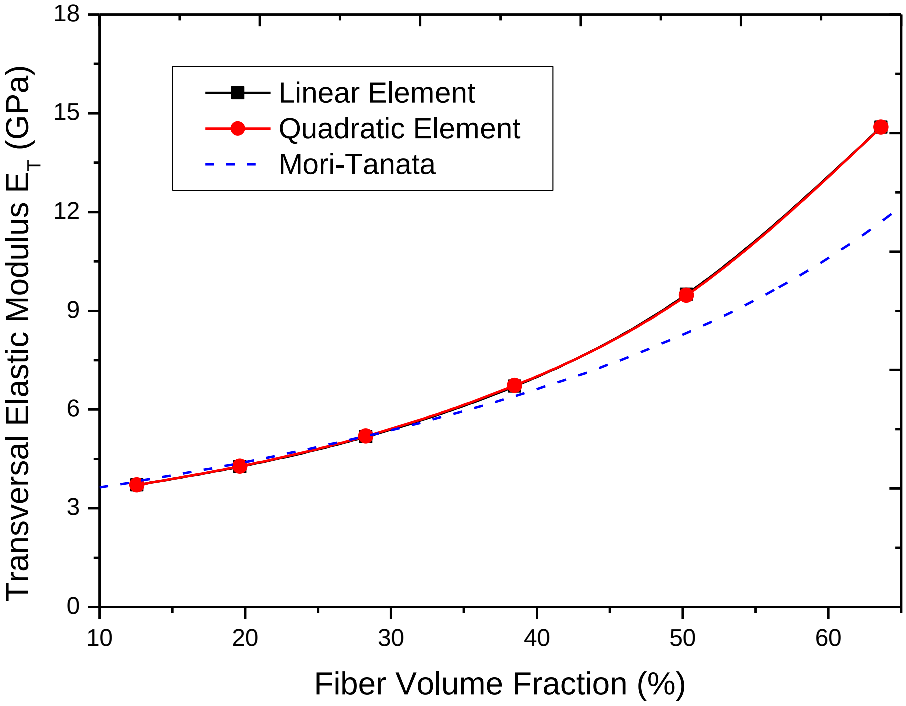

Figure 5.8 Variation of the Young's elastic modules E_T of composite with increasing FVF using HT-FEM.

Figure 5.8 and Figure 5.9 describe the variation of effective transversal Young's modulus E_T and Poisson's ratios v_T of the reinforced composite with FVF. The results from the Mori-Tanata method are also included in the figure for comparison. It can be seen that the effective transversal Young's modulus increases with FVF whereas the effective Poisson's ratio decreases. The analytical solutions from the Mori-Tanata method are in good agreement with those from HT-FEM when FVF<40%, but the predicted values from the Mori-Tanata method diverge from those by HT-FEM when FVF>40%. This phenomenon verifies the conclusion that the Mori-Tanata method is more accurate for medium FVFs (30%).

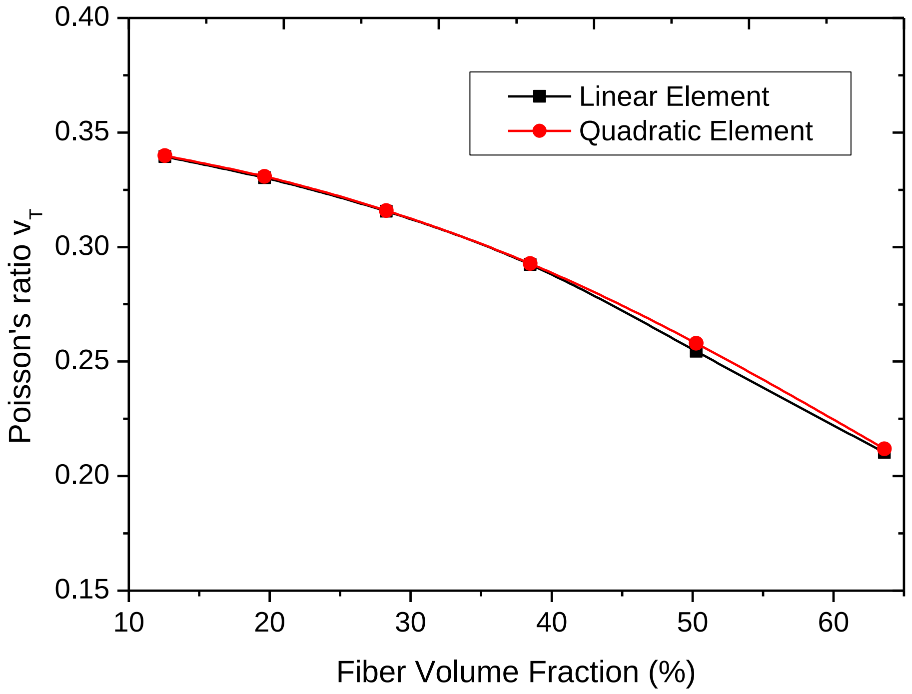

Figure 5.9 Variation of Poisson's ration v_T of the composite with increasing FVF using HT-FEM.

Table 5.5 Predicted effective stiffness parameters for different FVFs using HFS-FEM.

Fiber Fraction	12.57%	19.63%	28.27%	38.48%	50.27%	63.62%
C_{11}	5704.059	6346.786	7327.423	8882.773	11538.85	16904.75
C_{12}	2936.537	3136.388	3384.751	3676.242	4009.644	4544.372
C_{66}	1328.396	1459.782	1640.37	1901.328	2333.357	3261.719
E_T	3708.075	4272.178	5188.447	6730.572	9470.838	14979.135
v_T	0.340	0.331	0.316	0.293	0.258	0.212

It also demonstrates that the predicted transversal Young's modulus and Poisson's ratios are nearly the same when the linear and quadratic elements are employed in the HT-FEM. The effective properties for the same fiber fractions are also calculated using HFS-FEM with 8-node elements, as shown in Table 5.5. Comparison of the results in Table 5.4 and Table 5.5 shows that the results from the HT-FEM and the HFS-FEM are nearly identical.

5.5.2. Composites with orthotropic fibers

For composites with orthotropic fibers, the fiber stiffness parameters are assumed to be

$$C_{11} = 6.1622\times10^{4}\,\mathrm{Nm}^{-2}, C_{12} = 1.3911\times10^{4}\,\mathrm{Nm}^{-2},$$
$$C_{22} = 1.8908\times10^{4}\,\mathrm{Nm}^{-2}, C_{66} = 4.0502\times10^{3}\,\mathrm{Nm}^{-2}.$$

The Young's modulus and Poisson's ratio of the matrix remain the same as those of the composite with isotropic fibers, i.e. E_m = 3 GPa and υ_m = 0.35 respectively.

5.5.2.1. Effect of mesh density

The effect of mesh density on the accuracy of the method is investigated for the composite with orthotropic fibers by using the HFS-FEM. The three different meshes shown in Figure 5.5 are employed again for discretizing the square RVEs with orthotropic fibers. The coarse mesh uses 28 quadratic elements, medium mesh 135 quadratic elements, and fine mesh 522 quadratic elements. The effective material parameters calculated by HFS-FEM are given in Table 5.6, and also graphically demonstrated in Figure 5.10 for a clear view of the differences between them.

It can be seen from Table 5.6 and Figure 5.10 that there is little variation in the predicted effective parameters when the mesh density is decreased. The accuracy of HFS-FEM using the coarse mesh (28 8-node quadrilateral elements) is similar to that of the ABAQUS using the fine mesh (522 8-node quadrilateral elements). These results indicate that the micromechanical modal based on the HFS-FEM is also not sensitive to mesh density and element distortion for the case of orthotropic fiber. It is demonstrated that this method has the potential to be used in multiscale simulation to enhance computational efficiency while maintaining the required accuracy.

Table 5.6 Effective stiffness parameters obtained by HFS-FEM and ABAQUS with different mesh densities.

Mesh Density	Method	C_{11}	C_{12}	C_{22}	C_{66}
Coarse mesh (28)	HFS-FEM	7232.374	3246.842	6443.842	1448.592
	FEM(Quadratic)	7145.669	3212.689	6377.076	1437.549
	FEM(Linear)	6425.217	2610.608	5745.458	1365.512
Medium mesh (135)	HFS-FEM	7230.208	3247.765	6442.853	1447.489
	FEM(Quadratic)	7211.703	3241.617	6428.952	1444.831
	FEM(Linear)	7062.563	3125.867	6302.854	1429.705
Fine mesh (522)	HFS-FEM	7229.685	3251.708	6440.99	1447.614
	FEM(Quadratic)	7221.606	3241.769	6433.551	1446.791
	FEM(Linear)	7146.783	3168.411	6346.986	1602.323

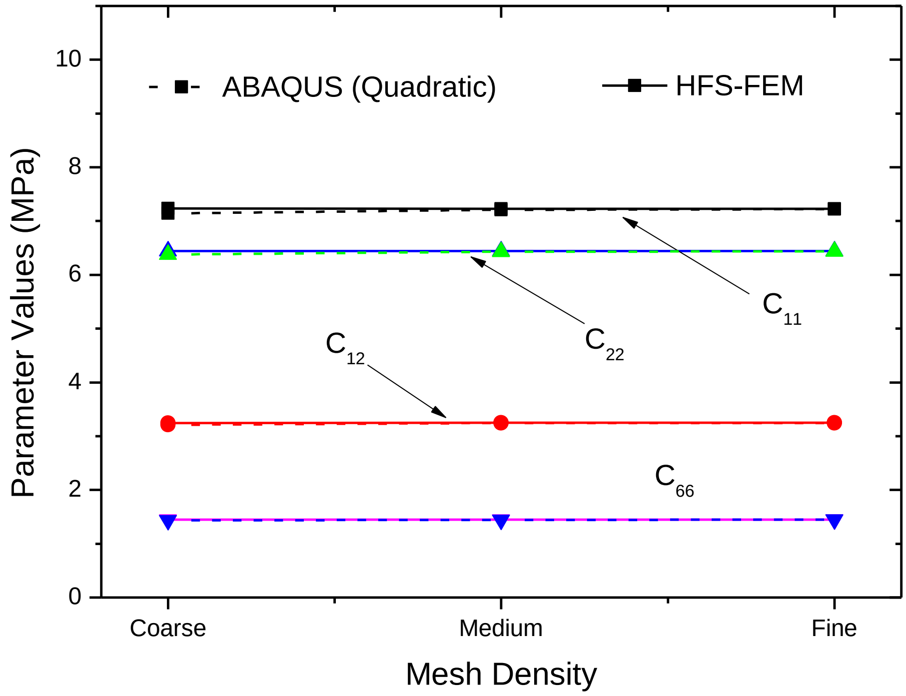

Figure 5.10 Comparison of effective stiffness parameters calculated by HFS-FEM and ABAQUS.

5.5.2.2. Effect of fiber volume fraction

The effect of FVF is also investigated in this section for composites with orthotropic fibers. Table 5.7 presents the four parameters: C_{11}, C_{12}, C_{22}, and C_{66} of the stiffness matrix for six different fiber fractions: 12.57%, 19.63%, 28.27%, 38.48%, 50.27%, and 63.62%, respectively. These FVFs are selected by changing the fiber radius from r=4 to r=9 as described in Section 5.5.1.

Table 5.7 Variation of effective parameters with the volume fraction of reinforced fibers.

Fiber Fraction	12.57%	19.63%	28.27%	38.48%	50.27%	63.62%
C_{11}	5703.923	6287.574	7230.208	8708.330	11182.148	15881.294
C_{12}	2936.343	3037.789	3247.765	3514.385	3889.846	4597.288
C_{22}	5439.596	5855.995	6442.853	7268.749	8448.530	10190.166
C_{66}	1253.403	1336.934	1447.489	1596.397	1810.012	2154.185

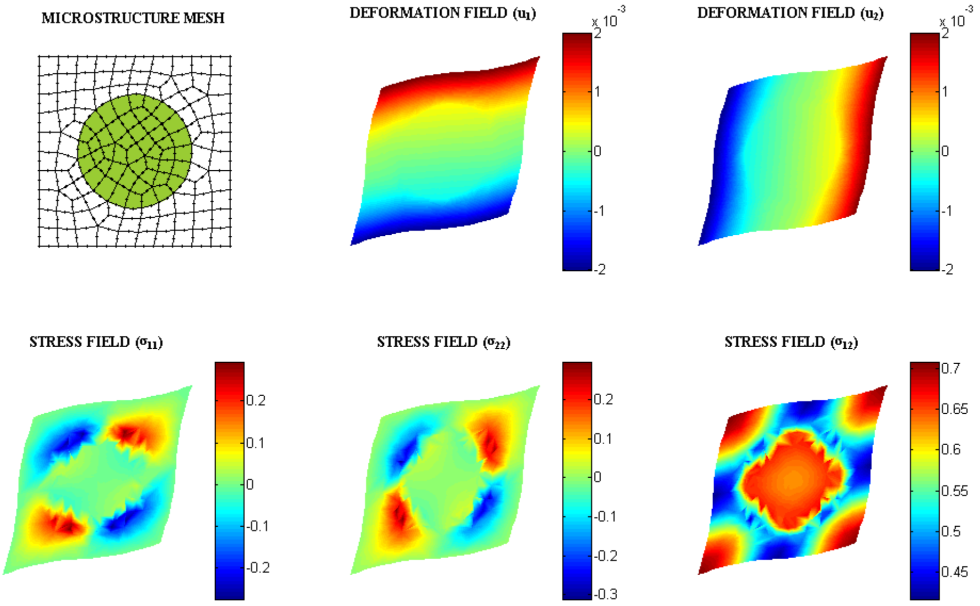

Figure 5.11 Mesh, deformation, and stress fields of the RVE of composites with orthotropic fiber under constant shear strain using HFS-FEM (FVF: 28.27%).

As is obvious from Table 5.7, all the investigated parameters increase with the FVF of the composites, displaying a similar trend to that found in the isotropic fiber case. It should be noted, however, that the rates of increases for these four parameters are not consistent when the FVF increases from 12.57% to 63.62%, as is graphically demonstrated in Figure 5.12. The effective parameter C_{11} reaches the value of 10177.4

MPa when FVF=63.62%, which is nearly 2.8 times its original value. For C_{22} and C_{66}, however, the changes are only about 1.6 times their original corresponding values. These results derive from the phenomenon that the composite, consisting of orthotropic fibers and isotropic matrix, demonstrates strong orthotropic properties, as expected. Figure 5.11 shows the mesh configuration, deformations and stress fields of the RVE for orthotropic fiber when the RVE is subjected to constant shear strain and FVF is equal to 28.27%.

5.5.2.3. Effect of fiber shape

In this section, the effect of the shape of fibers on the effective properties of composites is presented. As shown in Figure 5.13(a)-(d), four inclusion shapes, circle, ellipse, square, and triangle, are considered. For all the RVEs presented in this section, the FVF is kept constant at 28.27% (i.e. the radius of the circular fiber is equal to 6). The predicted effective parameters calculated by the HFS-FEM for the four different configurations are given in Table 5.8, and are also graphically depicted in Figure 5.15. It can be seen that compared to the other three forms, the reinforcement performance of the elliptical shape is significant, dramatically increasing the stiffness of the reinforced composite in the major axis direction while not significantly decreasing the other three stiffness parameters. It may be concluded that elliptical-shaped fiber is a promising reinforcement form and can be employed when extra reinforcement is needed in a particular direction. Furthermore, the triangle-shaped fiber also has good reinforcment performance, in that the reinforced composite has higher effective stiffness than its counterpart with circle shape inclusion.

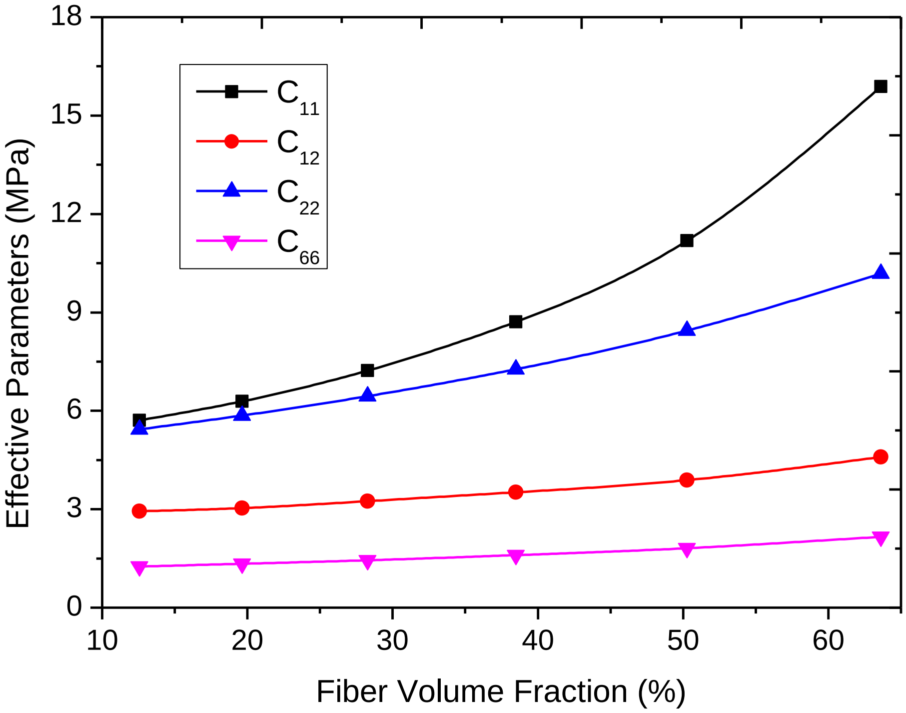

Figure 5.12 Variation of effective parameters with increasing FVF.

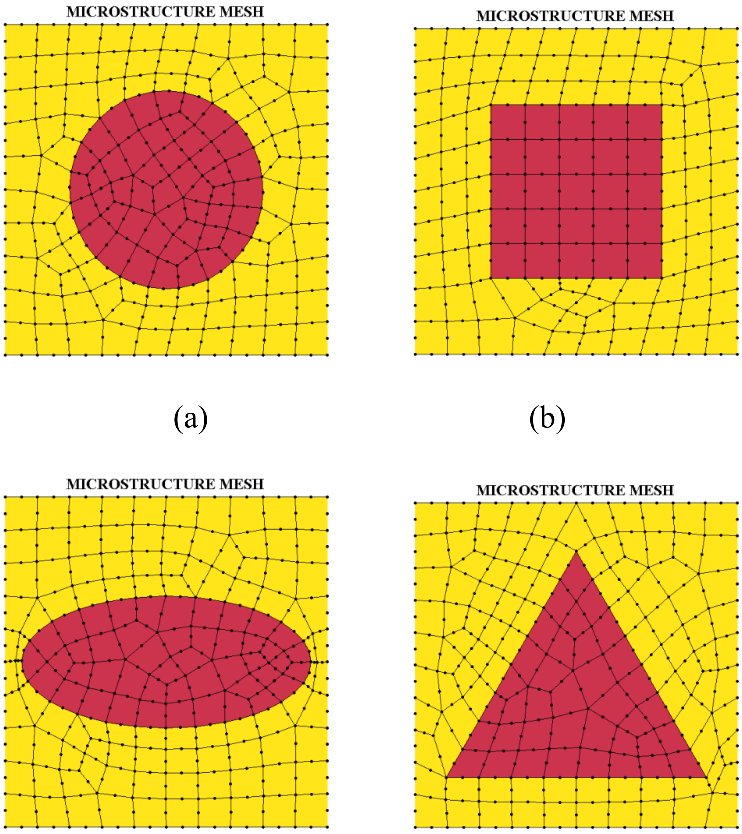

(a) (b)

(c) (d)

Figure 5.13 Meshes for RVE with different-shaped fibers.

Table 5.8 Effective parameters predicted by HFS-FEM for different inclusion shapes and configuration.

Inclusion Shape	Circle	Elliptical	Square	Triangle	Pattern 1	Pattern 2
C_{11}	7230.208	9715.192	7451.964	7675.534	7275.869	7078.099
C_{12}	3247.765	3331.026	3173.031	3261.295	3223.868	3384.242
C_{22}	6442.853	6180.894	6506.971	6525.828	6456.642	6400.636
C_{66}	1447.489	1423.143	1441.282	1472.153	1444.499	1501.981

5.5.2.4. Effect of fiber configuration

Two different configurations of reinforced fibers, as shown in Figure 5.14 (a) and (b), are studied to investigate the effect of the fiber configuration on the effective parameters of composites. The two patterns in Figure 5.14 have the same FVF and the arrangement of Pattern 2 is obtained by rotating Pattern 1 by an angle of 90°. The effective parameters of the composites are given in Table 5.8 together with the cases from one fiber. Here, for comparison, the FVFs of the two patterns are equal to the single fiber case investigated in previous section. From Table 5.8, little difference is observed when the one circular-fiber RVE is replaced by the four-fiber RVE as shown in Figure 5.14 (a) and (b). For these two patterns, it is also found that Pattern 2 has slightly higher values in C_{12} and C_{66} but slightly lower values in C_{11} and C_{22} compared with Pattern 1, as can be seen from Figure 5.15.

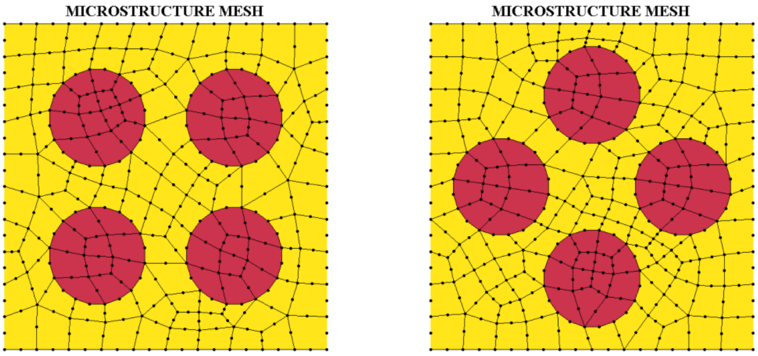

(a) Fiber pattern 1 (b) Fiber pattern 2

Figure 5.14 Meshes for RVE with different fiber configurations.

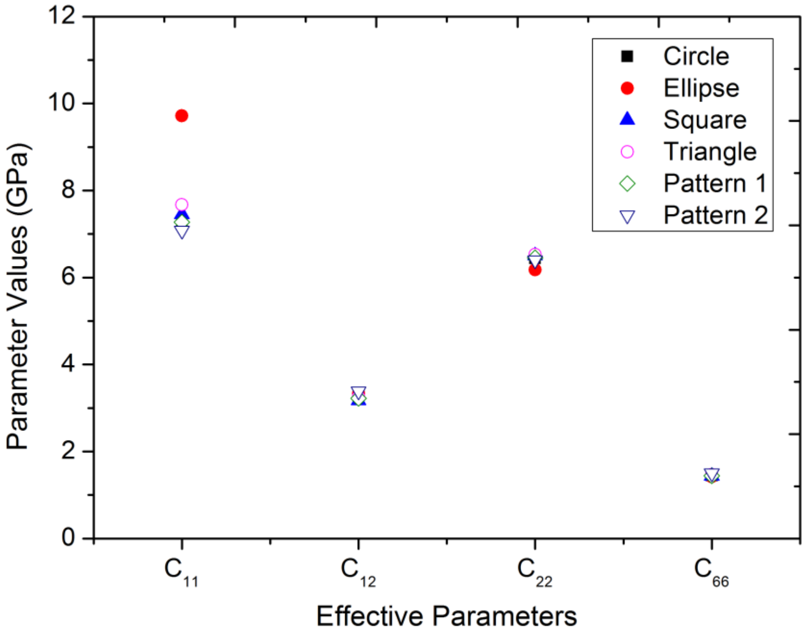

Figure 5.15 Difference of effective parameters among six configurations.

5.6. SUMMARY

A micromechanical analysis based on the HFS-FEM and HT-FEM is presented to determine the effective properties of heterogeneous composites. In this work, the homogenization technique is employed to average the microscale stresses and strains through the concept of the RVE. Two kinds of fiber reinforced composites are analyzed, including isotropic and orthotropic materials. Numerical results obtained from ABAQUS are also presented for comparison and verification. The numerical results show that the accuracy of the HFS-FEM and HT-FEM is promising when using coarse meshes. In the micromechanical modeling, the effective material parameters obtained from HT-FEM and HFS-FEM are insensitive to mesh density and element distortion. Generally both methods give better results than ABAQUS when using the same meshes.

The effect of microstructure factors, including the FVF, fiber shape, and fiber configuration in RVE, on the effective parameters of the composites are also studied in this chapter. For both isotropic- and orthotropic- fiber-reinforced composites, all the effective stiffness parameters increase with an increase in FVF, with the rates of increase of these parameters differing from one another. It may be concluded that the proposed micromechanical models based on the HFS-FEM and HT-FEM have the potential for further development in the consideration of various defects including cracks and pore voids in microstructures.

Chapter 6. Effective Thermal Conductivity of Fiber-reinforced Composites

6.1. INTRODUCTION

Fiber-reinforced composites are structural materials that usually consist of a fiber reinforcing phase and a matrix phase in which the fiber is embedded at a macroscopic level to possibly experience a range of mechanical, thermal, and chemical environments during their service life (Chung 1994). Due to the superiority of their physical properties over the single matrix, such as high thermal and electrical conductivity, high stiffness and strength etc., fiber-reinforced composites are widely used in engineering applications. Determination of the effective properties of composite materials is of paramount importance in engineering design and application of composite materials. The effective thermal conductivity and other thermo-physical properties of composites have attracted considerable interest from theoretical, numerical, and experimental researchers in the last several decades (Chen and Cheng 1967; Mauge and Kachanov 1994; Landis, Beyerlein et al. 2000; Tsukrov 2000; Tsukrov and Novak 2002; Brucker and Majdalani 2005; Kachanov and Sevostianov 2005; Farooqi and Sheikh 2006; Wang and Pan 2008; Brennan and Walrath 2009; Li, Li et al. 2011). It would save much effort, time, and expense if the properties of new reinforced composites could be predicted accurately or designed from microstructural properties of their constituents.

In the literatures, the averaged or homogenized method by RVE is usually employed in micromechanical modeling of composites (Miehe 2003; Zohdi and Wriggers 2008). Boundary value problems defined on the RVEs can be analyzed by appropriate numerical methods. In the past two decades, considerable attention has been paid to determination of the thermal or mechanical properties of composites by using FEM (Islam and Pramila 1999). The reason for using FEM is that it easily enables simulation of the effects of various possible defects on the mechanical properties, i.e., the effect of improper bond between fiber and matrix and the effect of cracks with different orientations. However, the drawback of this method is that refined meshes near the defects (cracks, holes or inclusions) are usually required to achieve the desired accuracy. This is not practical for the analysis of composites whose fiber distribution might change repeatedly. Unlike FEM, BEM simply requires division on the boundaries of the domain under consideration, reducing the dimensionality of the problem by one. This approach has been successfully applied to steady-state and transient heat conduction (Ma, Chatterjee et al. 2008), interface performance (Chen and Papathanasiou 2004), and thermoelastic behavior (Henry, Ma et al. 2007) of fiber-reinforced composites. Singular or hyper-singular integrals, however, are unavoidable in BEM. Moreover, the BEM solution process becomes extremely complex for imposing continuity conditions across the interface between fiber and matrix when solving multi-material problems such as fiber-reinforced composites (Gao and Davies 2002).

To overcome these difficulties, HT-FEM was developed based on the novel concept of two independent fields: an intra-element field and an auxiliary frame field (Qin 2000; Qin and Wang 2008). This approach involves the element boundary integrals only, inherits the advantages of both conventional FEM and BEM, and has been successfully applied to various engineering problems (Qin 1994; Qin 1995; Qin 1996; Qin 2003; Qin and Wang 2008). As an alternative, a novel hybrid finite formulation based on the fundamental solutions, the HFS-FEM, was developed by Wang and Qin for solving two-dimensional linear heat conduction problems (Wang and Qin 2009; Wang and Qin 2010a), and isotropic elastic (Wang and Qin 2011), functionally graded elastic (Wang and Qin 2011) and piezoelectric problems (Cao, Qin et al. 2012b). The HFS-FEM inherits all the advantages of HT-FEM and obviates the difficulties that occur in HT-FEM.

In this Chapter, the formulations of the HFS-FEM for the heat conduction problem are presented to model heterogeneous fiber-reinforced composites and to investigate the applicability of the new method in predicting the effective thermal conductivity of ideal fiber reinforced composites. Both the general element and a special element for circular fiber inclusion are proposed based on the relevant fundamental solutions. The special element is based on a special fundamental solution which analytically satisfies the continuity of temperature and heat flux on the interface between fiber and matrix and is constructed to reduce the mesh refinement effort in modeling heterogeneous composites. Then, independent intra-element and frame fields as well as a modified variational functional are constructed to derive final stiffness equations and determine the unknowns. The RVE is utilized for estimating the effective thermal property of the composites. Two examples are considered in order to obtain insight into the influence of the FVF and fiber arrangement pattern on effective thermal conductivity. The accuracy of the numerical results obtained by the proposed method is verified against those calculated by the commercial software package ABAQUS. The results indicate that the proposed method is efficient and accurate in analyzing the thermal behavior of fiber-composites and has the potential to be scaled up to macroscale modeling of large-scale practical problems of considerable interest.

This chapter is organized as follows: the governing equations of the heat conduction problem and the basic concepts of RVE and homogenization procedures are introduced in Section 6.2. Then, the fundamental solutions for interpolation of a temperature field within each element domain are given in Section 6.3. Further, the detailed solution procedures for the derivation of the HFS-FEM are presented in Section 6.4. Finally, two numerical examples for RVEs with simple and complex fiber patterns are considered in Section 6.5, and some concluding remarks are presented in Section 6.6. The majority of this chapter has been presented in a paper (Cao, Yu et al. 2012c) co-authored by the candidate.

6.2. HOMOGENIZATION OF HEAT CONDUCTION PROBLEMS

In this section, a brief review of the basic equations and concepts used in micromechanical analysis of heat conduction problems is presented to introduce the notation and provide a common source of reference for later sections.

6.2.1. Governing equations

In the absence of mechanical deformations, the thermal equilibrium governing equation for the temperature field can be expressed as (Temizer and Wriggers 2010)

$$\nabla \mathbf{q} = 0 \tag{6.1}$$

with the boundary conditions

$$\theta = \bar{\theta} \quad \text{on } \Gamma_\theta, \qquad h = \mathbf{q} \cdot \mathbf{n} = \bar{h} \quad \text{on } \Gamma_h \tag{6.2}$$

where $\nabla = [\partial / \partial x_1, \partial / \partial x_2]$ is the divergence operator, $\theta = T - T_0$ is the unknown temperature change, where T is the current absolute temperature and T_0 is a reference absolute temperature, and $\mathbf{g} = \nabla \theta$ is the temperature gradient. h is the normal heat flux, and $\mathbf{n}$ is the outward normal vector to the boundary $\Gamma = \Gamma_\theta \cup \Gamma_h$, and $\bar{\theta}$ and $\bar{h}$ are specified values on the related boundaries, respectively. The space derivatives are denoted by a comma, i.e. $\theta_{,i} = \partial \theta / \partial x_i$, and the subscript i takes values 1 and 2 in the present analysis.

The constitutive law for flux vector $\mathbf{q} = [q_1, q_2]^T$ is provided by the Fourier's law (Temizer and Wriggers 2010)

$$\mathbf{q = \text{-}kg} \tag{6.3}$$

where $\mathbf{k}$ is the thermal conductivity tensor, which is symmetry and positive-definite and depends on the local materials in the heterogeneous composites. The matrix and fiber are herein assumed to be locally isotropic and homogeneous, so $k_{11} = k_{22} = k_m$ in the matrix and is equal to k_f in the fiber area, respectively.

6.2.2. RVE for micro-thermal analysis

The microstructure of the composite, such as the shape, size distribution, spatial distribution, and orientation distribution of the reinforcing inclusions in the matrix, has a significant influence of the overall (effective) properties of heterogeneous materials (Nemat-Nasser and Hori 1999). Although most composites possess inclusions in random distributions, great insight into the effect of microstructure on the effective properties can be gained from investigation of composites with periodic structures. For a periodic composite, it is usually sufficient to draw conclusions for the whole structure from considering only a unit cell (i.e., one RVE as shown in Figure 6.1), as was done in Chapter 5 (Zohdi and Wriggers 2008).

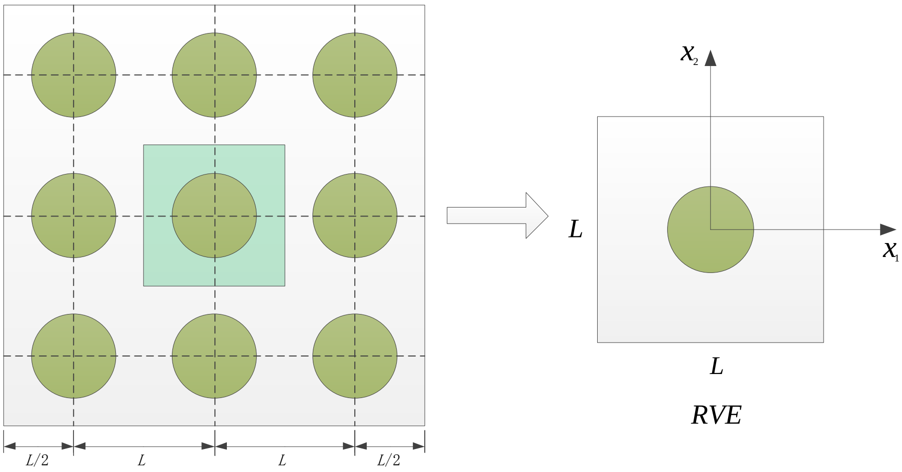

Figure 6.1 Periodic fiber-reinforced composites and RVE.

For simplification, the following assumptions for ideal fiber-reinforced composites are applied (Islam and Pramila 1999): (a) the composites are macroscopically homogeneous, (b) locally both the matrix and the fiber are homogeneous and isotropic, (c) the thermal contact resistance between the filament and the matrix is negligible, (d) the composite is free of voids, (e) the problem is 2D, and (f) the reinforced fibers are arranged in a square periodic array, i.e., they are uniformly distributed in the matrix. This last assumption implies that the fibers are equal and uniform in shape and size and are symmetrical about the x_1 and x_2 directions.

6.2.3. Homogenization for the RVE

The macroscopic constitutive formulation must be determined by materials testing of the RVE, from which the heterogeneous conduction problem is solved with specified boundary conditions. The macroscopic flux and the macroscopic gradient fields are identified as the volume averages of the microscopic counterparts and are related to each other by the macroscopic constitutive formulations.

The thermal constitutive law that governs each material or phase in a RVE is given by the standard Fourier's law as shown in Eq.(6.3). To evaluate the effective thermal conductivity of microscopically heterogeneous fiber-reinforced composites, the effective flux $\bar{\mathbf{q}}$ and the effective temperature gradient $\bar{\mathbf{g}}$ are defined as the volume average values of the respective fields in the RVE (Zohdi and Wriggers 2008)

$$\bar{\mathbf{q}} = \langle \mathbf{q} \rangle = \frac{1}{\Omega}\int_{\Omega} \mathbf{q} d\Omega = \frac{1}{\Omega}\int_{\Gamma} h\mathbf{X} d\Gamma \tag{6.4}$$

$$\bar{\mathbf{g}} = \langle \mathbf{g} \rangle = \frac{1}{\Omega}\int_{\Omega} \nabla \theta d\Omega = \frac{1}{\Omega}\int_{\Gamma} \theta \mathbf{n} d\Gamma \tag{6.5}$$

where Ω is the volume of the RVE. It can be seen from Eqs. (6.4) and (6.5) that the volume average gradient and flux are related only to the flux on the boundary of the RVE.

For the isotropic case, the thermal tensor $\mathbf{k}^*$ can be expressed as $\mathbf{k}^* = k^*\mathbf{I}$, where k^* is the conductivity coefficient and $\mathbf{I}$ is the identity tensor. Thus, according to Fourier's law, the effective thermal conductivity can be calculate by

$$k^* = \frac{\|\mathbf{q}^*\|}{\|\mathbf{g}^*\|} = \frac{\|\bar{\mathbf{q}}\|}{\|\bar{\mathbf{g}}\|} \tag{6.6}$$

It should be noted that, to eliminate any external influents or rate effects, the material test for the RVE must be conducted under steady-state conditions and there should be no external heat supply (Temizer and Wriggers 2010).

6.2.4. Boundary conditions for the RVE

Using the RVE model described above, three types of boundary conditions are usually employed to evaluate the overall/effective thermal properties of heterogeneous materials: (a) a uniform flux boundary condition (UF-BC), (b) a linear temperature gradient boundary condition (LT-BC), and (c) a periodic boundary condition (PR-BC) (Zohdi and Wriggers 2008; Temizer and Wriggers 2010). The three boundary conditions in detail are:

(a) Uniform flux boundary condition (UF-BC):

$$h = \mathbf{Q} \cdot \mathbf{n} \tag{6.7}$$

so that $\langle \mathbf{q} \rangle = \mathbf{Q}$.

(b) Linear temperature boundary condition (LT-BC):

$$\theta = \mathbf{G} \cdot \mathbf{X} \tag{6.8}$$

so that $\langle \mathbf{g} \rangle = \mathbf{G}$.

(c) Periodic boundary condition (PR-BC):

$$\theta^+ - \theta^- = \mathbf{G} \cdot \left(\mathbf{X}^+ - \mathbf{X}^- \right) \tag{6.9}$$

and

$$h^+ = -h^- \tag{6.10}$$

so that $\langle \mathbf{q} \rangle = \mathbf{Q}$, where $\mathbf{Q}$ and $\mathbf{G}$ are controlled constant vectors. Previous investigations have found that the periodic boundary condition is much the most accurate in micromechanical analysis of composite materials for both periodic materials and random materials (Huet 1990; Hazanov and Huet 1994). Consequently, the periodic boundary condition is employed for the RVE models in the present research.

From the above homogenization procedures, it is evident that the flux and temperature on the boundary of the RVE are sufficient to calculate the effective thermal conductivity of the composites. This feature easily permits employment of the special element introduced in Section 6.3 to evaluate the effective parameters of the RVE.

6.3. FUNDAMENTAL SOLUTIONS OF PLANE HEAT CONDUCTION PROBLEMS

For the HFS-FEM, it is essential to find the fundamental solutions of plane heat conduction problems to interpolate the intera-element approximation fields. The Green's function of the 2D heat transfer problem in an infinite domain can be defined by

$$k \nabla^2 G(\mathbf{x}, \mathbf{y}) + \delta(\mathbf{x}, \mathbf{y}) = 0 \tag{6.11}$$

where $\delta(\mathbf{x}, \mathbf{y})$ is the Dirac delta function, $\mathbf{x} = (x_1, x_2)$ denotes the field point where the response is calculated and $\mathbf{y} = (y_1, y_2)$ denotes the source point where unit concentrated heat is applied. For plane heat conduction problems of fiber-reinforced composites two kinds of fundamental solution are used, i.e., the general fundamental solution for homogeneous materials with no inclusions and a special fundamental solution which satisfies the interfacial conditions between the circular inclusion and the matrix.

6.3.1. General fundamental solution

For a unit heat source applied at the source point $z_0 = x_{10} + \mathrm{i}x_{20}$ in the infinite homogeneous domain Ω_{m}, as shown in Figure 6.2, the temperature response G_{m} at any field point z is given in the form (Chao and Shen 1997)

$$G_{\mathrm{m}}(z, z_0) = -\frac{1}{2\pi k_m}\mathrm{Re}\left\{\ln(z - z_0)\right\} \tag{6.12}$$

where Re denotes the real part of the bracketed expression, $z = x_1 + \mathrm{i}x_2$ and $\mathrm{i}=\sqrt{-1}$ is an imaginary number.

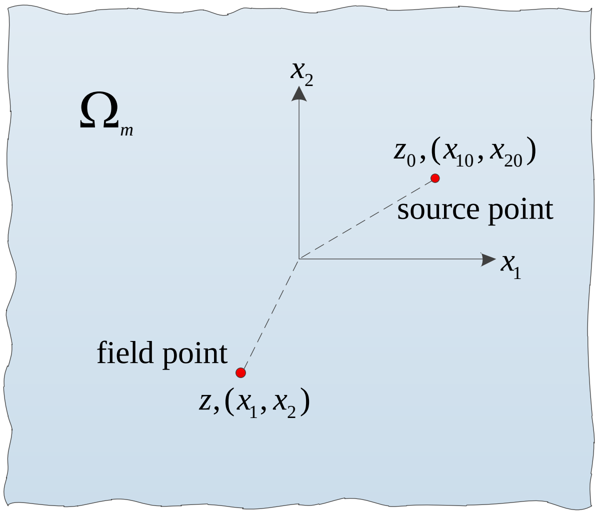

Figure 6.2 Schematic for the definition of general fundamental solutions of plane heat conduction problems.

6.3.2. Special fundamental solutions for hole in a plate

Now we consider a unit heat source located at the point $z_0 = x_{10} + \mathrm{i}x_{20}$ in the infinite domain containing a centered circular hole with radius R as shown in Figure 6.3. The special fundamental solutions or Green's functions refer to the singular solution which is required to satisfy not only the governing equation (6.11) but also specified free boundary conditions around the hole. Therefore, the temperature response at any field point $z = x_1 + \mathrm{i}x_2$ in this case is obtained in the following form (Ang 2007):

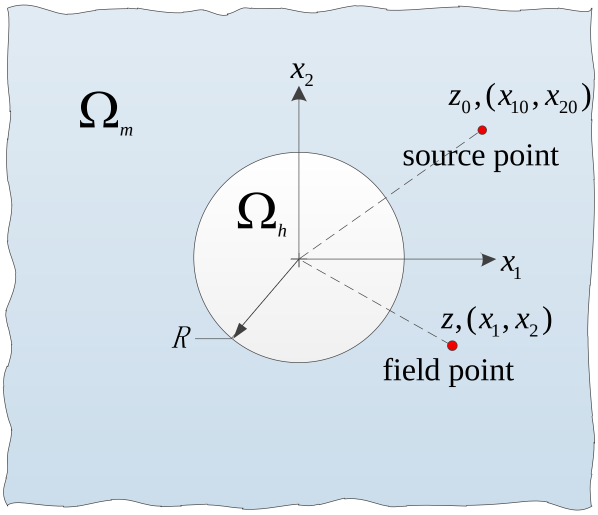

Figure 6.3 Schematic for the definition of special fundamental solutions (hole) of plane heat conduction problems.

$$G(z, z_0) = \frac{1}{2\pi k} \mathrm{Re}\left\{ \ln\left(\frac{z - z_0}{R} \right) \right\} - \frac{1}{2\pi k} \mathrm{Re}\left\{ \ln\left(1 - \frac{z\bar{z}_0}{R^2} \right) \right\} \tag{6.13}$$

for the case of $N = 0$ on the circular boundary, and

$$G(z, z_0) = \frac{1}{2\pi k} \mathrm{Re}\left\{ \ln\left(\frac{z - z_0}{R} \right) \right\} + \frac{1}{2\pi k} \mathrm{Re}\left\{ \ln\left(\frac{R^2 - z\bar{z}_0}{Rz} \right) \right\} \tag{6.14}$$

for the case of $\partial N / \partial n = 0$ on the circular boundary, where R denotes the radius of the embedded hole.

6.3.3. Special fundamental solutions for inclusion in a plate

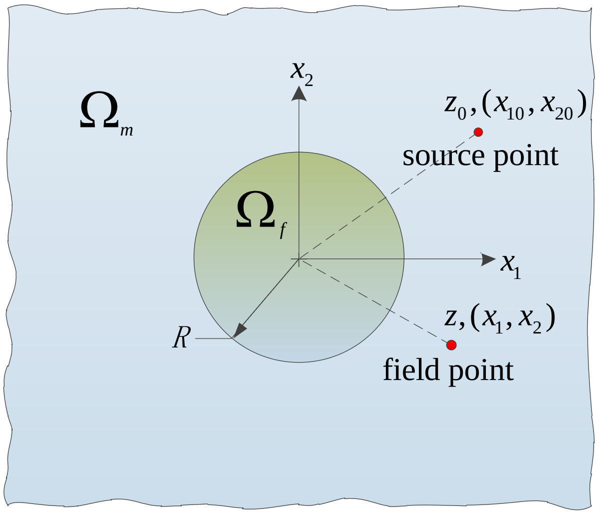

Figure 6.4 Schematic for the definition of special fundamental solutions (inclusion) of plane heat conduction in fiber-reinforced composites.

When a central circular inclusion is embedded in an infinite domain Ω_{m}, if a unit heat source is applied at the source point z_0 in Ω_{m}, as shown in Figure 6.4, the temperature responses G_{m} and G_{f} at any field point z in matrix or fiber regions can be obtained by using complex potential theory, considering the interface ($|z| = R$) continuity conditions between inclusion and matrix as (Chao and Shen 1997)

$$\begin{cases} G_{\mathrm{m}} = -\dfrac{1}{2\pi k_{\mathrm{m}}}\left[\mathrm{Re}[\ln(z-z_0)] + \dfrac{k_{\mathrm{m}}-k_{\mathrm{f}}}{k_{\mathrm{m}}+k_{\mathrm{f}}}\mathrm{Re}[\ln(\dfrac{R^2}{z}-\bar{z}_0)]\right] & z \in \Omega_{\mathrm{m}} \\ G_{\mathrm{f}} = -\dfrac{1}{(k_{\mathrm{m}}+k_{\mathrm{f}})\pi}\mathrm{Re}[\ln(z-z_0)] & z \in \Omega_{\mathrm{f}} \end{cases} \tag{6.15}$$

Similarly, the induced temperature G_{m} in the matrix shows proper singular behavior at the source point z_0, while G_{f} in the fiber is regular because the source point z_0 is outside the fiber.

6.4. FORMULATIONS OF THE HFS-FEM FOR HEAT TRANSFER PROBLEMS

The HFS-FEM, originated from the HT-FEM, utilizes two independent approximate fields: an intra-element field and an independent frame field along the element boundary. But, unlike the HT-FEM, intra-element fields in the HFS-FEM are constructed based on the fundamental solutions, rather than a truncated T-complete function set. In this section, the solution procedures of the HFS-FE model with the fundamental solutions as interior approximation functions are described for solving linear heat transfer problems of composite materials.

6.4.1. Intra-element field

For a particular element $\mathbf{e}$, which occupies sub-domain Ω_e, assume that the temperature field defined in the element domain is approximated by a linear combination of foundational solutions at different source points located outside the element domain (see Figure 6.5)

$$\theta_e(\mathbf{x}) = \sum_{j=1}^{n_s} N(\mathbf{x}, \mathbf{y}_{sj}) c_j = \mathbf{N}_e(\mathbf{x}) \mathbf{c}_e \qquad (\forall \mathbf{x} \in \Omega_e, \mathbf{y}_{sj} \notin \Omega_e) \tag{6.16}$$

where n_s is the number of source points outside the element domain, which is equal to the number of nodes of an element in the present research based on the generation approach of the source points, $\mathbf{c_e}$ is an unknown coefficient vector (not nodal temperature), $\mathbf{N_e}$ is the fundamental solution matrix, which can be written as

$$\mathbf{N_e} = \left[G_1^*(\mathbf{x}, \mathbf{y}_{s1}) \quad G_2^*(\mathbf{x}, \mathbf{y}_{s2}) \quad \dots \quad G_{n_s}^*(\mathbf{x}, \mathbf{y}_{sn_s}) \right] \tag{6.17}$$

$$\mathbf{c_e} = [c_1 \quad c_2 \quad \dots \quad c_{n_s}]^T \tag{6.18}$$

It should be pointed out that $G_i(\mathbf{x}, \mathbf{y}_{sj})$ represents the corresponding fundamental solution

$$G_i(\mathbf{x}, \mathbf{y}_{sj}) = \begin{cases} G_{\mathrm{m}}(\mathbf{x}, \mathbf{y}_{sj}) & \mathbf{x} \in \Omega_{\mathrm{m}} \\ G_{\mathrm{f}}(\mathbf{x}, \mathbf{y}_{sj}) & \mathbf{x} \in \Omega_{\mathrm{f}} \end{cases} \tag{6.19}$$

It is noted that since the fundamental solutions already include the presence of the interface between filler and matrix, it is not necessary to model the temperature and heat flux continuity conditions on the interface; thus the analysis is simplified. One of the advantages in the HFS-FEM is that it reduces computation effort by using special-purpose elements. Furthermore, due to the use of two groups of independent interpolation functions in the HFS-FEM, it is possible to construct arbitrarily shaped elements for use in analysis, as shown in Figure 6.5.

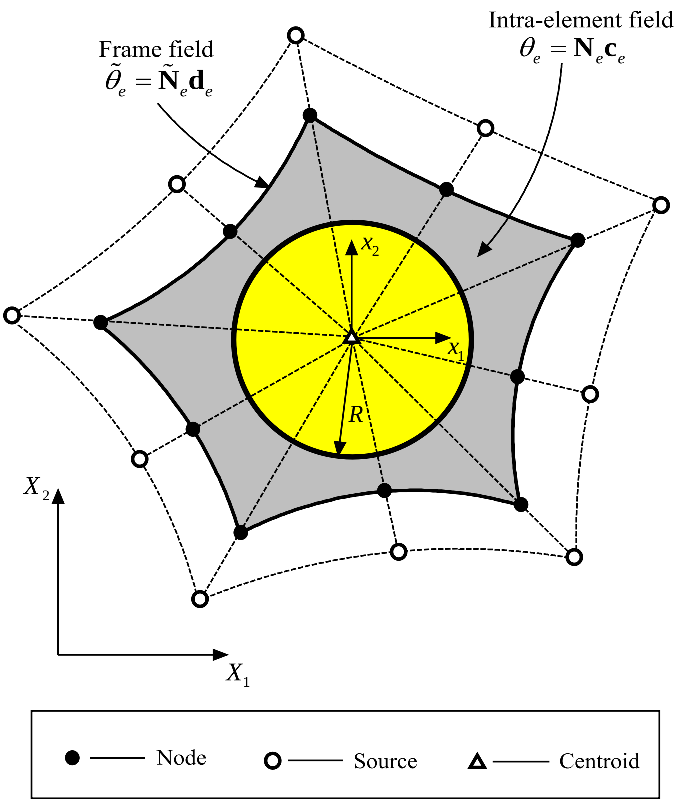

Figure 6.5 Intra-element field, frame field in a special element of HFS-FEM, and the generation of its source points.

For a particular element as shown in Figure 6.5, the nodes of the element can be used to generate related source points for simplicity, so that the singular sources are located on the pseudo boundary to achieve a certain numerical stability. Practically, the source point $\mathbf{y}_{sj}\,(j = 1, 2, \ldots, n_s)$ can be generated by means of the following method (Wang and Qin 2010a)

$$\mathbf{y}_s = \mathbf{x}_0 + \gamma(\mathbf{x}_0 - \mathbf{x}_c) \tag{6.20}$$

where γ is a dimensionless coefficient, $\mathbf{x}_0$ is the point on the element boundary (the nodal point in this work)and $\mathbf{x}_c$ is the geometrical centroid of the element.

The corresponding outward normal derivative of u_e on Γ_e is

$$h_e = -k\frac{\partial \theta_e}{\partial n} = \mathbf{Q}_e \mathbf{c}_e \tag{6.21}$$

where

$$\mathbf{Q}_e = -k\frac{\partial \mathbf{N}_e}{\partial n} = -k\mathbf{n}\mathbf{T}_e \tag{6.22}$$

with

$$\mathbf{T}_e = \begin{bmatrix} \dfrac{\partial \mathbf{N}_e}{\partial x_1} & \dfrac{\partial \mathbf{N}_e}{\partial x_2} \end{bmatrix}^{\mathrm{T}} \tag{6.23}$$

6.4.2. Auxiliary frame field

To enforce conformity on the field variable θ, for instance, $\theta_e = \theta_f$ on $\Gamma_e \cap \Gamma_f$ of any two neighboring elements *e* and *f*, an auxiliary inter-element frame field $\tilde{\theta}$ is used and expressed in terms of nodal displacement vector, $\mathbf{d}_e$, as used in conventional FEM. In this case, $\tilde{\theta}$ is confined to the whole element boundary, that is,

$$\tilde{\theta}_e(\mathbf{x}) = \tilde{\mathbf{N}}_e(\mathbf{x})\mathbf{d}_e \qquad \mathbf{x} \in \Gamma_e \tag{6.24}$$

which is independently assumed along the element boundary in terms of nodal DOF $\mathbf{d}_e$, where $\tilde{\mathbf{N}}_e$ represents the conventional finite element interpolating functions. For example, a simple interpolation of the frame field on the side with three nodes of a particular element can be given in the form

$$\tilde{\theta} = \tilde{N}_1\theta_1 + \tilde{N}_2\theta_2 + \tilde{N}_3\theta_3 \tag{6.25}$$

where $\tilde{N}_i$ ($i = 1, 2, 3$) stands for shape functions in terms of the natural coordinate ξ.

6.4.3. Hybrid variational functional

For the boundary value problem defined in Eq. (6.1) and Eq. (6.2), since the stationary conditions of the traditional potential or complementary variational functional cannot guarantee the required inter-element continuity condition in the HFS-FE model, a modified potential functional is developed as follows

$$\Pi_m = \sum_e \Pi_{me} \tag{6.26}$$

with

$$\Pi_{me} = -\frac{1}{2}\int_{\Omega_e} k\theta_{,i}\theta_{,i}\mathrm{d}\Omega - \int_{\Gamma_{qe}} \bar{h}\tilde{\theta}\mathrm{d}\Gamma + \int_{\Gamma_e} h\left(\tilde{\theta} - \theta\right)\mathrm{d}\Gamma \tag{6.27}$$

in which the governing equation Eq.(6.1) is assumed to be satisfied a priori. The boundary Γ_e of a particular element consists of the following parts

$$\Gamma_e = \Gamma_{\theta e} \cup \Gamma_{he} \cup \Gamma_{Ie} \tag{6.28}$$

where Γ_{Ie} represents the inter-element boundary of the element '*e*'.

Appling the divergence theorem, the domain integral can be eliminated to obtain the final form of the functional for the HFS-FE model

$$\Pi_{me} = -\frac{1}{2}\int_{\Gamma_e} h\theta \mathrm{d}\Gamma - \int_{\Gamma_{qe}} \bar{h}\tilde{\theta}\mathrm{d}\Gamma + \int_{\Gamma_e} h\tilde{\theta}\mathrm{d}\Gamma \tag{6.29}$$

Finally, substituting Eqs. (2.53), (2.56) and (2.59) into the functional (2.77) produces

$$\Pi_e = -\frac{1}{2}\mathbf{c}_e^{\mathrm{T}}\mathbf{H}_e\mathbf{c}_e - \mathbf{d}_e^{\mathrm{T}}\mathbf{g}_e + \mathbf{c}_e^{\mathrm{T}}\mathbf{G}_e\mathbf{d}_e \tag{6.30}$$

in which

$$\mathbf{H}_e = \int_{\Gamma_e} \mathbf{Q}_e^{\mathrm{T}}\mathbf{N}_e\mathrm{d}\Gamma \qquad \mathbf{G}_e = \int_{\Gamma_e} \mathbf{Q}_e^{\mathrm{T}}\tilde{\mathbf{N}}_e\mathrm{d}\Gamma \qquad \mathbf{g}_e = \int_{\Gamma_{eq}} \tilde{\mathbf{N}}_e^{\mathrm{T}}\bar{h}\mathrm{d}\Gamma$$

To enforce inter-element continuity on the common element boundary, the unknown vector $\mathbf{c}_e$ should be expressed in terms of nodal DOF $\mathbf{d}_e$. Minimization of the functional Π_e with respect to $\mathbf{c}_e$ and $\mathbf{d}_e$, respectively, yields

$$\begin{aligned} \frac{\partial \Pi_e}{\partial \mathbf{c}_e^{\mathrm{T}}} &= -\mathbf{H}_e\mathbf{c}_e + \mathbf{G}_e\mathbf{d}_e = \mathbf{0} \\ \frac{\partial \Pi_e}{\partial \mathbf{d}_e^{\mathrm{T}}} &= \mathbf{G}_e^{\mathrm{T}}\mathbf{c}_e - \mathbf{g}_e = \mathbf{0} \end{aligned} \tag{6.31}$$

from which the optional relationship between $\mathbf{c}_e$ and $\mathbf{d}_e$, and the stiffness equation can be produced

$$\mathbf{c}_e = \mathbf{H}_e^{-1}\mathbf{G}_e\mathbf{d}_e \tag{6.32}$$

and

$$\mathbf{K}_e\mathbf{d}_e = \mathbf{g}_e \tag{6.33}$$

where $\mathbf{K}_e = \mathbf{G}_e^{\mathbf{T}}\mathbf{H}_e^{-1}\mathbf{G}_e$ stands for the symmetric element stiffness matrix. The evaluation of the vector $\mathbf{g}_e$ in Eq. (6.33) is the same as that in the conventional FEM, which is obviously convenient for the implementation of HFS-FEM into an existing FEM program. The matrix $\mathbf{H}_e$, $\mathbf{G}_e$ and vector $\mathbf{g}_e$ can be calculated by the commonly used Gaussian numerical integration as described for potential problems in Chapter 2.

6.4.4. Recovery of rigid-body motion

Considering the physical definition of the fundamental solution, it is necessary to recover the missing rigid-body motion modes from the above results. Following the method presented by (Qin 2000), the missing rigid-body motion can be recovered by writing the internal potential field of a particular element *e* as

$$\theta_e(\mathbf{x}) = \mathbf{N}_e(\mathbf{x})\mathbf{c}_e + c_0 \tag{6.34}$$

where the undetermined rigid-body motion parameter c_0 can be calculated using the least square matching of θ_e and $\tilde{\theta}_e$ at element nodes

$$\sum_{i=1}^{n}\left[\theta_e(\mathbf{x})-\tilde{\theta}_e(\mathbf{x})\right]^2=\min \tag{6.35}$$

which finally gives

$$c_0=\frac{1}{n}\sum_{i=1}^{n}\Delta\theta_{ei} \tag{6.36}$$

in which $\Delta\theta_{ei}=\left(\tilde{\theta}_e-\mathbf{N}_e\mathbf{c}_e\right)\Big|_{\text{node } i}$ and n is the number of element nodes. Once the nodal field is determined by solving the final stiffness equation, the coefficient vector $\mathbf{c}_e$ can be evaluated from Eq. (6.16), and then c_0 is evaluated from Eq. (6.36). Finally, the temperature field θ at any internal point in an element can be determined by means of Eq. (6.34).

6.5. NUMERICAL EXAMPLES AND DISCUSSION

In this section, numerical experiments are conducted to demonstrate the performance and efficiency of the HFS-FEM and also to study the micro-thermal behavior of composites. Evaluating the effective thermal conductivity of composites implies a homogenization procedure that requires the application of several independent loading conditions on the RVE of the heterogeneous materials (Zohdi and Wriggers 2008). In the present work, a temperature gradient controlled method is employed to conduct the necessary tests. Resolving the heat flux field in heterogeneous materials through a steady-state heat transfer analysis allows calculation of the average flux field component $\bar{q}$. Since the average temperature gradient $\bar{g}$ is imposed, the effective thermal conductivity coefficient k^* for the equivalent homogeneous material can be directly calculated from Eq. (6.6).

In the following two examples, effective properties of two-phase composite materials are investigated by means of the HFS-FEM. It is assumed that both fiber and matrix are linear thermal conductive and that they are perfectly bonded at their interface. No complex inclusion geometry is included in the RVEs and the problem of how to generate realistic RVE micro-level geometry for numerical analysis is not discussed in the present work.

6.5.1. RVE with one reinforced fiber

In the first example, a square RVE with only one fiber as shown in Figure 6.6 is investigated by the proposed method. The thermal conductivities of the fiber and matrix are respectively assumed as $k_2 = 20$, and $k_1 = 1$. The mismatch ratio between fiber and matrix $m = k_2 / k_1 = 20$ is maintained in this analysis unless otherwise specified. For verification and comparison purposes, the numerical results from traditional FEM (ABAQUS) are also given in the analysis. It should be pointed out that a constant temperature gradient $G = [1,0]^T$ or $G = [0,1]^T$ is applied during analysis and the periodic boundary condition (PR-BC) illustrated in Section 2 is employed for both the HFS-FEM and ABAQUS modeling.

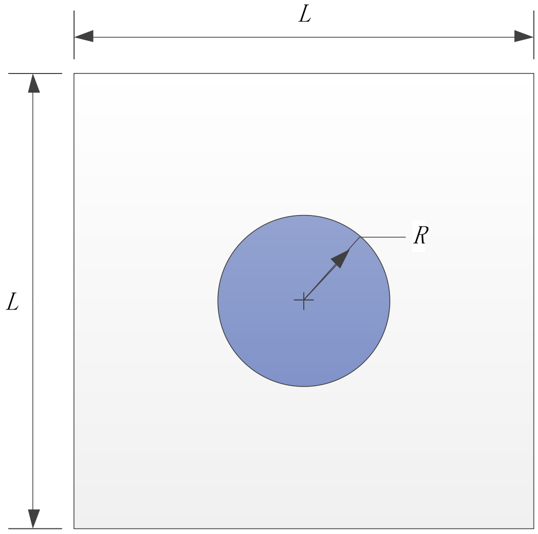

Figure 6.6 Schematic of RVE containing one central fiber.

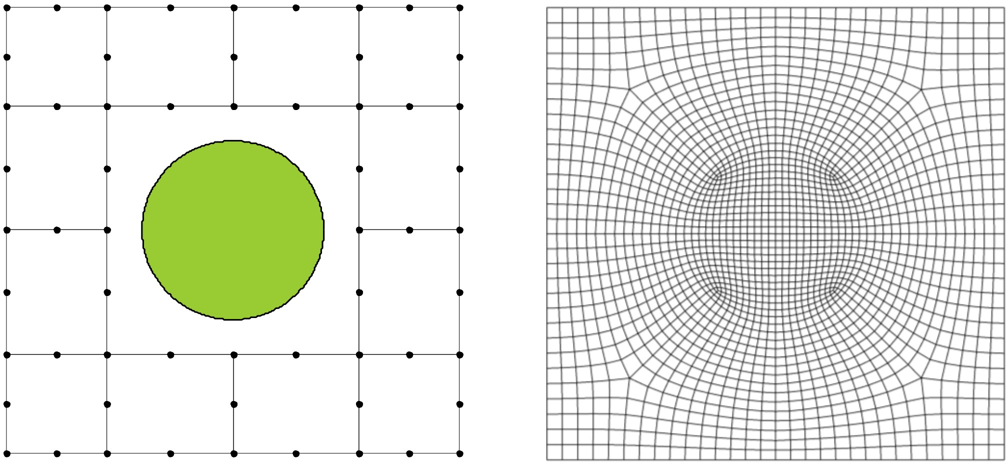

Figure 6.7 Mesh configurations for RVE by (a) HFS-FEM with special element (white: matrix, green: fiber) and by (b) ABAQUS.

6.5.1.1. Convergence verification of the method

Before employment of the HFS-FEM for heat transfer analysis of composite materials, a convergence study is first carried out by checking against the variables of interest. Three different meshes are employed: Mesh 1 (12 8-node elements and one 16-node special element, with a total of 60 nodes), Mesh 2 (32 8-node elements and one 16-node special elements, with a total of 128 nodes), and Mesh 3 (61 8-node elements and one 16-node special element with a total of 220 nodes). The results calculated by ABAQUS (FEM) using a very fine mesh (as shown in Figure 6.7,1940 3D8R elements with 5941 nodes) are provided as a reference benchmark for comparison.

Figure 6.8 presents the effective thermal conductivities k^* with the variation of the number of element meshes or nodes. It is evident that the results obtained from the HFS-FEM converge to the benchmark values with the increase in the number of DOF. It is also notable that, using only 128 nodes, HFS-FEM has similar accuracyto that from ABAQUS using thousands of nodes.

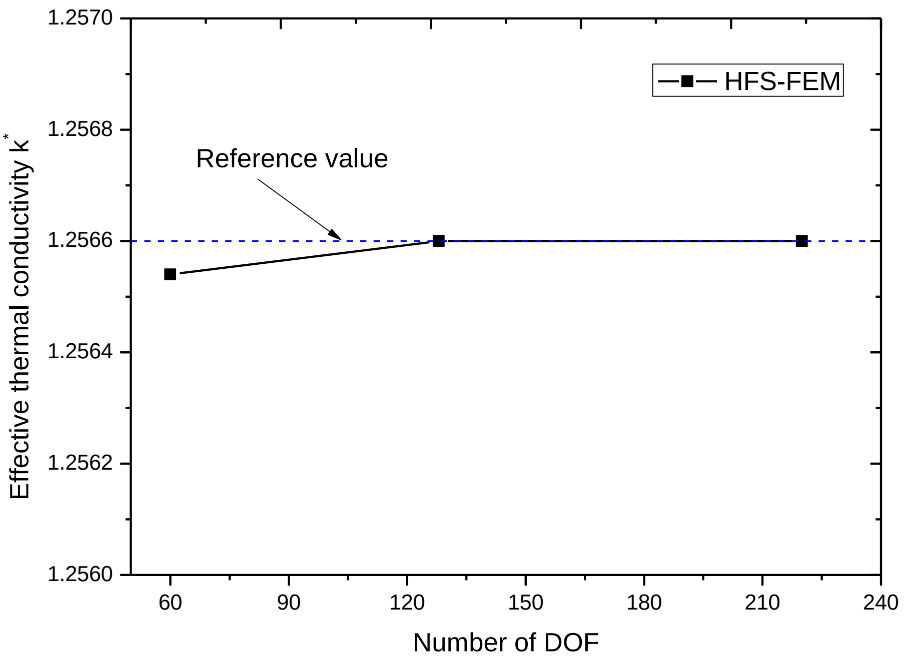

Figure 6.8 RVE with one central fiber: Convergence of the effective thermal conductivity.

6.5.1.2. Effect of fiber volume fraction

The FVF has a significant influence on the overall thermal conductivity of heterogeneous composites. In this section, the effect of FVF on the macroscopic effective thermal conductivities k^* of the composite is investigated. The FVF is modified from 3.14% to 63.62% by varying the radius of the fiber. The predicted effective thermal conductivities from HFS-FEM are graphically shown in Figure 6.9. It can be observed, as expected, that effective thermal conductivities k^* rises along with the increase in FVF. However, the rate of increase becomes greater as the FVF increases. When the fiber volume fraction increases to 63.62%, the effective thermal conductivity k^* is more than four times that of the thermal conductivity of the matrix material. It is also observed from Figure 6.9 that for all the cases investigated here, better accuracy can be achieved by HFS-FEM with special elements than from ABAQUS.

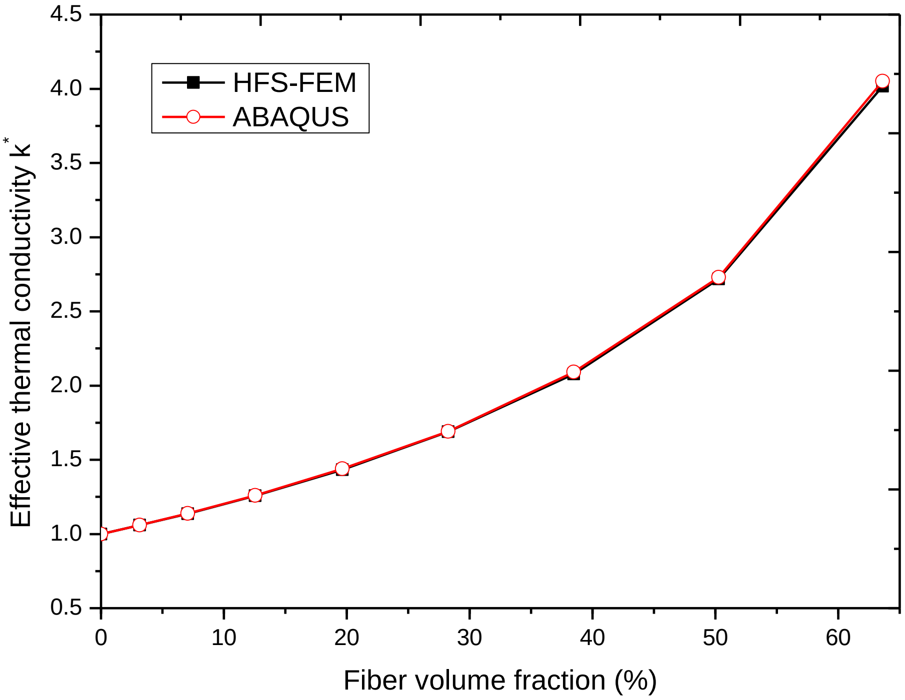

Figure 6.9 Effective thermal conductivity *k* of composite for different FVFs.

Compared to the results obtained from ABAQUS, which are achieved by refined meshes around and within the fiber, the specially-purpose inclusion elements achieved good accuracy. This conclusion is also confirmed by Figure 6.10 and Figure 6.11, which presents the variations of the effective thermal conductivities k^* with the change of materials mismatch ratio $m = k_2 / k_1$.

6.5.1.3. Effect of material mismatch ratio

Figure 6.10 shows the effective thermal conductivity k^* of the heterogeneous composite for different material mismatch ratios when the thermal conductivity k_2 of the fiber is greater than the thermal conductivity k_1 of the matrix, i.e. a conductive fiber embedded into an insulated matrix. The FVF is kept constant at 19.63%, i.e. R=2.5. It can be seen from Figure 6.10 that for a defined matrix, the effective thermal conductivity increases with the increase in conductivity of the fiber, and the heat conduction performance can be dramatically improved when adding the conductive fiber but the effect weakens when the thermal conductivity of the fiber is more than 20 times that of the matrix. For comparison, the predicted results obtained from

ABAQUS are also involved in Figure 6.10. The same conclusion can be drawn from the results, and both methods provide equivalent accuracy.

Figure 6.11 presents the variation of the effective thermal conductivity k^* for the different material mismatch ratios when the thermal conductivity k_2 of the fiber is lower than the thermal conductivity k_1 of the matrix, i.e. an insulate fiber embedded in a conductive matrix. The FVF is also kept constant at 19.63%. It is obvious that a nearly linear relationship between effective thermal conductivity k^* and the matrix thermal conductivity k_1 is found, which is different from the nonlinearity shown in Figure 6.10.

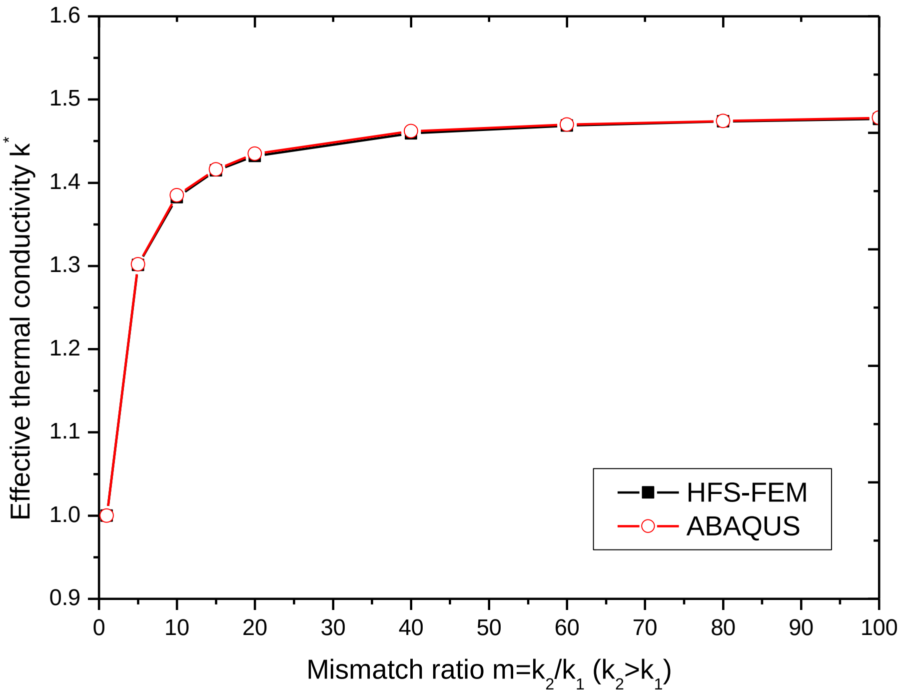

Figure 6.10 Effective thermal conductivity k^* of the composite for different mismatch ratios when $k_2 > k_1$.

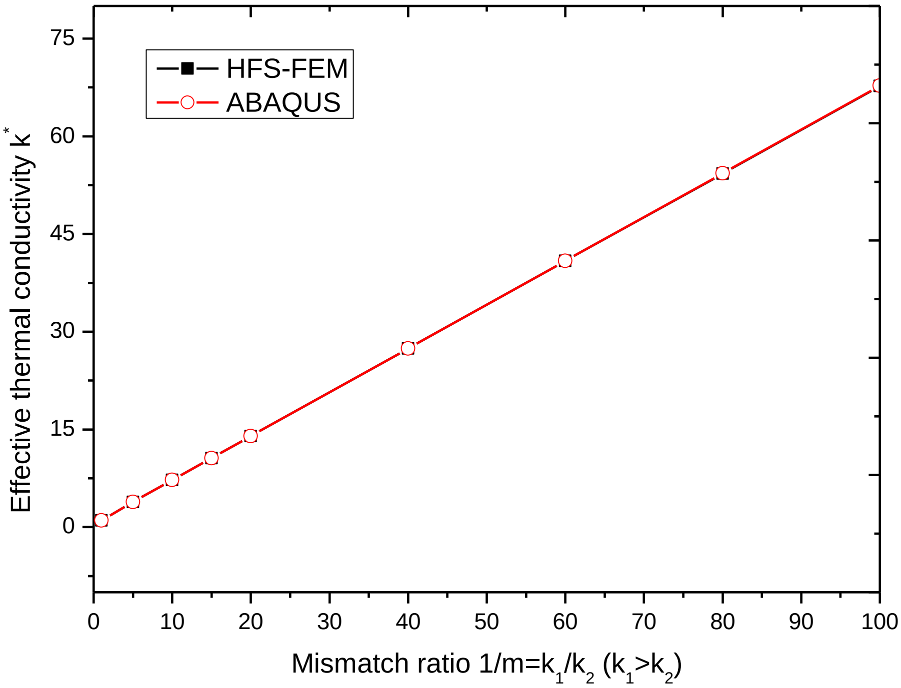

Figure 6.11 Effective thermal conductivity k^* of the composite for different mismatch ratios when $k_1>k_2$.

Contour plots of the temperature and heat flux distributions in the RVE under constant temperature gradient and periodic boundary conditions are shown in Figure 6.12 and Figure 6.13, in which the FVF is defined as 19.63%. It can be seen from Figure 6.12 that for the more conductive fiber the heat flux mainly passes through the fiber, whereas for the insulated fiber with lower conductivity than that of the matrix, most flux will be carried out through the matrix (Figure 6.13).

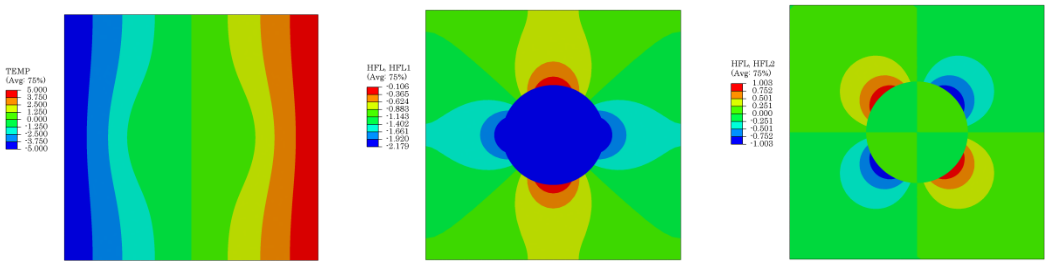

Figure 6.12 Contour plots of the temperature and heat flux distribution in the RVE (m=20, FVF=19.63%).

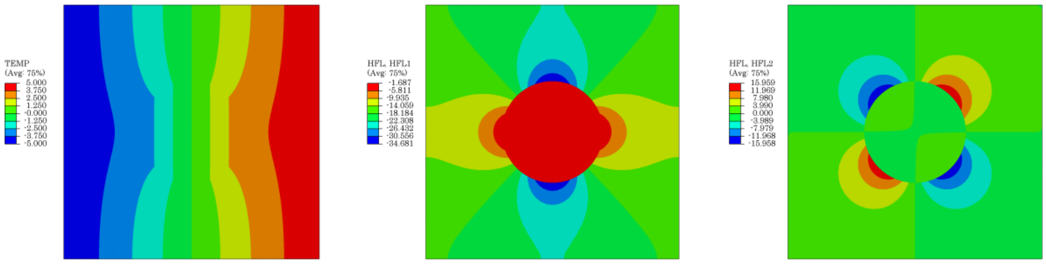

Figure 6.13 Contour plots of the temperature and heat flux distribution in the RVE (1/m=20, FVF=19.63%).

6.5.2. RVE with multiple-fibers

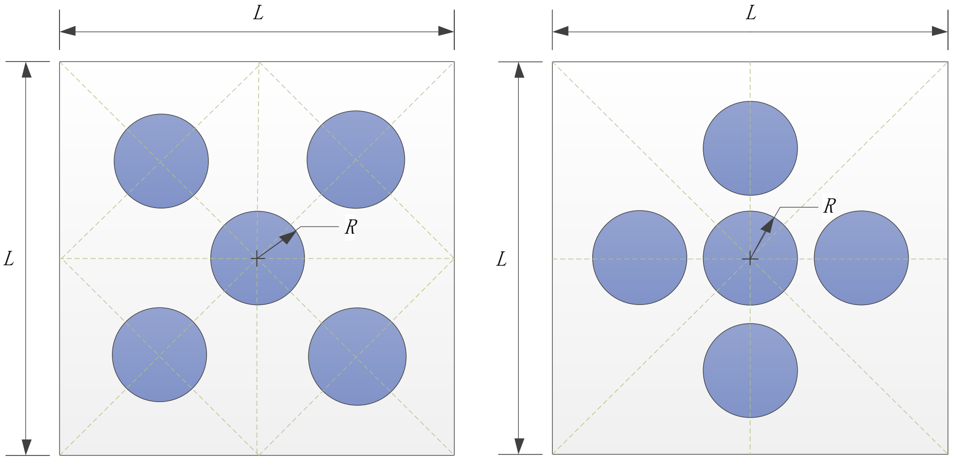

(a) (b)

Figure 6.14 RVEs of the composite with two different fiber configurations.

Two different fiber patterns as shown in Figure 6.14 are investigated to reveal the effect of fiber configuration on the effective thermal properties of heterogeneous composites. The geometry and dimensions of the RVEs are given in Figure 6.14 for Pattern 1 (a) and Pattern 2 (b), in which L=10 and R=1. In the two cases, the FVF is kept constant at 15.71%. The mesh configuration of the RVEs for HFS-FEM is shown in Figure 6.15, in which the 16-node special element (i.e. 8-edges) for fibers is employed. Mesh configurations of the RVEs for ABAQUS are shown in Figure 6.16.

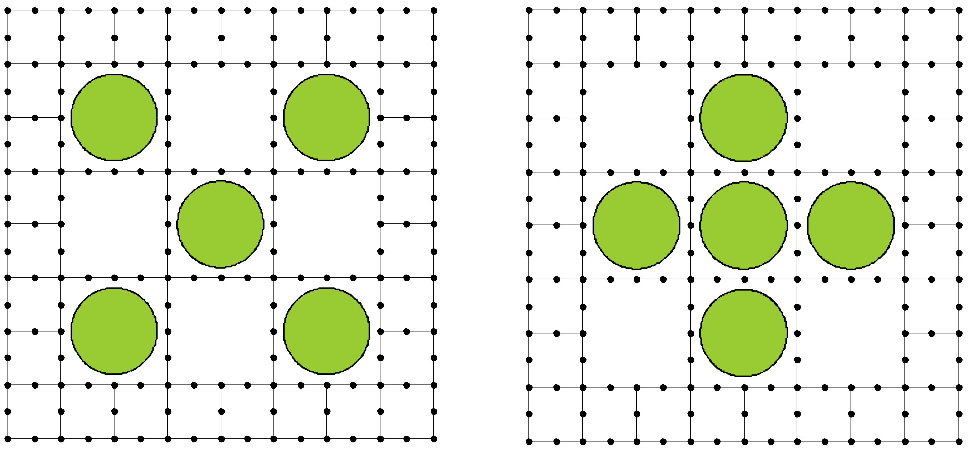
(a) (b)

Figure 6.15 Mesh configurations of the RVEs for HFS-FEM.

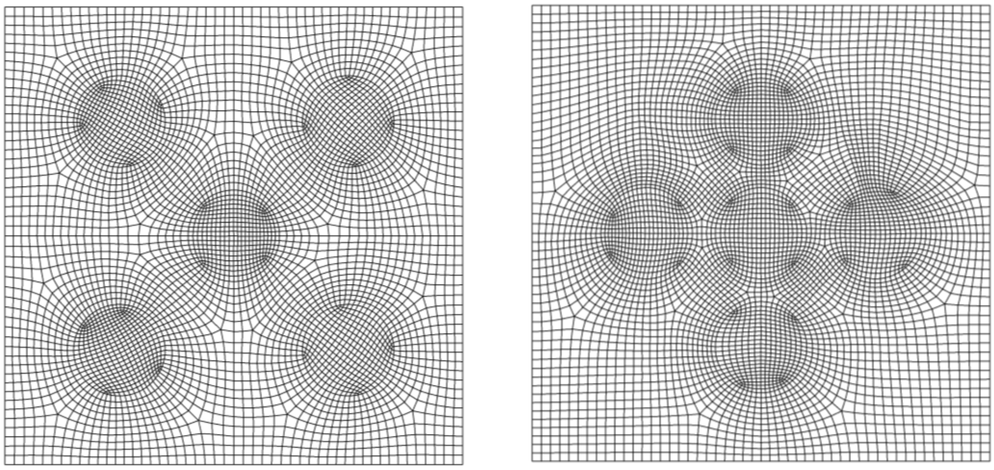
(a) (b)

Figure 6.16 Mesh configurations of the RVEs for ABAQUS.

6.5.2.1. Effect of material mismatch ratio

The predicted effective thermal conductivities k^* of the two-phase composites by the HFS-FEM for the two different patterns are given in Figure 6.17 and Figure 6.18, respectively. For the case of conductor embedded in an insulated matrix, i.e. $k_2>k_1$, Figure 6.17 shows that for both patterns the effective thermal conductivity k^* increases with the increase in fiber thermal conductivity k_2 and the rate of increase is dramatic between 1 and 20, then tends to be smoother. The relationship between effective thermal conductivities k^* and mismatch ratio m is nonlinear. When the thermal conductivity k_2 of the fiber is 20 times of that of the matrix, the effective thermal conductivity k^* of the composites, compared with the pure matrix materials, increases by 33.3% for Pattern 1 and 35.2% for Pattern 2. It is obvious from Figure 6.17 that the effective thermal conductivity k^* of Pattern 2 is slightly better than that of Pattern 2, and the beneficial influence becomes clearer as the mismatch ratio becomes larger (m>20).

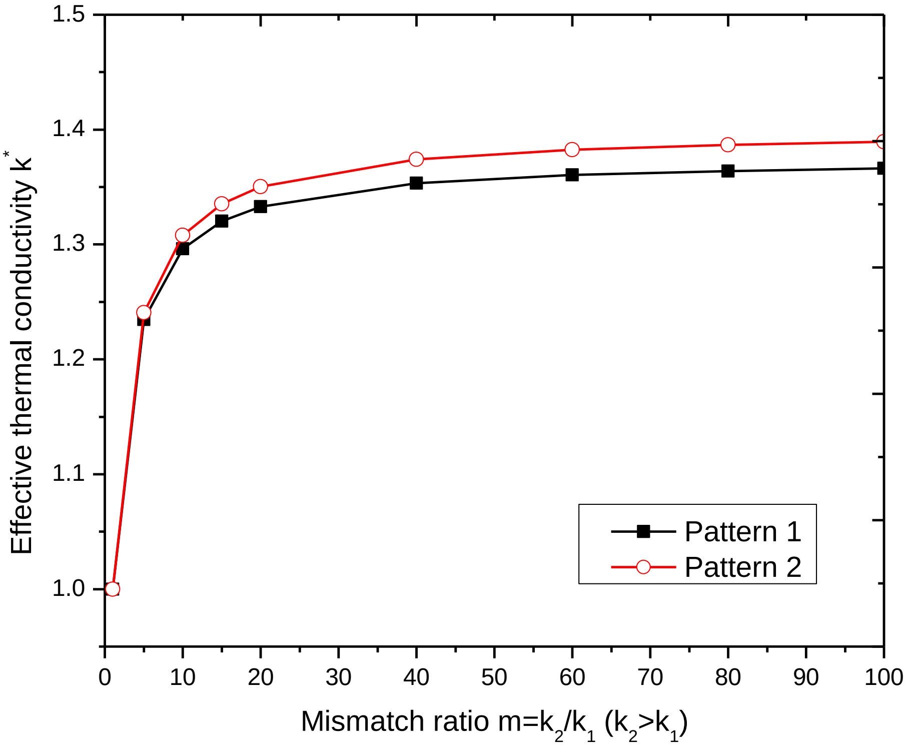

Figure 6.17 Effective thermal conductivity k^* of the composite for different mismatch ratios when $k_2>k_1$.

For the case of an insulated fiber embedded in a conductor matrix, i.e. $k_2<k_1$, Figure 6.18 shows that the effective thermal conductivity k^* for both patterns increases linearly with the matrix thermal conductivity k_1 if k_2 is fixed as a constant, which is completely different from the former case of nonlinearity. In this case, the thermal property of the matrix has a significant influence on the overall material property. The matrix conductivity reduces by 26.80% for Pattern 1 and 28.02% for Pattern 2, when the thermal conductivity k_1 of the matrix is 100 times that of the fiber. It can be observed from Figure 6.18 that the effective thermal conductivity k^* of Pattern 1 is

slightly better than that of Pattern 2; in other words, the conductivity reduction effect of Pattern 2 is slightly superior to that of Pattern 1, like the increasing effect for the case of $k_2>k_1$.

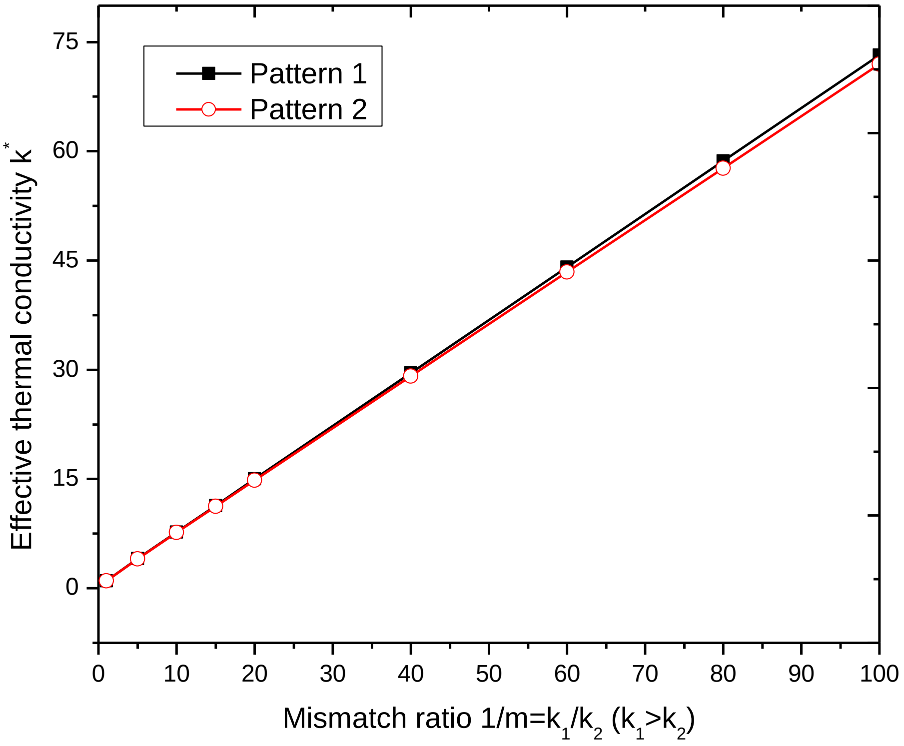

Figure 6.18 Effective thermal conductivity k^* of the composite for different mismatch ratios when $k_1>k_2$.

6.5.2.2. Effect of fiber pattern

Figure 6.19 presents the contour plots of the temperature distribution and heat flux components across the RVE when m=20 and the FVF is 15.71%. It is obvious that the fiber inclusions have a significant influence on the heat flux distribution in the RVE, and that the heat fluxes are concentrated through the fibers when a fiber appears at an intersection. Clearly, most of the heat is conveyed through the fibers in the composite when the thermal conductivity of the fiber is higher than that of the matrix. Conversely, Figure 6.20 shows that insulated fibers expel the heat flux to the matrix and most flux travels through the matrix, not the fiber. This phenomenon is much more significant for Pattern 2 than for Pattern 1. Numerical results in the above modeling also show that the results from HFS-FEM are in good agreement with those from

ABAQUS although much fewer meshes are employed by the HFS-FEM. It can be concluded that the proposed method is accurate and efficient in analyzing micro heat transfer problems.

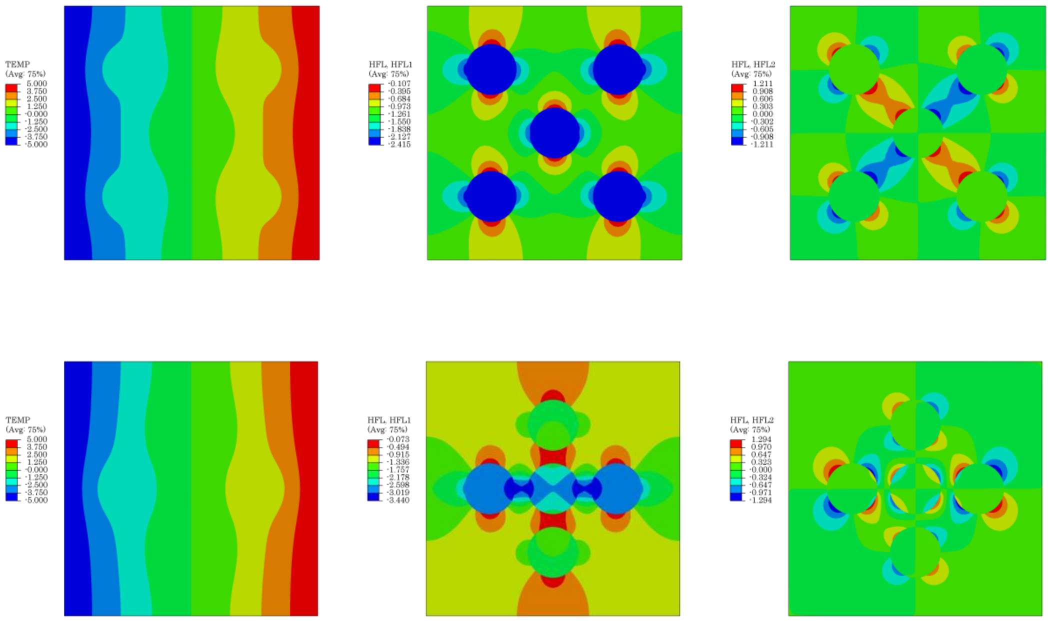

Figure 6.19 Contour plots of temperature and heat flux distribution in the RVE (m=20, FVF=15.71%).

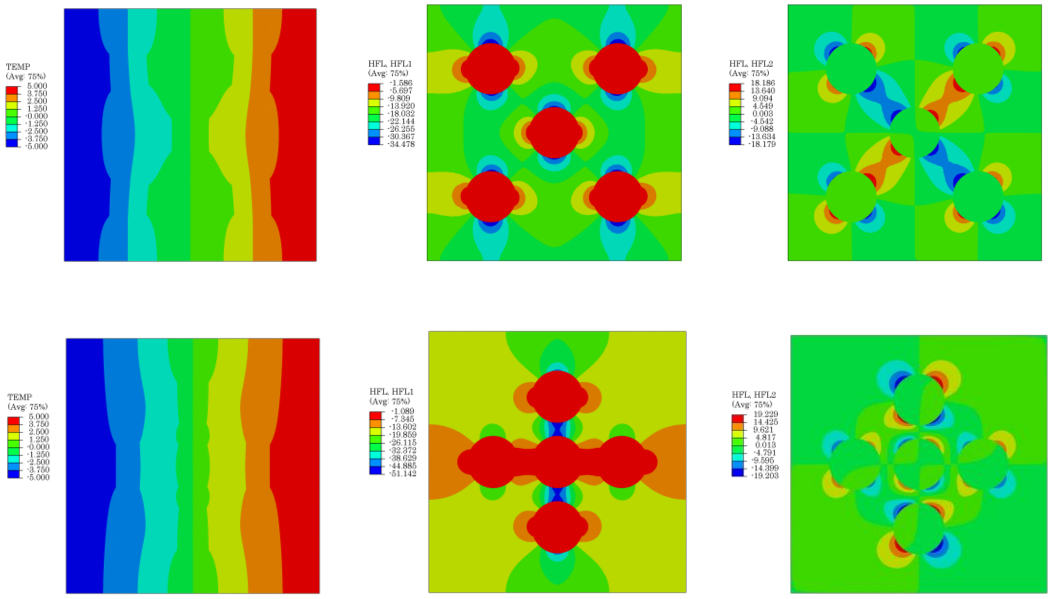

Figure 6.20 Contour plots of temperature and heat flux distribution in the RVE (1/m=20, FVF=15.71%).

6.6. SUMMARY

In this chapter, the HFS-FEM method is successfully applied to heat transfer problems of heterogeneous composites. The two independent intra-element and frame fields facilitate the construction of arbitrary-shaped elements and the modified variational functional for stiffness matrix derivation involves the element boundary integral only. Based on the special fundamental solution, a type of special element involving the inclusion/fiber is proposed for mesh reduction in analyzing heterogeneous composites.

The effective thermal conductivity of composites is evaluated through the RVEs with single or multiple fibers using the homogenization technique. The method is used to investigate the effect of fiber volume fraction and the mismatch ratio between fiber and matrix in the composites. Numerical results show that the proposed method is accurate and efficient in simulating the heat transfer problem. The employment of special elements significantly reduces the meshing effort and computing cost of the model, also obviating the need for mesh regeneration when the fiber volume fraction changes slightly. It can be concluded that the proposed micromechanical models based on the HFS-FEM have the potential to model fiber-reinforced composites and to be further developed for multi-scale simulation in future work.

Chapter 7. HFS-FEM for 2D and 3D Thermo-elasticity Problems

7.1. INTRODUCTION

Problems of thermoelasticity arise in many practical applications such as those encountered in the design of steam and gas turbines, jet engines, rocket motors and nuclear reactors. Thermal stress induced in such structures is one of the important concerns in product design and analysis. General thermoelasticity is governed by two time-dependent coupled differential equations: the heat conduction equation and the Navier equation with thermal body force (Henry and Banerjee 1988). In most practical engineering applications, the coupling term of the heat equation and the inertia term in Navier equation are generally negligible (Henry and Banerjee 1988). Consequently, most analyses employ the uncoupled thermo-elasticity theory, which is adopted in the present research.

Currently, numerical methods such as the FEM are widely employed to investigate thermoelasticity problems (Bahtui and Eslami ; R.J 1993; Aubry, Lucas et al. 1999; Carrazedo and Coda 2010; Solin, Cerveny et al. 2010). Despite many attractive features of FEM, it is still a nontrivial and time consuming task for complex domains, particularly for 3D problems. One alternative to circumvent this difficulty is to use the BEM, which requires only boundary discretization rather than domain discretization (Sládek and Sládek 1984; Chaudouet 1987; Shiah and Lin 2003). However, the treatment of singular or near-singular boundary integrals is usually quite tedious and inefficient and an extra boundary integral equation is also required to evaluate the fields inside the domain; additionally, for multi-domain problems, implementation of the BEM becomes quite complex and the nonsymmetrical coefficient matrix of the resulting equations offsets its advantages (Qin 2000; Qin 2004). Recently, a combination of the MFS and the dual reciprocity method has been utilized to solve 2D thermoelasticity with general body forces (de Medeiros, Partridge et al. 2004) and 3D thermoelasticity (Tsai 2009).

In the past three decades, HT-FEM a significant alternative to traditional FEM, has become popular and has been increasingly used to analyze various engineering problems (Jirousek and Guex 1986; Jirousek and Qin 1995; Qin 2003; Qin 2005; Wang, Qin et al. 2007; de Freitas and Toma 2009; Sze and Liu 2010; de Freitas and Moldovan 2011). However, the terms of truncated T-complete functions in HT-FEM must be carefully selected to achieve the desired results and the T-complete functions for some physical problems are difficult to develop (Qin 2000; Qin and Wang 2008). To overcome these drawbacks of HT-FEM, the HFS-FEM was developed for solving 2D heat conduction problem in single and multilayer-materials (Wang and Qin 2009; Wang and Qin 2010a) and isotropic elastic problems (Wang and Qin 2010b). The advantages of the method have been addressed in the previous chapters (Qin 2003; Gao, Wang et al. 2005; Dhanasekar, Han et al. 2006).

In this chapter, a new solution procedure based on the HFS-FEM is proposed to solve 2D and 3D thermoelastic problems with consideration of arbitrary body forces and temperature changes. The method of particular solution is used to decompose the displacement solution into two parts: a homogeneous solution and a particular solution. The homogeneous solution is obtained by using the HFS-FEM with elastic fundamental solutions and the particular solution related to the body force and temperature change is approximated by using the RBF interpolation. Five different numerical examples are presented here to demonstrate the accuracy and versatility of the proposed method. The examples show that, compared with the existing closed-form solutions or ABAQUS results, even when using a very coarse mesh, relatively accurate results can still be obtained by the new method.

This chapter is organized as follows. Section 7.2 reviews the basic equations of thermoelasticity. Sections 7.3 and 7.4 describe the method of particular solution and RBF approximation which are employed to deal with temperature change and body force. In this section, two different approaches are presented to treat this problem. Section 7.5 gives the derivation of the HFS-FEM formulations in detail. In Section 7.6, five numerical examples are presented to demonstrate the validity of the approach. Concluding remarks are given in Section 7.7. The majority of this chapter has been published in a paper (Cao, Yu et al. 2012d) co-authored by the candidate.

7.2. BASIC EQUATIONS FOR THERMOELASTICITY

Consider a finite isotropic material in domain Ω (see Figure 7.1), and let (x_1, x_2, x_3) denote the coordinates in Cartesian coordinate system. The equilibrium governing equations of thermoelasticity with the body force are expressed as

$$\sigma_{ij,j} = -b_i \tag{7.1}$$

where σ_{ij} is the stress tensor, b_i is the body force vector and $i, j = 1,2,3$. The generalized thermoelastic stress-strain relations and the generalized kinematical relation are given as

$$\sigma_{ij,j} = \frac{2G\nu}{1-2\nu}\delta_{ij}e + 2Ge_{ij} - m\delta_{ij}T \tag{7.2}$$

$$e_{ij} = \frac{1}{2}(u_{i,j} + u_{j,i}) \tag{7.3}$$

in which e_{ij} the strain tensor, u_i is the displacement vector, T is the temperature change, G is the shear modulus, ν is the Poisson's ratio, δ_{ij} is the Kronecker delta, and

$$m = 2G\alpha(1+v)/(1-2v) \tag{7.4}$$

is the thermal constant with α the coefficient of linear thermal expansion. By substituting Eqs. (7.2) and (7.3) into Eq. (7.1), the equilibrium equations may be rewritten as

$$Gu_{i,jj} + \frac{G}{1-2\nu}u_{j,ji} = mT_{,i} - b_i \tag{7.5}$$

For a well-posed boundary value problem, the following boundary conditions, either displacement or traction boundary condition, should be prescribed as

$$u_i = \bar{u}_i \quad \text{on } \Gamma_u, \tag{7.6}$$

$$t_i = \bar{t}_i \quad \text{on } \Gamma_t, \tag{7.7}$$

where $\Gamma_u \bigcup \Gamma_t = \Gamma$ is the boundary of the solution domain Ω, $\bar{u}_i$ and $\bar{t}_i$ are the prescribed boundary values, and

$$t_i = \sigma_{ij} n_j , \tag{7.8}$$

is the boundary traction, in which n_j denotes the boundary outward normal.

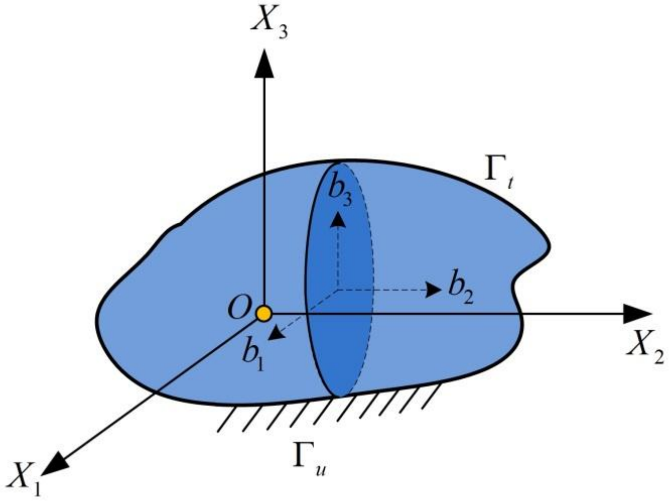

Figure 7.1 Geometrical definitions and boundary conditions for general 3D problems.

7.3. THE METHOD OF PARTICULAR SOLUTION

For the governing equation (7.5) in the previous section, the inhomogeneous term $mT_{,i} - b_i$ can be eliminated by employing the method of particular solution (Henry and Banerjee 1988; Wang, Qin et al. 2007; Wang and Qin 2010b). Using superposition principle, the displacement u_i is decomposed into two parts, the homogeneous solution u_i^h and the particular solution u_i^p as follows:

$$u_i = u_i^h + u_i^p \tag{7.9}$$

in which the particular solution u_i^p should satisfy the governing equation

$$G u_{i,jj}^p + \frac{G}{1-2\nu} u_{j,ji}^p = mT_{,i} - b_i \tag{7.10}$$

but does not necessarily satisfy any boundary condition. It should be pointed out that the solution is not unique and can be obtained by various numerical techniques. However, the homogeneous solution should satisfy

$$G u_{i,jj}^h + \frac{G}{1-2\nu} u_{j,ji}^h = 0 \tag{7.11}$$

with modified boundary conditions

$$u_i^h = \bar{u}_i - u_i^p, \quad \text{on } \Gamma_u \tag{7.12}$$

$$t_i^h = \bar{t}_i + mTn_i - t_i^p, \quad \text{on } \Gamma_t \tag{7.13}$$

From the above equations, it can be seen that once the particular solution u_i^p is known, the homogeneous solution u_i^h in Eq.(7.9) can be solved by Eqs. (7.11)-(7.13). In the following section, radial basis function approximation is introduced to obtain the particular solution, and the HFS-FEM is derived for solving Eqs. (7.11)-(7.13).

7.4. RADIAL BASIS FUNCTION APPROXIMATION

It is usually impossible to find an analytical solution for Eq.(7.10) except for some special cases. As a consequence, RBFs (Golberg, Chen et al. 1999; Cheng, Chen et al. 2001) are used in this analysis to approximate the body force b_i and the temperature field T in order to obtain the particular solution. There are two different ways to implement this approximation: **Method 1** is to treat the body force b_i and the temperature field T separately, as done by Tsai (Tsai 2009). **Method 2** is to treat $mT_{,i} - b_i$ as a whole. However, the performance of the two approaches differs, as discussed in the numerical examples in Section 7.6.

7.4.1. Method 1: Interpolating temperature and body force separately

The body force b_i and temperature T are assumed by the following two equations

$$b_i \approx \sum_{j=1}^{N} \alpha_i^j \varphi^j \quad (\text{i=1,2 in } \Re^2 \text{ and } \text{i=1,2,3 in } \Re^3) \tag{7.14}$$

and

$$T \approx \sum_{j=1}^{N} \beta^j \varphi^j \tag{7.15}$$

where N is the number of interpolation points, φ^j are the basis functions, and α_i^j and β^j are the coefficients to be determined by collocation. Then, the approximate particular solution can be written as follows

$$u_i^p = \sum_{k=1}^{3}\sum_{j=1}^{N} \alpha_i^j \Phi_{ik}^j + \sum_{j=1}^{N} \beta^j \Psi_i^j \tag{7.16}$$

where Φ_{ik}^{j} and Ψ_{i}^{j} are the approximated particular solution kernels. Once the RBF is selected, the problem of finding a particular solution is reduced to solving the following equations

$$G\Phi_{il,kk} + \frac{G}{1-2\nu}\Phi_{kl,ki} = -\delta_{il}\varphi \tag{7.17}$$

$$G\Psi_{i,kk} + \frac{G}{1-2\nu}\Psi_{k,ki} = m\varphi_{,i} \tag{7.18}$$

To solve Eq.(7.17), the displacement is expressed in terms of the Galerkin - Papkovich vectors (A.H.-D 2000; Cheng, Chen et al. 2001)

$$\Phi_{ik} = \frac{1-\nu}{G}F_{ik,mm} - \frac{1}{2G}F_{mk,mi} \tag{7.19}$$

Substituting Eq. (7.19) into Eq. (7.17) yields the following bi-harmonic equation:

$$\nabla^4 F_{il} = -\frac{1}{1-\nu}\delta_{il}\varphi \tag{7.20}$$

Taking the spline type RBF $\varphi = r^{2n-1}$ the following solutions can be obtained:

$$F_{li} = -\frac{\delta_{li}}{1-v}\frac{r^{2n+3}}{(2n+1)^2(2n+3)^2} \quad (\Re^2) \text{ for n=1,2,3\ldots} \tag{7.21}$$

$$\Phi_{li} = A_0\left(A_1\delta_{li} + A_2 r_{,i} r_{,l}\right) \quad (\Re^2) \text{ for n=1,2,3\ldots} \tag{7.22}$$

where

$$\begin{aligned} A_0 &= -\frac{1}{2G(1-v)}\frac{r^{2n+1}}{(2n+1)^2(2n+3)} \\ A_1 &= 5+4n-2v(2n+3) \\ A_2 &= -(2n+1) \end{aligned} \tag{7.23}$$

for 2D problems and

$$F_{li} = -\frac{\delta_{li}}{1-v}\frac{r^{2n+3}}{(2n+1)(2n+2)(2n+3)(2n+4)} \quad (\Re^3) \text{ for n=1,2,3\ldots} \tag{7.24}$$

$$\Phi_{li} = A_0\left(A_1\delta_{li} + A_2 r_{,i} r_{,l}\right) \quad (\Re^3) \text{ for n=1,2,3\ldots} \tag{7.25}$$

where

$$\begin{aligned} A_0 &= -\frac{1}{8G(1-v)}\frac{r^{2n+1}}{(n+1)(n+2)(2n+1)} \\ A_1 &= 7+4n-4v(n+2) \\ A_2 &= -(2n+1) \end{aligned} \tag{7.26}$$

for 3D problems, where r_j represents the Euclidean distance of a given point (x, y) from a fixed point (x_j, y_j) in the domain of interest. The corresponding stress particular solution can be obtained by

$$S_{lij} = G(\Phi_{li,j} + \Phi_{lj,i}) + \lambda\delta_{ij}\Phi_{lk,k} \tag{7.27}$$

where $\lambda = \dfrac{2v}{1-2v}G$. Substituting Eq. (7.25) into (7.27) yields

$$S_{lij} = B_0\left\{B_1\left(r_{,j}\delta_{li} + r_{,i}\delta_{jl}\right) + B_2\delta_{ij}r_{,l} + B_3 r_{,i}r_{,j}r_{,l}\right\} \qquad (\Re^2) \text{ for n=1,2,3...} \tag{7.28}$$

where

$$\begin{aligned} B_0 &= -\frac{1}{(1-v)}\frac{r^{2n}}{(2n+1)(2n+3)} \\ B_1 &= (2n+2) - v(2n+3) \\ B_2 &= v(2n+3) - 1 \\ B_3 &= 1 - 2n \end{aligned} \tag{7.29}$$

for 2D problems, and substituting Eq. (7.25) into (7.27), one can obtain

$$S_{lij} = B_0\left\{B_1\left(r_{,j}\delta_{li} + r_{,i}\delta_{jl}\right) + B_2\delta_{ij}r_{,l} + B_3 r_{,i}r_{,j}r_{,l}\right\} \qquad (\Re^3) \text{ for n=1,2,3...} \tag{7.30}$$

where

$$\begin{aligned} B_0 &= -\frac{1}{4(1-v)}\frac{r^{2n}}{(n+1)(n+2)} \\ B_1 &= 3 + 2n - 2v(n+2) \\ B_2 &= 2v(n+2) - 1 \\ B_3 &= 1 - 2n \end{aligned} \tag{7.31}$$

for 3D problems.

To solve Eq. (7.18), Ψ_i can be treated as the gradient of a scalar function

$$\Psi_i = U_{,i} \tag{7.32}$$

Substituting Eq. (7.32) into Eq. (7.18) obtains the Poisson's equation

$$\nabla^2 U = \frac{m(1-2\nu)}{2G(1-\nu)}\varphi \tag{7.33}$$

Thus, taking $\varphi = r^{2n-1}$, its particular solution can be obtained (A.H.-D 2000)

$$U = \frac{m(1-2\nu)}{2G(1-\nu)}\frac{r^{2n+1}}{(2n+1)^2} \quad (\Re^2) \text{ for n=1,2,3...} \tag{7.34}$$

$$U = \frac{m(1-2\nu)}{2G(1-\nu)}\frac{r^{2n+1}}{(2n+1)(2n+2)} \quad (\Re^3) \text{ for n=1,2,3...} \tag{7.35}$$

Then from Eq. (7.32), Ψ_i can be obtain as follows

$$\Psi_i = \frac{m(1-2\nu)}{2G(1-\nu)}\frac{r_{,i}r^{2n}}{2n+1} \quad (\Re^2) \text{ for n=1,2,3...} \tag{7.36}$$

$$\Psi_i = \frac{m(1-2\nu)}{2G(1-\nu)}\frac{r_{,i}r^{2n}}{(2n+2)} \quad (\Re^3) \text{ for n=1,2,3...} \tag{7.37}$$

The corresponding stress particular solution can be obtained by substituting Eq. (7.25) into (7.27)

$$S_{ij} = G(\Psi_{i,j} + \Psi_{j,i}) + \lambda\delta_{ij}\Psi_{k,k} \tag{7.38}$$

Then we have

$$S_{ij} = \frac{mr^{2n-1}}{(1-\nu)(2n+1)}\left\{(1+2n\nu)\delta_{ij} + (1-2\nu)(2n-1)r_{,i}r_{,j}\right\} \quad (\Re^2) \text{ for n=1,2,3...} \tag{7.39}$$

$$S_{ij} = \frac{mr^{2n-1}}{(1-\nu)(2n+2)}\left\{(1-2\nu)(2n-1)r_{,i}r_{,j} + \delta_{ij}(1+2n\nu)\right\} \quad (\Re^3) \text{ for n=1,2,3...} \tag{7.40}$$

7.4.2. Method 2: Interpolating temperature and body force together

Considering that the temperature gradient plays a role in body force, $mT_{,i} - b_i$ can be approximated together by the following equation

$$mT_{,i} - b_i \approx \sum_{j=1}^{N} \alpha_i^j \varphi^j \tag{7.41}$$

Thus the approximate particular solution can be written as

$$u_i^p = \sum_{k=1}^{3}\sum_{j=1}^{N} \alpha_i^j \Phi_{ik}^j \tag{7.42}$$

Consequently, for body force the same approach can be followed as in Method 1 employing Eq. (7.17) and Eqs. (7.19)-(7.28) to obtain the desired Φ_{ik}^j and S_{lij}, which are the same as those for the case of body force only. This second approach has a relatively smaller number of equations to solve for the coefficients and the condition number of the coefficient matrix is smaller as well, which is beneficial to the solution. At this time the particular solutions of Eq. (7.9) have been obtained, can then be used to obtain the modified boundary conditions in Eqs. (7.12) and (7.13) so as to solve the homogeneous solution by Eq.(7.11). In the following section, the HFS-FEM is employed to obtain this homogeneous part.

7.5. FORMULATIONS OF THE HFS-FEM

7.5.1. Assumed fields for 2D problems

In the HFS-FEM approach, two different assumed fields are employed: an intra-element and a frame field. Intra-element continuity is enforced on a nonconforming internal displacement field chosen as the fundamental solution of the problem (Wang and Qin 2010b). In this approach, the intra-element displacement field is approximated in terms of a linear combination of the fundamental solutions of the problem of interest

$$\mathbf{u}(\mathbf{x}) = \begin{Bmatrix} u_1(\mathbf{x}) \\ u_2(\mathbf{x}) \end{Bmatrix} = \sum_{j=1}^{n_s} \begin{bmatrix} u_{11}^*(\mathbf{x},\mathbf{y}_{sj}) & u_{12}^*(\mathbf{x},\mathbf{y}_{sj}) \\ u_{21}^*(\mathbf{x},\mathbf{y}_{sj}) & u_{22}^*(\mathbf{x},\mathbf{y}_{sj}) \end{bmatrix} \begin{Bmatrix} c_{1j} \\ c_{2j} \end{Bmatrix} = \mathbf{N_e c_e} \quad (\mathbf{x} \in \Omega_e, \mathbf{y}_{sj} \notin \Omega_e) \tag{7.43}$$

where n_s is the number of source points outside the element domain, which is equal to the number of nodes of an element in the present research based on the generation approach of the source points, $\mathbf{c_e}$ is an unknown coefficient vector (not nodal displacements), and $\mathbf{N_e}$ is the fundamental solution matrix, which can be written as

$$\mathbf{N_e} = \begin{bmatrix} u_{11}^*(\mathbf{x},\mathbf{y}_{s1}) & u_{12}^*(\mathbf{x},\mathbf{y}_{s1}) & \ldots & u_{11}^*(\mathbf{x},\mathbf{y}_{sn_s}) & u_{12}^*(\mathbf{x},\mathbf{y}_{sn_s}) \\ u_{21}^*(\mathbf{x},\mathbf{y}_{s1}) & u_{22}^*(\mathbf{x},\mathbf{y}_{s1}) & \ldots & u_{21}^*(\mathbf{x},\mathbf{y}_{sn_s}) & u_{22}^*(\mathbf{x},\mathbf{y}_{sn_s}) \end{bmatrix} \tag{7.44}$$

$$\mathbf{c_e} = [c_{11} \quad c_{21} \quad \ldots\ldots \quad c_{1n} \quad c_{2n}]^T \tag{7.45}$$

in which $\mathbf{x}$ and $\mathbf{y}_{sj}$ are respectively the field point and source point in the local coordinate system (X_1, X_2). The components $u_{ij}^*(\mathbf{x},\mathbf{y}_{sj})$ represent the fundamental solution, i.e. the induced displacement component in the *i*-direction at the field point $\mathbf{x}$ due to a unit point load applied in the *j*-direction at source point $\mathbf{y}_{sj}$, as given by (Sauter and Schwab 2010)

$$u_{ij}^*(\mathbf{x},\mathbf{y}_{sj}) = \frac{-1}{8\pi(1-\nu)G}\left\{(3-4\nu)\delta_{ij}\ln r - r_{,i}r_{,j}\right\} \tag{7.46}$$

where $r_i = x_i - x_{is}$, $r = \sqrt{r_1^2 + r_2^2}$.

In this analysis, the number of source points is taken to be same as the number of element nodes, which is free of spurious energy modes and can maintain the stiffness equations in full rank, as indicated by (Qin 2000). The source point $\mathbf{y}_{sj}\,(j = 1, 2, \ldots, n_s)$ can be generated by means of the following method (Wang and Qin 2010b)

$$\mathbf{y}_s = \mathbf{x}_0 + \gamma(\mathbf{x}_0 - \mathbf{x}_c) \tag{7.47}$$

where γ is a dimensionless coefficient, $\mathbf{x}_0$ is the point on the element boundary (the nodal point in this work)and $\mathbf{x}_c$ is the geometrical centroid of the element (see Figure 7.2). Determination of γ was discussed by (Wang and Qin 2009; Wang and Qin 2010b), and γ=5 is used in the following analysis.

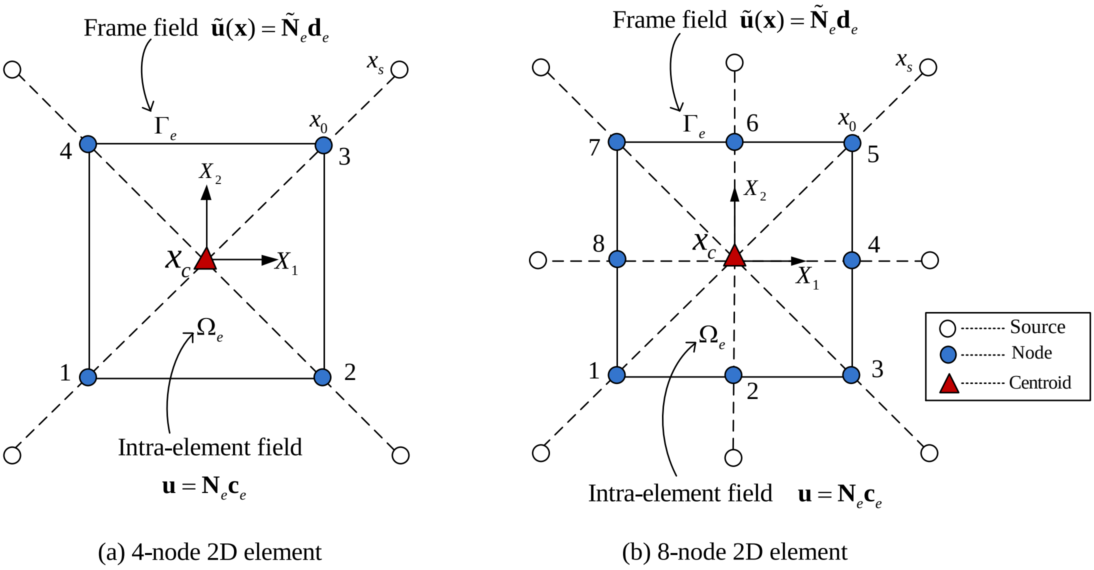

Figure 7.2 Intra-element field and frame field of a HFS-FEM element for 2D thermoelastic problems.

With the assumption of intra-element field of Eq. (7.43), the corresponding stress fields can be obtained by the constitutive Eq. (1)

$$\boldsymbol{\sigma}(\mathbf{x}) = \begin{bmatrix} \sigma_{11} & \sigma_{22} & \sigma_{12} \end{bmatrix}^T = \mathbf{T_e c_e} \tag{7.48}$$

where

$$\mathbf{T_e} = \begin{bmatrix} \sigma^*_{111}(\mathbf{x},\mathbf{y}_1) & \sigma^*_{211}(\mathbf{x},\mathbf{y}_1) & \ldots\ldots & \sigma^*_{111}(\mathbf{x},\mathbf{y}_{n_s}) & \sigma^*_{211}(\mathbf{x},\mathbf{y}_{n_s}) \\ \sigma^*_{122}(\mathbf{x},\mathbf{y}_1) & \sigma^*_{222}(\mathbf{x},\mathbf{y}_1) & \ldots\ldots & \sigma^*_{122}(\mathbf{x},\mathbf{y}_{n_s}) & \sigma^*_{222}(\mathbf{x},\mathbf{y}_{n_s}) \\ \sigma^*_{112}(\mathbf{x},\mathbf{y}_1) & \sigma^*_{212}(\mathbf{x},\mathbf{y}_1) & \ldots\ldots & \sigma^*_{112}(\mathbf{x},\mathbf{y}_{n_s}) & \sigma^*_{212}(\mathbf{x},\mathbf{y}_{n_s}) \end{bmatrix} \tag{7.49}$$

As a consequence, the traction is written as

$$\begin{Bmatrix} t_1 \\ t_2 \end{Bmatrix} = \mathbf{n}\boldsymbol{\sigma} = \mathbf{Q_e c_e} \tag{7.50}$$

in which

$$\mathbf{Q_e} = \mathbf{n}\mathbf{T_e}, \ \mathbf{n} = \begin{bmatrix} n_1 & 0 & n_2 \\ 0 & n_2 & n_1 \end{bmatrix} \tag{7.51}$$

The components $\sigma^*_{ijk}(\mathbf{x},\mathbf{y})$ for plane strain problems are given as

$$\sigma^*_{ijk}(\mathbf{x},\mathbf{y}) = \frac{-1}{4\pi(1-\nu)r}\left[(1-2\nu)(r_{,k}\delta_{ij} + r_{,j}\delta_{ki} - r_{,i}\delta_{jk}) + 2r_{,i}r_{,j}r_{,k}\right] \tag{7.52}$$

The unknown $\mathbf{c_e}$ in Eq. (7.43) can be calculated using a hybrid technique (Wang and Qin 2009) in which the elements are linked through an auxiliary conforming displacement frame which has the same form as in conventional FEM (see Figure 7.2). This means that in the HFS-FEM, a conforming displacement field should be independently defined on the element boundary to enforce the field continuity between elements and also to link the unknown **c** with nodal displacement $\mathbf{d}_e$. Thus, the frame is defined as

$$\tilde{\mathbf{u}}(\mathbf{x}) = \begin{Bmatrix} \tilde{u}_1 \\ \tilde{u}_2 \end{Bmatrix} = \begin{Bmatrix} \tilde{\mathbf{N}}_1 \\ \tilde{\mathbf{N}}_2 \end{Bmatrix} \mathbf{d}_e = \tilde{\mathbf{N}}_e \mathbf{d}_e, \qquad (\mathbf{x} \in \Gamma_e) \tag{7.53}$$

where the symbol "~" is used to specify that the field is defined on the element boundary only, $\tilde{\mathbf{N}}_e$ is the matrix of shape functions, $\mathbf{d}_e$ is the nodal displacements of elements. Taking the side 3-4-5 of a particular 8-node quadrilateral element (see Figure 7.2) as an example, $\tilde{\mathbf{N}}_e$ and $\mathbf{d}_e$ can be expressed as

$$\tilde{\mathbf{N}}_e = \begin{bmatrix} 0\cdots0 & \tilde{N}_1 & 0 & \tilde{N}_2 & 0 & \tilde{N}_3 & 0 & 0\cdots0 \\ \underset{4}{0\cdots0} & 0 & \tilde{N}_1 & 0 & \tilde{N}_2 & 0 & \tilde{N}_3 & \underset{6}{0\cdots0} \end{bmatrix} \tag{7.54}$$

$$\mathbf{d_e} = \begin{bmatrix} u_{11} & u_{21} & u_{12} & u_{22} & \cdots & u_{18} & u_{28} \end{bmatrix}^T \tag{7.55}$$

where $\tilde{N}_1$, $\tilde{N}_2$ and $\tilde{N}_3$ can be expressed by natural coordinate

$$\tilde{N}_1 = -\frac{\xi(1-\xi)}{2}, \; \tilde{N}_2 = 1-\xi^2, \; \tilde{N}_3 = \frac{\xi(1+\xi)}{2} \quad (\xi \in [-1,1]) \tag{7.56}$$

7.5.2. Assumed fields for 3D problems

For 3D cases, the intra-element displacement fields are approximated by

$$\mathbf{u(x)} = \begin{Bmatrix} u_1(\mathbf{x}) \\ u_2(\mathbf{x}) \\ u_3(\mathbf{x}) \end{Bmatrix} = \mathbf{N_e c_e} \quad (\mathbf{x} \in \Omega_e, \mathbf{y}_{sj} \notin \Omega_e) \tag{7.57}$$

where the matrix $\mathbf{N_e}$ and vector $\mathbf{c_e}$ for 3D elements can be written as

$$\mathbf{N_e} = \begin{bmatrix} u^*_{11}(\mathbf{x},\mathbf{y}_{s1}) & u^*_{12}(\mathbf{x},\mathbf{y}_{s1}) & u^*_{13}(\mathbf{x},\mathbf{y}_{s1})\cdots & \cdots u^*_{11}(\mathbf{x},\mathbf{y}_{sn_s}) & u^*_{12}(\mathbf{x},\mathbf{y}_{sn_s}) & u^*_{13}(\mathbf{x},\mathbf{y}_{sn_s}) \\ u^*_{12}(\mathbf{x},\mathbf{y}_{s1}) & u^*_{22}(\mathbf{x},\mathbf{y}_{s1}) & u^*_{23}(\mathbf{x},\mathbf{y}_{s1})\cdots & \cdots u^*_{12}(\mathbf{x},\mathbf{y}_{sn_s}) & u^*_{22}(\mathbf{x},\mathbf{y}_{sn_s}) & u^*_{23}(\mathbf{x},\mathbf{y}_{sn_s}) \\ u^*_{13}(\mathbf{x},\mathbf{y}_{s1}) & u^*_{32}(\mathbf{x},\mathbf{y}_{s1}) & u^*_{33}(\mathbf{x},\mathbf{y}_{s1})\cdots & \cdots u^*_{13}(\mathbf{x},\mathbf{y}_{sn_s}) & u^*_{32}(\mathbf{x},\mathbf{y}_{sn_s}) & u^*_{33}(\mathbf{x},\mathbf{y}_{sn_s}) \end{bmatrix} \tag{7.58}$$

$$\mathbf{c_e} = [c_{11} \quad c_{21} \quad c_{31} \quad \cdots\cdots \quad c_{1n} \quad c_{2n} \quad c_{3n}]^T \tag{7.59}$$

in which the fundamental solution components $u^*_{ij}(\mathbf{x}, \mathbf{y}_{sj})$ are given by

$$u^*_{ij}(\mathbf{x}, \mathbf{y}_{sj}) = \frac{1}{16\pi(1-\nu)Gr}\left\{(3-4\nu)\delta_{ij} + r_{,i}r_{,j}\right\} \tag{7.60}$$

where $r_i = x_i - x_{is}$, $r = \sqrt{r_1^2 + r_2^2 + r_3^2}$. In 3D analysis, the number of source points is also taken to be same as the number of element nodes as done for 2D cases.

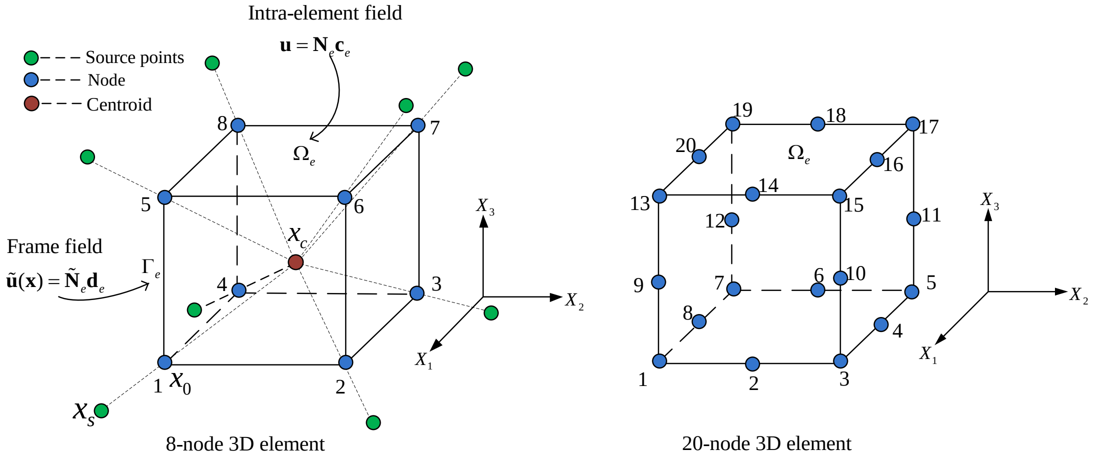

Figure 7.3 Intra-element field and frame field of a hexahedron HFS-FEM element for 3D thermoelastic problems (The source points and centroid of the 20-node element are omitted in the figure for a clear view: they are similar to those of the 8-node element).

The corresponding stress fields in 3D can be expressed as

$$\boldsymbol{\sigma}(\mathbf{x}) = \left[\sigma_{11} \quad \sigma_{22} \quad \sigma_{33} \quad \sigma_{23} \quad \sigma_{31} \quad \sigma_{12}\right]^T = \mathbf{T_e c_e} \tag{7.61}$$

where

$$\mathbf{T_e} = \begin{bmatrix} \sigma^*_{111}(\mathbf{x},\mathbf{y}_1) & \sigma^*_{211}(\mathbf{x},\mathbf{y}_1) & \sigma^*_{311}(\mathbf{x},\mathbf{y}_1) & \cdots & \sigma^*_{111}(\mathbf{x},\mathbf{y}_{n_s}) & \sigma^*_{211}(\mathbf{x},\mathbf{y}_{n_s}) & \sigma^*_{311}(\mathbf{x},\mathbf{y}_{n_s}) \\ \sigma^*_{122}(\mathbf{x},\mathbf{y}_1) & \sigma^*_{222}(\mathbf{x},\mathbf{y}_1) & \sigma^*_{322}(\mathbf{x},\mathbf{y}_1) & \cdots & \sigma^*_{122}(\mathbf{x},\mathbf{y}_{n_s}) & \sigma^*_{222}(\mathbf{x},\mathbf{y}_{n_s}) & \sigma^*_{322}(\mathbf{x},\mathbf{y}_{n_s}) \\ \sigma^*_{133}(\mathbf{x},\mathbf{y}_1) & \sigma^*_{233}(\mathbf{x},\mathbf{y}_1) & \sigma^*_{333}(\mathbf{x},\mathbf{y}_1) & \cdots & \sigma^*_{133}(\mathbf{x},\mathbf{y}_{n_s}) & \sigma^*_{233}(\mathbf{x},\mathbf{y}_{n_s}) & \sigma^*_{333}(\mathbf{x},\mathbf{y}_{n_s}) \\ \sigma^*_{123}(\mathbf{x},\mathbf{y}_1) & \sigma^*_{223}(\mathbf{x},\mathbf{y}_1) & \sigma^*_{323}(\mathbf{x},\mathbf{y}_1) & \cdots & \sigma^*_{123}(\mathbf{x},\mathbf{y}_{n_s}) & \sigma^*_{223}(\mathbf{x},\mathbf{y}_{n_s}) & \sigma^*_{323}(\mathbf{x},\mathbf{y}_{n_s}) \\ \sigma^*_{131}(\mathbf{x},\mathbf{y}_1) & \sigma^*_{231}(\mathbf{x},\mathbf{y}_1) & \sigma^*_{331}(\mathbf{x},\mathbf{y}_1) & \cdots & \sigma^*_{131}(\mathbf{x},\mathbf{y}_{n_s}) & \sigma^*_{231}(\mathbf{x},\mathbf{y}_{n_s}) & \sigma^*_{331}(\mathbf{x},\mathbf{y}_{n_s}) \\ \sigma^*_{112}(\mathbf{x},\mathbf{y}_1) & \sigma^*_{212}(\mathbf{x},\mathbf{y}_1) & \sigma^*_{312}(\mathbf{x},\mathbf{y}_1) & \cdots & \sigma^*_{112}(\mathbf{x},\mathbf{y}_{n_s}) & \sigma^*_{212}(\mathbf{x},\mathbf{y}_{n_s}) & \sigma^*_{312}(\mathbf{x},\mathbf{y}_{n_s}) \end{bmatrix} \tag{7.62}$$

in which the components $\sigma^*_{ijk}(\mathbf{x}, \mathbf{y})$ are given as

$$\sigma^*_{ijk}(\mathbf{x}, \mathbf{y}) = \frac{-1}{8\pi(1-\nu)r^2}\left\{(1-2\nu)(r_{,k}\delta_{ij} + r_{,j}\delta_{ki} - r_{,i}\delta_{jk}) + 3r_{,i}r_{,j}r_{,k}\right\} \tag{7.63}$$

As a consequence, the traction is expressed as

$$\begin{Bmatrix} t_1 \\ t_2 \\ t_3 \end{Bmatrix} = \mathbf{n}\boldsymbol{\sigma} = \mathbf{Q_e c_e} \tag{7.64}$$

where

$$\mathbf{Q_e} = \mathbf{nT_e}, \quad \mathbf{n} = \begin{bmatrix} n_1 & 0 & 0 & 0 & n_3 & n_2 \\ 0 & n_2 & 0 & n_3 & 0 & n_1 \\ 0 & 0 & n_3 & n_2 & n_1 & 0 \end{bmatrix} \tag{7.65}$$

The frame field for the element surfaces, which is different from the line frame field of the 2D case, is defined as

$$\tilde{\mathbf{u}}(\mathbf{x}) = \begin{Bmatrix} \tilde{u}_1 \\ \tilde{u}_2 \\ \tilde{u}_3 \end{Bmatrix} = \begin{Bmatrix} \tilde{\mathbf{N}}_1 \\ \tilde{\mathbf{N}}_2 \\ \tilde{\mathbf{N}}_3 \end{Bmatrix} \mathbf{d}_e = \tilde{\mathbf{N}}_e \mathbf{d}_e, \qquad (\mathbf{x} \in \Gamma_e) \tag{7.66}$$

For the face 1-2-3-10-15-14-13-9 of a particular 20-node 3D brick element (see Figure 7.3), $\tilde{\mathbf{N}}_e$ and $\mathbf{d}_e$ can be expressed as

$$\tilde{\mathbf{N}}_e = \begin{bmatrix} \bar{\mathbf{N}}_1 & \bar{\mathbf{N}}_2 & \bar{\mathbf{N}}_3 & \underbrace{\mathbf{0}\cdots\mathbf{0}}_{5} & \bar{\mathbf{N}}_8 & \bar{\mathbf{N}}_4 & \underbrace{\mathbf{0}\cdots\mathbf{0}}_{2} & \bar{\mathbf{N}}_7 & \bar{\mathbf{N}}_6 & \bar{\mathbf{N}}_5 & \underbrace{\mathbf{0}\cdots\mathbf{0}}_{5} \end{bmatrix} \tag{7.67}$$

$$\mathbf{d}_e = \begin{bmatrix} u_{11} & u_{21} & u_{31} & u_{12} & u_{22} & u_{32} & \cdots & u_{120} & u_{220} & u_{320} \end{bmatrix}^T \tag{7.68}$$

where the shape functions are expressed as

$$\bar{\mathbf{N}}_\mathbf{i} = \begin{bmatrix} \tilde{N}_i & 0 & 0 \\ 0 & \tilde{N}_i & 0 \\ 0 & 0 & \tilde{N}_i \end{bmatrix}, \mathbf{0} = \begin{bmatrix} 0 & 0 & 0 \\ 0 & 0 & 0 \\ 0 & 0 & 0 \end{bmatrix} \tag{7.69}$$

and

$$\begin{aligned} \tilde{N}_i &= \frac{1}{4}\left(1+\xi_i\xi\right)\left(1+\eta_i\eta\right)\left(\xi_i\xi+\eta_i\eta-1\right) \qquad \text{(i=1,3,5,7)} \\ \tilde{N}_i &= \frac{1}{2}\left(1-\xi^2\right)\left(1+\eta_i\eta\right) \qquad \text{(i=2,6)} \\ \tilde{N}_i &= \frac{1}{2}\left(1-\eta^2\right)\left(1+\xi_i\xi\right) \qquad \text{(i=4,8)} \qquad \xi,\eta \in [-1,1] \end{aligned} \tag{7.70}$$

where $\left(\xi_i,\eta_i\right)$ is the natural coordinate of the *i*-node of the element (Figure 7.4).

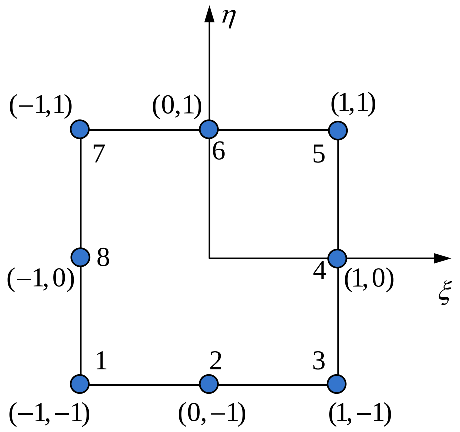

Figure 7.4 Typical quadratic interpolation for the frame fields.

7.5.3. Modified functional for HFS-FEM

The HFS-FEM formulations for 3D thermoelastic problem can be established by the variational approach. In the absence of body forces, the hybrid functional Π_{me} used to derive the present HFS-FEM can be constructed as (Qin and Wang 2008)

$$\Pi_{me} = \frac{1}{2}\iint_{\Omega_e} \sigma_{ij}\varepsilon_{ij} d\Omega - \int_{\Gamma_t} \bar{t}_i \tilde{u}_i d\Gamma + \int_{\Gamma_e} t_i(\tilde{u}_i - u_i) d\Gamma \tag{7.71}$$

where $\tilde{u}_i$ and u_i are the intra-element displacement field defined within the element and the frame displacement field defined on the element boundary, respectively. Ω_e and Γ_e are the element domain and element boundary, respectively. Γ_t, Γ_u, and Γ_I stand respectively for the specified traction boundary, specified displacement boundary, and inter-element boundary ($\Gamma_e = \Gamma_t + \Gamma_u + \Gamma_I$).

Compared to the functional employed in the conventional FEM, the present hybrid functional is constructed by adding a hybrid integral term related to the intra-element and element frame displacement fields to guarantee the satisfaction of displacement and traction continuity conditions on the common boundary of two adjacent elements. By applying the Gaussian theorem, Eq. (7.71) can be simplified as

$$\begin{aligned}\Pi_{me} &= \frac{1}{2}\iint_{\Omega_e} \sigma_{ij}\varepsilon_{ij} d\Omega - \int_{\Gamma_t} \bar{t}_i \tilde{u}_i d\Gamma + \int_{\Gamma_e} t_i(\tilde{u}_i - u_i) d\Gamma \\ &= \frac{1}{2}(\int_{\Gamma_e} t_i u_i d\Gamma - \iint_{\Omega_e} \sigma_{ij,j} u_i d\Omega) - \int_{\Gamma_t} \bar{t}_i \tilde{u}_i d\Gamma + \int_{\Gamma_e} t_i(\tilde{u}_i - u_i) d\Gamma\end{aligned} \tag{7.72}$$

For the equilibrium equation with the constructed intra-element fields, the following expression for the HFS-FE model is obtained

$$\begin{aligned}\Pi_{me} &= \frac{1}{2}\int_{\Gamma_e} t_i u_i d\Gamma - \int_{\Gamma_t} \bar{t}_i \tilde{u}_i d\Gamma + \int_{\Gamma_e} t_i(\tilde{u}_i - u_i) d\Gamma \\ &= -\frac{1}{2}\int_{\Gamma_e} t_i u_i d\Gamma + \int_{\Gamma_e} t_i \tilde{u}_i d\Gamma - \int_{\Gamma_t} \bar{t}_i \tilde{u}_i d\Gamma\end{aligned} \tag{7.73}$$

The functional Eq. (7.73) contains boundary integrals only and is used to derive HFS-FEM formulations for 2D and 3D thermoelastic problems.

7.5.4. Element stiffness matrix

The element stiffness equation can be generated by setting $\delta\Pi_{me} = 0$. Substituting Eqs. (7.57), (7.64) and (7.66) into the functional (7.73) yields

$$\Pi_{me} = -\frac{1}{2}\mathbf{c}_e{}^{\mathrm{T}}\mathbf{H}_e\mathbf{c}_e + \mathbf{c}_e{}^{\mathrm{T}}\mathbf{G}_e\mathbf{d}_e - \mathbf{d}_e{}^{\mathrm{T}}\mathbf{g}_e \tag{7.74}$$

where

$$\mathbf{H}_e = \int_{\Gamma_e} \mathbf{Q}_e^{\mathrm{T}}\mathbf{N}_e \mathrm{d}\Gamma, \quad \mathbf{G}_e = \int_{\Gamma_e} \mathbf{Q}_e^{\mathrm{T}}\tilde{\mathbf{N}}_e \mathrm{d}\Gamma, \quad \mathbf{g}_e = \int_{\Gamma_t} \tilde{\mathbf{N}}_e^{\mathrm{T}}\bar{\mathbf{t}} d\Gamma \tag{7.75}$$

To enforce inter-element continuity on the common element boundary, the unknown vector $\mathbf{c}_e$ should be expressed in terms of nodal DOF $\mathbf{d}_e$. The stationary condition of the functional Π_{me} with respect to $\mathbf{c}_e$ and $\mathbf{d}_e$ yields, respectively,

$$\frac{\partial\Pi_{me}}{\partial\mathbf{c}_e{}^{\mathrm{T}}} = -\mathbf{H}_e\mathbf{c}_e + \mathbf{G}_e\mathbf{d}_e = \mathbf{0} \tag{7.76}$$

$$\frac{\partial\Pi_{me}}{\partial\mathbf{d}_e{}^{\mathrm{T}}} = \mathbf{G}_e{}^{T}\mathbf{c}_e - \mathbf{g}_e = \mathbf{0} \tag{7.77}$$

Therefore, the relationship between $\mathbf{c}_e$ and $\mathbf{d}_e$, and the stiffness equation can be obtained as

$$\mathbf{c}_e = \mathbf{H}_e^{-1}\mathbf{G}_e\mathbf{d}_e \tag{7.78}$$

$$\mathbf{K}_e\mathbf{d}_e = \mathbf{g}_e \tag{7.79}$$

where $\mathbf{K}_e = \mathbf{G}_e{}^{\mathbf{T}}\mathbf{H}_e{}^{-1}\mathbf{G}_e$ is the element stiffness matrix. Consequently, the homogeneous solution can be obtained by Eq. (7.43) for 2D problems and Eq. (7.57) for 3D problems.

7.5.5. Recovery of rigid-body motion terms

When using the above procedures to obtain $\mathbf{u}_\mathbf{e}$ the rigid-body motion modes are not included so as to prevent singularity of the inversion of matrix $\mathbf{H}_e$. It is necessary, therefore, to reintroduce the discarded rigid-body motion terms after obtaining the internal field of an element. The least squares method can be employed for this purpose and the missing terms can be recovered easily by setting for the augmented internal field

$$\mathbf{u}_e = \mathbf{N}_e \mathbf{c}_e + \begin{bmatrix} 1 & 0 & x_2 \\ 0 & 1 & -x_1 \end{bmatrix} \mathbf{c}_0 \quad (\text{for } \Re^2) \tag{7.80}$$

$$\mathbf{u}_e = \mathbf{N}_e \mathbf{c}_e + \begin{bmatrix} 1 & 0 & 0 & 0 & x_3 & -x_2 \\ 0 & 1 & 0 & -x_3 & 0 & x_1 \\ 0 & 0 & 1 & x_2 & -x_1 & 0 \end{bmatrix} \mathbf{c}_0 \quad (\text{for } \Re^3) \tag{7.81}$$

For detailed formulations please refer to Chapter 3.

7.6. NUMERICAL RESULTS AND DISCUSSION

In this section, five different numerical examples are presented to test the performance of the proposed methodology, including 2D and 3D elastic and thermoelastic problems with body force and temperature change. The first three examples are used to investigate the capability of the method to treat 2D problems with temperature change or body force, or both. The latter two examples are used to show the method's ability to deal with 3D thermoelasticity with arbitrary body force and temperature. Analytical results or numerical results from ABAQUS with fine meshes are presented to check the accuracy of the method.

7.6.1. Circular cylinder with axisymmetric temperature change

In this example, a long circular cylinder with axisymmetric temperature change in the domain is considered to show the performance of the proposed method. The inside and outside surfaces of the cylinder are both assumed to be free of traction. The temperature T changes logarithmically along the radial direction. With the symmetry condition of the problem, only one quarter of the cylinder is modeled. The configurations of geometry and the boundary conditions are shown in Figure 7.5. Under the assumption of plane strain, the analytical solutions for stress components without body forces are given as (Timoshenko and Goodier 1970)

$$
\begin{aligned}
\sigma_r &= -\frac{E\alpha T_0}{2(1\text{-}v)}\left[\frac{\ln(b/r)}{\ln\left(b/a\right)}-\frac{\left(b/r\right)^2-1}{\left(b/a\right)^2-1}\right]\\
\sigma_\theta &= -\frac{E\alpha T_0}{2(1\text{-}v)}\left[\frac{\ln(b/r)-1}{\ln\left(b/a\right)}+\frac{\left(b/r\right)^2+1}{\left(b/a\right)^2-1}\right]\\
T &= \frac{\ln(r/b)}{\ln\left(a/b\right)}T_0
\end{aligned}
\tag{7.82}
$$

for reference. In the computation, the parameters a=5, b=20, E=1000, v=0.3, α=0.001, and T_0 =10. As shown in Figure 7.6, two different meshes with 16 8-node elements and 128 CPE8R elements, respectively, are employed to show the influence of the mesh density. The two approaches listed in Section 7.4 to approximate body force and temperature are discussed and analyzed in this example.

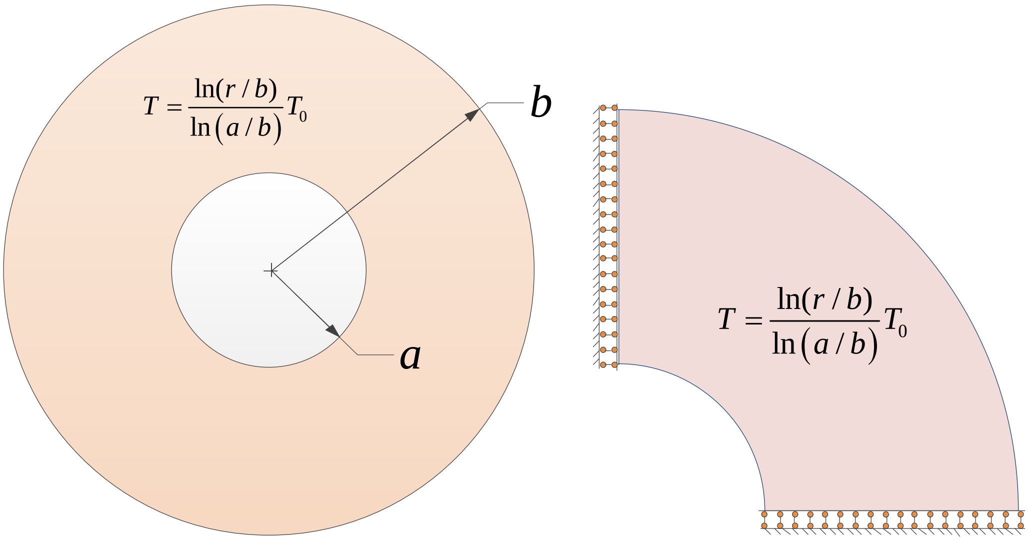

Figure 7.5 Geometry and boundary conditions of the long cylinder with axisymmetric temperature change.

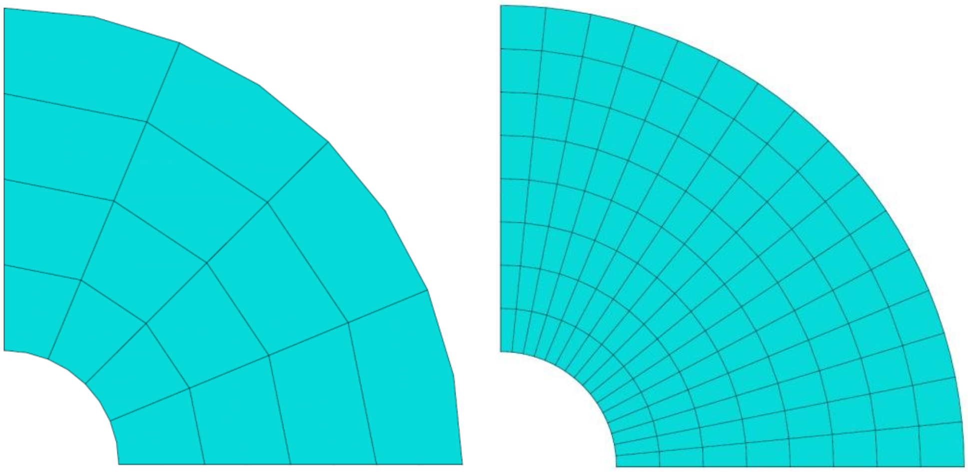

Figure 7.6 Mesh configurations of a quarter of the circular cylinder: (a) Coarse mesh (left: 16 elements) and (b) Fine mesh (right: 128 elements).

Figure 7.7 and Figure 7.8 present the variation of the radial and the circumferential thermal stresses with the cylinder radius for both coarse mesh and fine mesh, in which the theoretical values are given for comparison. It is seen from these figures that the results from **Method 2** are much better than those obtained from **Method 1** for both coarse mesh and fine mesh. When coarse mesh is used with **Method 2**, the radial stress near to the outer surface of the cylinder exhibits very large errors, but when the mesh is refined the error decreases dramatically and the results agree well with the analytical ones. It can be inferred that the error may be to a large extent due to the RBF interpolation, for which the number of interpolation points has a significant influence on its accuracy. However, no significant improvement is observed using **Method 1** when refining the mesh to 128 8-node elements.

The circumferential thermal stresses obtained from the coarse (left) and fine (right) meshes in Figure 7.6 through **Method 1** also show a smaller error compared to the radial stresses. However, these errors are still larger than those from **Method 2**, as can be seen clearly from Figure 7.8.

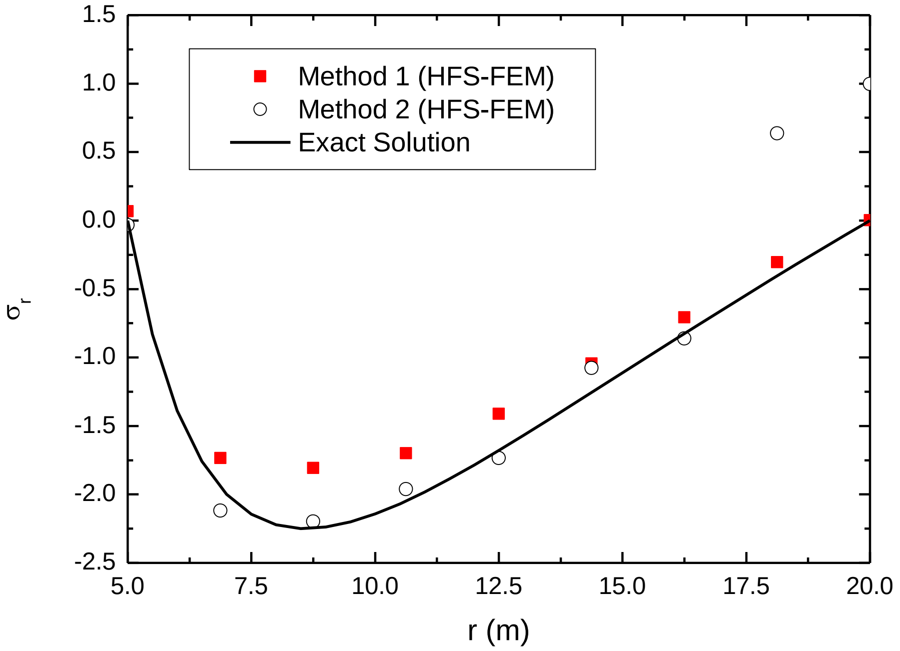

(a)

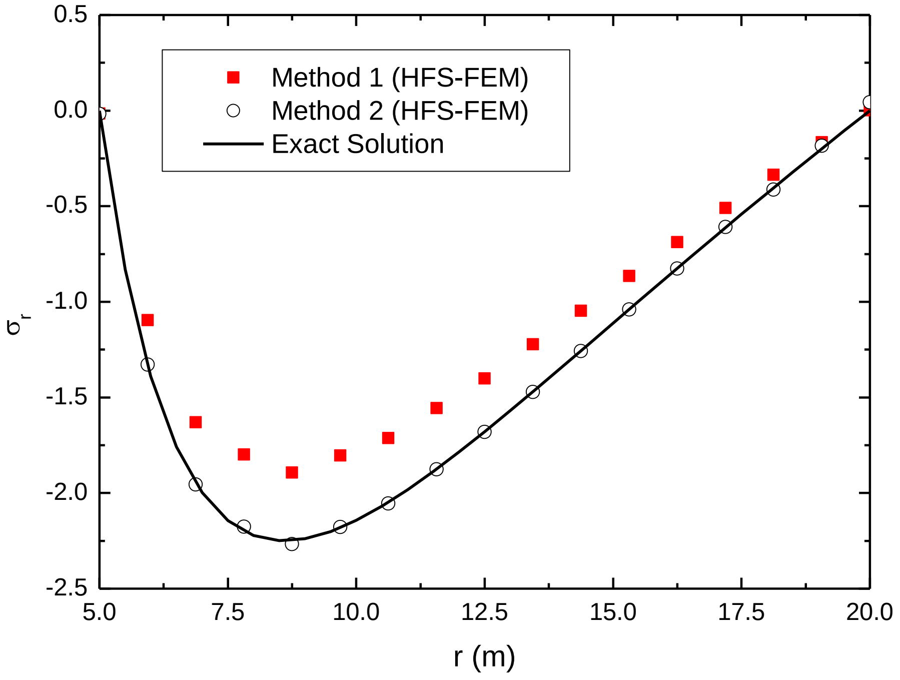

(b)

Figure 7.7 Variation of the radial thermal stresses with the cylinder radius using (a) coarse mesh and (b) fine mesh.

Figure 7.9 shows the variation of the radial displacement with the cylinder radius using (a) coarse mesh and (b) fine mesh. It can be seen that for both meshes **Method 1** does not give a result that has good agreement the analytical solution. But with **Method 2**, even using the coarse mesh, good agreement can be obtained. This result further verifies the conclusion that the second strategy (**Method 2**) of approximating temperature and body force together is a much better choice.

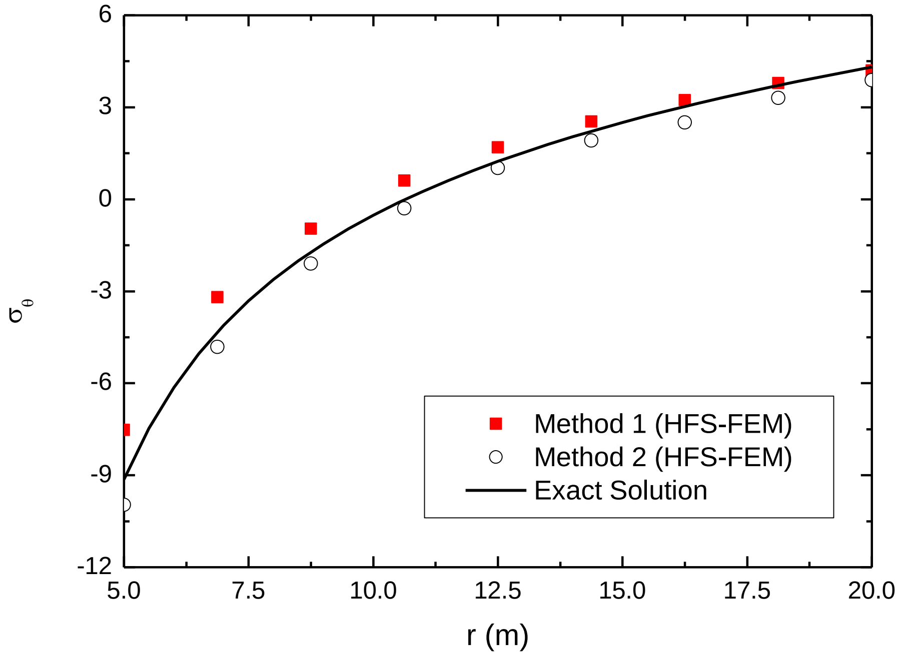

(a)

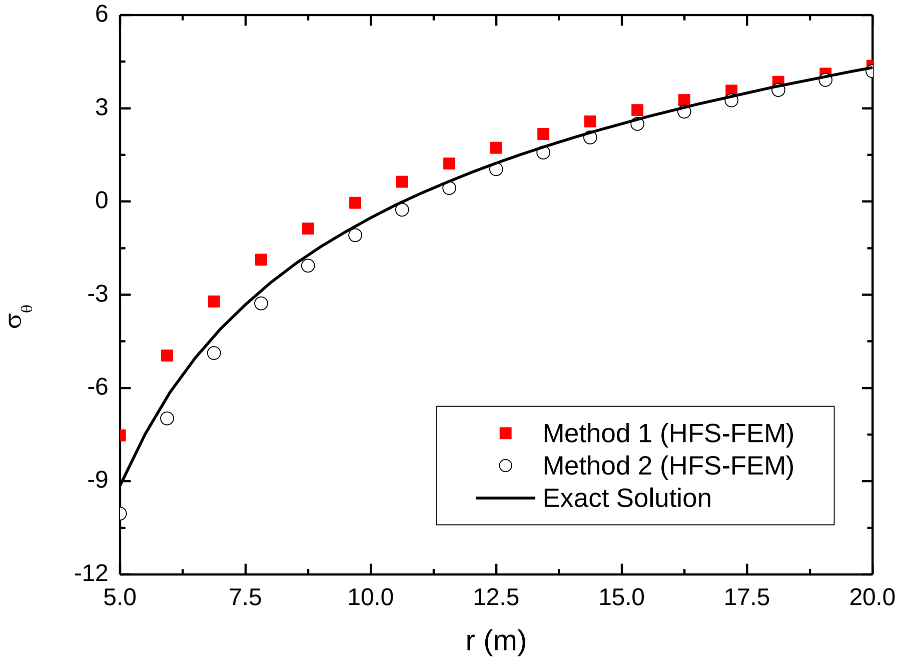

(b)

Figure 7.8 Variation of the circumferential thermal stresses with the cylinder radius using (a) coarse mesh and (b) fine mesh.

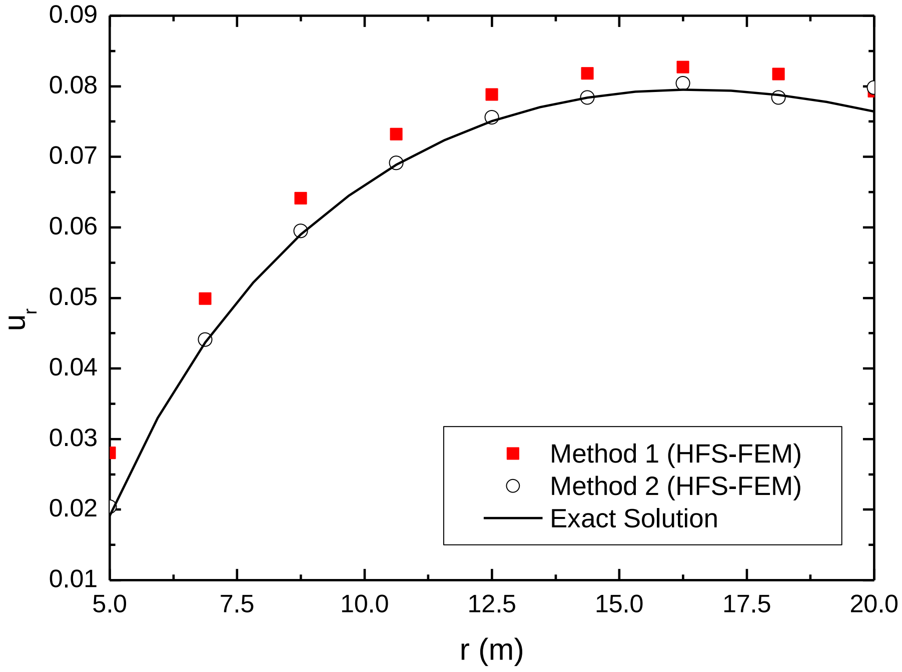

(a)

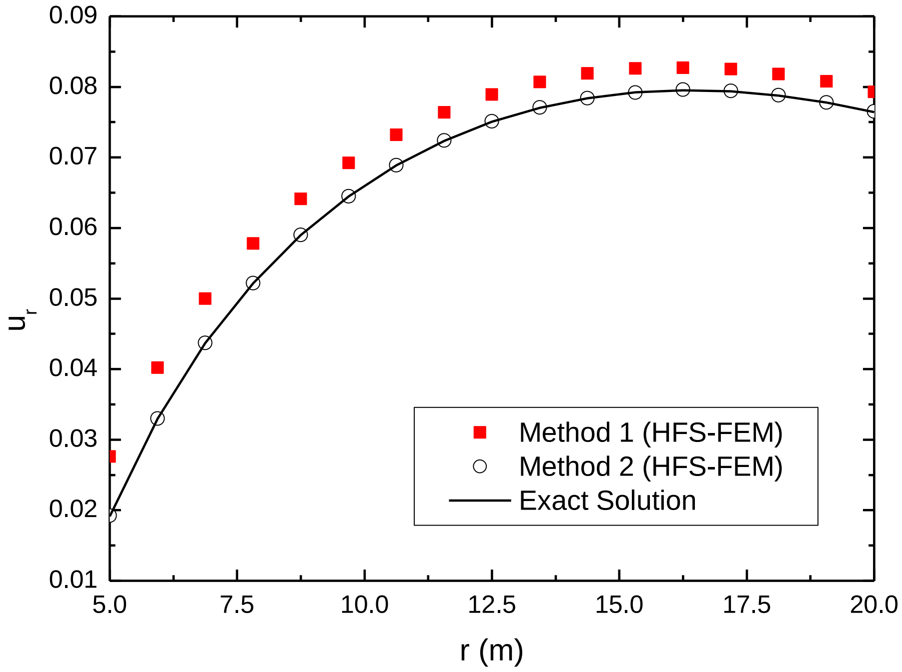

(b)

Figure 7.9 Variation of the radial displacement with the cylinder radius using (a) coarse mesh and (b) fine mesh.

Figure 7.10 displays the contour plots of (a) radial and (b) circumferential thermal stresses (the meshes used for the contour plot is different from that for calculation due to the use of quadratic elements). It demonstrates that treating temperature gradient and body force together is superior to treating them separately. In subsequent examples, therefore, Method 2 is employed in the analysis. It should be pointed out that it is necessary to apply Method 1 when the temperature change is discretely distributed or when the gradient of the temperature field is not available.

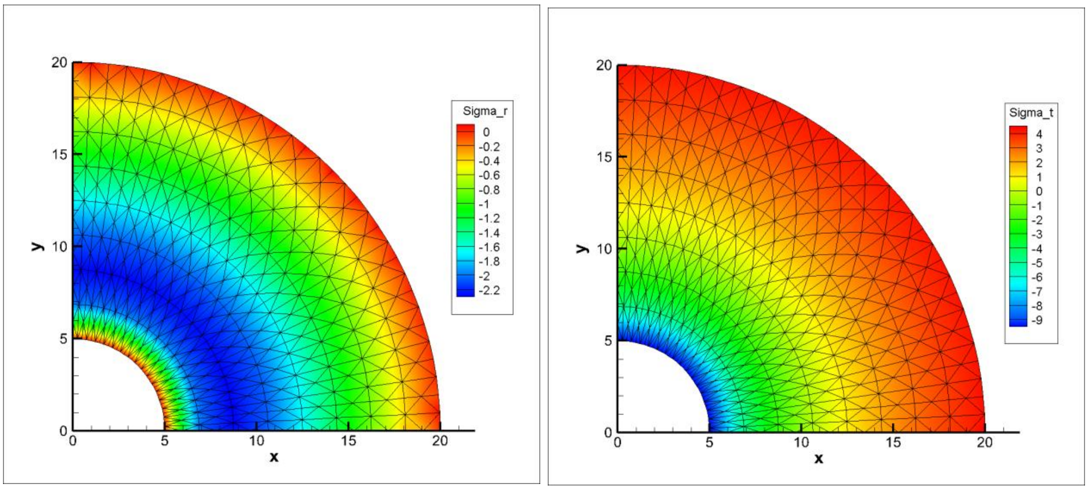

Figure 7.10 Contour plots of (a) radial and (b) circumferential thermal stresses (the meshes used for the contour plots are different from those used for calculation due to the use of quadratic elements).

7.6.2. Long beam under gravity

The second exampleis a long beam with rectangular cross-section subjected to gravity. The geometry of the rectangular cross-section and the corresponding boundary conditions are shown in Figure 7.11, in which g denotes the gravity accelerator, and ρ is the density of material. The problem can be viewed as a plane strain problem, and the analytical solutions of displacements and stresses are given by

$$u_1 = 0, \;\; u_2 = -\frac{(1+\nu)(1-2\nu)\rho g}{2E(1-\nu)}\left[L^2 - \left(x_2 - L\right)^2\right]$$

$$\sigma_{11} = \frac{\rho g \nu}{1-\nu}(x_2 - L), \;\; \sigma_{22} = \rho g (x_2 - L), \;\; \sigma_{12} = 0$$

Let L = 20, E = 1000, ν = 0.25, α = 0.001 and ρg = 9.8, and four 8-node quadratic elements are used to model the entire square cross-section domain (see Figure 7.11).

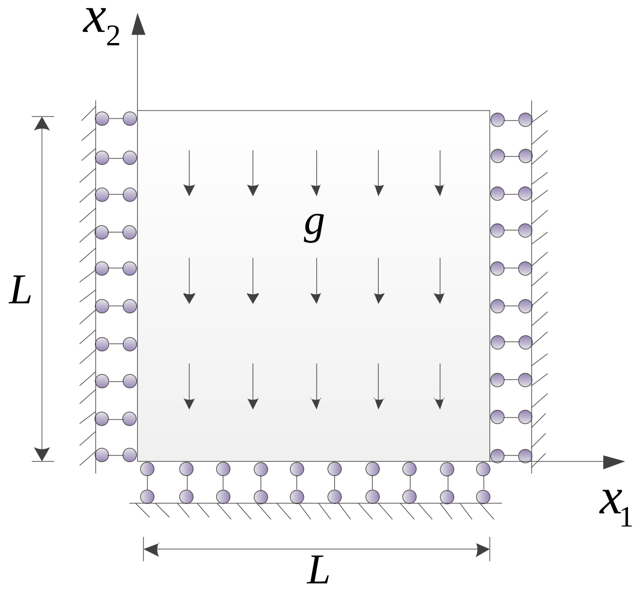

Figure 7.11 Long square cross-section beam under gravity.

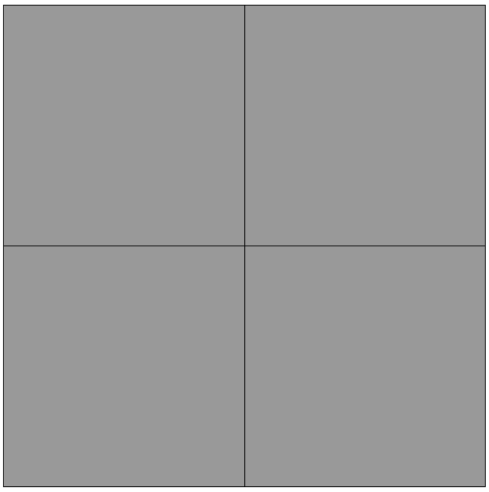

Figure 7.12 Mesh configuration of square cross-section beam.

The numerical results for the distribution of nodal displacement component u_2 along $x_1 = 10$ are shown in Figure 7.13, from which it can be seen that the numerical results agree very well with the analytical solutions. Moreover, the stress results at element nodes along $x_1 = 10$ are also compared with the exact solutions in Figure 7.13, from which it is obvious that the numerical results obtained from the HFS-FEM with RBF interpolation are in good agreement with the analytical results.

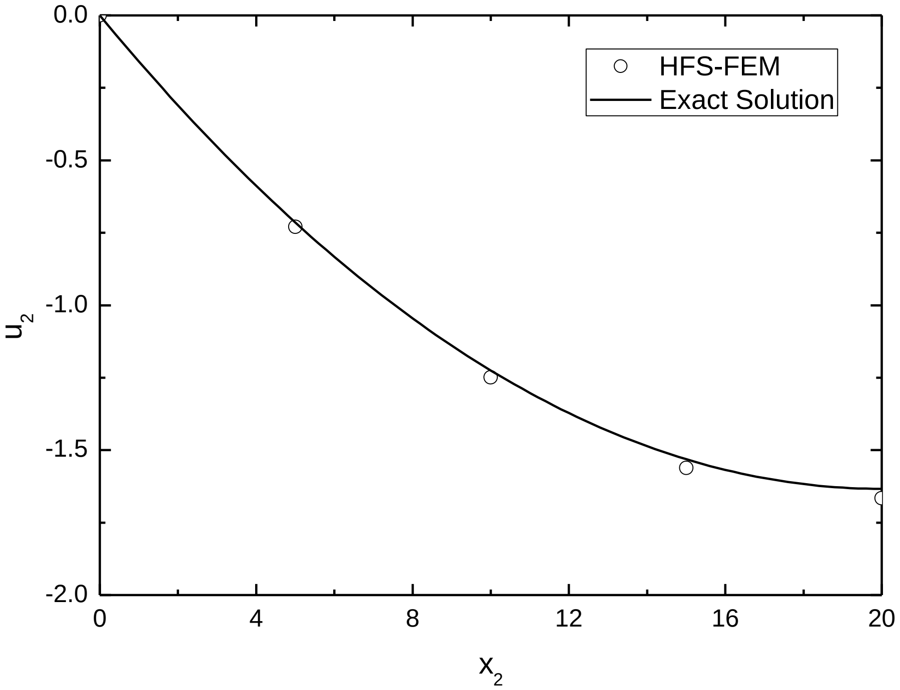
0.0
-0.5
-1.0
-1.5
-2.0
u_2
0
4
8
12
16
20
x_2
HFS-FEM
Exact Solution

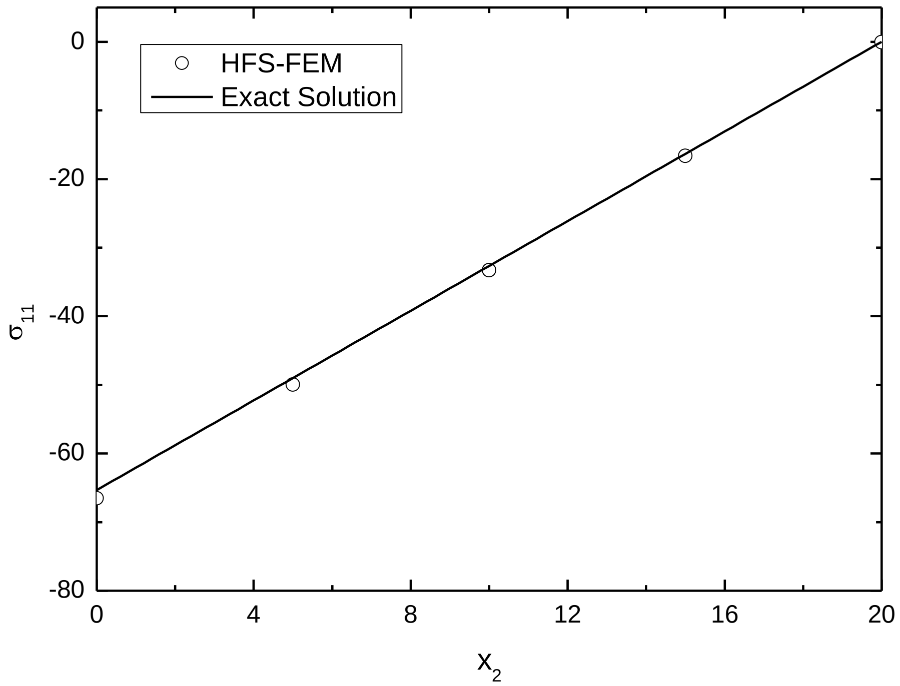
0
-20
-40
-60
-80
σ_{11}
0
4
8
12
16
20
x_2
HFS-FEM
Exact Solution

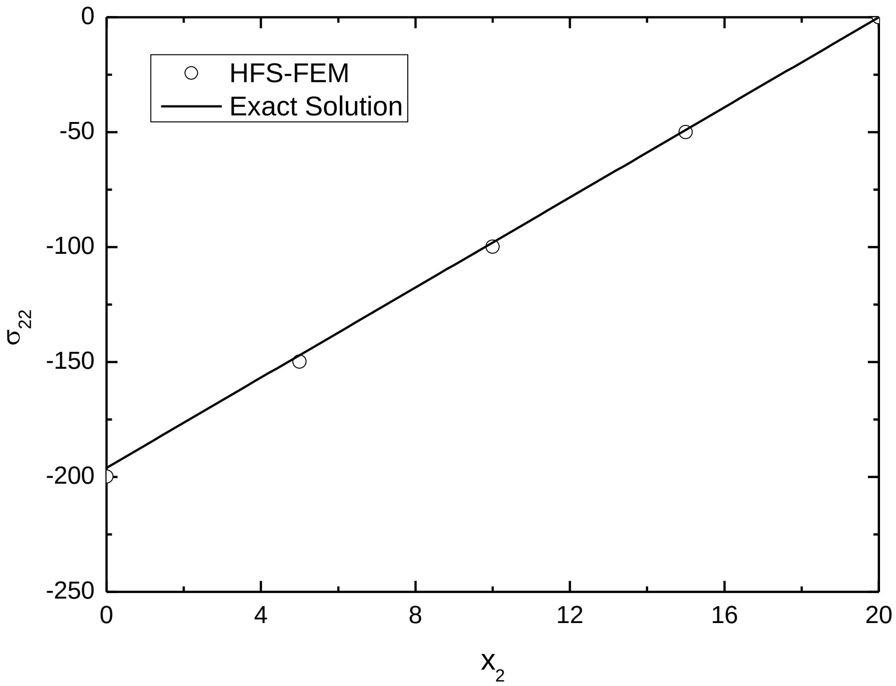

Figure 7.13 Displacement and stresses along x_1=10 of square cross-section of the beam.

Figure 7.14 gives the stress contour plots of the beam cross-section beam under gravity. It can be seen that the stresses change linearly with x_2 coordinates and independently of the x_1 coordinate, which is consistent with the analytical solution.

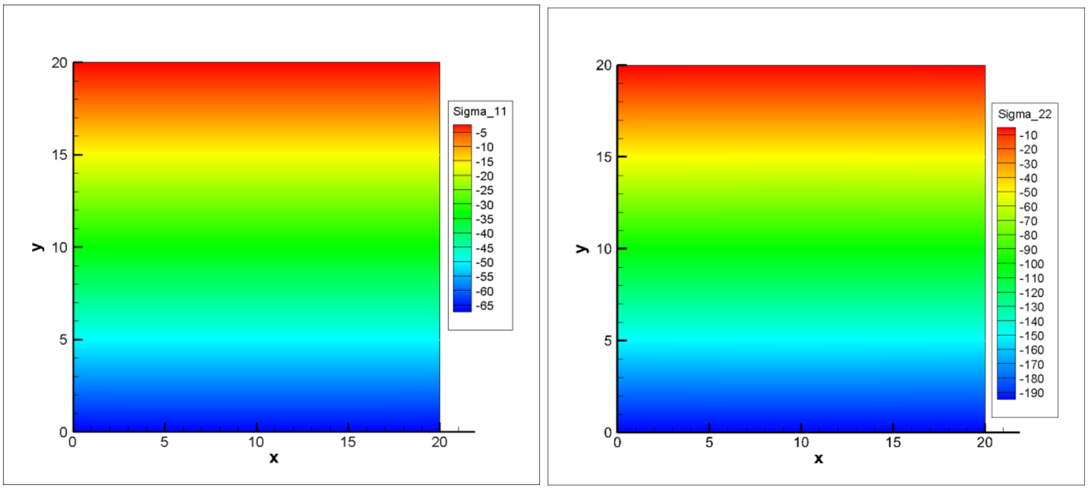

Figure 7.14 Contour plots of the stresses of square cross-section beam.

7.6.3. T-shaped domain with body force and temperature change

In this example, the proposed numerical method is used to model a T-shaped domain with changes in both temperature and body force. The boundary condition and temperature distribution are shown in Figure 7.15. The material properties are E = 30000, v = 0.15, α = 0.001, ρ=2.3 and g = 9.8.

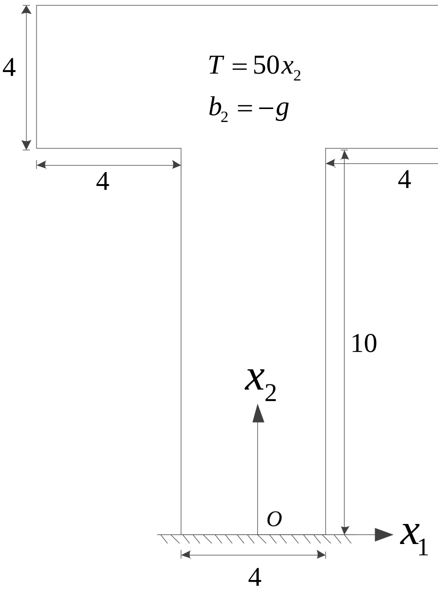

Figure 7.15 Dimension and boundary condition of the T-Shaped domain.

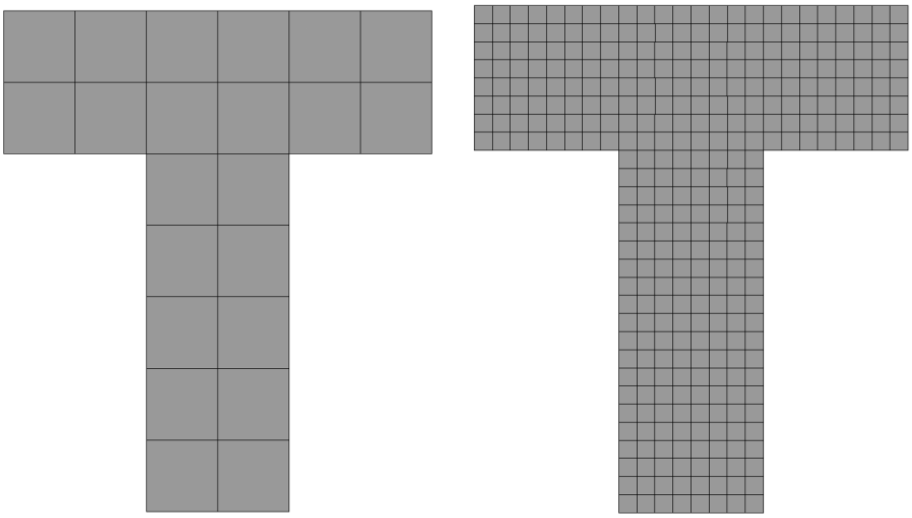

(a) HFS-FEM (22 elements) (b) ABAQUS (352 element)

Figure 7.16 Mesh configuration of T-Shaped domain.

In this example, 22 8-node quadrilateral elements are utilized to model the T-shaped domain by the HFS-FEM. Because there is no analytical solution for comparison, the results from ABAQUS using 352 CPE8R elements are employed as reference. Figure 7.17 shows the thermal stresses σ_{11} along the line $x_2 = 14$ and σ_{22} along the line $x_1 = 0$. It is obvious that the results from HFS-FEM using the coarse mesh in Figure 7.16 agree very well with the results from ABAQUS with a fine mesh in Figure 7.16. It should be noted that in order to obtain accurate results at the two sharp corners of the T-shaped domain, a refined mesh is necessary due to the stress concentration at these points, which is also applied in the traditional FEM (ABAQUS). The contour plots of the displacement components and stresses components are presented in Figure 7.18.

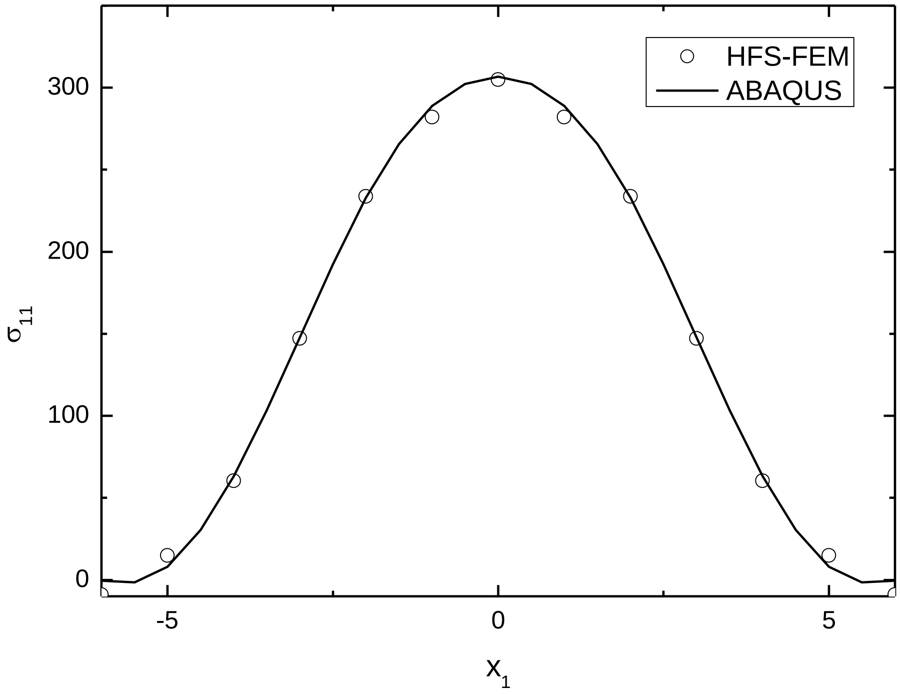

(a) σ_{11} along line $x_2 = 14$

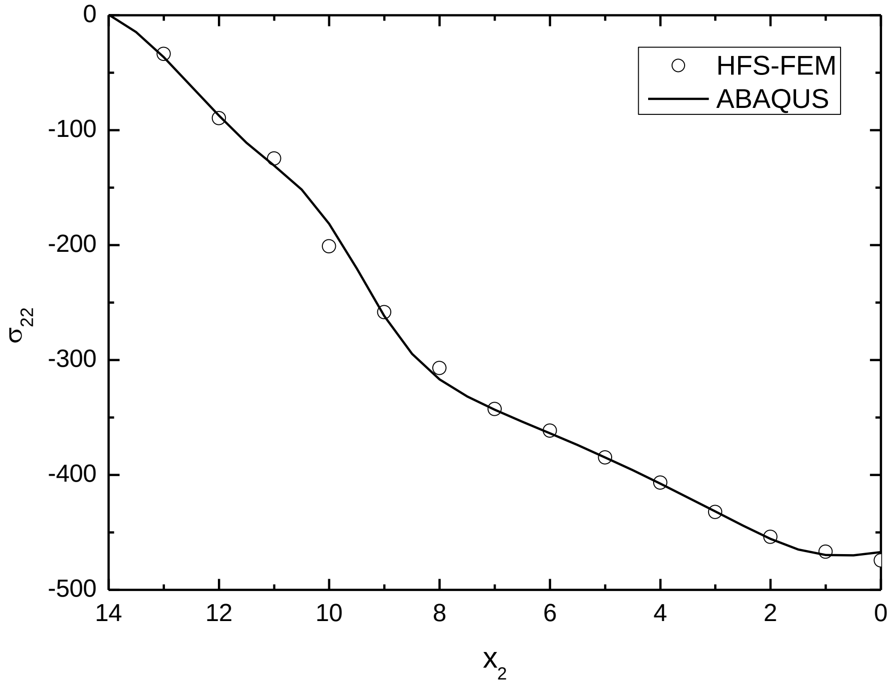

(b) σ_{22} along line $x_1 = 0$

Figure 7.17 Variation of the thermal stresses of T-shaped domain: (a) σ_{11} along line $x_2 = 14$ and (b) σ_{22} along line $x_1 = 0$.

7.6.4. 3D cube under arbitrary temperature and body force

In this example, a 3D cube of $1 \times 1 \times 1$ with center located at (0.5, 0.5, 0.5) is considered, which is shown in Figure 7.19. The material properties of the cube are Young's modulus $E = 5000$, Poisson's ratio $v = 0.3$, and linear thermal expansion coefficient $\alpha = 0.001$. The lower surface is fixed on the ground and the temperature distribution and body force are assumed to be

$$T = 30x_3,\ b_1 = 0,\ b_2 = 0,\ b_3 = -2000\left[(x-0.5)^2 + (y-0.5)^2\right]$$

Because there is no analytical solution available, the results from ABAQUS are employed for comparison. The meshes used by HFS-FEM and ABAQUS are given in Figure 7.20, in which the coarse mesh consists of 125 20-node brick elements and the fine mesh for ABAQUS has 8000 C3D20R elements.

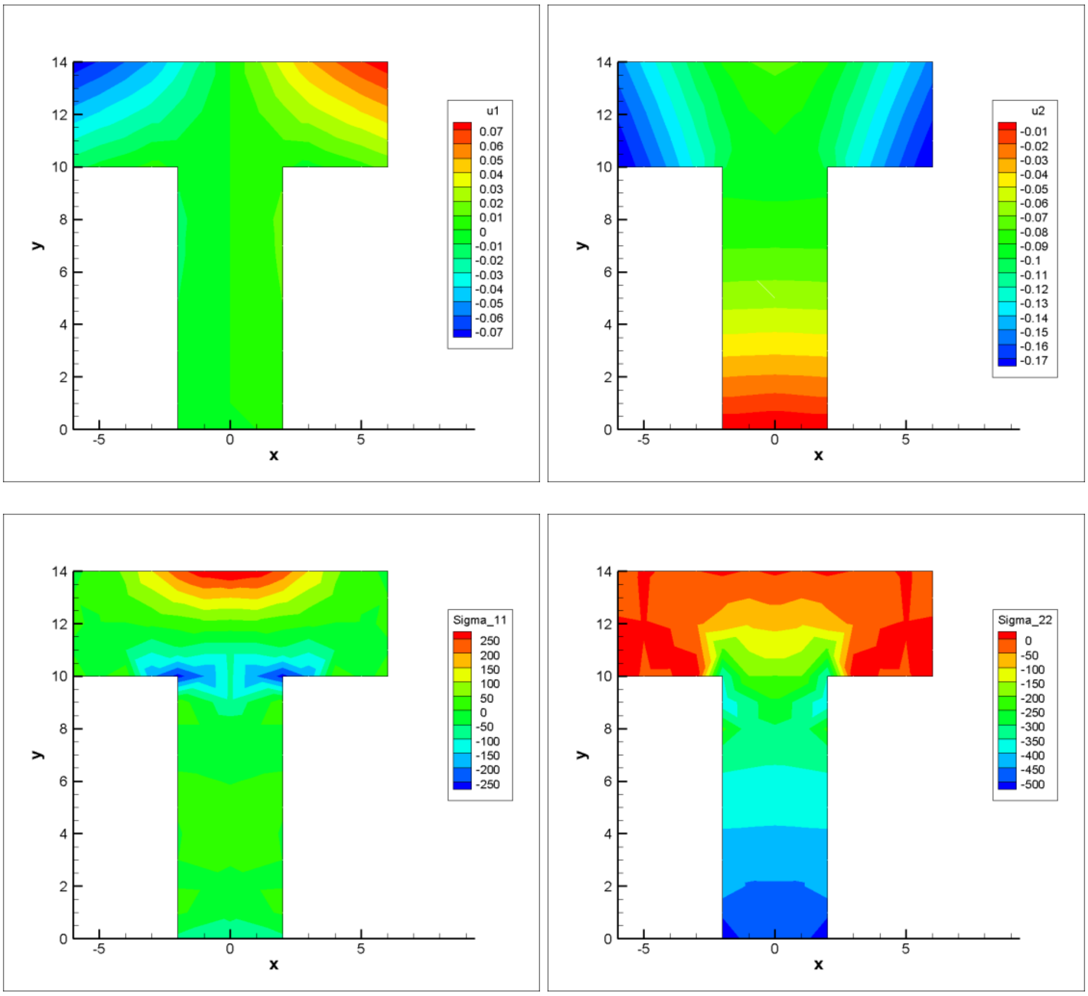

Figure 7.18 Contour plots of the displacement and stresses of T-shaped domain under change of temperature and body force.

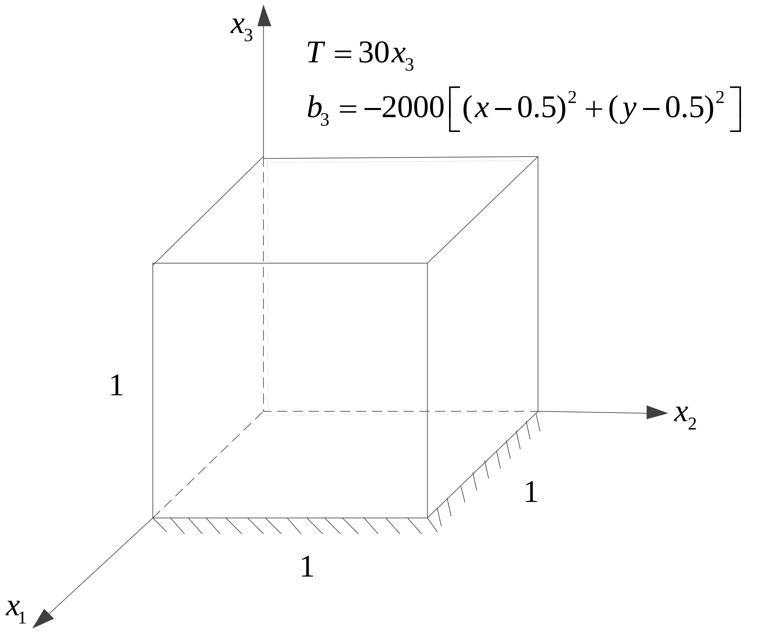

Figure 7.19 Schematic of the cube under arbitrary temperature and body force.

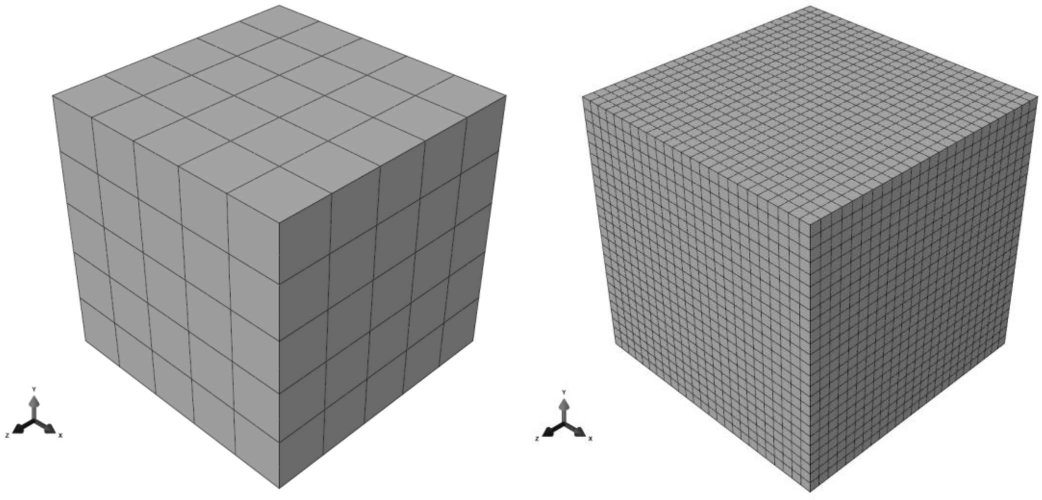
(a) HFS-FEM (125 elements) (b) ABAQUS (8000 element)

Figure 7.20 Mesh configurations of the 3D cube under arbitrary temperature and body force.

Figure 7.20 presents the displacement u_3 and stress σ_{33} along one edge of the cube which coincides with the x_3 axis. It can be seen that the results from HFS-FEM again agree very well with those from ABAQUS. It is demonstrated that procedure based on HFS-FEM can predict the response of 3D thermoelastic problems under arbitrary temperature and body force. It is also shown that the HFS-FEM with RBF interpolation can give satisfactory results using very coarse meshes.

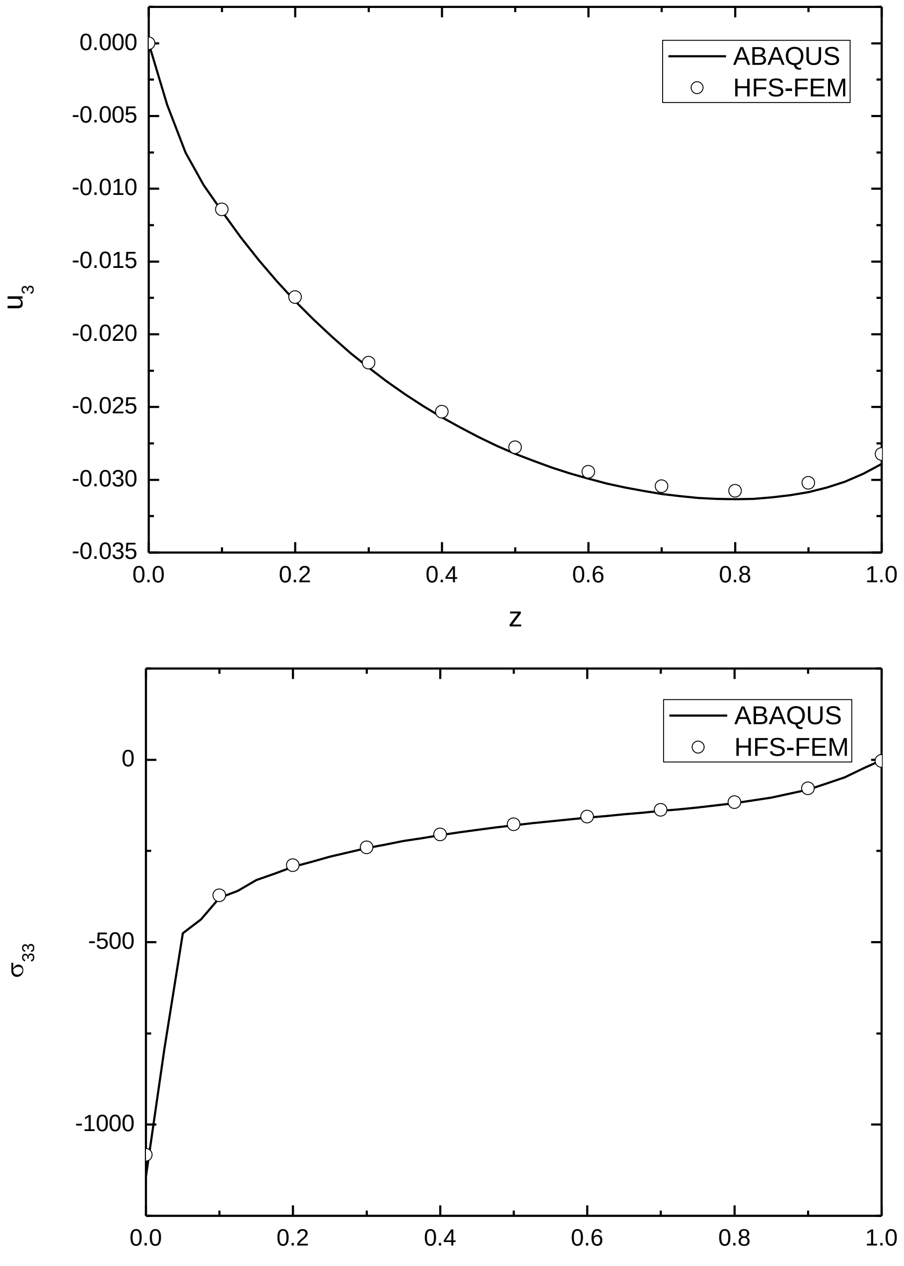

Figure 7.21 Displacement u_3 and stress σ_{33} along one cube edge when subjected to arbitrary temperature and body force.

7.6.5. A heated hollow ball under varied temperature field

Finally, a heated hollow ball is considered to show the capability of the method to solve 3D thermal stress problems with complex geometry. As shown in Figure 7.22, the radius of the inner hole is a and the radius of the outer ball is b. The temperature distribution is given by $T = T_0(2-10/r)$.

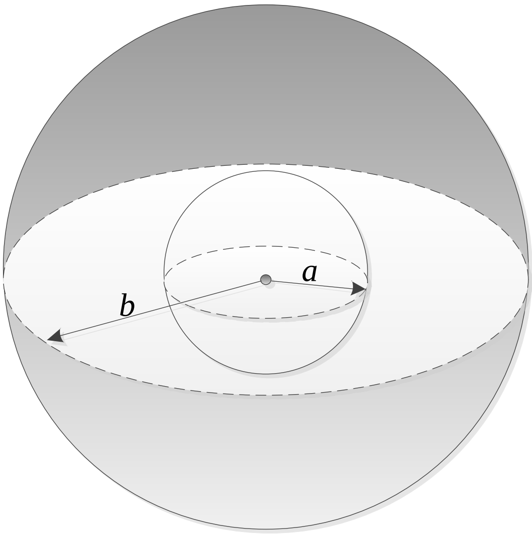

Figure 7.22 Schematic and dimension of heated hollow ball

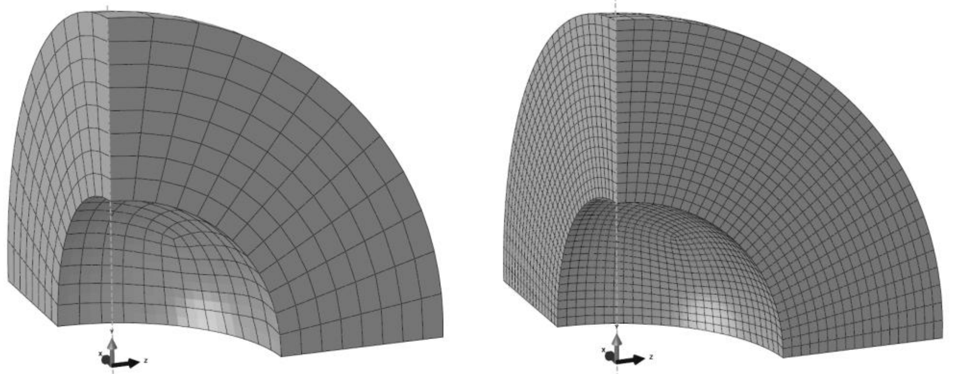

(a) HFS-FEM (864 elements) (b) ABAQUS (11088 element)

Figure 7.23 Mesh configurations of the heated hollow ball: (a) for HFS-FEM and (b) for ABAQUS.

In the calculation, $a = 5, b = 10, T_0 = 20$ are assumed. Considering the symmetry property of the problems, only one eighth of the ball is modeled. The mesh used for

HFS-FEM is given in Figure 7.23, in which a total of 864 20-node brick elements are employed. As a reference, the results from ABAQUS are calculated using a much finer mesh with 11088 C3D20R elements as shown in Figure 7.23.

Figure 7.24 shows the radial displacement u_r and von Mises stress of the hollow ball along its radial direction. The radial displacement increases with the radius from 0.071 to 0.143 except for a slight reduction when $5 < r < 6.3$. It can be seen from Figure 7.23 that the inner surface of the hollow ball suffers maximum von Mises stress up to 20 and this value dramatically reduces to about 0.15 at $r = 6.5$, then it experiences a moderate increase to about 8.2 at the outer surface. It is obvious from Figure 7.24 that the results obtained by HFS-FEM are in a good agreement with the results from ABAQUS. This again demonstrates the good performance of the proposed procedure in predicting the thermoelastic response of 3D problems with complex geometry.

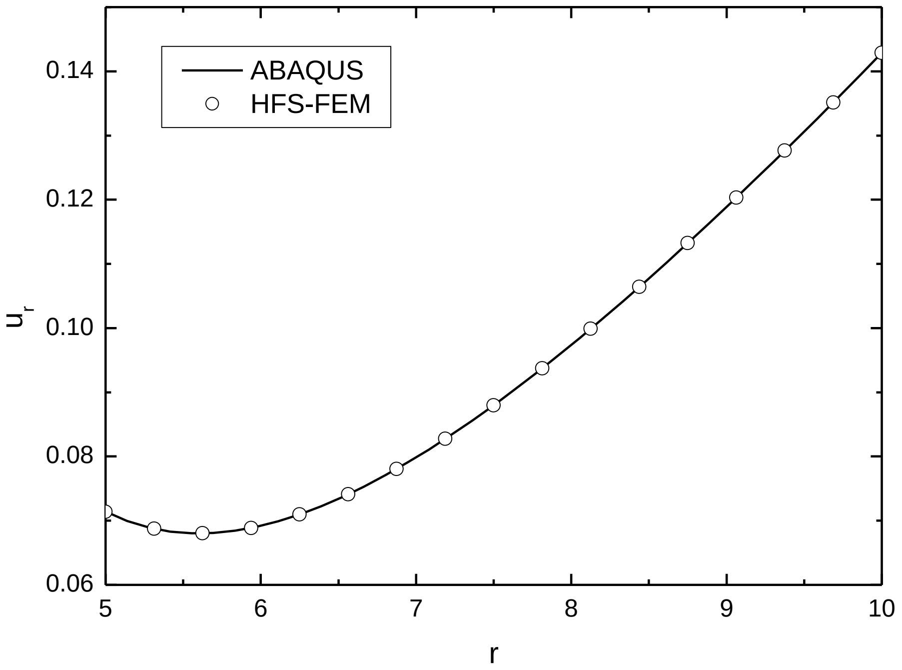

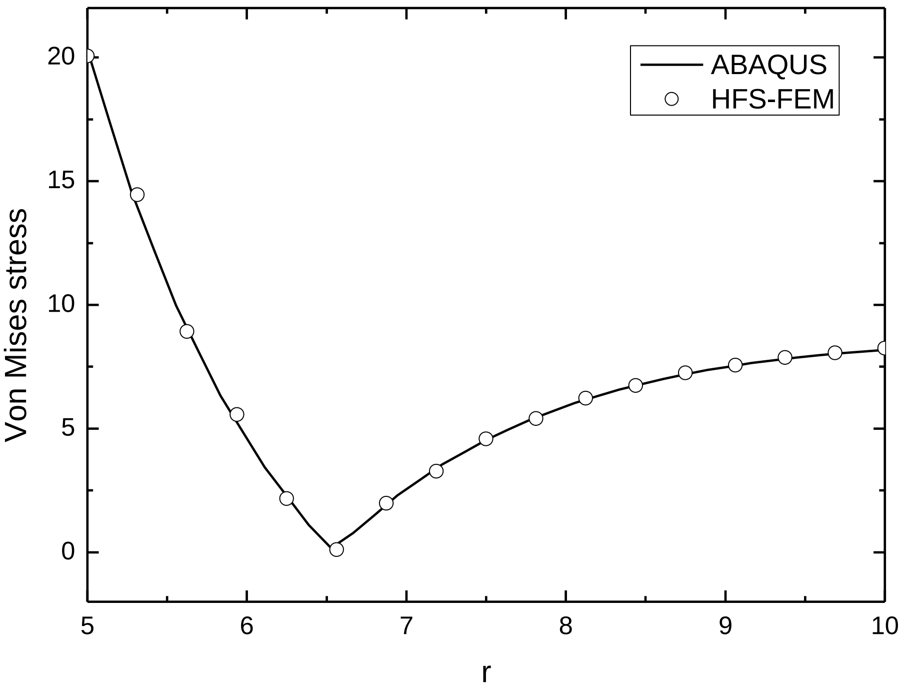

Figure 7.24 Radial displacement and von Mises stress along radius of the heated hollow ball subjected to temperature change.

7.7. SUMMARY

In this chapter, the HFS-FEM is extended to model multifield problems and a new solution procedure based on HFS-FEM is proposed to solve 2D and 3D thermoelastic problems with arbitrary body forces and temperature changes. The body force and temperature change are treated by the method of particular solution, in which the homogeneous solution is obtained by using the HFS-FEM with elastic fundamental solutions, and the particular solution is approximated by the RBF. It is found that treating body force and temperature change as a whole is superior to approximating them separately. The five numerical examples presented in this chapter show that the proposed method is able to predict the thermoelastic response of 2D and 3D thermoelasticity problems with complex geometry, arbitrary body force and arbitrary temperature changes. It is a promising methodology for mesh reduction, which is capable of obtaining satisfactory results with much coarser meshes than the traditional FEM. It is also possible to improve the results by only increasing the interpolation points while keeping the meshes at a lower density.

Chapter 8. HFS-FEM for Piezoelectric Materials

8.1. INTRODUCTION

Piezoelectric materials have the property of converting electrical energy into mechanical energy and vice versa. This reciprocity in energy conversion makes them very attractive for use in electromechanical devices, such as sensors, actuators, transducers and frequency generators. In past decades, piezoelectric composite materials have also been developed by combining piezoceramics with passive non-piezoelectric polymers. Superior properties are achieved by taking advantage of the most desirable properties of each constituent, and a great variety of structures have been produced. It has been demonstrated that the presence of defects such as voids and cracks results in degeneration of the service performance of piezoelectric materials (Barsoum 1997; Park, Park et al. 1998). The analysis of electroelastic fields around defects in piezoelectric materials is of paramount importance for evaluating the failure of such materials.

To enhance understanding of the electromechanical coupling mechanism in piezoelectric materials and to explore their potential applications in practical engineering, numerous investigations, both analytical and numerical, have been conducted over the past decades. Barnett and Lothe (1975) extended Stroh formalism (Stroh 1958) to an eight-dimensional framework to solve the problem of a line dislocation and a line charge in anisotropic piezoelectric materials. Chung and Ting (1996) studied the 2D problem of an elliptic hole in a solid of anisotropic piezoelectric material by using Stroh formalism. Dunn and Taya (1993), Qin and Yu (1998) and Zhao et al (2011) conducted micromechanics analysis of piezoelectric composites to predict their effective properties. Sosa (1991) derived the analytical solution for a transversely isotropic piezoelectric material containing an elliptical hole with the impermeable electric boundary condition by using the theory of complex variables.

On the basis of Sosa's work, Xu and Rajapakse (1999) presented an analytical solution for arbitrarily oriented elliptical voids. Park and Sun (1995) derived the closed-form solutions for an infinite piezoelectric medium containing a horizontal center crack by Stroh formalism. Using Stroh's formalism, Qin and Yu (1997) derived the explicit solutions for an arbitrarily oriented crack terminating at the interface between dissimilar piezoelectric materials.

The afore-mentioned analytical methods, however, are limited to relatively simple geometries because of material anisotropy and electromechanical coupling. As a consequence, numerical methods are usually employed in solving most practical problems. For example, the FEM has been used for the design and analysis of piezoelectric devices and adaptive structures (Kumar and Singh 1997; Béchet, Scherzer et al. 2009; Jański, Scherzer et al. 2010). However, mesh refinement near holes or cracks is required for FEM to achieve the necessary accuracy, which is a very time-consuming and complex task (Yu, Guo et al. 2008). The BEM has also been extended to piezoelectric problems (Lee and Jiang 1994; Ding, Wang et al. 1998; Xu and Rajapakse 2001; García-Sánchez, Zhang et al. 2008; Denda and Wang 2009). Compared with the FEM, the BEM is computationally efficient and highly accurate in dealing with linear fracture analyses. Lee and Jiang (1994) developed a boundary element formulation for piezoelectric solids using the method of weighted residuals and the Green's functions for a transversely isotropic piezoelectric plate. Pan (1999) presented a single-domain boundary element analysis of fracture mechanics in 2D anisotropic piezoelectric solids based on Green's functions derived by Stroh's formalism. Xu and Rajapakse (2001) performed a BEM analysis of crack problem based on the Green's functions derived by Lekhnitskii's formalism.

To avoid mesh refinement, special Green's functions for 2D anisotropic and piezoelectric materials have been derived (Ting 1996; Hwu 2010) and a linear boundary element has been developed to analyze problems involving multiple-holes and cracks by utilizing special Green's functions (Hwu and Yen 1991; Hwu 2010). In this method, a special Green’s function related to elliptical holes is required to satisfy the proper singularity at the source point and the traction-free-hole boundary conditions along the rim of the elliptical hole, which makes meshing around the hole boundary unnecessary. Thus, a vast amount of computer time and storage in numerical calculation can be saved. Moreover, due to the exact satisfaction of the traction-free-hole boundary condition, the results are more accurate than those obtained by using conventional boundary elements (Hwu and Yen 1991).

The Trefftz method, such as HT-FEM, Trefftz BEM and Trefftz collocation method, has also been successfully applied to problems of piezoelasticity. Qin (2003) derived the corresponding Trefftz finite element formulation for anti-plane problems of piezoelectric materials by constructing a pair of dual variational functional. Wang, Sze et al. (2006) analyzed singular electromechanical stress field in piezoelectrics by combining the eigensolution approach and Trefftz finite element models. Qin (2003) presented a family of modified variational principles of piezoelectricity and succeeded in applying them to establish a Trefftz finite element formulation. Jin, Sheng et al. (2005) formulated the Trefftz collocation and the Trefftz Galerkin methods for plane piezoelectricity based on solution sets derived from the complex variables method. Sheng et al (2006) developed a multi-domain Trefftz boundary collocation method for plane piezoelectricity with defects according to the plane piezoelectricity solution derived by Lekhnitskii’s formalism. As an alternative to the HT-FEM, the HFS-FEM was recently developed for solving 2D or 3D elastic and thermal problems for isotropic (Cao, Qin et al. 2013a) and orthotropic materials (Wang and Qin 2010a). This method inherits the advantages of the HT-FEM over the FEM and the BEM, such as the possibility of high accuracy using coarse meshes of high-degree elements, enhanced insensitivity to mesh distortion, great liberty in element shape and the possibility of accurately representing various local effects (Qin 2000).

In this chapter, a new HFS-FEM is developed for modeling plane piezoelectricity with/without defects (holes or cracks) based on Lekhnitskii’s formalism and the extended Stroh formalism, respectively. The fundamental solutions derived from these formalisms are employed to approximate the intra-element displacement and electrical potential field (DEP). A modified variational functional, which satisfies the governing equation, boundary and continuity conditions, is proposed to derive the element stiffness equation for piezoelectric materials. The stationary conditions of the variational functional and its theorem on the existence of extremum are also presented to show their suitability for deriving the proposed hybrid finite element formulations. Several numerical examples are presented to demonstrate the accuracy and efficiency of the proposed formulations. The majority of this chapter has been published in papers (Cao, Qin et al. 2012b; Cao, Yu et al. 2013c) co-authored by the candidate.

8.2. BASIC EQUATIONS FOR PIEZOELECTRIC MATERIALS

In the Cartesian coordinate system (x_1, x_2, x_3), for a linear piezoelectric material, the differential governing equations are given by

$$\sigma_{ij,j} + f_i = 0, \quad D_{i,i} - q = 0 \quad \text{in } \Omega \tag{8.1}$$

where σ_{ij} is the stress tensor, D_i the electric displacement vector, f_i the body force, q the free charge densities, and Ω the solution domain. Subscript commas denote partial differentiation with respect to the coordinates. The summation convention is invoked over repeated indices.

With strain and electric field as the independent variables, the constitutive equations are

$$\sigma_{ij} = C_{ijkl}\varepsilon_{kl} - e_{kij}E_k, \quad D_i = e_{ikl}\varepsilon_{kl} + \kappa_{ik}E_k \tag{8.2}$$

where C_{ijkl} is the elasticity tensor measured under a constant electric field (E=0), e_{ikl} and κ_{ij} are respectively the piezoelectric tensor and dielectric tensor measured under constant strain (ε=0), ε_{ij} and E_i are the elastic strain tensor and the electric field vector, respectively. The strain-displacement and electric field-electric potential relations are given as

$$\varepsilon_{ij} = \frac{1}{2}(u_{i,j} + u_{j,i}), \quad E_i = -\phi_{,i} \tag{8.3}$$

where u_i and ϕ are the displacement and the electric potential, respectively.

The boundary conditions of the boundary value problem (8.1)-(8.3) can be given by

$$u_i = \bar{u}_i \qquad \text{on } \Gamma_u \tag{8.4}$$

$$t_i = \sigma_{ij} n_j = \bar{t}_i \qquad \text{on } \Gamma_t \tag{8.5}$$

$$\phi = \bar{\phi} \qquad \text{on } \Gamma_\phi \tag{8.6}$$

$$D_n = D_i n_i = -\bar{q} \qquad \text{on } \Gamma_D \tag{8.7}$$

where t_i is the traction, q is the surface charge, $\bar{u}_i$, $\bar{t}_i$, $\bar{\phi}$ and $\bar{q}$ are the prescribed boundary values, and n_i is the unit outward normal vector. The barred quantities indicate that their values are prescribed. $\Gamma=\Gamma_u+\Gamma_t=\Gamma_D+\Gamma_\phi$ is the boundary of the problem domain Ω.

For a transversely isotropic material, if x_1-x_2 is taken as the isotropic plane, one can employ either x_1-x_3 or x_2-x_3 plane to study the plane electromechanical phenomenon. Thus, choosing the former and considering the plane strain conditions ($\varepsilon_{22} = \varepsilon_{32} = \varepsilon_{12} = 0$ and $E_2 = 0$) Eq.(8.2) can be reduced to

$$\begin{gathered}
\begin{Bmatrix} \sigma_{11} \\ \sigma_{33} \\ \sigma_{13} \end{Bmatrix} = \begin{bmatrix} c_{11} & c_{13} & 0 \\ c_{13} & c_{33} & 0 \\ 0 & 0 & c_{44} \end{bmatrix} \begin{Bmatrix} \varepsilon_{11} \\ \varepsilon_{33} \\ 2\varepsilon_{13} \end{Bmatrix} - \begin{bmatrix} 0 & e_{31} \\ 0 & e_{33} \\ e_{15} & 0 \end{bmatrix} \begin{Bmatrix} E_1 \\ E_3 \end{Bmatrix} \\
\begin{Bmatrix} D_1 \\ D_3 \end{Bmatrix} = \begin{bmatrix} 0 & 0 & e_{15} \\ e_{31} & e_{33} & 0 \end{bmatrix} \begin{Bmatrix} \varepsilon_{11} \\ \varepsilon_{33} \\ 2\varepsilon_{13} \end{Bmatrix} + \begin{bmatrix} \kappa_{11} & 0 \\ 0 & \kappa_{33} \end{bmatrix} \begin{Bmatrix} E_1 \\ E_3 \end{Bmatrix}
\end{gathered} \tag{8.8}$$

For a plane stress piezoelectric problem ($\sigma_{22} = \sigma_{32} = \sigma_{12} = 0$ and $D_2 = 0$), the constitutive equations can be obtained by replacing the coefficients $c_{11}, c_{13}, c_{33}, c_{44}, e_{15}, e_{31}, e_{33}, \kappa_{11}, \kappa_{33}$ in Eq. (8.8) as

$$\begin{gathered}
c_{11}^* = c_{11} - c_{12}^2 / c_{11},\ c_{13}^* = c_{13} - c_{12}c_{13} / c_{11}, \\
c_{33}^* = c_{33} - c_{13}^2 / c_{11},\ c_{44}^* = c_{44},\ e_{15}^* = e_{15}, \\
e_{31}^* = e_{31} - c_{12}e_{31} / c_{11},\ e_{33}^* = e_{33} - c_{13}e_{31} / c_{11}, \\
\kappa_{11}^* = \kappa_{11},\ \kappa_{33}^* = \kappa_{33} + e_{31}^2 / c_{11}
\end{gathered} \tag{8.9}$$

8.3. HFS-FEM BASED ON LEKHNITSKII'S FORMALISM

8.3.1. Assumed fields

The main idea of the proposed hybrid finite element method originated from the HT-FEM, which utilizes two independent approximate fields: an intra-element field and an independent frame field along the element boundary. Unlike the HT-FEM, however, the intra-element fields in the HFS-FEM are constructed based on the fundamental solutions, rather than a truncated T-complete function set. For piezoelectric problems, the HFS-FEM is based on assuming two distinct DEP fields: an intra-element DEP field $\mathbf{u}$ and an independent DEP frame field $\tilde{\mathbf{u}}$ along the element boundaries (Qin 2000; Qin 2003).

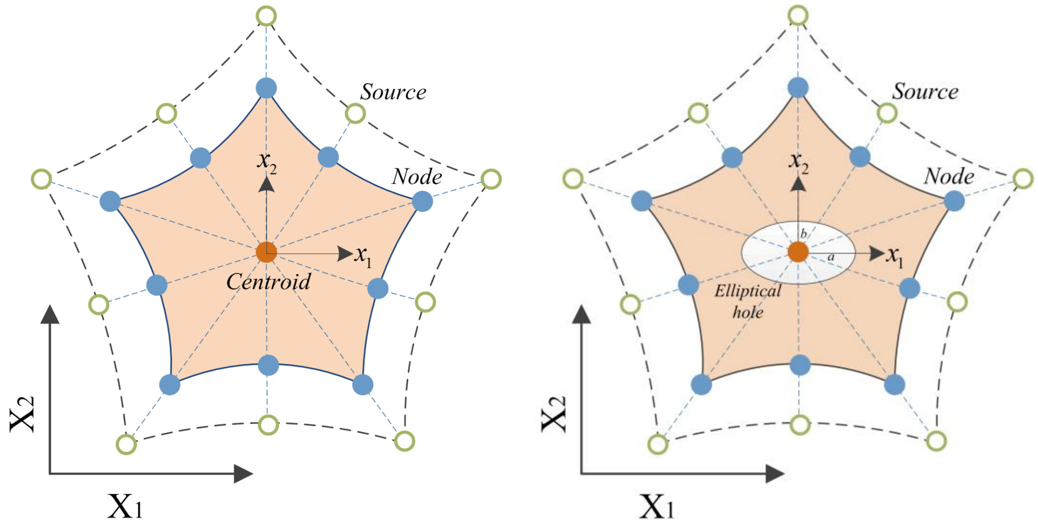

Figure 8.1 Intra-element field and frame field of HFS-FEM element for 2D piezoelectric problem: general element (left) and special element with central elliptical hole (right).

The intra-element DEP field u identically fulfills the governing differential equations (8.1) and is approximated by a linear combination of foundational solutions at different source points located outside the element domain

$$\mathbf{u_e} = \begin{Bmatrix} u_1 \\ u_2 \\ \phi \end{Bmatrix} = \sum_{j=1}^{n_s} \begin{bmatrix} u^*_{11}(\mathbf{x},\mathbf{y}_{sj}) & u^*_{21}(\mathbf{x},\mathbf{y}_{sj}) & u^*_{31}(\mathbf{x},\mathbf{y}_{sj}) \\ u^*_{12}(\mathbf{x},\mathbf{y}_{sj}) & u^*_{22}(\mathbf{x},\mathbf{y}_{sj}) & u^*_{32}(\mathbf{x},\mathbf{y}_{sj}) \\ u^*_{13}(\mathbf{x},\mathbf{y}_{sj}) & u^*_{23}(\mathbf{x},\mathbf{y}_{sj}) & u^*_{33}(\mathbf{x},\mathbf{y}_{sj}) \end{bmatrix} \begin{Bmatrix} c_{1j} \\ c_{2j} \\ c_{3j} \end{Bmatrix} = \mathbf{N_e c_e} \quad (\mathbf{x} \in \Omega_e, \mathbf{y}_{sj} \notin \Omega_e) \tag{8.10}$$

where n_s is the number of source points outside the element domain, which is equal to the number of nodes of an element in the present research based on the generation approach of the source points (see Figure 8.1), $\mathbf{c_e}$ an unknown coefficient vector (not nodal displacements), $\mathbf{N_e}$ the fundamental solution matrix, which can be written as

$$\mathbf{N_e} = \begin{bmatrix} u_{11}^*(\mathbf{x},\mathbf{y}_{s1}) & u_{21}^*(\mathbf{x},\mathbf{y}_{s1}) & u_{31}^*(\mathbf{x},\mathbf{y}_{s1}) & \dots & u_{33}^*(\mathbf{x},\mathbf{y}_{sn_s}) & u_{33}^*(\mathbf{x},\mathbf{y}_{sn_s}) & u_{33}^*(\mathbf{x},\mathbf{y}_{sn_s}) \\ u_{12}^*(\mathbf{x},\mathbf{y}_{s1}) & u_{22}^*(\mathbf{x},\mathbf{y}_{s1}) & u_{32}^*(\mathbf{x},\mathbf{y}_{s1}) & \dots & u_{33}^*(\mathbf{x},\mathbf{y}_{sn_s}) & u_{33}^*(\mathbf{x},\mathbf{y}_{sn_s}) & u_{33}^*(\mathbf{x},\mathbf{y}_{sn_s}) \\ u_{13}^*(\mathbf{x},\mathbf{y}_{s1}) & u_{23}^*(\mathbf{x},\mathbf{y}_{s1}) & u_{33}^*(\mathbf{x},\mathbf{y}_{s1}) & \dots & u_{33}^*(\mathbf{x},\mathbf{y}_{sn_s}) & u_{33}^*(\mathbf{x},\mathbf{y}_{sn_s}) & u_{33}^*(\mathbf{x},\mathbf{y}_{sn_s}) \end{bmatrix} \tag{8.11}$$

$$\mathbf{c_e} = [c_{11} \quad c_{21} \quad c_{31} \quad \dots \quad c_{1n_s} \quad c_{2n_s} \quad c_{3n_s}]^T \tag{8.12}$$

in which $\mathbf{x}$ and $\mathbf{y}_{sj}$ are respectively the field points (i.e. the nodal points of the element in this work) and source points in the local coordinate system (X$_1$, X$_2$). The component $u_{ij}^*(\mathbf{x},\mathbf{y}_{sj})$ is the induced displacement component (*i*=1, 2) or electric potential (*i*=3) in the *i*-direction at the field point *x* due to a unit point load (*j*=1, 2) or point charge (*j*=3) applied in the *j*-direction at the source point $\mathbf{y}_{sj}$. The fundamental solution $u_{ij}^*(\mathbf{x},\mathbf{y}_{sj})$ is given as (Ding, Wang et al. 1996)

$$\begin{cases} u_{11}^* = \dfrac{1}{\pi M_{11}} \displaystyle\sum_{j=1}^{3} s_{j1} t_{(2j)1}^1 \ln r_j \\ u_{12}^* = \dfrac{1}{\pi M_{12}} \displaystyle\sum_{j=1}^{3} s_{j2} t_{(2j)2}^1 arctg \dfrac{x_1 - x_{s1}}{s_j \left(x_3 - x_{s3}\right)} \\ u_{13}^* = \dfrac{1}{\pi M_{13}} \displaystyle\sum_{j=1}^{3} s_{j3} t_{(2j)3}^1 arctg \dfrac{x_1 - x_{s1}}{s_j \left(x_3 - x_{s3}\right)} \end{cases} \tag{8.13}$$

$$\begin{cases} u_{21}^* = \dfrac{1}{\pi M_{11}} \displaystyle\sum_{j=1}^{3} d_{j1} t_{(2j)1}^1 arctg \dfrac{x_1 - x_{s1}}{s_j \left(x_3 - x_{s3}\right)} \\ u_{22}^* = \dfrac{1}{\pi M_{12}} \displaystyle\sum_{j=1}^{3} d_{j2} t_{(2j)2}^1 \ln r_j \\ u_{23}^* = \dfrac{1}{\pi M_{13}} \displaystyle\sum_{j=1}^{3} d_{j3} t_{(2j)3}^1 \ln r_j \end{cases} \tag{8.14}$$

$$\begin{cases} u_{31}^* = \dfrac{1}{\pi M_{11}} \displaystyle\sum_{j=1}^{3} g_{j1} t_{(2j)1}^1 arctg \dfrac{x_1 - x_{s1}}{s_j \left(x_3 - x_{s3}\right)} \\ u_{32}^* = \dfrac{1}{\pi M_{12}} \displaystyle\sum_{j=1}^{3} g_{j2} t_{(2j)2}^1 \ln r_j \\ u_{33}^* = \dfrac{1}{\pi M_{13}} \displaystyle\sum_{j=1}^{3} g_{j3} t_{(2j)3}^1 \ln r_j \end{cases} \tag{8.15}$$

where $r_j = \sqrt{\left(x_1 - x_{s1}\right)^2 + s_j^2\left(x_3 - x_{s3}\right)^2}$, and s_j are the three different roots of the characteristic equation $as_i^6 - bs_i^4 + cs_i^3 - d = 0$. The source point $\mathbf{y}_{sj}\,(j = 1, 2, \ldots, n_s)$ can be generated by means of the following method

$$\mathbf{y}_s = \mathbf{x}_0 + \gamma(\mathbf{x}_0 - \mathbf{x}_c) \tag{8.16}$$

where γ is a dimensionless coefficient used to determine the distance between the source point $\mathbf{y}_s$ and the geometrical centroid of the element $\mathbf{x}_c$, and $\mathbf{x}_0$ is a point on the element boundary (i.e. the nodal points in this work) as shown in Figure 8.1.

Making use of Eq.(8.3) and the expression of the intra-element DEP field $\mathbf{u}$ in Eq. (8.10), the corresponding stress and electric displacement Eq.(8.8) can be further written as

$$\boldsymbol{\sigma} = \mathbf{T_e c_e} \tag{8.17}$$

where $\boldsymbol{\sigma} = \begin{bmatrix}\sigma_{11} & \sigma_{22} & \sigma_{12} & D_1 & D_2\end{bmatrix}^T$ and

$$\mathbf{T_e} = \begin{bmatrix} \sigma_{11}^*(\mathbf{x},\mathbf{y}_{s1}) & \sigma_{12}^*(\mathbf{x},\mathbf{y}_{s1}) & \sigma_{13}^*(\mathbf{x},\mathbf{y}_{s1}) & \cdots & \sigma_{11}^*(\mathbf{x},\mathbf{y}_{sn_s}) & \sigma_{12}^*(\mathbf{x},\mathbf{y}_{sn_s}) & \sigma_{13}^*(\mathbf{x},\mathbf{y}_{sn_s}) \\ \sigma_{21}^*(\mathbf{x},\mathbf{y}_{s1}) & \sigma_{22}^*(\mathbf{x},\mathbf{y}_{s1}) & \sigma_{23}^*(\mathbf{x},\mathbf{y}_{s1}) & \cdots & \sigma_{21}^*(\mathbf{x},\mathbf{y}_{sn_s}) & \sigma_{22}^*(\mathbf{x},\mathbf{y}_{sn_s}) & \sigma_{23}^*(\mathbf{x},\mathbf{y}_{sn_s}) \\ \sigma_{31}^*(\mathbf{x},\mathbf{y}_{s1}) & \sigma_{32}^*(\mathbf{x},\mathbf{y}_{s1}) & \sigma_{33}^*(\mathbf{x},\mathbf{y}_{s1}) & \cdots & \sigma_{31}^*(\mathbf{x},\mathbf{y}_{sn_s}) & \sigma_{32}^*(\mathbf{x},\mathbf{y}_{sn_s}) & \sigma_{33}^*(\mathbf{x},\mathbf{y}_{sn_s}) \\ \sigma_{41}^*(\mathbf{x},\mathbf{y}_{s1}) & \sigma_{42}^*(\mathbf{x},\mathbf{y}_{s1}) & \sigma_{43}^*(\mathbf{x},\mathbf{y}_{s1}) & \cdots & \sigma_{41}^*(\mathbf{x},\mathbf{y}_{sn_s}) & \sigma_{42}^*(\mathbf{x},\mathbf{y}_{sn_s}) & \sigma_{43}^*(\mathbf{x},\mathbf{y}_{sn_s}) \\ \sigma_{51}^*(\mathbf{x},\mathbf{y}_{s1}) & \sigma_{52}^*(\mathbf{x},\mathbf{y}_{s1}) & \sigma_{53}^*(\mathbf{x},\mathbf{y}_{s1}) & \cdots & \sigma_{51}^*(\mathbf{x},\mathbf{y}_{sn_s}) & \sigma_{52}^*(\mathbf{x},\mathbf{y}_{sn_s}) & \sigma_{53}^*(\mathbf{x},\mathbf{y}_{sn_s}) \end{bmatrix} \tag{8.18}$$

in which $\sigma_{ij}^*(\mathbf{x},\mathbf{y}_{\mathrm{sj}})$ denotes the corresponding stress components (*i*=1,2,3) or electric displacement (*i*=4,5) along the *i*-direction at the field point $\mathbf{x}$ due to a unit point load (*j*=1,2) or a unit point charge (*j*=3) applied in the *j*-direction at the source point $\mathbf{y}_\mathrm{s}$ and can be derived from Eqs.(8.13)-(8.15), as listed below, which are derived by substituting the fundamental solutions into constitutive equations (Yao and Wang 2005).

$$\begin{cases} \sigma_{11}^* = \dfrac{1}{\pi M_{11}} \displaystyle\sum_{j=1}^{3} \left[\left(c_{11}s_{j1} - c_{13}d_{j1}s_j - e_{31}g_{j1}s_j\right) t_{(2j)1}^1 \dfrac{x_1 - x_{s1}}{r_j^2} \right] \\ \sigma_{12}^* = \dfrac{1}{\pi M_{12}} \displaystyle\sum_{j=1}^{3} \left[\left(c_{11}s_{j2} + c_{13}d_{j2}s_j + e_{31}g_{j2}s_j\right) t_{(2j)2}^1 \dfrac{s_j\left(x_3 - x_{s3}\right)}{r_j^2} \right] \\ \sigma_{13}^* = \dfrac{1}{\pi M_{13}} \displaystyle\sum_{j=1}^{3} \left[\left(c_{11}s_{j3} + c_{13}d_{j3}s_j + e_{31}g_{j3}s_j\right) t_{(2j)3}^1 \dfrac{s_j\left(x_3 - x_{s3}\right)}{r_j^2} \right] \end{cases} \tag{8.19}$$

$$\begin{cases} \sigma_{21}^{*} = \dfrac{1}{\pi M_{11}} \sum_{j=1}^{3} \left[\left(c_{13} s_{j1} - c_{33} d_{j1} s_j - e_{33} g_{j1} s_j \right) t_{(2j)1}^{1} \dfrac{x_1 - x_{s1}}{r_j^2} \right] \\ \sigma_{22}^{*} = \dfrac{1}{\pi M_{12}} \sum_{j=1}^{3} \left[\left(c_{13} s_{j2} + c_{33} d_{j2} s_j + e_{33} g_{j2} s_j \right) t_{(2j)2}^{1} \dfrac{s_j \left(x_3 - x_{s3} \right)}{r_j^2} \right] \\ \sigma_{23}^{*} = -\dfrac{1}{\pi M_{13}} \sum_{j=1}^{3} \left[\left(c_{13} s_{j3} + c_{33} d_{j3} s_j + e_{33} g_{j3} s_j \right) t_{(2j)3}^{1} \dfrac{s_j \left(x_3 - x_{s3} \right)}{r_j^2} \right] \end{cases} \tag{8.20}$$

$$\begin{cases} \sigma_{31}^{*} = \dfrac{1}{\pi M_{11}} \sum_{j=1}^{3} \left[\left(c_{44} s_{j1} s_j + c_{44} d_{j1} + e_{15} g_{j1} \right) t_{(2j)1}^{1} \dfrac{s_j \left(x_3 - x_{s3} \right)}{r_j^2} \right] \\ \sigma_{32}^{*} = \dfrac{1}{\pi M_{12}} \sum_{j=1}^{3} \left[\left(-c_{44} s_{j2} s_j + c_{44} d_{j2} + e_{15} g_{j2} \right) t_{(2j)2}^{1} \dfrac{x_1 - x_{s1}}{r_j^2} \right] \\ \sigma_{33}^{*} = -\dfrac{1}{\pi M_{13}} \sum_{j=1}^{3} \left[\left(-c_{44} s_{j3} s_j + c_{44} d_{j3} + e_{15} g_{j3} \right) t_{(2j)3}^{1} \dfrac{x_1 - x_{s1}}{r_j^2} \right] \end{cases} \tag{8.21}$$

$$\begin{cases} \sigma_{41}^{*} = \dfrac{1}{\pi M_{11}} \sum_{j=1}^{3} \left[\left(e_{15} s_{j1} s_j + e_{15} d_{j1} - \lambda_{11} g_{j1} \right) t_{(2j)1}^{1} \dfrac{s_j \left(x_3 - x_{s3} \right)}{r_j^2} \right] \\ \sigma_{42}^{*} = \dfrac{1}{\pi M_{12}} \sum_{j=1}^{3} \left[\left(-e_{15} s_{j2} s_j + e_{15} d_{j2} - \lambda_{11} g_{j2} \right) t_{(2j)2}^{1} \dfrac{x_1 - x_{s1}}{r_j^2} \right] \\ \sigma_{43}^{*} = -\dfrac{1}{\pi M_{13}} \sum_{j=1}^{3} \left[\left(-e_{15} s_{j3} s_j + e_{15} d_{j3} - \lambda_{11} g_{j3} \right) t_{(2j)3}^{1} \dfrac{x_1 - x_{s1}}{r_j^2} \right] \end{cases} \tag{8.22}$$

$$\begin{cases} \sigma_{51}^{*} = \dfrac{1}{\pi M_{11}} \sum_{j=1}^{3} \left[\left(e_{31} s_{j1} - e_{33} d_{j1} s_j + \lambda_{33} g_{j1} s_j \right) t_{(2j)1}^{1} \dfrac{x_1 - x_{s1}}{r_j^2} \right] \\ \sigma_{52}^{*} = \dfrac{1}{\pi M_{12}} \sum_{j=1}^{3} \left[\left(e_{31} s_{j2} + e_{33} d_{j2} s_j - \lambda_{33} g_{j2} s_j \right) t_{(2j)2}^{1} \dfrac{s_j \left(x_3 - x_{s3} \right)}{r_j^2} \right] \\ \sigma_{53}^{*} = -\dfrac{1}{\pi M_{13}} \sum_{j=1}^{3} \left[\left(e_{31} s_{j3} + e_{33} d_{j3} s_j - \lambda_{33} g_{j3} s_j \right) t_{(2j)3}^{1} \dfrac{s_j \left(x_3 - x_{s3} \right)}{r_j^2} \right] \end{cases} \tag{8.23}$$

in which the coefficients $s_{ij}, d_{ij}, g_{ij}, t_{ij}, M_{11}, M_{12}, M_{13}$ are defined as below (Ding, Wang et al. 1996).

$$\begin{aligned} a_{i1} &= -c_{13} m_1 + m_6 s_i^2 + m_7 s_i^4 \\ b_{i1} &= m_8 s_i + m_9 s_i^3 + c_{44} m_3 s_i^5 \\ p_{i1} &= -e_{31} m_1 + m_{10} s_i^2 + m_{11} s_i^4 \\ d_{i1} &= -h_1 s_i + h_2 s_i^3 \\ s_{i1} &= m_1 - m_2 s_i^2 + m_3 s_i^4 \\ g_{i1} &= m_4 s_i - m_5 s_i^3 \end{aligned} \tag{8.24}$$

$$\begin{aligned} a_{i2} &= h_7 s_i^5 + h_6 s_i^3 + h_5 s_i \\ b_{i2} &= h_{10} s_i^4 - h_9 s_i^2 - h_8 \\ p_{i2} &= h_{12} s_i^3 + h_{11} s_i \\ d_{i2} &= c_{44} f_{33} s_i^4 - h_3 s_i^2 + c_{11} f_{11} \\ s_{i2} &= h_2 s_i^3 - h_1 s_i \\ g_{i2} &= c_{44} e_{33} s_i^4 - h_4 s_i^2 + c_{11} e_{15} \end{aligned} \tag{8.25}$$

$$\begin{aligned}
a_{i3} &= n_2 s_i + n_3 s_i^3 \\
b_{i3} &= -n_4 s_i^2 + n_5 s_i^4 \\
p_{i3} &= n_6 s_i + n_7 s_i^3 + n_8 s_i^5 \\
d_{i3} &= -c_{11} e_{15} + h_4 s_i^2 - c_{44} e_{33} s_i^4 \\
s_{i3} &= -m_4 s_i + m_5 s_i^3 \\
g_{i3} &= c_{11} c_{44} - n_1 s_i^2 + c_{44} c_{33} s_i^4
\end{aligned} \tag{8.26}$$

$$\begin{aligned}
M_{11} &= -2[b_{11} t_{21}^1 + b_{21} t_{41}^1 + b_{31} t_{61}^1] \\
M_{12} &= -2[a_{12} t_{22}^1 + a_{22} t_{42}^1 + a_{32} t_{62}^1] \\
M_{13} &= -2[p_{13} t_{23}^1 + p_{23} t_{43}^1 + p_{33} t_{63}^1]
\end{aligned} \tag{8.27}$$

$$\begin{aligned}
&t_{21}^1 = d_{21} g_{31} - d_{31} g_{21}, \quad t_{41}^1 = d_{31} g_{11} - d_{11} g_{31}, \quad t_{61}^1 = d_{11} g_{21} - d_{21} g_{11}, \\
&t_{22}^1 = p_{32} s_{22} - p_{22} s_{32}, \quad t_{42}^1 = p_{12} s_{32} - p_{32} s_{12}, \quad t_{62}^1 = p_{22} s_{12} - p_{12} s_{22}, \\
&t_{23}^1 = a_{23} s_{33} - a_{33} s_{23}, \quad t_{43}^1 = a_{33} s_{13} - a_{13} s_{33}, \quad t_{63}^1 = a_{13} s_{23} - a_{23} s_{13},
\end{aligned} \tag{8.28}$$

$$\begin{aligned}
n_1 &= c_{11} c_{33} - c_{13} c_{13} - 2 c_{13} c_{44}; & n_5 &= c_{44}(m_5 + c_{44} e_{33} - c_{33} e_{15}); \\
n_2 &= -c_{13} m_4 + c_{11}(c_{44} e_{33} - c_{33} e_{15}); & n_6 &= -e_{33} m_4 + c_{11}(e_{15} e_{33} + c_{44} \kappa_{33}); \\
n_3 &= c_{13} m_5 + c_{33} h_4 - e_{33} n_1; & n_7 &= e_{31} m_5 + e_{33} h_4 + n_1 \kappa_{33}; \\
n_4 &= c_{44}(m_4 + h_4) - e_{15} n_1; & n_8 &= -c_{44} e_{33} e_{33} - c_{33} c_{44} \kappa_{33};
\end{aligned} \tag{8.29}$$

$$\begin{aligned}
h_1 &= (c_{13} + c_{44}) \kappa_{11} + (e_{15} + e_{31}) e_{15}; \\
h_2 &= (c_{13} + c_{44}) \kappa_{33} + (e_{15} + e_{31}) e_{33}; \\
h_3 &= c_{11} \kappa_{33} + c_{44} \kappa_{11} + (e_{15} + e_{31})(e_{15} + e_{31}); \\
h_4 &= c_{11} e_{33} - c_{13}(e_{15} + e_{31}) - c_{44} e_{31}; \\
h_5 &= c_{11}(c_{33} \kappa_{11} + e_{15} e_{33}) - c_{13} h_1; \\
h_6 &= c_{13} h_2 - c_{33} h_3 - e_{33} h_4; \\
h_7 &= c_{44}(c_{33} \kappa_{33} + e_{33} e_{33}); \\
h_8 &= c_{11}(c_{44} \kappa_{11} + e_{15} e_{15}); \\
h_9 &= c_{44}(h_1 - h_3) - e_{15} h_4; \\
h_{10} &= c_{44}(h_2 - c_{44} \kappa_{33} - e_{15} e_{33}); \\
h_{11} &= c_{11}(\kappa_{11} e_{33} - \kappa_{33} e_{15}) - e_{31} h_1; \\
h_{12} &= e_{31} h_2 - e_{33} h_3 + \kappa_{33} h_4;
\end{aligned} \tag{8.30}$$

$$\begin{aligned}
m_1 &= c_{44} \kappa_{11} + e_{15} e_{15}; \\
m_2 &= c_{44} \kappa_{33} + c_{33} \kappa_{11} + 2 e_{15} e_{33}; \\
m_3 &= c_{33} \kappa_{33} + e_{33} e_{33}; \\
m_4 &= c_{44} e_{31} - c_{13} e_{15}; \\
m_5 &= -(c_{13} + c_{44}) e_{33} + (e_{15} + e_{31}) c_{33}; \\
m_6 &= c_{13} m_2 - c_{33} h_1 + e_{33} m_4; \\
m_7 &= -c_{13} m_3 + c_{33} h_2 - e_{33} m_5; \\
m_8 &= c_{44} m_1 - c_{44} h_1 + e_{15} m_4; \\
m_9 &= -c_{44} m_2 + c_{44} h_2 - e_{15} m_5; \\
m_{10} &= e_{31} m_2 - e_{33} h_1 - \kappa_{33} m_4; \\
m_{11} &= -e_{31} m_3 + e_{33} h_2 + \kappa_{33} m_5;
\end{aligned} \tag{8.31}$$

From Eqs. (8.2), (8.5) and (8.7), the generalized traction forces and electric displacement can be given as

$$\begin{Bmatrix} t_1 \\ t_2 \\ D_n \end{Bmatrix} = \begin{Bmatrix} \mathbf{Q}_1 \\ \mathbf{Q}_2 \\ \mathbf{Q}_3 \end{Bmatrix} \mathbf{c_e} = \mathbf{Q_e} \mathbf{c_e} \tag{8.32}$$

where

$$\mathbf{Q_e} = \mathbf{n} \mathbf{T_e} \tag{8.33}$$

$$\mathbf{n}=\begin{bmatrix} n_1 & 0 & n_2 & 0 & 0 \\ 0 & n_2 & n_1 & 0 & 0 \\ 0 & 0 & 0 & n_1 & n_2 \end{bmatrix} \tag{8.34}$$

The unknown coefficient $\mathbf{c_e}$ may be calculated from the conditions on the external boundary and/or the continuity conditions on the inter-element boundary. In the majority of cases a hybrid technique is used, whereby the elements are linked through an auxiliary conforming displacement frame which has the same form as in the conventional FEM. This means that a conforming DEP field should be independently defined on the element boundary to enforce field continuity between elements and also to link the coefficient $\mathbf{c_e}$, appearing in Eq.(8.10), with nodal DEP $\mathbf{d_e}$. For the 2D piezoelectric problem under consideration, the frame field is assumed as

$$\tilde{\mathbf{u}}(\mathbf{x})=\begin{Bmatrix} \tilde{u}_1 \\ \tilde{u}_2 \\ \tilde{\phi} \end{Bmatrix}=\begin{Bmatrix} \tilde{\mathbf{N}}_1 \\ \tilde{\mathbf{N}}_2 \\ \tilde{\mathbf{N}}_3 \end{Bmatrix}\mathbf{d}_e=\tilde{\mathbf{N}}_e\mathbf{d}_e, \qquad (\mathbf{x}\in\Gamma_e) \tag{8.35}$$

where the symbol "~" is used to specify that the field is defined on the element boundary only, $\mathbf{d}_e=\mathbf{d}_e(\mathbf{c}_e)$ stands for the vector of the nodal displacements which are the final unknowns of the problem, Γ_e represents the boundary of element *e*, and $\tilde{\mathbf{N}}_e$ is a matrix of the corresponding shape functions which are the same as those used in the conventional FEM. For example, for the side 3-4-5 of a particular quadratic element as shown in Figure 8.1, the shape function matrix $\tilde{\mathbf{N}}_e$ and nodal vector $\mathbf{d_e}$ can be given in the form

$$\tilde{\mathbf{N}}_e=\begin{bmatrix} \underset{6}{0\cdots0} & \tilde{N}_1 & 0 & 0 & \tilde{N}_2 & 0 & 0 & \tilde{N}_3 & 0 & 0 & 0\cdots0 \\ 0\cdots0 & 0 & \tilde{N}_1 & 0 & 0 & \tilde{N}_2 & 0 & 0 & \tilde{N}_3 & 0 & 0\cdots0 \\ 0\cdots0 & 0 & 0 & \tilde{N}_1 & 0 & 0 & \tilde{N}_2 & 0 & 0 & \tilde{N}_3 & \underset{9}{0\cdots0} \end{bmatrix} \tag{8.36}$$

$$\mathbf{d_e}=\begin{bmatrix} u_{11} & u_{21} & \phi_1 & \cdots & u_{14} & u_{24} & \phi_4 & \cdots & u_{18} & u_{28} & \phi_8 \end{bmatrix}^T \tag{8.37}$$

where the shape functions are expressed by natural coordinate ξ

$$\tilde{N}_1=-\frac{\xi(1-\xi)}{2},\ \tilde{N}_2=1-\xi^2,\ \tilde{N}_3=\frac{\xi(1+\xi)}{2} \quad (\xi\in[-1,1]) \tag{8.38}$$

8.3.2. Variational principles

Based on the assumption of two distinct DEP fields, the Euler equations of the proposed variational functional should also satisfy the following inter-element continuity requirements in addition to Eqs.(8.4)-(8.7):

$$u_{ie} = u_{if} \quad \phi_e = \phi_f \qquad (\text{on } \Gamma_e \cap \Gamma_f \text{, conformity}) \tag{8.39}$$

$$t_{ie} + t_{if} = 0 \quad D_{ne} + D_{nf} = 0 \quad (\text{on } \Gamma_e \cap \Gamma_f \text{, reciprocity}) \tag{8.40}$$

where '*e*' and '*f*' stand for any two neighboring elements. Eqs. (8.1)-(8.7) together with Eq. (8.39) and Eq. (8.40) can now be taken as the basis to establish the modified variational principle for the hybrid FEM of piezoelectric materials (Qin 2000; Qin 2003).

Since the stationary conditions of the traditional potential or complementary variational functional cannot satisfy the inter-element continuity condition required in the proposed HFS-FEM, new modified variational functional must be developed. In the absence of the body forces and electric charge density, the hybrid functional Π_{me} for a particular element *e* is constructed as

$$\Pi_{me} = \Pi_e + \int_{\Gamma_e} t_i(\tilde{u}_i - u_i)d\Gamma + \int_{\Gamma_e} D_n(\tilde{\phi} - \phi)d\Gamma \tag{8.41}$$

where

$$\Pi_e = \frac{1}{2}\iint_{\Omega_e} (\sigma_{ij}\varepsilon_{ij} + D_i E_i)d\Omega - \int_{\Gamma_t} \bar{t}_i \tilde{u}_i d\Gamma - \int_{\Gamma_D} \bar{D}_n \tilde{\phi} d\Gamma \tag{8.42}$$

and the boundary Γ_e of the element *e* is

$$\Gamma_e = \Gamma_{eu} \cup \Gamma_{et} \cup \Gamma_{eI} = \Gamma_{e\phi} \cup \Gamma_{eD} \cup \Gamma_{eI} \tag{8.43}$$

and

$$\Gamma_{eu} = \Gamma_e \cap \Gamma_u, \Gamma_{et} = \Gamma_e \cap \Gamma_t, \Gamma_{e\phi} = \Gamma_e \cap \Gamma_\phi, \Gamma_{eD} = \Gamma_e \cap \Gamma_D \tag{8.44}$$

and Γ_{eI} is the inter-element boundary of element *e*. Compared to the functional employed in conventional FEM, the present hybrid functional is constructed by adding two integral terms related to the intra-element and element frame DEP fields to guarantee the satisfaction of the DEP continuity condition on the common boundary of two adjacent elements.

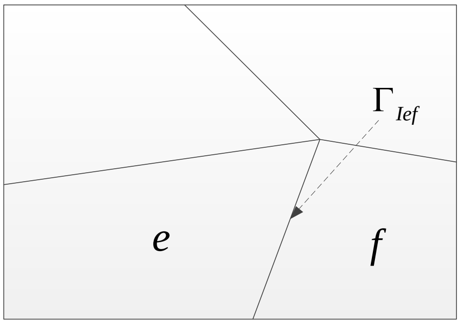

Figure 8.2 Illustration of continuity between two adjacent elements '*e*' and '*f*'.

It can be proved that the stationary conditions of the above functional (8.42) leads to Eqs.(8.1)-(8.7). To this end, performing a variation of Π_m, one obtains

$$\delta\Pi_{me} = \delta\Pi_e + \int_{\Gamma_e} [(\tilde{u}_i - u_i)\delta t_i + t_i(\delta\tilde{u}_i - \delta u_i)]d\Gamma + \int_{\Gamma_e} [(\tilde{\phi} - \phi)\delta D_n + D_n(\delta\tilde{\phi} - \delta\phi)]d\Gamma \tag{8.45}$$

in which the first term is

$$\delta\Pi_e = \iint_{\Omega_e} \sigma_{ij}\delta u_{i,j} d\Omega + \iint_{\Omega_e} D_i \delta\phi_{,i} d\Omega - \int_{\Gamma_{et}} \bar{t}_i \delta\tilde{u}_i d\Gamma - \int_{\Gamma_{eD}} \bar{D}_n \delta\tilde{\phi} d\Gamma \tag{8.46}$$

Applying Gaussian theorem

$$\iint_{\Omega_e} f_{,i} d\Omega = \int_{\Gamma_e} f \cdot n_i d\Gamma \tag{8.47}$$

and the definitions of traction force and electrical displacement

$$t_i = \sigma_{ij} n_j, \quad D_n = D_i n_i \tag{8.48}$$

and considering the fact

$$\int_{\Gamma_{eu}} t_i \delta\tilde{u}_i d\Gamma = 0, \ \int_{\Gamma_{e\phi}} D_n \delta\tilde{\phi} d\Gamma = 0 \tag{8.49}$$

following form is finally derived

$$\begin{aligned} \delta\Pi_{me} = &-\iint_{\Omega_e} \sigma_{ij,j}\delta u_i d\Omega - \iint_{\Omega_e} D_{i,i}\delta\phi d\Omega + \int_{\Gamma_{et}} (t_i - \bar{t}_i)\delta\tilde{u}_i d\Gamma + \int_{\Gamma_{eD}} (D_n - \bar{D}_n)\delta\tilde{\phi} d\Gamma \\ &+ \int_{\Gamma_e} (\tilde{u}_i - u_i)\delta t_i d\Gamma + \int_{\Gamma_e} (\tilde{\phi} - \phi)\delta D_n d\Gamma + \int_{\Gamma_I} t_i \delta\tilde{u}_i d\Gamma + \int_{\Gamma_I} D_n \delta\tilde{\phi} d\Gamma \end{aligned} \tag{8.50}$$

Therefore, the Euler equations for Eq. (8.50) result in Eqs. (8.1)-(8.7) and Eq. (8.39) because the quantities δu_i, δt_i, $\delta\phi$, δD_n, $\delta\tilde{u}_i$, and $\delta\tilde{\phi}$ may be arbitrary. As for the continuity condition of Eq. (8.40), it can easily be seen from the following variational of two adjacent elements such as *e* and *f*:

$$\begin{aligned} \delta\Pi_{m(e\cup f)} = &-\iint\limits_{\Omega_e \cup \Omega_f} \sigma_{ij,j}\delta u_i d\Omega - \iint\limits_{\Omega_e \cup \Omega_f} D_{i,i}\delta\phi d\Omega + \int\limits_{\Gamma_{et}+\Gamma_{et}} (t_i - \bar{t}_i)\delta\tilde{u}_i d\Gamma + \int\limits_{\Gamma_{eD}+\Gamma_{fD}} (D_n - \bar{D}_n)\delta\tilde{\phi} d\Gamma \\ &+ \int\limits_{\Gamma_e+\Gamma_f} (\tilde{u}_i - u_i)\delta t_i d\Gamma + \int\limits_{\Gamma_e+\Gamma_f} (\tilde{\phi} - \phi)\delta D_n d\Gamma + \int_{\Gamma_{efI}} \left(t_{ie} + t_{if}\right)\delta\tilde{u}_i + \int_{\Gamma_{efI}} \left(D_{ne} + D_{nf}\right)\delta\tilde{\phi} d\Gamma \end{aligned} \tag{8.51}$$

This indicates that the stationary condition of the functional satisfies both the required boundary and inter-element continuity equations. In addition, the existence of extremum of functional (8.41) can be easily proved by the so-called “second variational approach” as well, which indicates that functional (8.41) has a local extreme. Therefore, it can be concluded that functional (8.41) can be used for deriving hybrid finite element formulations.

8.3.3. Element stiffness equation

The element stiffness equation can be generated by setting $\delta\Pi_{me}=0$. To simplify the derivation, all domain integrals in Eq. (8.41) are first transformed into boundary ones. Making use of the Gaussian theorem, the functional in Eq. (8.41) may be simplified as

$$\begin{aligned}\Pi_{me}=&\frac{1}{2}\left(\int_{\Gamma_e}t_iu_i d\Gamma-\iint_{\Omega_e}\sigma_{ij,j}u_i d\Omega\right)+\frac{1}{2}\left(\int_{\Gamma_e}D_n\phi d\Gamma-\iint_{\Omega_e}D_{i,i}\phi d\Omega\right)\\&-\int_{\Gamma_t}\bar{t}_i\tilde{u}_i d\Gamma-\int_{\Gamma_D}\bar{D}_n\tilde{\phi}d\Gamma+\int_{\Gamma_e}t_i(\tilde{u}_i-u_i)d\Gamma+\int_{\Gamma_e}D_n(\tilde{\phi}-\phi)d\Gamma\end{aligned}\tag{8.52}$$

Due to satisfaction of the equilibrium equation with the constructed intra-element fields, we have the following expression for the HT finite element model

$$\Pi_{me}=-\frac{1}{2}\int_{\Gamma_e}(t_iu_i+D_n\phi)d\Gamma+\int_{\Gamma_e}(t_i\tilde{u}_i+D_n\tilde{\phi})d\Gamma-\int_{\Gamma_t}\bar{t}_i\tilde{u}_i d\Gamma-\int_{\Gamma_D}\bar{D}_n\tilde{\phi}d\Gamma\tag{8.53}$$

Substituting Eqs. (8.10), (8.35) and (8.32) into the above functional yields the formulation as

$$\Pi_{me}=-\frac{1}{2}\mathbf{c}_e^{T}\mathbf{H}_e\mathbf{c}_e+\mathbf{c}_e^{T}\mathbf{G}_e\mathbf{d}_e-\mathbf{d}_e^{T}\mathbf{g}_e\tag{8.54}$$

where

$$\mathbf{H}_e=\int_{\Gamma_e}\mathbf{Q}_e^{\mathrm{T}}\mathbf{N}_e\mathrm{d}\Gamma,\quad \mathbf{G}_e=\int_{\Gamma_e}\mathbf{Q}_e^{\mathrm{T}}\tilde{\mathbf{N}}_e\mathrm{d}\Gamma,\quad \mathbf{g}_e=\int_{\Gamma_t}\tilde{\mathbf{N}}_e^{\mathrm{T}}\bar{\mathbf{t}}d\Gamma+\int_{\Gamma_D}\tilde{\mathbf{N}}_e^{\mathrm{T}}\bar{\mathbf{D}}d\Gamma\tag{8.55}$$

To enforce inter-element continuity on the common element boundary, the unknown vector $\mathbf{c}_e$ should be expressed in terms of nodal DOF $\mathbf{d}_e$. The stationary condition of the functional Π_{me} with respect to $\mathbf{c}_e$ and $\mathbf{d}_e$, respectively, yields

$$\frac{\partial\Pi_{me}}{\partial\mathbf{c}_e^{\mathrm{T}}}=-\mathbf{H}_e\mathbf{c}_e+\mathbf{G}_e\mathbf{d}_e=\mathbf{0}\tag{8.56}$$

$$\frac{\partial\Pi_{me}}{\partial\mathbf{d}_e^{\mathrm{T}}}=\mathbf{G}_e^{T}\mathbf{c}_e-\mathbf{g}_e=\mathbf{0}\tag{8.57}$$

from which the relationship between $\mathbf{c}_e$ and $\mathbf{d}_e$, and the stiffness equation can be obtained

$$\mathbf{c}_e = \mathbf{H}_e^{-1}\mathbf{G}_e\mathbf{d}_e \tag{8.58}$$

$$\mathbf{K}_e\mathbf{d}_e = \mathbf{g}_e \tag{8.59}$$

where $\mathbf{K}_e = \mathbf{G}_e{}^{\mathrm{T}}\mathbf{H}_e{}^{-1}\mathbf{G}_e$ is the element stiffness matrix.

The missing rigid-body motion can be recovered by setting the augmented internal field of a particular element e as

$$\mathbf{u}_e = \mathbf{N}_e\mathbf{c}_e + \begin{bmatrix} 1 & 0 & x_2 & 0 \\ 0 & 1 & -x_1 & 0 \\ 0 & 0 & 0 & 1 \end{bmatrix}\mathbf{c}_0 \tag{8.60}$$

where the undetermined rigid-body motion parameter $\mathbf{c}_0$ can be calculated using the least square matching of $\mathbf{u_e}$ and $\tilde{\mathbf{u}}_\mathbf{e}$ at element nodes

$$\min = \sum_{i=1}^{n}\left[\left(u_{1i} - \tilde{u}_{1i}\right)^2 + \left(u_{2i} - \tilde{u}_{2i}\right)^2 + \left(\phi_i - \tilde{\phi}_i\right)^2\right] \tag{8.61}$$

which finally gives

$$\mathbf{c_0} = \mathbf{R}_e^{-1}\mathbf{r_e} \tag{8.62}$$

$$\mathbf{R_e} = \sum_{i=1}^{n}\begin{bmatrix} 1 & 0 & x_{2i} & 0 \\ 0 & 1 & -x_{1i} & 0 \\ x_{2i} & -x_{1i} & x_{1i}^2 + x_{2i}^2 & 0 \\ 0 & 0 & 0 & 1 \end{bmatrix} \tag{8.63}$$

$$\mathbf{r_e} = \sum_{i=1}^{n}\begin{bmatrix} \Delta u_{e1i} \\ \Delta u_{e2i} \\ \Delta u_{e1i}x_{2i} - \Delta u_{e2i}x_{1i} \\ \Delta\phi_{ei} \end{bmatrix} \tag{8.64}$$

and $\Delta\mathbf{u}_{ei} = \left(\tilde{\mathbf{u}}_e - \hat{\mathbf{u}}_e\right)\big|_{\mathbf{node\,i}}$, n is the number of element nodes. As a consequence, $\mathbf{c}_0$ can be calculated by Eq.(8.62) once the nodal DEP fields $\mathbf{d}_e$ and the interpolation coefficients $\mathbf{c}_e$ are respectively determined by Eqs. (8.59) and (8.58). Then the complete DEP fields $\mathbf{u}_e$ can be obtained from Eq. (8.60).

8.3.4. Normalization of the variables

The orders of magnitude of the material constants and the corresponding field variables in piezoelectricity have a wide spectrum as large as 10^{19} in SI units. This will lead to an ill-conditioned matrix of the system. To resolve this problem, normalization of each quantity by its reference value should be employed in dealing with piezoelectric problems. The reference values for the stiffness, piezoelectric stress constant, dielectric constants, and strain are selected to be $c_0 = 10^{11}\left(N/m^2\right)$, $e_0 = 10^1 (N/mV)$, $k_0 = 10^{-9}\left(C/mV\right)$, and $\varepsilon_0 = 10^{-3}\left(V/m\right)$, respectively. The reference values of other quantities, as shown in Table 8.1, are determined in terms of these four fundamental reference variables and the characteristic length $x_0 = 10^0\left(m\right)$ of the problem, so that the normalized governing equations remain in exactly the same form as the original equations.

Table 8.1 Reference values for material constants and field variables in piezoelectricity derived from basic reference variables: $c_0, e_0, k_0, \varepsilon_0$ and x_0.

Displacement	$u_0 = x_0\varepsilon_0 = 10^{-3}(m)$	Electric Potential	$\phi_0 = x_0 E_0 = 10^7 (V)$
Stress	$\sigma_0 = c_0\varepsilon_0 = 10^8 (N/m^2)$	Electric induction	$D_0 = k_0 E_0 = 10^{-2}(C/m^2)$
Compliance	$s_0 = \dfrac{\varepsilon_0}{\sigma_0} = 10^{-11}(m^2/N)$	Impermeability	$\beta_0 = \dfrac{E_0}{D_0} = 10^9 (mV/C)$
Electric field	$E_0 = \dfrac{\sigma_0}{e_0} = 10^7 (V/m)$	Piezoelectric strain constant	$g_0 = \dfrac{E_0}{\sigma_0} = 10^{-1}(mV/N)$

8.3.5. Numerical results

Numerical examples are presented in this section to illustrate the effectiveness and accuracy of the proposed method. In the first example, a piezoelectric panel subjected to a linearly varying stress at one edge is modeled. The stability, convergence, and accuracy of the method are discussed. Simple tension of a piezoelectric prism is then simulated to investigate the effect of mesh distortion, and a simply supported bimorph beam made of PZT-4 with different poling directions is investigated. Finally, an infinite plate with a circular hole subjected to remote tension is studied to demonstrate the influence of the hole's radius on the stress concentration factor (SCF), and a recommended dimension for modeling the infinite piezoelectric plate is presented. It should be noted that the plane strain condition is considered in the following examples.

Example 1: Bending of a piezoelectric panel

As shown in Figure 8.3, a 1×1mm piezoelectric panel made of PZT-4 is subjected to a linearly varying stress at the right edge. The corresponding boundary conditions are

$$\sigma_{xx} = z, \quad \sigma_{xz} = D_x = 0, \qquad \text{at } x = L/2 \tag{8.65}$$

$$u_x = 0, u_z = 0, D_x = 0 \qquad \text{at } x = -L/2, z = 0 \tag{8.66}$$

$$u_x = 0, \sigma_{xz} = D_x = 0 \qquad \text{at } x = -L/2, z \neq 0 \tag{8.67}$$

$$\phi = 0, \sigma_{xz} = \sigma_z = 0 \qquad \text{at } x = h/2 \tag{8.68}$$

$$u_x = 0, \sigma_{xz} = \sigma_{zz} = D_z = 0 \qquad \text{at } x = h/2 \tag{8.69}$$

The properties of the material PZT-4 (Sze, Yang et al. 2004) are given in Table 8.2. In this example, 16 quadratic elements are used to model the piezoelectric panel as shown in Figure 8.4. In the proposed hybrid FEM, the position of source points will affect the accuracy and stability of the numerical results. Thus, it is of interest and importance to determine a suitable range of the parameter γ, which is used in the present analysis to generate the source points according to the related element nodes. In this analysis, the variation of the stress σ_{xx} at point A (0, 0.5 mm), the condition number of matrix **H** and the condition number of global stiffness matrix **K** with parameter γ are presented in Figure 8.5 and Figure 8.6, respectively.

Table 8.2 Properties of the material PZT-4 used in Example 1.

Parameters	Values	Parameters	Values
c_{11}	$13.9\times10^{10}\,\mathrm{Nm^{-2}}$	e_{15}	$13.44\,\mathrm{Cm^{-2}}$
c_{12}	$7.78\times10^{10}\,\mathrm{Nm^{-2}}$	e_{31}	$-6.98\,\mathrm{Cm^{-2}}$
c_{13}	$7.43\times10^{10}\,\mathrm{Nm^{-2}}$	e_{33}	$13.84\,\mathrm{Cm^{-2}}$
c_{33}	$11.3\times10^{10}\,\mathrm{Nm^{-2}}$	κ_{11}	$6.0\times10^{-9}\,\mathrm{C/Nm}$
c_{44}	$2.56\times10^{10}\,\mathrm{Nm^{-2}}$	κ_{33}	$5.47\times10^{-9}\,\mathrm{C/Nm}$

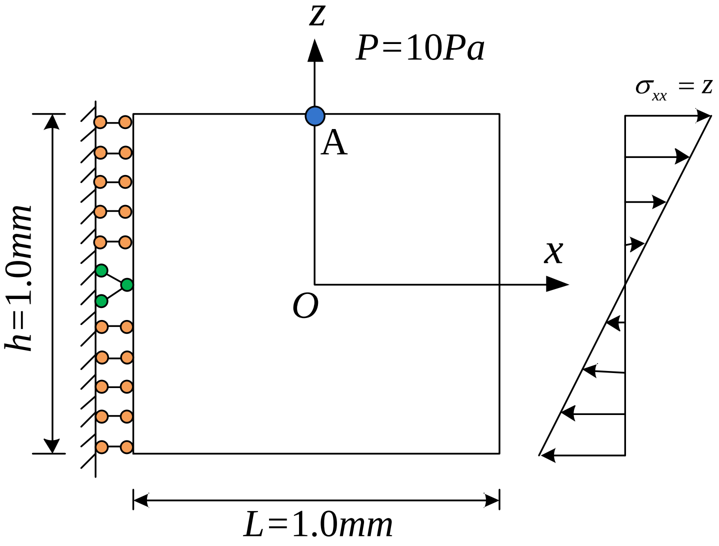

Figure 8.3 Bending of a piezoelectric panel.

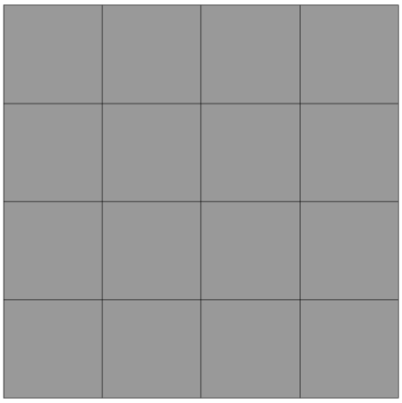

Figure 8.4 Mesh used for the piezoelectric panel by HFS-FEM.

It can be seen from Figure 8.5 and Figure 8.6 that the results of both stress and condition number are stable when $3 < \gamma < 15$ for the investigated range, but they fluctuate dramatically when $\gamma < 3$. This can be explained by the fact that for small values of γ ($\gamma < 3$), the source points are close to the element boundary, which results in strong disturbance of the singularity of the fundamental solutions to numerical accuracy. Conversely, for larger γ the source points are distant from the element boundary, so that the potential round-off error will lead to some components of the **H** matrix having nearly the same value, which in turn gives **H** a larger condition number and results in a large round-off error in the inverse manipulation of the **H** matrix [30]. Therefore, it is advised to choose the parameter 3 < γ < 10. In the following computations, γ is chosen to be 5.

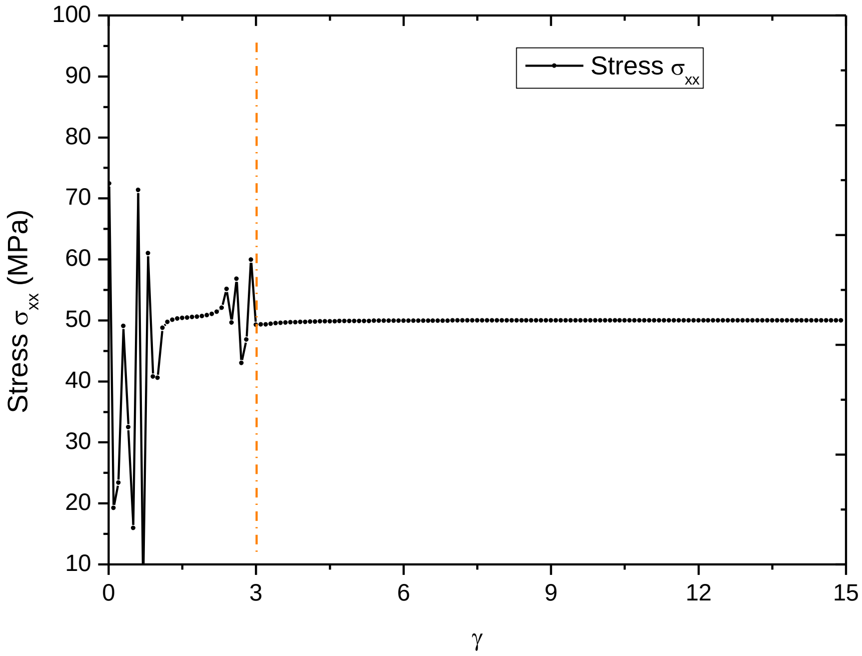

Figure 8.5 Variation of the stress σ_{xx} at point A (0, 0.5mm) with parameter γ.

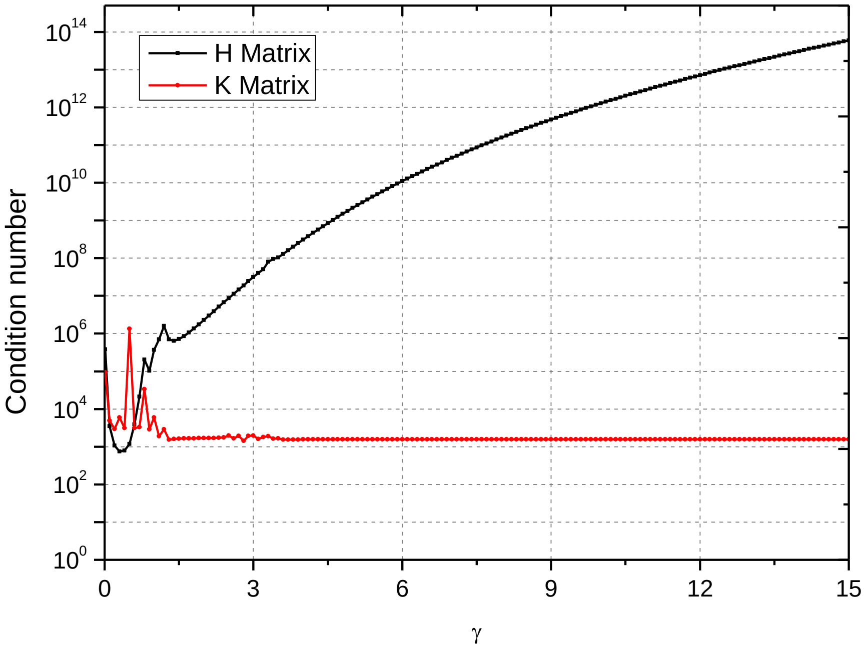

Figure 8.6 Variation of the condition number of H matrix and K matrix with parameter γ.

Table 8.3 Comparison of HFS-FEM and analytical results (Sze, Yang et al. 2004) for the piezoelectric panel

Position (x, z) (mm, mm)	u_x (10^{-17}m)		u_z (10^{-17}m)		ϕ (10^{-8}V)	
	HFS-FEM	Exact	HFS-FEM	Exact	HFS-FEM	Exact
(0.0, 0.5)	1.9805	1.9805	-1.3691	-1.3691	0.0000	0.0000
(0.5, 0.0)	0.0000	0.0000	-3.9609	-3.9610	2.2225	2.2225
(0.25, 0.5)	2.9707	2.9708	-2.6069	-2.6069	0.0000	0.0000
(0.5, 0.25)	1.9804	1.9805	-4.0556	-4.0557	1.6667	1.6669
(0.5, 0.5)	3.9609	3.9610	-4.3398	-4.3399	0.0000	0.0000

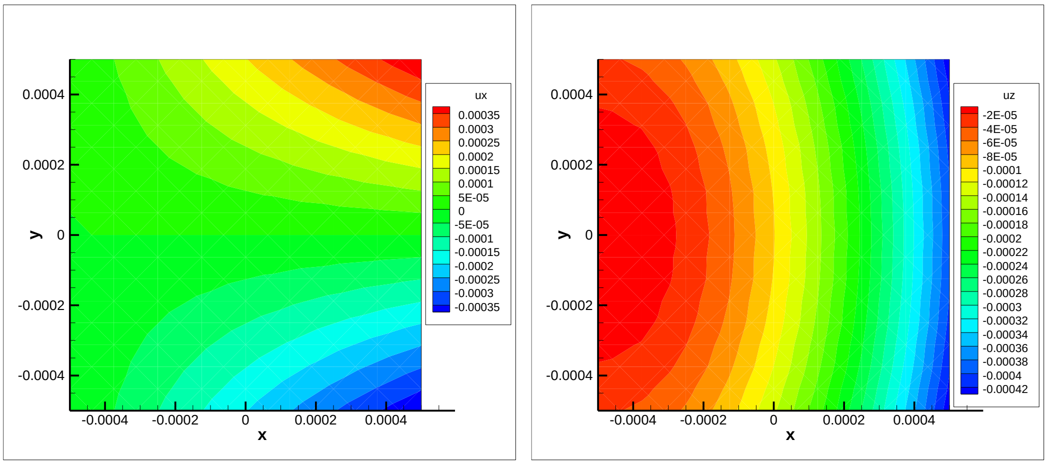

(a) u_x (unit: $10^{-13} m$) (b) u_z (unit: $10^{-13} m$)

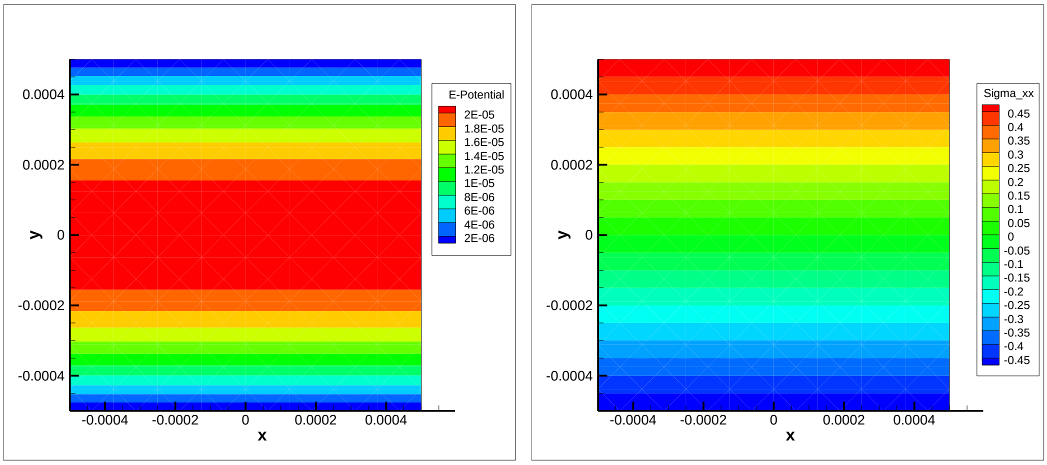

(c) ϕ (unit: $10^{-3} V$) (d) σ_{xx} (unit: $10^{-5} Pa$)

Figure 8.7 Contour plots of displacements, electrical potential and stress.

Table 8.3 lists the DEP at five different reference points, in which the analytical results (Sze, Yang et al. 2004) are also presented for comparison. It is obvious that the proposed approach has good accuracy and the results agree very well with the analytical solutions. Figure 8.7 shows the contour plots for the displacements u_x, u_z, electrical potential ϕ and stress σ_{xx}, clearly demonstrating the distribution of the variables of interest.

Example 2: Simple tension of a piezoelectric prism

In this example a PZT-4 piezoelectric prism subjected to simple tension, as shown in Figure 8.8, is considered. The properties of the material PZT-4 (Ding, Wang et al. 1998) are given in Table 8.4. The corresponding boundary conditions are

$$\sigma_{xx} = \sigma_{xz} = D_x = 0 \quad \text{at } x = \pm a \tag{8.70}$$

$$\sigma_{zz} = P, \ \sigma_{xz} = D_z = 0 \quad \text{at } z = \pm h \tag{8.71}$$

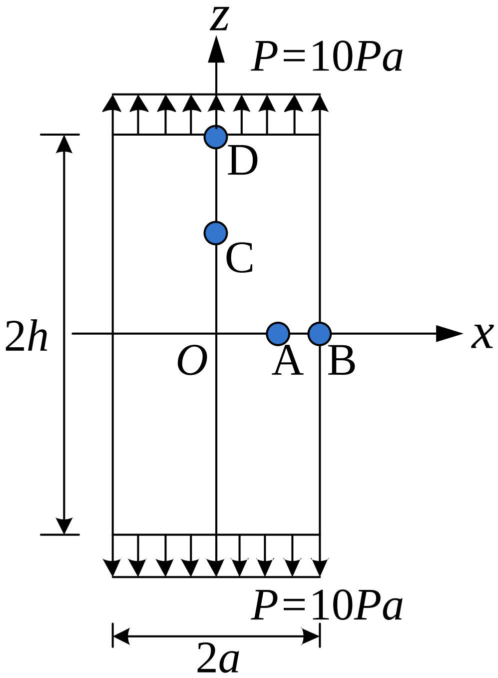

Figure 8.8 Geometry and boundary conditions of the piezoelectric prism.

In the analysis, the dimensions of the geometry are set as a = 3 m, h = 10 m, P = 10 Pa. Considering the symmetry conditions of the problem, only one quadrant of the prism is analyzed. As shown in Figure 8.9, 30 8-node quadrilateral elements are used in the analysis. The displacements and electric potential at the four selected reference points, A (2,0), B (3,0), C (0,5), and D (0,10), are listed in Table 8.5. The analytical results of the corresponding points are also given for comparison (Ding, Wang et al.

1998). It is found that the HFS-FEM results are in good agreement with the analytical ones.

Table 8.4 Properties of the material PZT-4 used in Example 2.

Parameters	Values	Parameters	Values
c_{11}	$12.6\times10^{10}\,\mathrm{Nm}^{-2}$	e_{15}	$12.7\mathrm{Cm}^{-2}$
c_{12}	$7.78\times10^{10}\,\mathrm{Nm}^{-2}$	e_{31}	$-5.2\mathrm{Cm}^{-2}$
c_{13}	$7.43\times10^{10}\,\mathrm{Nm}^{-2}$	e_{33}	$15.1\mathrm{Cm}^{-2}$
c_{33}	$11.5\times10^{10}\,\mathrm{Nm}^{-2}$	κ_{11}	$6.463\times10^{-9}\,\mathrm{C/Nm}$
c_{44}	$2.56\times10^{10}\,\mathrm{Nm}^{-2}$	κ_{33}	$5.622\times10^{-9}\,\mathrm{C/Nm}$

Table 8.5 Comparison of the predicted results from HFS-FEM with the analytical results.

Position	u_x $(10^{-10}\mathrm{m})$	u_z $(10^{-9}\mathrm{m})$	ϕ (V)	σ_{xx} $(\mathrm{N\cdot m^{-2}})$	σ_{zz} $(\mathrm{N\cdot m^{-2}})$	D_z $(\mathrm{N\cdot m^{-2}})$
A	-0.7220 (-0.7222)	0.0000 (0.0000)	0.0000 (0.0000)	0.0018 (0.0000)	9.9991 (10.000)	-0.0000 (0.0000)
B	-1.0831 (-1.0834)	0.0000 (0.0000)	0.0000 (0.0000)	0.0019 (0.0000)	9.9992 (10.000)	-0.0003 (0.0000)
C	0.0000 (0.0000)	0.3914 (0.3915)	1.2187 (1.2183)	0.0018 (0.0000)	9.9992 (10.000)	-0.0000 (0.0000)
D	0.0000 (0.0000)	0.7828 (0.7829)	2.4373 (2.4367)	0.0019 (0.0000)	9.9991 (10.000)	-0.0001 (0.0000)

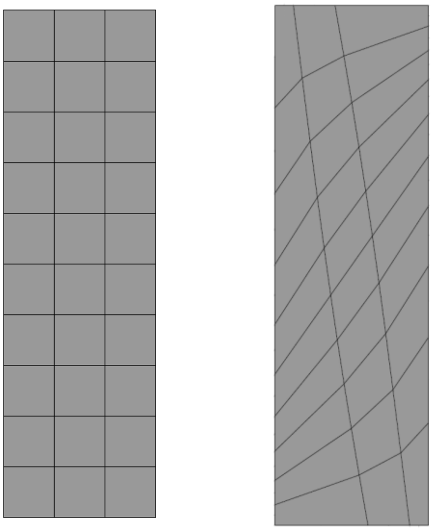

Figure 8.9 Regular (left) and distorted (right) meshes used for modeling the piezoelectric prism.

Table 8.6 Comparison of the predicted results from HFS-FEM on distorted meshes with the analytical results.

Position	u_x (10^{-10}m)	u_z (10^{-9}m)	ϕ (V)	σ_{xx} ($\mathrm{N\cdot m^{-2}}$)	σ_{zz} ($\mathrm{N\cdot m^{-2}}$)	D_z ($\mathrm{N\cdot m^{-2}}$)
B	-1.0847 (-1.0834)	0.0000 (0.0000)	0.0000 (0.0000)	0.0023 (0.0000)	10.0289 (10.000)	-0.0003 (0.0000)
D	0.0000 (0.0000)	0.7825 (0.7829)	2.4375 (2.4367)	0.0041 (0.0000)	9.9297 (10.000)	-0.0000 (0.0000)

To study the sensitivity of the proposed element model, a distorted mesh as shown in Figure 8.9 is used and the results are listed in Table 8.6. It can be seen that the results are still in good agreement with the analytical ones, indicating that the HFS-FEM is not sensitive to the mesh distortion and can produce highly accurate results when using severely distorted elements. The contour plots of the piezoelectric plate under simple tension are given in Figure 8.10, clearly demonstrating that the displacement field and electrical distribution are in linear variation as expected.

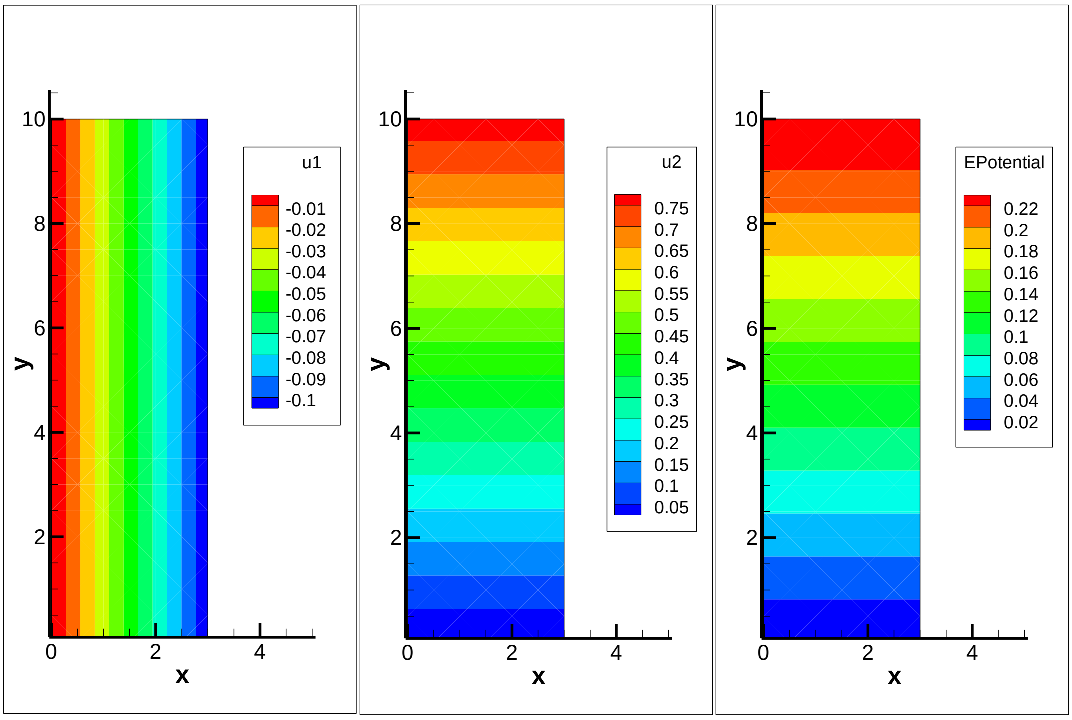

(a) u_x (unit: $10^{-9}m$) (b) u_z (unit: $10^{-9}m$) (c) ϕ (unit: $10^{-1}V$)

Figure 8.10 Contour plot of the displacements and electric potential of the plate.

Example 3: Bimorph beam with two electrodes

As shown in Figure 8.11, a 10×1 mm simply supported bimorph beam is considered in this example. The material properties are the same as those in Example 1. To obtain a large displacement, the upper and lower halves of the bimorph are poled upward and downward, respectively. Through the electrodes at $z = \pm h/2$, equal-potential conditions $\phi = \pm 100V$ are prescribed. In this analysis the bimorph beam is modeled by using 40 8-node elements, as shown in Figure 8.12.

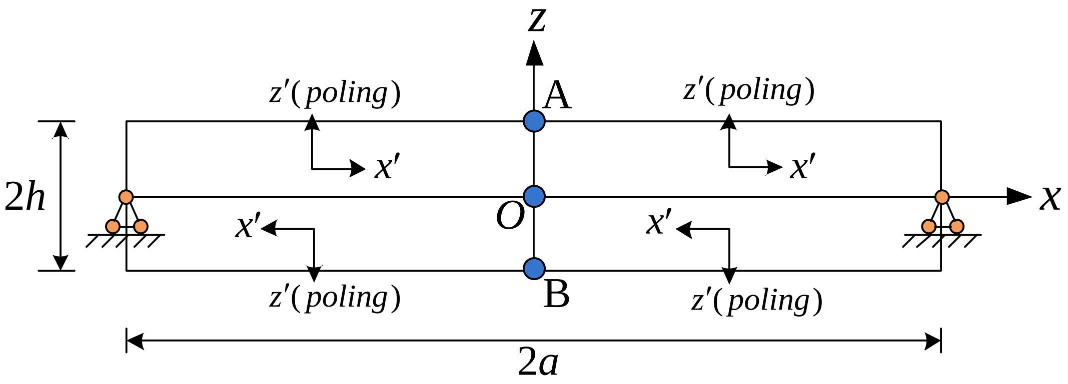

Figure 8.11 A simply supported bimorph piezoelectric beam ($x'z'$: local material coordinate system).

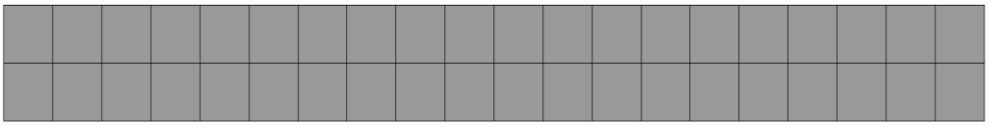

Figure 8.12 Element mesh used for modeling the bimorph piezoelectric beam in HFS-FEM analysis.

The mid-span predictions are listed in Table 8.7. For comparison, the analytical solution of the beam is also given in the table, which can be calculated by following equations without considering the localized boundary effect (Sze, Yang et al. 2004).

$$
\begin{aligned}
u_x &= \frac{-24 s_{11} g_{31} z x}{h^2 (4 s_{11} f_{33} + g_{31}^2)}, \phi = \frac{4 g_{31}^2 [2h - 3z \cdot \mathrm{sgn}(z)] z + 8 s_{11} f_{33} h z}{h^2 (4 s_{11} f_{33} + g_{31}^2)} \\
u_z &= \frac{12 g_{31} [s_{11}(x^2 - a^2) - s_{13} z^2] + 8 z h (s_{13} g_{31} - s_{11} g_{33}) \cdot \mathrm{sgn}(z)}{h^2 (4 s_{11} f_{33} + g_{31}^2)} \qquad (8.72) \\
\sigma_{xx} &= \frac{8 [h \cdot \mathrm{sgn}(z) - 3z] g_{31}}{h (4 s_{11} f_{33} + g_{31}^2)}
\end{aligned}
$$

where $\mathrm{sgn}(z)$ denotes the sign of z. It can be seen from Table 8.7 that the results from HFS-FEM are in good agreement with the analytical results. The errors for stresses are less than 1% and the error for displacement of the mid-span of the beam is less than 0.1% even when a coarse mesh is used (Figure 8.12).

Table 8.7 Mid-span predictions for bimorph beam under electric loading.

Method	$u_z\|_{z=0}$ (μm)	$\sigma_{xx}\|_{z=h/2}$, $-\sigma_{xx}\|_{z=-h/2}$ (MPa)	$\sigma_{xx}\|_{z=0^+}$, $-\sigma_{xx}\|_{z=0^-}$ (MPa)
HFS-FEM	1.2146	2.0341	-4.0862
Analytical	1.216	2.047	-4.094
Error	0.082%	0.635%	0.195%

Example 4: Infinite piezoelectric medium with hole

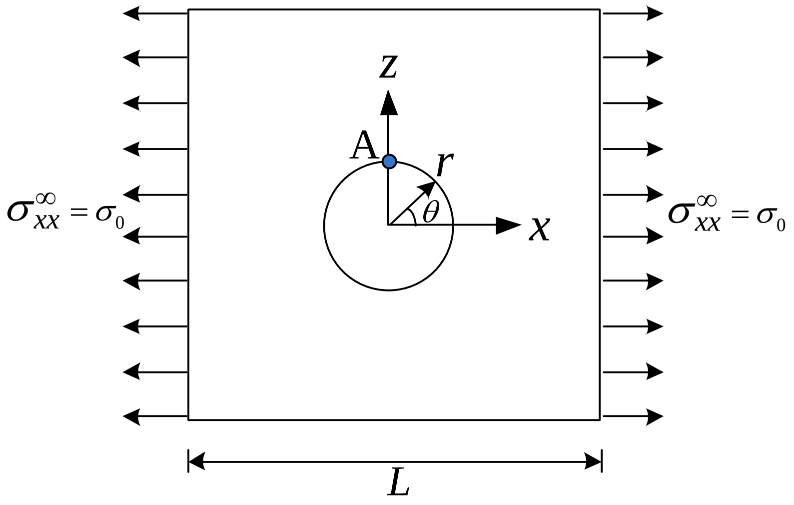

Figure 8.13 An infinite piezoelectric plate with a circular hole subjected to remote stress.

Consider an infinite piezoelectric plate with a circular hole as shown in Figure 8.13. The material parameters are the same as those in Example 1. Suppose that a mechanical load $\sigma_{xx}^{\infty}=\sigma_0=10$ parallel to the x axis is imposed at infinity with the boundary of the hole being traction- and electric charge- free. In this calculation, the radius of the hole is set to be r = 1 and the L can vary within a wide range.

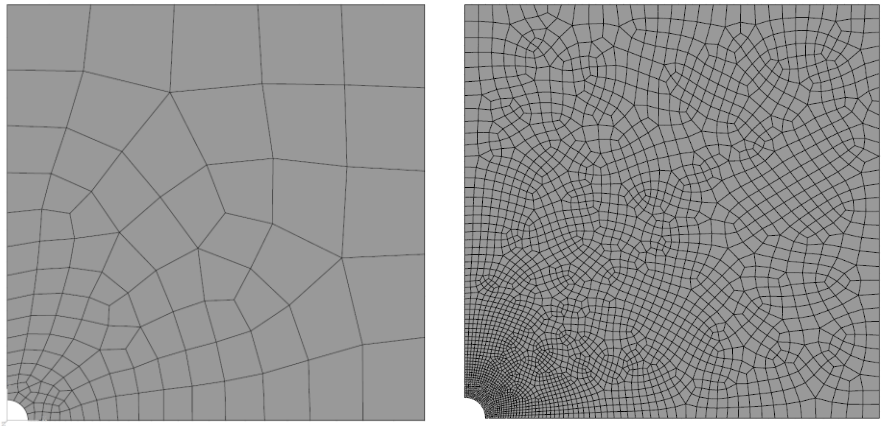

Figure 8.14 Element meshes used for HFS-FEM (left) and ABAQUS (right) in the case of *L/r*=20.

In the literature, different *L/r* ratios have been used for simulating the infinite plate, which may cause confusion among researchers as to which one should be taken as a reference. To clarify this, the influence of the *L/r* ratio on the SCFs is investigated using both the HFS-FEM method and ABAQUS. Table 8.8 shows the SCF results as a function of *L/r*. It should be mentioned that, in the analysis, different meshes are employed to ensure the accuracy of the simulation, and the numbers of 8-node quadratic elements for the six cases (*L/r*=5, 10, 20, 30, 40, and 50) shown in the first column of Table 8.8 are, respectively, 114, 117, 140, 227, 401, and 405 for HFS-FEM, and 2545, 2562, 2735, 9909, 13005, and 18247 for ABAQUS. The corresponding SCFs without considering the piezoelectric effect (i.e. pure elasticity) are also presented for reference. It is obvious that the application of the HFS-FEM with roughly coarse meshes obtains accurate results compared with those from conventional FEM (ABAQUS). It can be found from Table 8.8 that the SCF decreases with an increase in *L/r* and tends to be a constant when *L/r* =40 and above. Noting that an error of less than 1% is acceptable in most practical engineering, it is recommended that *L/r*=20 (error: about 0.56%) be used to evaluate the SCF of an infinite piezoelectric. Considering the recommendation above *L/r* =20 is employed in the following analysis. The corresponding meshes (for *L*/*r*=20) used by HFS-FEM and ABAQUS in the calculation are shown in Figure 8.14.

From Table 8.8, it is noted that a significant difference exists (about 17.1%) in SCF between the piezoelectric medium loaded in the poling direction (*z* axis) and in its perpendicular direction (*x* axis). The SCFs also display certain differences between piezoelectric and pure elastic. In comparison with pure elasticity, it can be seen that the piezoelectric-mechanical coupling alleviates the stress concentration by about 7.7% for circular holes in the poling direction but enhances the stress concentration by about 3.9% in the other direction. Therefore, it cannot be simply concluded that the electromechanical coupling effect is helpful for the safety of materials and structures (Dai, Guo et al. 2006). These findings can also be clearly seen from Figure 8.15 and Figure 8.16, in which the present results are in excellent agreement with the corresponding results of Sosa (Sosa 1991).

Table 8.8 Comparison of the SCFs obtained by HFS-FEM and ABAQUS.

L/*r*	Elastic		Piezoelastic			
	SCF ($\sigma_{xx}^{\infty}=\sigma_0$)	SCF ($\sigma_{zz}^{\infty}=\sigma_0$)	SCF ($\sigma_{xx}^{\infty}=\sigma_0$)		SCF ($\sigma_{zz}^{\infty}=\sigma_0$)	
	ABAQUS	ABAQUS	HFS-FEM	ABAQUS	HFS-FEM	ABAQUS
5	3.4955	3.2280	3.6789	3.6630	2.9497	2.9553
10	3.1949	2.9743	3.3101	3.3265	2.7352	2.7382
20	3.1251	2.9151	3.2346	3.2475	2.6844	2.6883
30	3.1093	2.9025	3.2212	3.2303	2.6793	2.6779
40	3.1050	2.8990	3.2192	3.2255	2.6711	2.6750
50	3.1034	2.8975	3.2186	3.2236	2.6710	2.6734

Figure 8.15 shows the distribution of hoop stress σ_θ and radial stress σ_r along the line *z*=0 for remote loading σ_{xx}^{∞} and along the line *x*=0 for remote loading σ_{zz}^{∞}. The results obtained from HFS-FEM agree well with the results from ABAQUS and Sosa (Sosa 1991). It can be seen that hoop the stress σ_θ has maximum value on the rim of the hole and it decreases dramatically with the increase of the distance from the edge

of the hole. It is also shown that σ_θ tends to be equal to the remote applied load σ_0 when r increases toward infinity. Compared with the hoop stress σ_θ, it is obvious that the radial stress σ_r is much smaller and usually does not need to be considered.

Figure 8.16 presents the variation of the normalized stress σ_θ / σ_0 along the edge of the hole. It can be seen that the results from HFS-FEM and the analytical solution of Sosa almost coincide with each other, which indicates that the proposed model works quite well. It is also noted that the two curves under the different loading conditions: σ_{xx}^∞ and σ_{zz}^∞ have different magnitude, as described in Table 8.8. It is obvious that loading along the poling direction produces lower stress concentration due to the coupling effect. The maximum values of σ_θ appears at $\theta = 90^\circ$ for case of σ_{xx}^∞ and at $\theta = 0^\circ$ and $\theta = 180^\circ$ for case of loading σ_{zz}^∞, both of which agree well with the analytical solution from Sosa (Sosa 1991).

Figure 8.17 shows the variation of the normalized electric displacement $D_\theta / \sigma_0 \times 10^{10}$ on the hole edge under remote mechanical loading. The results from HFS-FEM agree well with the analytical solution. The electric displacement $D_\theta / \sigma_0 \times 10^{10}$ produced by σ_{xx}^∞ and σ_{zz}^∞ are nearly identical, and are symmetrical with respect to the x axis. The maximum values of D_θ appears at $\theta = 65^\circ$ and $\theta = 115^\circ$, which also agrees well with the analytical solution from Sosa (1991).

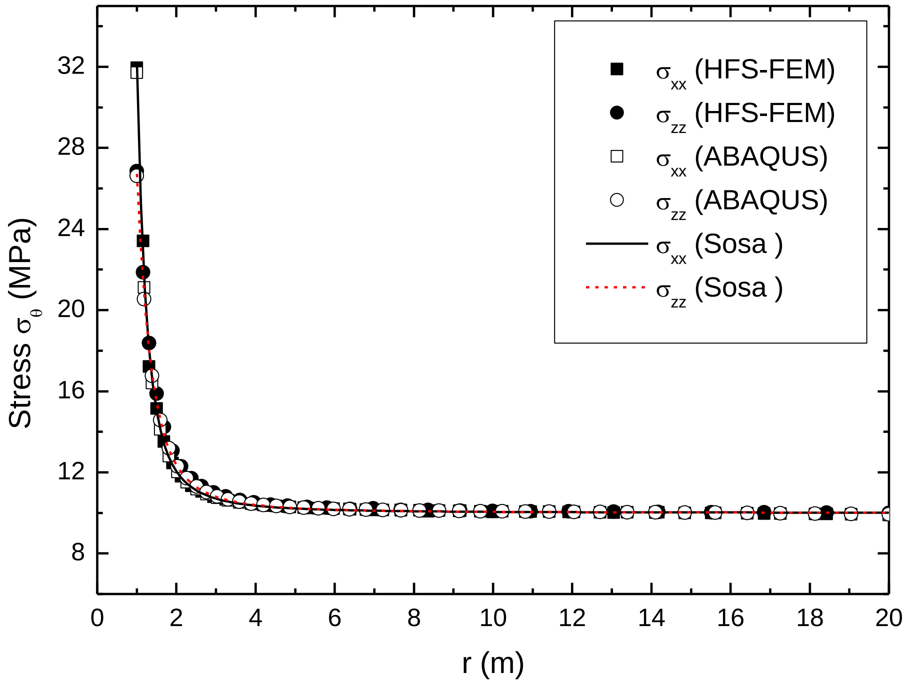

(a)

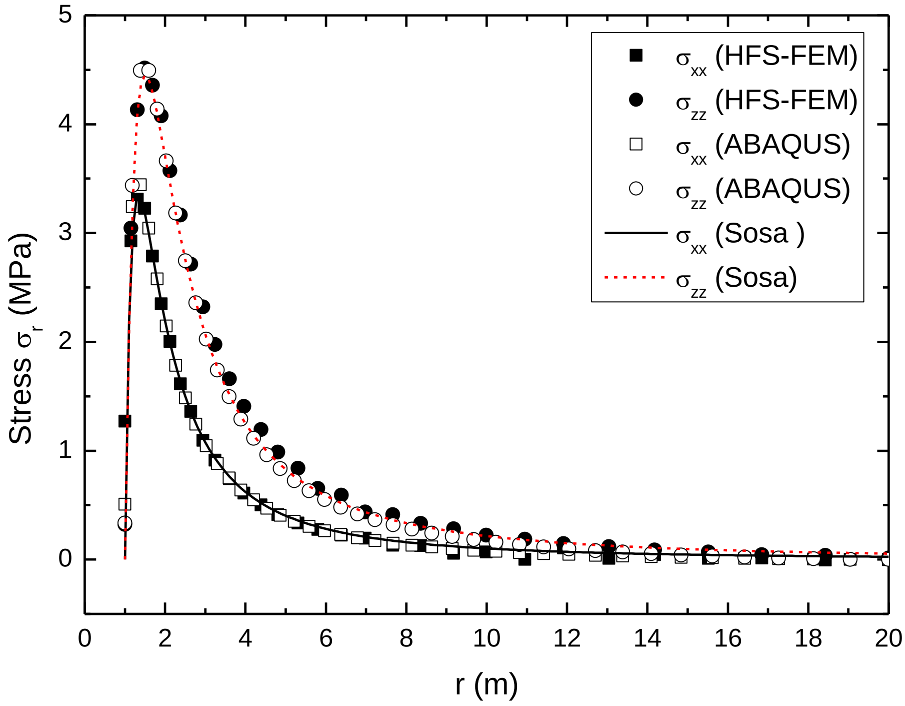

(b)

Figure 8.15 Distribution of (a) hoop stress σ_θ and (b) radial stress σ_r along the line z=0 when subjected to remote mechanical load σ_{xx}^{∞} and along the line x=0 when subjected to remote mechanical load σ_{zz}^{∞}.

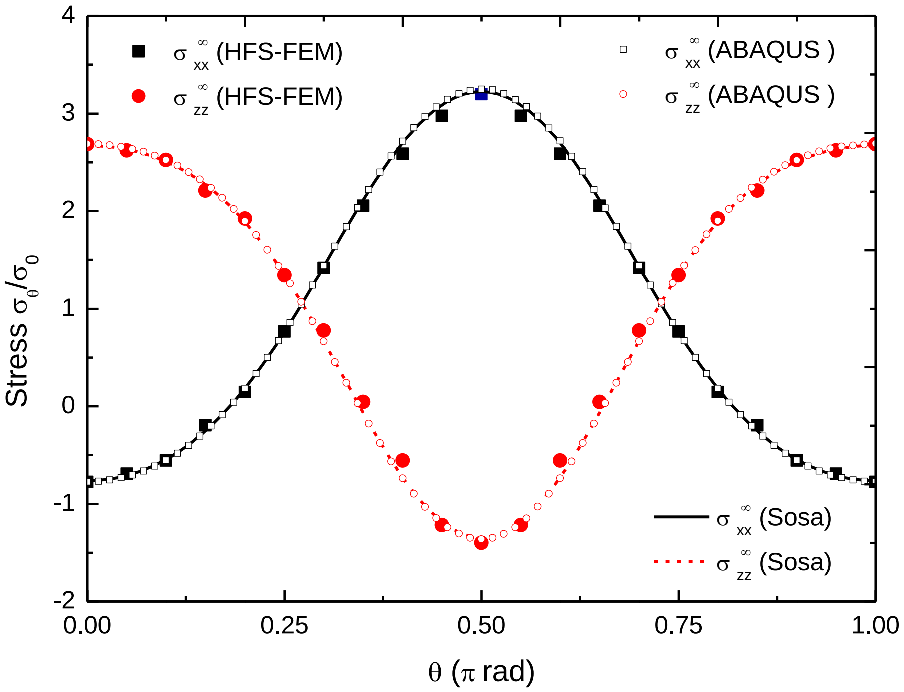

Figure 8.16 Variation of normalized stress σ_θ / σ_0 along the hole boundary under remote mechanical loading.

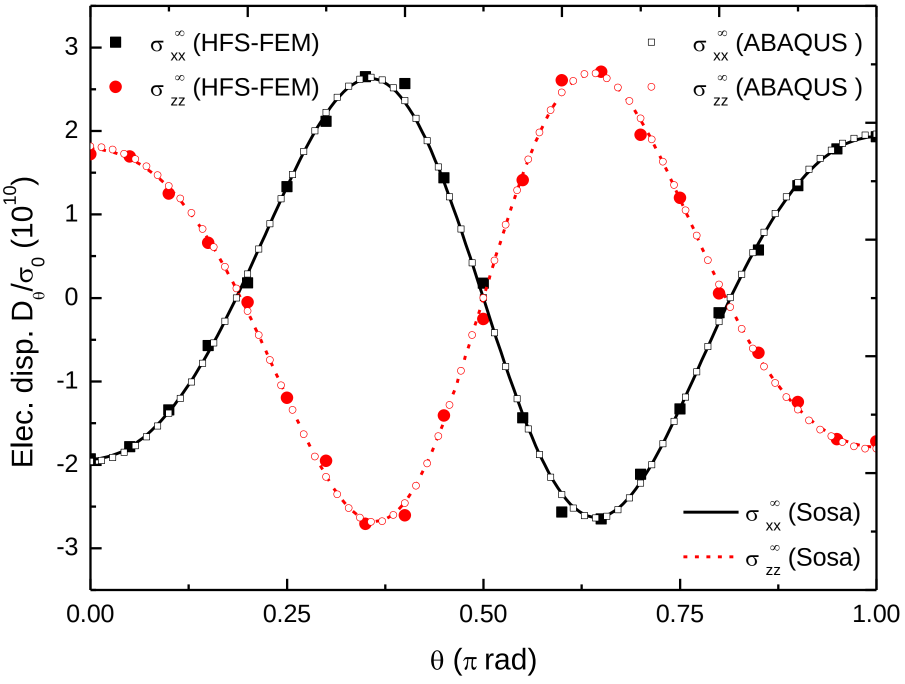

Figure 8.17 Variation of normalized electrical displacement $D_\theta / \sigma_0 \times 10^{10}$ along the hole boundary under remote mechanical loading.

8.4. HFS-FEM BASED ON STROH FORMALISM

8.4.1. Extended Stroh formalism

If we neglect the body force f_i and surface charge q and let (Ting 1996)

$$C_{IJKL} = \begin{cases} C_{ijkl} & i, j, k, l = 1, 2, 3 \\ e_{lij} & k = 4,\ i, j, l = 1, 2, 3 \\ e_{jkl} & i = 4,\ j, k, l = 1, 2, 3 \\ -\kappa_{jl} & i = k = 4,\ j, l = 1, 2, 3 \end{cases} \tag{8.73}$$

$$D_j = \sigma_{4j},\ \ -E_j = u_{4,j} = 2\varepsilon_{4j},\ \ j = 1, 2, 3 \tag{8.74}$$

the basic equations (8.1)-(8.3) can be expressed as an expanded tensor notation

$$\sigma_{IJ,J} = 0,\ \ \sigma_{IJ} = C_{IJKL}\varepsilon_{KL},\ \ \varepsilon_{IJ} = \frac{1}{2}(u_{I,J} + u_{J,I}),\ \ I, J, K, L = 1, 2, 3, 4 \tag{8.75}$$

where C_{IJKL} has the following symmetry property

$$C_{IJKL} = C_{JIKL} = C_{IJLK} = C_{KLIJ} \tag{8.76}$$

It is noted that the governing equations (8.75) and (8.76) for piezoelectric anisotropic materials have the same form as those of pure anisotropic elasticity. For the generalized 2D deformation (u_i depends on x_1 and x_2 only), an extended version of Stroh formalism satisfying the governing Eq. (8.75) has been proposed by Kuo and Barnett as (Stroh 1958; Ting 1996)

$$\mathbf{u} = 2\,\mathrm{Re}\{\mathbf{A}\mathbf{f}(z)\}, \boldsymbol{\varphi} = 2\,\mathrm{Re}\{\mathbf{B}\mathbf{f}(z)\} \tag{8.77}$$

where $\mathbf{u} = [u_1, u_2, u_3, \phi]^T$ is the displacement vector, $\boldsymbol{\varphi} = [\varphi_1, \varphi_2, \varphi_3, \varphi_4]^T$ is the stress function vector, $\mathbf{f}(z) = [f_1(z_1),\ f_2(z_2),\ f_3(z_3),\ f_4(z_4)]^T$ is a function vector composed of four holomorphic complex function $f_\alpha(z_\alpha)$, $\alpha = 1, 2, 3, 4$, which is an arbitrary function with argument $z_\alpha = x_1 + p_\alpha x_2$ (p_α are the material eigenvalues with positive imaginary part) and will be determined by satisfying the boundary and loading conditions of a given problem. In Eq. (8.77), Re stands for the real part of a complex number, $\mathbf{A} = [\mathbf{a}_1, \mathbf{a}_2, \mathbf{a}_3, \mathbf{a}_4]$ and $\mathbf{B} = [\mathbf{b}_1, \mathbf{b}_2, \mathbf{b}_3, \mathbf{b}_4]$ are 4×4 complex matrices formed by the material eigenvector associated with p_α, which can be obtained by the following eigenrelations (Ting 1996; Hwu 2010):

$$\mathbf{N}\boldsymbol{\xi} = p\boldsymbol{\xi} \tag{8.78}$$

where $\mathbf{N}$ is a 8×8 foundational elasticity matrix and $\boldsymbol{\xi}$ is a 8×1 column vector defined by

$$\mathbf{N}=\begin{bmatrix}\mathbf{N_1} & \mathbf{N_2}\\ \mathbf{N_3} & \mathbf{N_1^T}\end{bmatrix},\ \xi=\begin{Bmatrix}\mathbf{a}\\ \mathbf{b}\end{Bmatrix} \tag{8.79}$$

where $\mathbf{N_1} = \mathbf{-T^{-1}R^T}$, $\mathbf{N_2} = \mathbf{T^{-1}} = \mathbf{N_2^T}$, $\mathbf{N_3} = \mathbf{RT^{-1}R^T - Q} = \mathbf{N_3^T}$ and the matrices $\mathbf{Q}$, $\mathbf{R}$ and $\mathbf{T}$ are 4×4 matrices extracted from C_{IJKL} as follows

$$Q_{ik}=C_{i1k1}, R_{ik}=C_{i1k2}, T_{ik}=C_{i2k2} \qquad i,k=1,2,3,4 \tag{8.80}$$

the detailed matrix components are shown below as

$$\mathbf{Q}=\begin{bmatrix}C_{11} & C_{16} & C_{15} & e_{11}\\ C_{16} & C_{66} & C_{56} & e_{16}\\ C_{15} & C_{56} & C_{55} & e_{15}\\ e_{11} & e_{16} & e_{15} & -k_{11}\end{bmatrix}, \mathbf{R}=\begin{bmatrix}C_{16} & C_{12} & C_{14} & e_{21}\\ C_{66} & C_{26} & C_{46} & e_{26}\\ C_{56} & C_{25} & C_{45} & e_{25}\\ e_{16} & e_{12} & e_{14} & -k_{12}\end{bmatrix}, \mathbf{T}=\begin{bmatrix}C_{66} & C_{26} & C_{46} & e_{26}\\ C_{26} & C_{22} & C_{24} & e_{22}\\ C_{46} & C_{24} & C_{44} & e_{24}\\ e_{26} & e_{22} & e_{24} & -k_{22}\end{bmatrix} \tag{8.81}$$

Since $\xi=[\mathbf{a},\mathbf{b}]^T$ is the right eigenvector of matrix $\mathbf{N}$, normalization is required to obtain unique values of $\mathbf{a}_k$ and $\mathbf{b}_k$. As with anisotropic elasticity, following the orthogonality relation for material eigenvetor matrices $\mathbf{A}$ and $\mathbf{B}$ can be used for this purpose

$$\begin{bmatrix}\mathbf{A} & \bar{\mathbf{A}}\\ \mathbf{B} & \bar{\mathbf{B}}\end{bmatrix}\begin{bmatrix}\mathbf{B^T} & \mathbf{A^T}\\ \bar{\mathbf{B}}^{\mathbf{T}} & \bar{\mathbf{A}}^{\mathbf{T}}\end{bmatrix}=\begin{bmatrix}\mathbf{I} & \mathbf{0}\\ \mathbf{0} & \mathbf{I}\end{bmatrix} \tag{8.82}$$

It should be noted that when using transversely piezoelectric materials (e.g. x_1-x_2 as the isotropic plane), and taking the x_3 as the poling direction, then the Stroh formalism will fail for such degenerate materials, namely, $\mu_1=\mu_2=\mu_3=\mu_4=i$. In these cases, a small perturbation must be given to enable the Stroh formalism to work. Based on the relation in Eq. (8.82), the Barnett–Lothe tensors **L**, **S** and **H** can be defined by (Ting 1996)

$$\mathbf{H = i2AA^T},\ \ \mathbf{L = -i2BB^T},\ \ \mathbf{S = i(2AB^T - I)} \tag{8.83}$$

The stresses and electric displacement can be obtained from the derivation of the generalized stress function $\boldsymbol{\varphi}$ as follows

$$\sigma_{i1}=-\phi_{i,2},\ \ \sigma_{i2}=\phi_{i,1},\qquad i=1,2,3 \tag{8.84}$$

$$\sigma_{41}=D_1=-\phi_{4,2},\ \ \sigma_{42}=D_2=\phi_{4,1} \tag{8.85}$$

8.4.2. Foundational solutions

To find the fundamental solution needed in this analysis, it is necessary first to derive the Green's function of the problem: an infinite homogeneous anisotropic elastic medium loaded by a concentrated point force or electric charge

$\hat{\mathbf{p}} = (\hat{p}_1, \hat{p}_2, \hat{p}_3, \hat{p}_4)$ applied at an internal point $\hat{\mathbf{x}} = (\hat{x}_1, \hat{x}_2)$ distant from the boundary. The boundary conditions of this problem can be written as

$$\begin{aligned} &\int_C d\boldsymbol{\phi} = \hat{\mathbf{p}} \quad \text{for any closed curve } C \text{ enclosing } \hat{\mathbf{x}} \\ &\int_C d\mathbf{u} = \hat{\mathbf{p}} \quad \text{for any closed curve } C \\ &\lim_{\mathbf{x}\to\infty} \sigma_{ij} = 0, \quad \lim_{\mathbf{x}\to\infty} D_i = 0 \end{aligned} \tag{8.86}$$

The Green's function satisfying the above boundary conditions has been found to be (Ting 1996)

$$f(z) = \frac{1}{2\pi i} \langle \ln(z_\alpha - \hat{z}_\alpha) \rangle \mathbf{A}^T \hat{\mathbf{p}} \tag{8.87}$$

Therefore, the fundamental solutions of the problem can be expressed as

$$\begin{aligned} \mathbf{u} &= \frac{1}{\pi} \operatorname{Im}\left\{ \mathbf{A} \left\langle \ln\left(z_\alpha - \hat{z}_\alpha\right) \right\rangle \mathbf{A}^{\mathrm{T}} \right\} \hat{\mathbf{p}} \\ \phi &= \frac{1}{\pi} \operatorname{Im}\left\{ \mathbf{B} \left\langle \ln\left(z_\alpha - \hat{z}_\alpha\right) \right\rangle \mathbf{A}^{\mathrm{T}} \right\} \hat{\mathbf{p}} \end{aligned} \tag{8.88}$$

The corresponding stress components can be obtained from stress function ϕ

$$\begin{aligned} \sigma_{i1}^* &= -\phi_{,2} = -\frac{1}{\pi} \operatorname{Im}\left\{ \mathbf{B} \left\langle p_\alpha / \left(z_\alpha - \hat{z}_\alpha\right) \right\rangle \mathbf{A}^{\mathrm{T}} \right\} \hat{\mathbf{p}} \\ \sigma_{i2}^* &= \phi_{,1} = \frac{1}{\pi} \operatorname{Im}\left\{ \mathbf{B} \left\langle 1 / \left(z_\alpha - \hat{z}_\alpha\right) \right\rangle \mathbf{A}^{\mathrm{T}} \right\} \hat{\mathbf{p}} \end{aligned} \tag{8.89}$$

where $\hat{\mathbf{p}}$ is chosen to be $(1,0,0,0)^T$, $(0,1,0,0)^T$, $(0,0,1,0)^T$, and $(0,0,0,1)^T$, respectively, $<\cdot>$ stands for the diagonal matrix corresponding to subscript α, Im denotes the imaginary part of a complex number, and superscript T denotes the matrix transpose.

Special foundational solutions for plate with hole

Consider an infinite anisotropic plate containing a traction- and electric charge-free elliptical hole under a concentrated force or electric charge $\hat{\mathbf{p}} = (\hat{p}_1, \hat{p}_2, \hat{p}_3, \hat{p}_4)$ applied at point $\hat{\mathbf{x}} = (\hat{x}_1, \hat{x}_2)$, as shown in Figure 8.18.

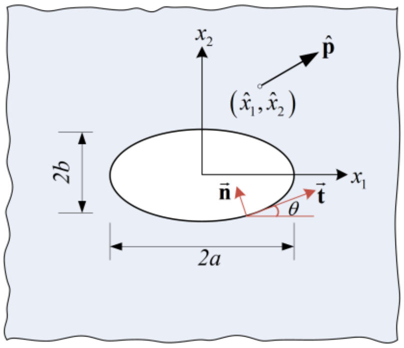

Figure 8.18 Schematic of an infinite anisotropic plate with an elliptical hole.

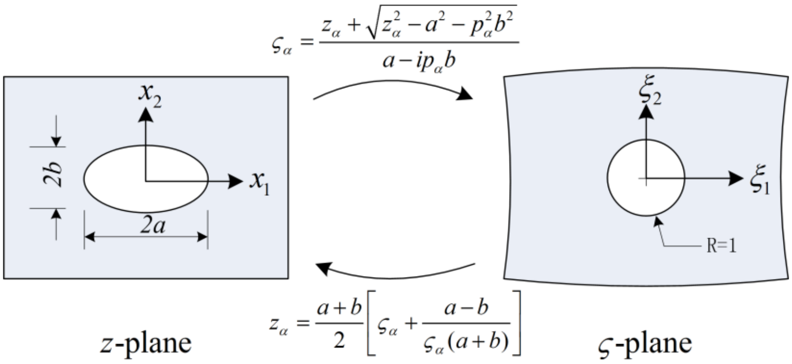

Figure 8.19 Conformal mapping of an infinite plane with an elliptical hole.

The Green's function of this problem can be obtained by employing the conformal mapping technique shown in Figure 8.19, which transforms the region outside the elliptical hole in the z-plane onto the exterior of a unit circle in the ς-plane. The expressions of the Green function have been derived as (Hwu and Yen 1991; Ting 1996)

$$\begin{aligned}\mathbf{u} &= \frac{1}{\pi}\operatorname{Im}\left\{\mathbf{A}\left\langle \ln\left(\zeta_\alpha - \hat{\varsigma}_\alpha\right)\right\rangle \mathbf{A}^{\mathbf{T}} + \sum_{k=1}^{4}\mathbf{A}\left\langle \ln(\varsigma_\alpha^{-1} - \bar{\hat{\varsigma}}_k)\right\rangle \mathbf{B}^{\text{-}\mathbf{1}}\bar{\mathbf{B}}\mathbf{I_k}\bar{\mathbf{A}}^{\mathbf{T}}\right\}\hat{\mathbf{p}} \\ \phi &= \frac{1}{\pi}\operatorname{Im}\left\{\mathbf{B}\ln\left(\zeta_\alpha - \hat{\varsigma}_\alpha\right)\mathbf{A}^{\mathbf{T}} + \sum_{k=1}^{4}\mathbf{B}\left\langle \ln(\varsigma_\alpha^{-1} - \bar{\hat{\varsigma}}_k)\right\rangle \mathbf{B}^{\text{-}\mathbf{1}}\bar{\mathbf{B}}\mathbf{I_k}\bar{\mathbf{A}}^{\mathbf{T}}\right\}\hat{\mathbf{p}}\end{aligned} \tag{8.90}$$

in which the unknown complex function vector $f(z)$ is better expressed in terms of the arguments ζ_α

$$\varsigma_\alpha = \frac{z_\alpha + \sqrt{z_\alpha^2 - a^2 - p_\alpha^2 b^2}}{a - ip_\alpha b}, \hat{\varsigma}_\alpha = \frac{\hat{z}_\alpha + \sqrt{\hat{z}_\alpha^2 - a^2 - p_\alpha^2 b^2}}{a - ip_\alpha b} \tag{8.91}$$

where $2a$ and $2b$ are the lengths of the major and minor axis of the elliptical hole

$$z_\alpha = x_1 + p_\alpha x_2, \quad \hat{z}_\alpha = \hat{x}_1 + p_\alpha \hat{x}_2 \tag{8.92}$$

The derivation of ζ_α with respect to z_α can be expressed as

$$\frac{\partial \varsigma_\alpha}{\partial z_\alpha} = \frac{1}{a - ip_\alpha b}\left(1 + \frac{z_\alpha}{\sqrt{z_\alpha^2 - a^2 - p_\alpha^2 b^2}}\right) = \frac{2\varsigma_\alpha^2}{\left(a - ip_\alpha b\right)\varsigma_\alpha^2 - \left(a + ip_\alpha b\right)} \tag{8.93}$$

Then the derivation of ζ_α with respect to x_1 and x_2 can be expressed as

$$\begin{aligned} \frac{\partial \varsigma_\alpha}{\partial x_1} &= \frac{\partial \varsigma_\alpha}{\partial z_\alpha} . \frac{\partial z_\alpha}{\partial x_1} = \frac{\partial \varsigma_\alpha}{\partial z_\alpha} = \frac{2\varsigma_\alpha^2}{\left(a - ip_\alpha b\right)\varsigma_\alpha^2 - \left(a + ip_\alpha b\right)} \\ \frac{\partial \varsigma_\alpha}{\partial x_2} &= \frac{\partial \varsigma_\alpha}{\partial z_\alpha} . \frac{\partial z_\alpha}{\partial x_2} = \frac{\partial \varsigma_\alpha}{\partial z_\alpha} . p_\alpha = \frac{2 p_\alpha \varsigma_\alpha^2}{\left(a - ip_\alpha b\right)\varsigma_\alpha^2 - \left(a + ip_\alpha b\right)} \end{aligned} \tag{8.94}$$

Using Eq. (8.94) and letting $\chi = \left(a - ip_\alpha b\right)\varsigma_\alpha^2 - \left(a + ip_\alpha b\right)$, the corresponding stress components can be expressed as

$$\begin{aligned} \sigma_{i1}^* &= -\phi_{,2} = -\frac{1}{\pi}\mathrm{Im}\left\{\mathbf{B}\left\langle \frac{2\varsigma_\alpha^2 p_\alpha}{\left(\varsigma_\alpha - \hat{\varsigma}_\alpha\right)\chi}\right\rangle \mathbf{A}^{\mathbf{T}}\right\}\hat{\mathbf{p}} - \frac{1}{\pi}\sum_{k=1}^{3}\mathrm{Im}\left\{\mathbf{B}\left\langle \frac{-2\varsigma_\alpha p_\alpha}{\left(1 - \varsigma_\alpha \bar{\hat{\varsigma}}_k\right)\chi}\right\rangle \mathbf{B}^{\text{-1}}\bar{\mathbf{B}}\mathbf{I}_{\mathbf{k}}\bar{\mathbf{A}}^{\mathbf{T}}\right\}\hat{\mathbf{p}} \\ \sigma_{i2}^* &= \phi_{,1} = \frac{1}{\pi}\mathrm{Im}\left\{\mathbf{B}\left\langle \frac{2\varsigma_\alpha^2}{\left(\varsigma_\alpha - \hat{\varsigma}_\alpha\right)\chi}\right\rangle \mathbf{A}^{\mathbf{T}}\right\}\hat{\mathbf{p}} + \frac{1}{\pi}\sum_{k=1}^{3}\mathrm{Im}\left\{\mathbf{B}\left\langle \frac{-2\varsigma_\alpha}{\left(1 - \varsigma_\alpha \bar{\hat{\varsigma}}_k\right)\chi}\right\rangle \mathbf{B}^{\text{-1}}\bar{\mathbf{B}}\mathbf{I}_{\mathbf{k}}\bar{\mathbf{A}}^{\mathbf{T}}\right\}\hat{\mathbf{p}} \end{aligned} \tag{8.95}$$

The fundamental solutions for an infinite anisotropic medium with a crack of length $2a$ can be obtained easily by letting b =0 in Eq. (8.90) (Ting 1996). For the crack problem, it is always of interest to know the stress fields near the crack tips. Differentiating the generalized stress function with respect to x_1 and letting $x_2 = 0$, $x_1 > a$, the stresses $\boldsymbol{\sigma}_2 = \left\{\sigma_{21}, \sigma_{22}, \sigma_{23}\right\}^T$ ahead of the crack tip along the x_1 axis are obtained as

$$\boldsymbol{\sigma}_2 = \boldsymbol{\varphi}_{,1} = \frac{1}{\pi a}\left(1 + \frac{x_1}{\sqrt{x_1^2 - a^2}}\right)\mathrm{Im}\left\{\mathbf{B}\left\langle \frac{1}{\zeta - \hat{\zeta}_\alpha} + \frac{1}{\zeta - \zeta^2 \hat{\zeta}_\alpha}\right\rangle \mathbf{A}^T\right\}\hat{\mathbf{p}} \tag{8.96}$$

where

$$\zeta = \frac{x_1 + \sqrt{x_1^2 - a^2}}{a}, \quad \hat{\zeta}_\alpha = \frac{\hat{z}_\alpha + \sqrt{\hat{z}_\alpha^2 - a^2}}{a} \tag{8.97}$$

With the definition of the stress and electric displacement intensity factors of cracks (Lu and Williams 1998) and using the following relations,

$$\frac{1}{1 - \hat{\zeta}_\alpha} = \frac{1}{2}\left(1 - \frac{\hat{z}_\alpha + a}{\sqrt{\hat{z}_\alpha^2 - a^2}}\right) = \frac{1}{2}\left(1 + \frac{\sqrt{\hat{z}_\alpha^2 - a^2}}{a - \hat{z}_\alpha}\right), \quad \lim_{x_1 \to a} \zeta = 1 \tag{8.98}$$

one can obtain

$$K=\begin{Bmatrix} K_{II} \\ K_{I} \\ K_{III} \\ K_{IV} \end{Bmatrix}=\lim_{x_1\to a}\sqrt{2\pi(x_1-a)}\ \boldsymbol{\sigma}_2=\frac{2}{\sqrt{\pi a}}\operatorname{Im}\left\{\mathbf{B}\left\langle\frac{1}{1-\hat{\zeta}_{\alpha}}\right\rangle\mathbf{A}^T\right\}\hat{\mathbf{p}} \qquad (8.99)$$

where K_I, K_{II} and K_{III} are the stress intensity factors, and K_{IV} is the electric displacement intensity factor (Suo 1992).

8.4.3. Assumed independent fields

To solve the piezoelectricity problem governed by Eq. (8.75) using the HFS-FEM approach, the solution domain Ω must be divided into a series of elements as in conventional FEM. For each element, two independent DEP fields, i.e. an intra-element DEP field and a frame DEP field. In this approach, the intra-element DEP field $\mathbf{u_e}$ for a particular element e is approximated in terms of a linear combination of fundamental solutions of the problem as

$$\mathbf{u_e}=\mathbf{N_e}\mathbf{c_e} \quad (\mathbf{x}\in\Omega_e,\mathbf{y}_{sj}\notin\Omega_e) \qquad (8.100)$$

where $\mathbf{u_e}=[u_1,u_2,u_3,\phi]^T$, the fundamental solution matrix $\mathbf{N_e}$ and unknown vector $\mathbf{c_e}$ (not nodal displacements) can be written as

$$\mathbf{N_e}=\begin{bmatrix} u_{11}^*(\mathbf{x},\mathbf{y}_{s1}) & u_{21}^*(\mathbf{x},\mathbf{y}_{s1}) & u_{31}^*(\mathbf{x},\mathbf{y}_{s1}) & \dots & u_{11}^*(\mathbf{x},\mathbf{y}_{sn_s}) & u_{21}^*(\mathbf{x},\mathbf{y}_{sn_s}) & u_{31}^*(\mathbf{x},\mathbf{y}_{sn_s}) \\ u_{12}^*(\mathbf{x},\mathbf{y}_{s1}) & u_{22}^*(\mathbf{x},\mathbf{y}_{s1}) & u_{32}^*(\mathbf{x},\mathbf{y}_{s1}) & \dots & u_{12}^*(\mathbf{x},\mathbf{y}_{sn_s}) & u_{22}^*(\mathbf{x},\mathbf{y}_{sn_s}) & u_{32}^*(\mathbf{x},\mathbf{y}_{sn_s}) \\ u_{13}^*(\mathbf{x},\mathbf{y}_{s1}) & u_{23}^*(\mathbf{x},\mathbf{y}_{s1}) & u_{33}^*(\mathbf{x},\mathbf{y}_{s1}) & \dots & u_{13}^*(\mathbf{x},\mathbf{y}_{sn_s}) & u_{23}^*(\mathbf{x},\mathbf{y}_{sn_s}) & u_{33}^*(\mathbf{x},\mathbf{y}_{sn_s}) \\ \phi_{14}^*(\mathbf{x},\mathbf{y}_{s1}) & \phi_{24}^*(\mathbf{x},\mathbf{y}_{s1}) & \phi_{34}^*(\mathbf{x},\mathbf{y}_{s1}) & \dots & \phi_{14}^*(\mathbf{x},\mathbf{y}_{sn_s}) & \phi_{24}^*(\mathbf{x},\mathbf{y}_{sn_s}) & \phi_{34}^*(\mathbf{x},\mathbf{y}_{sn_s}) \end{bmatrix} \qquad (8.101)$$

$$\mathbf{c_e}=[c_{11}\quad c_{21}\quad c_{31}\quad c_{41}\quad \dots\quad c_{1n_s}\quad c_{2n_s}\quad c_{3n_s}\quad c_{4n_s}]^T \qquad (8.102)$$

in which n_s is the number of source points located outside element domain, $\mathbf{x}$ and $\mathbf{y}_{sj}$ are respectively the field point (i.e. the nodal points of the element in this work) and source point in the coordinate system (X_1, X_2) local to the element under consideration. The component $u_{ij}^*(\mathbf{x},\mathbf{y}_{sj})$ is the induced displacement component (*i*=1, 2, 3) or electric potential (*i*=4) in the *i*-direction at the field point x due to a unit point load (*j*=1, 2, 3) or point charge (*j*=4) applied in the *j*-direction at the source point $\mathbf{y}_{sj}$. The fundamental solution $u_{ij}^*(\mathbf{x},\mathbf{y}_{sj})$ is given by Eq. (8.88) for general elements or by Eq. (8.90) for special elements.

With Eq. (8.75) and the expression of intra-element DEP field $\mathbf{u}$ in Eq. (8.100), the corresponding stress and electric displacement Eq. (8.75) can be further written as

$$\boldsymbol{\sigma} = \mathbf{T_e c_e} \tag{8.103}$$

where $\boldsymbol{\sigma} = \begin{bmatrix} \sigma_{11} & \sigma_{22} & \sigma_{23} & \sigma_{31} & \sigma_{12} & D_1 & D_2 \end{bmatrix}^T$ and

$$\mathbf{T_e} = \begin{bmatrix}
\sigma_{11}^*(\mathbf{x},\mathbf{y}_{s1}) & \sigma_{12}^*(\mathbf{x},\mathbf{y}_{s1}) & \sigma_{13}^*(\mathbf{x},\mathbf{y}_{s1}) & \sigma_{14}^*(\mathbf{x},\mathbf{y}_{s1}) & \dots & \sigma_{11}^*(\mathbf{x},\mathbf{y}_{sn_s}) & \sigma_{12}^*(\mathbf{x},\mathbf{y}_{sn_s}) & \sigma_{13}^*(\mathbf{x},\mathbf{y}_{sn_s}) & \sigma_{14}^*(\mathbf{x},\mathbf{y}_{sn_s}) \\
\sigma_{21}^*(\mathbf{x},\mathbf{y}_{s1}) & \sigma_{22}^*(\mathbf{x},\mathbf{y}_{s1}) & \sigma_{23}^*(\mathbf{x},\mathbf{y}_{s1}) & \sigma_{24}^*(\mathbf{x},\mathbf{y}_{s1}) & \dots & \sigma_{21}^*(\mathbf{x},\mathbf{y}_{sn_s}) & \sigma_{22}^*(\mathbf{x},\mathbf{y}_{sn_s}) & \sigma_{23}^*(\mathbf{x},\mathbf{y}_{sn_s}) & \sigma_{24}^*(\mathbf{x},\mathbf{y}_{sn_s}) \\
\sigma_{31}^*(\mathbf{x},\mathbf{y}_{s1}) & \sigma_{32}^*(\mathbf{x},\mathbf{y}_{s1}) & \sigma_{33}^*(\mathbf{x},\mathbf{y}_{s1}) & \sigma_{34}^*(\mathbf{x},\mathbf{y}_{s1}) & \dots & \sigma_{31}^*(\mathbf{x},\mathbf{y}_{sn_s}) & \sigma_{32}^*(\mathbf{x},\mathbf{y}_{sn_s}) & \sigma_{33}^*(\mathbf{x},\mathbf{y}_{sn_s}) & \sigma_{34}^*(\mathbf{x},\mathbf{y}_{sn_s}) \\
\sigma_{41}^*(\mathbf{x},\mathbf{y}_{s1}) & \sigma_{42}^*(\mathbf{x},\mathbf{y}_{s1}) & \sigma_{43}^*(\mathbf{x},\mathbf{y}_{s1}) & \sigma_{44}^*(\mathbf{x},\mathbf{y}_{s1}) & \dots & \sigma_{41}^*(\mathbf{x},\mathbf{y}_{sn_s}) & \sigma_{42}^*(\mathbf{x},\mathbf{y}_{sn_s}) & \sigma_{43}^*(\mathbf{x},\mathbf{y}_{sn_s}) & \sigma_{44}^*(\mathbf{x},\mathbf{y}_{sn_s}) \\
\sigma_{51}^*(\mathbf{x},\mathbf{y}_{s1}) & \sigma_{52}^*(\mathbf{x},\mathbf{y}_{s1}) & \sigma_{53}^*(\mathbf{x},\mathbf{y}_{s1}) & \sigma_{54}^*(\mathbf{x},\mathbf{y}_{s1}) & \dots & \sigma_{51}^*(\mathbf{x},\mathbf{y}_{sn_s}) & \sigma_{52}^*(\mathbf{x},\mathbf{y}_{sn_s}) & \sigma_{53}^*(\mathbf{x},\mathbf{y}_{sn_s}) & \sigma_{54}^*(\mathbf{x},\mathbf{y}_{sn_s}) \\
\sigma_{61}^*(\mathbf{x},\mathbf{y}_{s1}) & \sigma_{62}^*(\mathbf{x},\mathbf{y}_{s1}) & \sigma_{63}^*(\mathbf{x},\mathbf{y}_{s1}) & \sigma_{64}^*(\mathbf{x},\mathbf{y}_{s1}) & \dots & \sigma_{61}^*(\mathbf{x},\mathbf{y}_{sn_s}) & \sigma_{62}^*(\mathbf{x},\mathbf{y}_{sn_s}) & \sigma_{63}^*(\mathbf{x},\mathbf{y}_{sn_s}) & \sigma_{64}^*(\mathbf{x},\mathbf{y}_{sn_s}) \\
\sigma_{71}^*(\mathbf{x},\mathbf{y}_{s1}) & \sigma_{72}^*(\mathbf{x},\mathbf{y}_{s1}) & \sigma_{73}^*(\mathbf{x},\mathbf{y}_{s1}) & \sigma_{74}^*(\mathbf{x},\mathbf{y}_{s1}) & \dots & \sigma_{71}^*(\mathbf{x},\mathbf{y}_{sn_s}) & \sigma_{72}^*(\mathbf{x},\mathbf{y}_{sn_s}) & \sigma_{73}^*(\mathbf{x},\mathbf{y}_{sn_s}) & \sigma_{74}^*(\mathbf{x},\mathbf{y}_{sn_s})
\end{bmatrix} \tag{8.104}$$

in which $\sigma_{ij}^*(\mathbf{x},\mathbf{y}_{\mathrm{s}j})$ denotes the corresponding stress components (i =1,2,3) or electric displacement (i =4,5) along the i -direction at the field point $\mathbf{x}$ due to a unit point load (j =1,2) or a unit point charge (j =3) applied in the j -direction at the source point $\mathbf{y}_{sj}$. The components $\sigma_{ijk}^*(\mathbf{x},\mathbf{y})$ are given by Eq. (8.89) for general elements or by Eq. (8.95) for special elements. Consequently, the generalized traction forces and electric displacement can be given as

$$\begin{Bmatrix} t_1 \\ t_2 \\ t_3 \\ D_n \end{Bmatrix} = \begin{Bmatrix} \mathbf{Q}_1 \\ \mathbf{Q}_2 \\ \mathbf{Q}_3 \\ \mathbf{Q}_4 \end{Bmatrix} \mathbf{c_e} = \mathbf{Q_e c_e} \tag{8.105}$$

where

$$\mathbf{Q_e} = \mathbf{n T_e} \tag{8.106}$$

$$\mathbf{n} = \begin{bmatrix} n_1 & 0 & 0 & 0 & n_2 & 0 & 0 \\ 0 & n_2 & 0 & 0 & n_1 & 0 & 0 \\ 0 & 0 & n_2 & n_1 & 0 & 0 & 0 \\ 0 & 0 & 0 & 0 & 0 & n_1 & n_2 \end{bmatrix} \tag{8.107}$$

The unknown $\mathbf{c}_e$ in Eq. (8.100) and Eq. (8.105) may be calculated using a hybrid technique (Wang and Qin 2009), in which the elements are linked through an auxiliary conforming displacement frame which has the same form as in conventional FEM. Thus, for the 2D piezoelectric problem under consideration, the frame field is assumed as

$$\tilde{\mathbf{u}}(\mathbf{x})=\begin{Bmatrix}\tilde{u}_1\\ \tilde{u}_2\\ \tilde{u}_3\\ \tilde{\phi}\end{Bmatrix}=\begin{Bmatrix}\tilde{\mathbf{N}}_1\\ \tilde{\mathbf{N}}_2\\ \tilde{\mathbf{N}}_3\\ \tilde{\mathbf{N}}_4\end{Bmatrix}\mathbf{d}_e=\tilde{\mathbf{N}}_e\mathbf{d}_e,\qquad(\mathbf{x}\in\Gamma_e)\tag{8.108}$$

where the symbol "~" is used to specify that the field is defined on the element boundary only, $\mathbf{d}_e=\mathbf{d}_e\left(\mathbf{c}_e\right)$ stands for the vector of the nodal displacements which are the final unknowns of the problem, Γ_e represents the boundary of element *e*, and $\tilde{\mathbf{N}}_e$ is the matrix of shape functions. Taking the side 3-4-5 of a particular 8-node quadrilateral element as an example, $\tilde{\mathbf{N}}_e$ and $\mathbf{d}_e$ can be expressed as

$$\tilde{\mathbf{N}}_e=\begin{bmatrix}0\cdots0 & \tilde{N}_1 & 0 & 0 & 0 & \tilde{N}_2 & 0 & 0 & 0 & \tilde{N}_3 & 0 & 0 & 0 & 0\cdots0\\ 0\cdots0 & 0 & \tilde{N}_1 & 0 & 0 & 0 & \tilde{N}_2 & 0 & 0 & 0 & \tilde{N}_3 & 0 & 0 & 0\cdots0\\ 0\cdots0 & 0 & 0 & \tilde{N}_1 & 0 & 0 & 0 & \tilde{N}_2 & 0 & 0 & 0 & \tilde{N}_3 & 0 & 0\cdots0\\ \underbrace{0\cdots0}_{8} & 0 & 0 & 0 & \tilde{N}_1 & 0 & 0 & 0 & \tilde{N}_2 & 0 & 0 & 0 & \tilde{N}_3 & \underbrace{0\cdots0}_{12}\end{bmatrix}$$

(8.109)

$$\mathbf{d_e}=\begin{bmatrix}u_{11} & u_{21} & u_{31} & \phi_1 & \cdots & u_{14} & u_{24} & u_{34} & \phi_4 & \cdots & u_{18} & u_{28} & u_{38} & \phi_8\end{bmatrix}^T\tag{8.110}$$

and $\tilde{N}_1$, $\tilde{N}_2$ and $\tilde{N}_3$ are expressed by the natural coordinate $\xi\in[-1,1]$

$$\tilde{N}_1=-\frac{\xi(1-\xi)}{2},\ \tilde{N}_2=1-\xi^2,\ \tilde{N}_3=\frac{\xi(1+\xi)}{2}\qquad\left(\xi\in[-1,1]\right)\tag{8.111}$$

8.4.4. Variational principles

Like the modified variational principles in Section 8.3.4, the hybrid functional Π_{me} for a particular element *e*, without body forces and electric charge density, is constructed as

$$\Pi_{me}=\Pi_e+\int_{\Gamma_e}t_i(\tilde{u}_i-u_i)d\Gamma+\int_{\Gamma_e}D_n(\tilde{\phi}-\phi)d\Gamma\tag{8.112}$$

where

$$\Pi_e=\frac{1}{2}\iint_{\Omega_e}(\sigma_{ij}\varepsilon_{ij}+D_iE_i)d\Omega-\int_{\Gamma_t}\bar{t}_i\tilde{u}_id\Gamma-\int_{\Gamma_D}\bar{D}_n\tilde{\phi}d\Gamma\tag{8.113}$$

and the boundary Γ_e of the element *e* is

$$\Gamma_e=\Gamma_{eu}\cup\Gamma_{et}\cup\Gamma_{eI}=\Gamma_{e\phi}\cup\Gamma_{eD}\cup\Gamma_{eI}\tag{8.114}$$

and

$$\Gamma_{eu}=\Gamma_e\cap\Gamma_u,\Gamma_{et}=\Gamma_e\cap\Gamma_t,\Gamma_{e\phi}=\Gamma_e\cap\Gamma_\phi,\Gamma_{eD}=\Gamma_e\cap\Gamma_D\tag{8.115}$$

With Gaussian theorem and equilibrium equations, the functional in Eq. (8.112) may be simplified as

$$\Pi_{me} = -\frac{1}{2}\int_{\Gamma_e}(t_i u_i + D_n\phi)d\Gamma + \int_{\Gamma_e}(t_i\tilde{u}_i + D_n\tilde{\phi})d\Gamma - \int_{\Gamma_t}\bar{t}_i\tilde{u}_i d\Gamma - \int_{\Gamma_D}\bar{D}_n\tilde{\phi}d\Gamma \qquad (8.116)$$

As shown in Section 8.3.2, it can be easily proved that the stationary conditions of the above functional leads to Eqs. (8.1)-(8.7).

8.4.5. Element stiffness equation

Substituting Eqs. (8.100), (8.108) and (8.105) into the above functional (8.112) yields the formulation

$$\Pi_{me} = -\frac{1}{2}\mathbf{c}_e^{\,T}\mathbf{H}_e\mathbf{c}_e + \mathbf{c}_e^{\,T}\mathbf{G}_e\mathbf{d}_e - \mathbf{d}_e^{\,T}\mathbf{g}_e \qquad (8.117)$$

where

$$\mathbf{H}_e = \int_{\Gamma_e}\mathbf{Q}_e^{\mathrm{T}}\mathbf{N}_e \mathrm{d}\Gamma \;,\quad \mathbf{G}_e = \int_{\Gamma_e}\mathbf{Q}_e^{\mathrm{T}}\tilde{\mathbf{N}}_e \mathrm{d}\Gamma \;,\quad \mathbf{g}_e = \int_{\Gamma_t}\tilde{\mathbf{N}}_e^{\mathrm{T}}\bar{\mathbf{t}}d\Gamma + \int_{\Gamma_D}\tilde{\mathbf{N}}_e^{\mathrm{T}}\bar{\mathbf{D}}d\Gamma \qquad (8.118)$$

The stationary condition of the functional Π_{me} with respect to $\mathbf{c}_e$ and $\mathbf{d}_e$, respectively, yields

$$\frac{\partial\Pi_{me}}{\partial\mathbf{c}_e^{\mathrm{T}}} = -\mathbf{H}_e\mathbf{c}_e + \mathbf{G}_e\mathbf{d}_e = \mathbf{0}, \quad \frac{\partial\Pi_{me}}{\partial\mathbf{d}_e^{\mathrm{T}}} = \mathbf{G}_e^{\,T}\mathbf{c}_e - \mathbf{g}_e = \mathbf{0} \qquad (8.119)$$

from which the relationship between $\mathbf{c}_e$ and $\mathbf{d}_e$, and the stiffness equation can be obtained

$$\mathbf{c}_e = \mathbf{H}_e^{-1}\mathbf{G}_e\mathbf{d}_e \qquad (8.120)$$

$$\mathbf{K}_e\mathbf{d}_e = \mathbf{g}_e \qquad (8.121)$$

where $\mathbf{K}_e = \mathbf{G}_e^{\mathrm{T}}\mathbf{H}_e^{-1}\mathbf{G}_e$ is the element stiffness matrix.

Following the procedure in (Qin 2000), the missing rigid-body motion can be recovered by setting the augmented internal field of a particular element e as

$$\mathbf{u}_e = \mathbf{N}_e\mathbf{c}_e + \begin{bmatrix} 1 & 0 & 0 & 0 & 0 & -x_2 & 0 \\ 0 & 1 & 0 & 0 & 0 & x_1 & 0 \\ 0 & 0 & 1 & x_2 & -x_1 & 0 & 0 \\ 0 & 0 & 0 & 0 & 0 & 0 & 1 \end{bmatrix}\mathbf{c}_0 \qquad (8.122)$$

where the undetermined rigid-body motion parameter $\mathbf{c}_0$ can be calculated using the least square matching of $\mathbf{u_e}$ and $\tilde{\mathbf{u}}_\mathbf{e}$ at element nodes

$$\min = \sum_{i=1}^{n}\left[\left(u_{1i}-\tilde{u}_{1i}\right)^2 + \left(u_{2i}-\tilde{u}_{2i}\right)^2 + \left(u_{3i}-\tilde{u}_{3i}\right)^2 + \left(\phi_i-\tilde{\phi}_i\right)^2\right] \qquad (8.123)$$

which finally gives

$$\mathbf{c_0} = \mathbf{R}_e^{-1}\mathbf{r_e} \qquad (8.124)$$

$$\mathbf{R_e} = \sum_{i=1}^{n} \begin{bmatrix} 1 & 0 & 0 & 0 & 0 & -x_{2i} & 0 \\ 0 & 1 & 0 & 0 & 0 & x_{1i} & 0 \\ 0 & 0 & 1 & x_{2i} & -x_{1i} & 0 & 0 \\ 0 & 0 & x_{2i} & x_{2i}^2 & -x_{1i}x_{2i} & 0 & 0 \\ 0 & 0 & -x_{1i} & -x_{1i}x_{2i} & x_{1i}^2 & 0 & 0 \\ -x_{2i} & x_{1i} & 0 & 0 & 0 & x_{1i}^2+x_{2i}^2 & 0 \\ 0 & 0 & 0 & 0 & 0 & 0 & 1 \end{bmatrix} \tag{8.125}$$

$$\mathbf{r_e} = \sum_{i=1}^{n} \begin{Bmatrix} \Delta u_{e1i} \\ \Delta u_{e2i} \\ \Delta u_{e3i} \\ \Delta u_{e3i} x_{2i} \\ -\Delta u_{e3i} x_{1i} \\ \Delta u_{e2i} x_{1i} - \Delta u_{e1i} x_{2i} \\ \Delta \phi_{ei} \end{Bmatrix} \tag{8.126}$$

in which $\mathbf{\Delta u}_{ei} = \left(\tilde{\mathbf{u}}_e - \hat{\mathbf{u}}_e\right)\big|_{\mathbf{node\,i}}$ and n is the number of element nodes.

8.4.6. Numerical examples

Several numerical examples are presented in this section to illustrate the application of the HFS-FEM and to demonstrate its effectiveness and accuracy.

Example 1: Simple tension of a piezoelectric prism

In this example a PZT-4 piezoelectric prism subjected to simple tension, as shown in Fig. 8.20, is investigated by the proposed HFS-FEM. The properties of the material PZT-4 are as follows (Ding, Wang et al. 1998):

$$c_{11} = 12.6\times10^{10}\,\mathrm{Nm}^{-2}, c_{12} = 7.78\times10^{10}\,\mathrm{Nm}^{-2}, c_{13} = 7.43\times10^{10}\,\mathrm{Nm}^{-2},$$

$$c_{33} = 11.5\times10^{10}\,\mathrm{Nm}^{-2}, c_{44} = 2.56\times10^{10}\,\mathrm{Nm}^{-2}$$

$$e_{15} = 12.7\mathrm{Cm}^{-2}, e_{31} = -5.2\mathrm{Cm}^{-2}, e_{33} = 15.1\mathrm{Cm}^{-2}$$

$$\kappa_{11} = 730\kappa_0, \kappa_{33} = 635\kappa_0, \kappa_0 = 8.854\times10^{-12}\,\mathrm{C/Nm}$$

In this analysis, the dimensions of the geometry are set as a = 3 m, h = 10 m, P = 10 Pa. Considering the symmetry conditions of the problem, only one quadrant of the prism is modeled by HFS-FEM. The corresponding boundary conditions are

$$\sigma_{xx} = \sigma_{xz} = D_x = 0 \quad \text{at } x = \pm a$$

$$\sigma_{zz} = P, \quad \sigma_{xz} = D_z = 0 \quad \text{at } z = \pm h$$

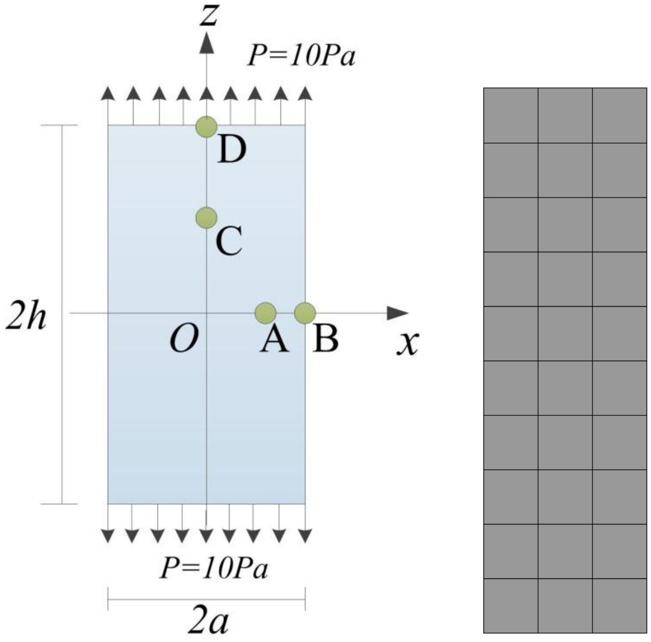

Figure 8.20 Geometry, boundary conditions and mesh configuration of the piezoelectric prism.

Table 8.9 Comparison of the predicted results from HFS-FEM with the analytical results.

Position	u_x $(10^{-10}\,\mathrm{m})$	u_z $(10^{-9}\,\mathrm{m})$	ϕ (V)	σ_{xx} $(\mathrm{N}\cdot\mathrm{m}^{-2})$	σ_{zz} $(\mathrm{N}\cdot\mathrm{m}^{-2})$	D_z $(\mathrm{N}\cdot\mathrm{m}^{-2})$
A	-0.7220 (-0.7222)	0.0000 (0.0000)	0.0000 (0.0000)	0.0018 (0.0000)	9.9991 (10.000)	-0.0000 (0.0000)
B	-1.0831 (-1.0834)	0.0000 (0.0000)	0.0000 (0.0000)	0.0019 (0.0000)	9.9992 (10.000)	-0.0003 (0.0000)
C	0.0000 (0.0000)	0.3914 (0.3915)	1.2187 (1.2183)	0.0018 (0.0000)	9.9992 (10.000)	-0.0000 (0.0000)
D	0.0000 (0.0000)	0.7828 (0.7829)	2.4373 (2.4367)	0.0019 (0.0000)	9.9991 (10.000)	-0.0001 (0.0000)

As shown in Figure 8.20, thirty quadrilateral elements are used in this model. The displacements and electric potential of the four selected reference points: A (2,0), B (3,0), C (0,5), and D (0,10), are listed in Table 8.9. The analytical results of the corresponding points are also given for comparison (Ding, Wang et al. 1998). It can be seen that the HFS-FEM results are in good agreement with the analytical ones. The contour plots of the piezoelectric plate under simple tension are given in Figure 8.21, clearly demonstrating that the displacement field and electrical distribution are in linear variation as expected.

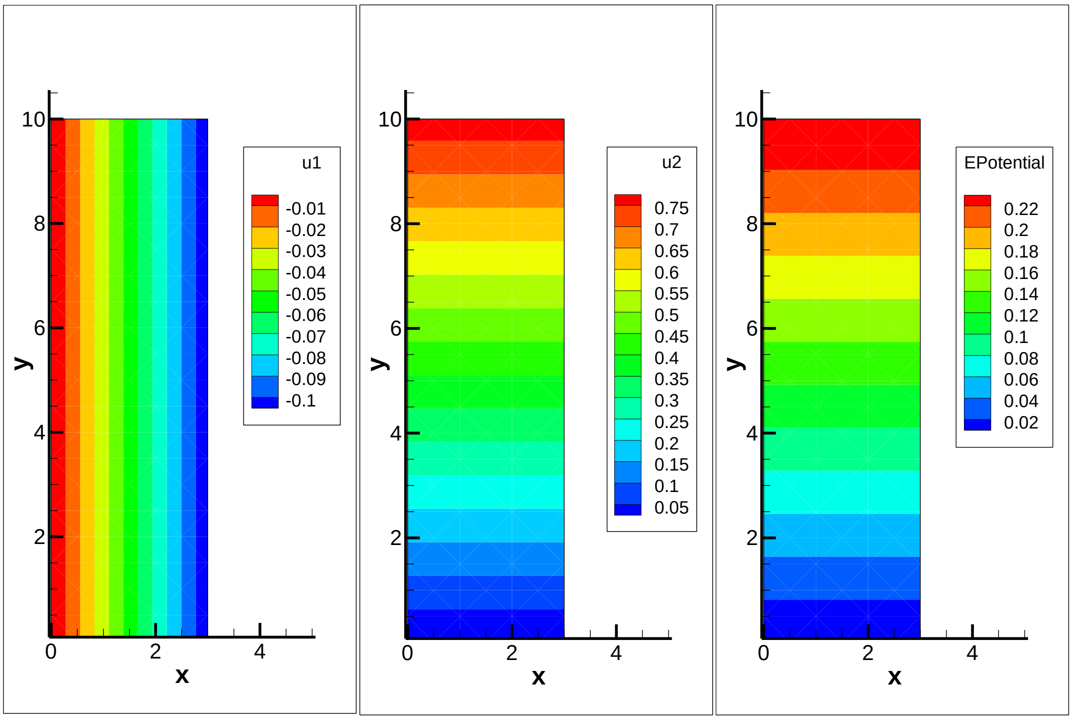

Figure 8.21 Contour plot of the displacement and electric potential of the plate.

Example 2: Infinite piezoelectric plate with a circular hole

In this example, an infinite piezoelectric plate with a circular hole as shown in Figure 8.13 is assessed by the new HFS-FEM based on Stroh formalism. The material parameters used are given in Table 8.10. It is assumed that a remote mechanical load $\sigma_{zz}^{\infty}=\sigma_0$ or electrical load $D_{zz}^{\infty}=D_0$ is applied to the plate along the z-axis direction (poling direction), while traction- and electric charge-free boundary conditions are applied on the edge of the hole. As in our previous study (Cao, Qin et al. 2012), we assume the radius of the hole to be $r=1$ and L/r=20 to approximate the infinite piezoelectric plate in this work. In this analysis, 117 eight-node quadratic elements are employed for the one-quarter piezoelectric plate. The results for the stress σ_θ and electric displacement D_θ are normalized with respect to either the far field applied stress $\sigma_{zz}^{\infty}=\sigma_0$ or the far field applied electric displacement $D_{zz}^{\infty}=D_0$.

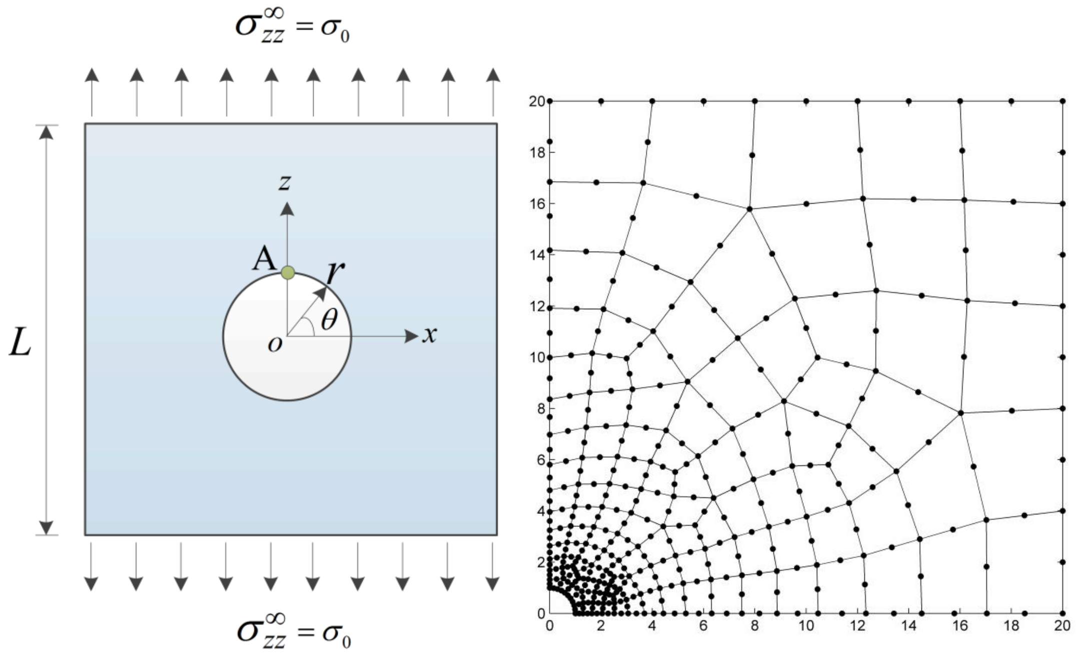

Figure 8.22 An infinite piezoelectric plate with a circular hole subjected to remote stress.

Figure 8.16 presents the variations of the normalized stress σ_θ/σ_0 and the normalized electric displacement $D_\theta/\sigma_0\times10^{10}$ along the edge of the hole under remote mechanical load. It is obvious that the results obtained from HFS-FEM agree very well with the results from analytical solution by Sosa (Sosa 1991). It is also verified that when loading along the poling direction, the electromechanical coupling effect is able to alleviate the stress concentration occurring in the plate.

Table 8.10 Properties of the material PZT-4 used in Example 2.

Parameters	Values	Parameters	Values
c_{11}	$13.9\times10^{10}\,\mathrm{Nm}^{-2}$	e_{15}	$13.44\mathrm{Cm}^{-2}$
c_{12}	$7.78\times10^{10}\,\mathrm{Nm}^{-2}$	e_{31}	$-6.98\mathrm{Cm}^{-2}$
c_{13}	$7.43\times10^{10}\,\mathrm{Nm}^{-2}$	e_{33}	$13.84\mathrm{Cm}^{-2}$
c_{33}	$11.3\times10^{10}\,\mathrm{Nm}^{-2}$	κ_{11}	$6.0\times10^{-9}\,\mathrm{C/Nm}$
c_{44}	$2.56\times10^{10}\,\mathrm{Nm}^{-2}$	κ_{33}	$5.47\times10^{-9}\,\mathrm{C/Nm}$

It can be observed from Figure 8.16 that the maximum values of σ_θ appears at $\theta = 0^\circ$ and $\theta = 180^\circ$ for the applied load σ_{zz}^{∞}, which also agrees well with the analytical solution from Sosa (Sosa 1991). It is found from Figure 8.24 that the maximum values of D_θ appear at $\theta = 65^\circ$ and $\theta = 115^\circ$, which also agrees well with the analytical solution from Sosa.

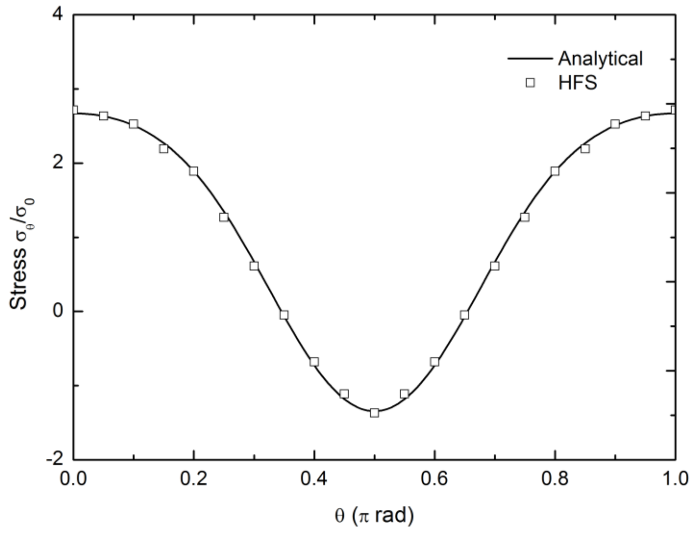

Figure 8.23 Variation of normalized stress σ_θ / σ_0 along the hole boundary under remote mechanical load.

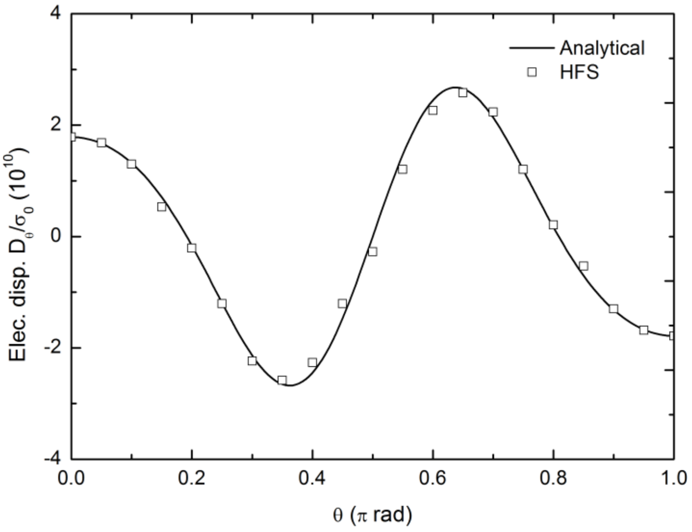

Figure 8.24 Variation of normalized electrical displacement $D_\theta / \sigma_0 \times 10^{10}$ along the hole boundary under remote mechanical load.

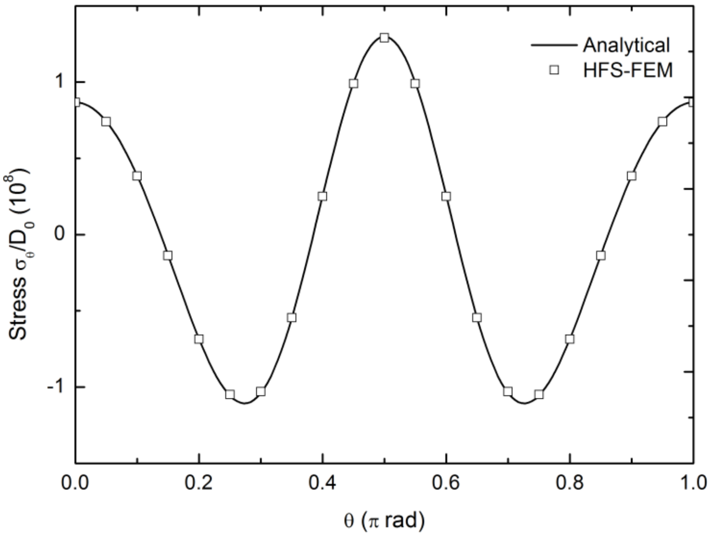

Figure 8.25 Variation of normalized stress $\sigma_\theta / D_0 \times 10^8$ along the hole boundary under remote electrical load.

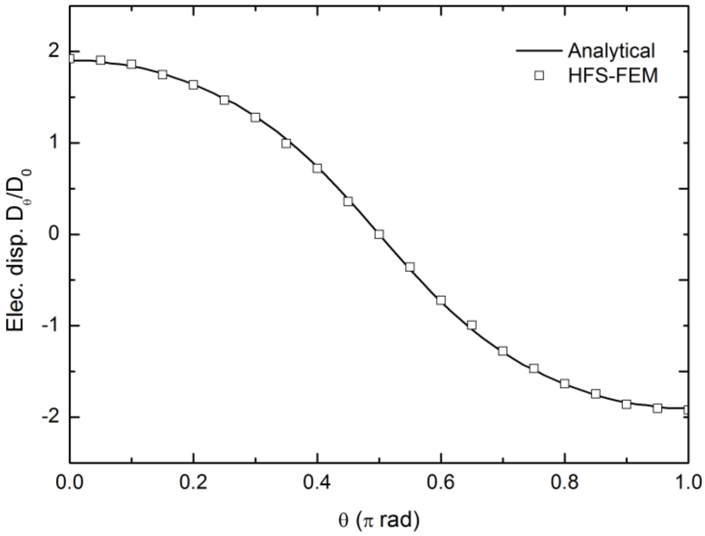

Figure 8.26 Variation of normalized electrical displacement D_θ / D_0 along the hole boundary under remote electrical load.

Figure 8.25 shows the variation of normalized stress $\sigma_\theta / D_0 \times 10^8$ and electrical displacement D_θ / D_0 along the hole boundary under remote electrical load. It can be seen from Figure 8.25 that electrical displacement can induce strong stress concentration problems in piezoelectric materials with defects, which the stress concentration can be up to $\sigma_\theta / D_0 \times 10^8$ times the applied D_0. It can be seen from Figure 8.26 that D_θ reaches its maximum at $\theta = 0^\circ$ and its minimum at $\theta = 180^\circ$, which also agrees well with the analytical solution from Sosa (1991). To achieve the same accuracy, 960 8-node ordinary parametric elements are needed to model a quarter of the plate (Deng and Wang 2002). It is obvious that the computational efficiency of the HFS-FEM is superior for this investigated case.

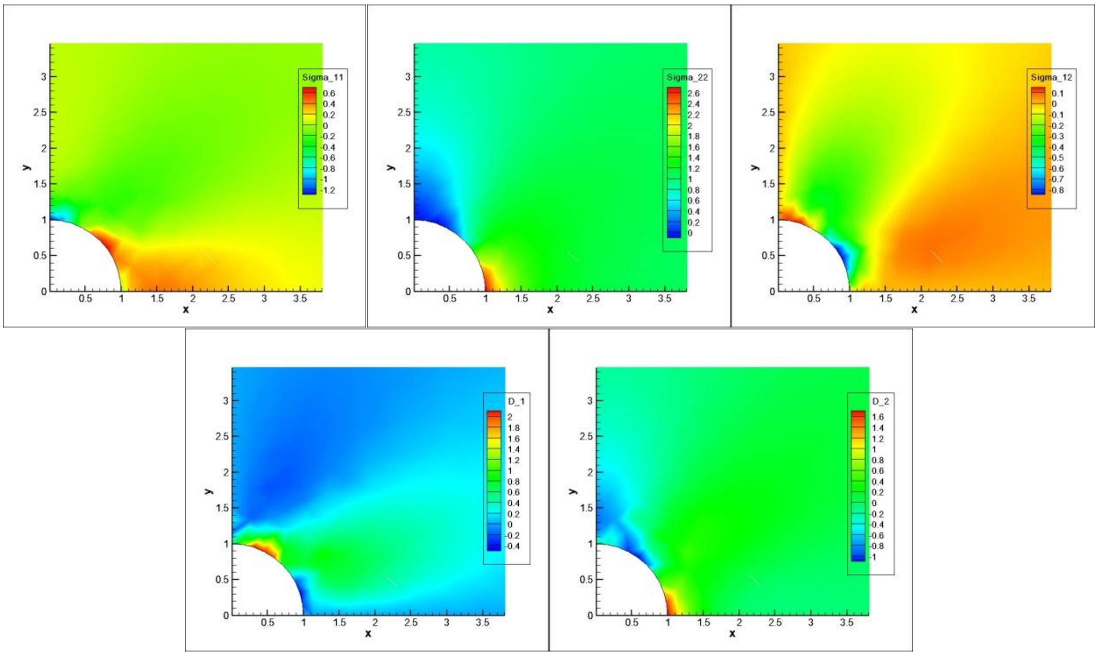

Figure 8.27 Contour plots of stress and electric displacement components around the elliptical hole in the piezoelectric plate under remote mechanical load.

Example 3: Infinite piezoelectric plate with elliptical hole

To investigate the performance of the special element, an infinite piezoelectric plate with an elliptical hole is modeled by the HFS-FEM. A uniform remote tension σ_0 is applied in z direction. The material parameters are the same as those used in Example 2. In this analysis, as shown in Figure 8.28, the infinite plate is approximated by a finite domain with the length and width assumed to be *L=W=20* mm, and the geometry of the ellipse being $a=2b=2$ mm. In this case, it is not necessary to use numerous elements to capture the concentrated stress as in traditional FEM. A relatively coarse mesh can be employed and the elliptical hole can be analyzed by only one special element. There are total 49 elements with a total of 176 nodes: 48 8-node conventional hybrid elements and one central special element containing the elliptical hole, which is given in Figure 8.29.

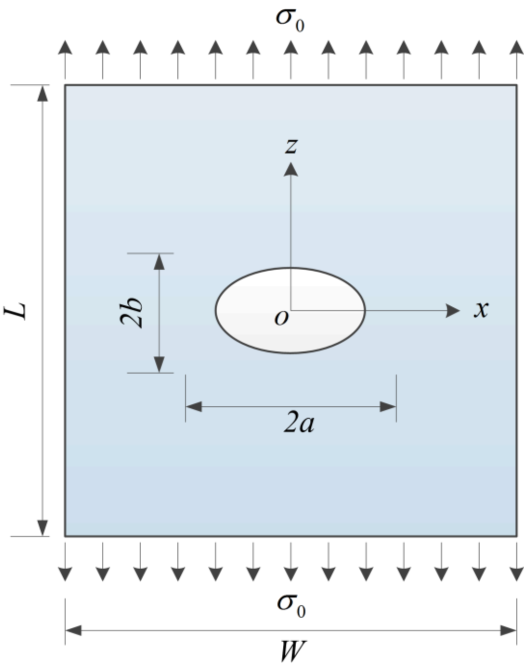

Figure 8.28 Schematic of an infinite piezoelectric plate with an elliptical hole under remote tension.

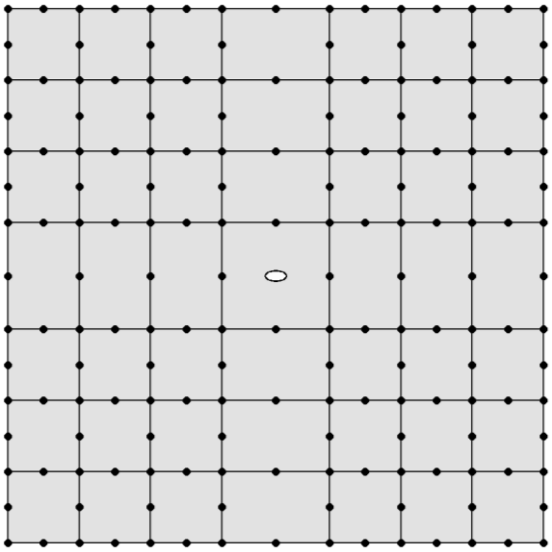

Figure 8.29 Mesh configuration with special element for the piezoelectric plate.

Figure 8.30 shows the variations of the normalized hoop stress σ_θ / σ_0 and electric displacement D_θ / σ_0 along the rim of the elliptical hole. It can be seen from

Figure 8.30 that the results obtained from HFS-FEM are in very good agreement with the analytical solutions. This indicates that the proposed method with the special element can capture the dramatic variations of hoop stress and electric displacement induced by the elliptical hole in the plate.

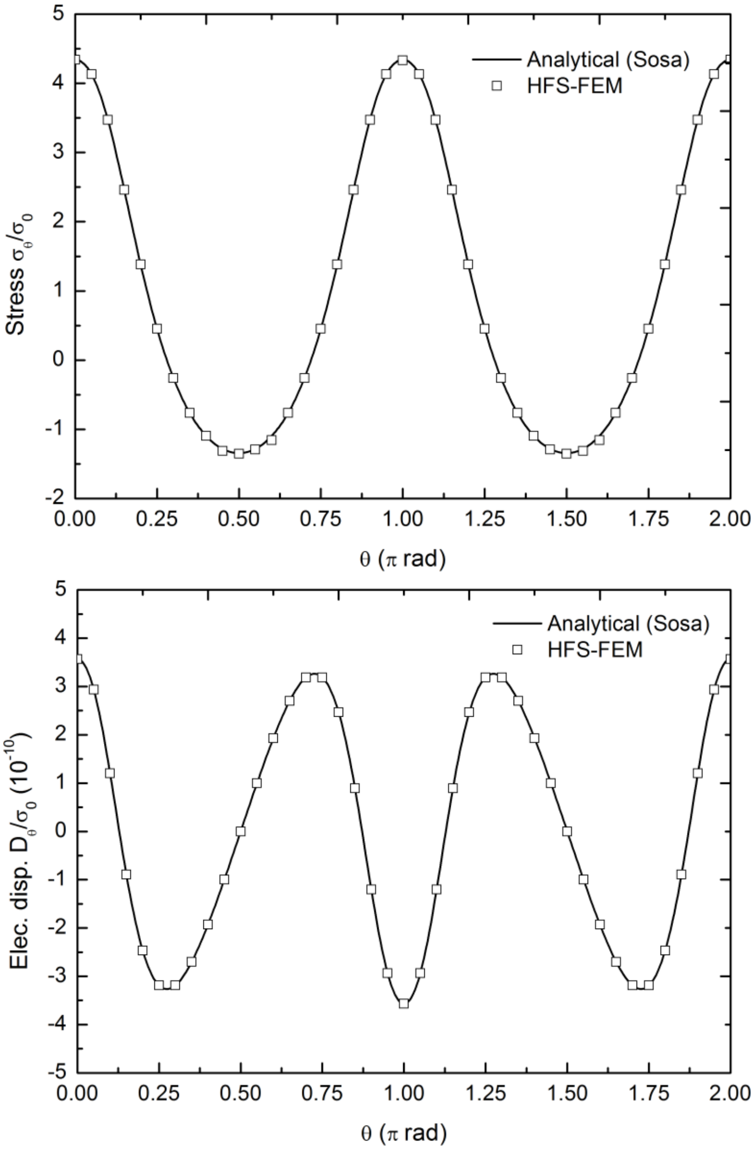

Figure 8.30 Variations of the normalized hoop stress σ_θ / σ_0 and electric displacement D_θ / σ_0 along the rim of the elliptical hole.

Example 4: An infinite piezoelectric plate with a center crack

In this example the extreme case of the elliptical hole is considered. By setting the minor axis b equal to zero, an elliptical hole can be made into a crack of length

$2a$. The geometry and loading for this problem are shown in Figure 8.31. The dimensions are assumed to be $2a/W$ =0.1 and L/W =1, so that it can be approximated to an infinite plate with a finite crack. The plate is made of PZT-5H ceramic and the material parameters are listed in Table 8.11 . The remote mechanical loading and electric loading are $\sigma_{zz}^{\infty} = 1.0\times10^6$ Pa, $\sigma_{zx}^{\infty} = 1.0\times10^6$ Pa and $D_{zz}^{\infty} = 1.0\times10^6$ C/m^2. The same mesh as used in Example 3 is employed for this problem.

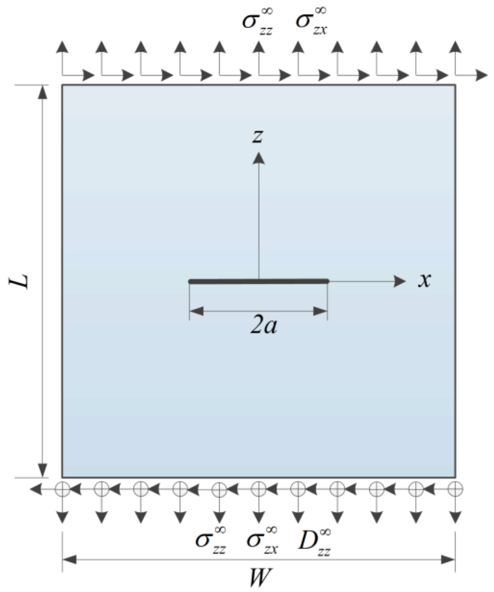

Figure 8.31 An orthotropic plate with a center crack under uniform tension.

Table 8.11 Properties of the material PZT-5H used in Example 4

Parameters	Values	Parameters	Values
c_{11}	$12.6\times10^{10}\,\mathrm{Nm}^{-2}$	e_{15}	$17.0\mathrm{Cm}^{-2}$
c_{12}	$5.5\times10^{10}\,\mathrm{Nm}^{-2}$	e_{31}	$-6.5\mathrm{Cm}^{-2}$
c_{13}	$5.3\times10^{10}\,\mathrm{Nm}^{-2}$	e_{33}	$23.3\mathrm{Cm}^{-2}$
c_{33}	$11.7\times10^{10}\,\mathrm{Nm}^{-2}$	κ_{11}	$15.1\times10^{-9}\,\mathrm{C/Nm}$
c_{44}	$3.53\times10^{10}\,\mathrm{Nm}^{-2}$	κ_{33}	$13.0\times10^{-9}\,\mathrm{C/Nm}$

The stress and electric intensity factors K_I, K_{II} and K_{IV} calculated by the proposed HFS-FEM are given in Table 8.12, in which the analytical solutions obtained from the formulations of Sosa and the BEM results (Sosa 1991; Ding, Wang et al. 1998) are listed for comparison. Figure 8.32 shows the variation of K_{IV} with respect to the applied remote electric displacement D_{zz}^{∞}. It can be seen from Table 8.13 and Figure 8.32 that the results from the HFS-FEM exhibit a good agreement with the analytical solutions and have similar accuracy to that of the BEM.

Table 8.14 The stress and electric intensity factors K_I, K_{II} and K_{IV}.

Method	$K_I\,(10^6 N\cdot m^{-3/2})$	$K_{II}\,(10^6 N\cdot m^{-3/2})$	$K_{IV}\,(10^{-3} N\cdot m^{-3/2})$
HFS-FEM	0.1761	0.1707	0.1753
BEM	0.1757	0.1708	0.1750
Analytical	0.1772	0.1772	0.1772

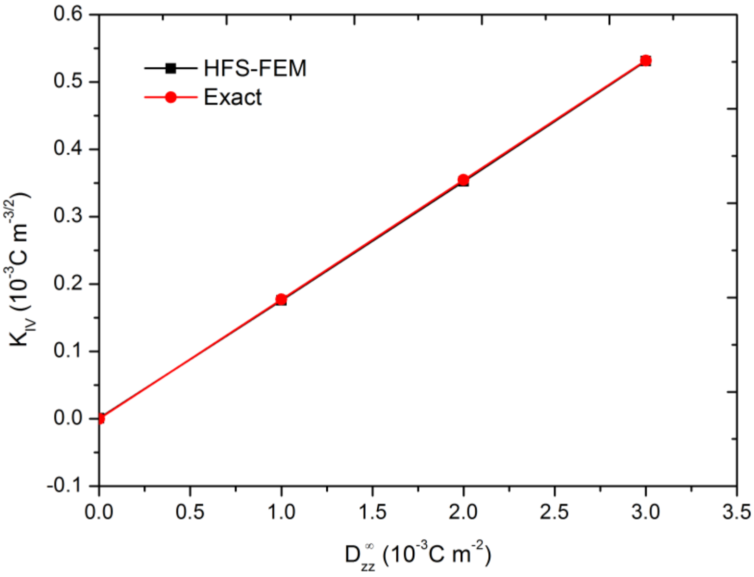

Figure 8.32 The variation of K_{IV} with respect to the applied remote electric displacement D_{zz}^{∞}.

8.5. SUMMARY

In this chapter the HFS-FEM is developed to predict the coupling behaviors of plane piezoelectric materials. Two different series of formulations are developed, based on the foundational solutions derived from Lekhnitskii formalism and Stroh formalism for piezoelectric materials. Based on the fundamental solutions derived from the elegant Stroh formalism, a special hybrid finite element for the HFS-FEM is also developed for modeling plane piezoelectric materials with cracks or elliptical holes. In this method, the general or special foundational solutions of the piezoelectric materials are employed to approximate the intra-element DEP, and the element frame field is interpolated by the common shape functions. A modified variational functional, satisfying the governing equation, boundary and continuity conditions, is proposed to derive the element stiffness equation of the proposed method for piezoelectric materials.

To verify and assess the performance of the new method, numerical examples are considered and the results from the HFS-FEM are compared with those from analytical solutions or the literatures. It is found that the HFS-FEM has good performance in the analysis of the coupling behavior of piezoelectric materials under various different loading conditions. It is also found that the electromechanical coupling effect on the SCF is dependent on the loading direction. In comparison with pure elastic materials, stress concentration is smaller when loaded in the poling direction but larger when loaded in the direction perpendicular to the poling direction.

The numerical results show that the special element is able to capture the strong stress/electric displacement concentration around the elliptical hole and can obtain accurate SIFs for cracks while simultaneously eliminating the need for very fine meshing around such defects. The HFS-FEM offers the attractive possibility of developing accurate crack, corner or perforated elements, simply by using appropriate special fundamental solutions as the trial functions of the intra-element displacements. It can be concluded that the HFS-FEM is a promising numerical method for solving complex piezoelectric problems.

Chapter 9. Conclusions and Outlook

The main objective of this research has been to develop the newly proposed HFS-FEM for modeling elasticity problems (2D and 3D) and multifield materials, and to demonstrate its capability and performance in predicting the behaviors of heterogeneous composite materials at both micro and macro scales. The scope of the thesis covers: review and summary of the formulations of the HFS-FEM for modeling the macroscale behaviors of elasticity problems and thermal transfer problems and extension of this approach to dealing with 3D problems; development of the method for predicting the micromechanical behaviors of composites by considering their microstructures; and development of the method for modeling multifield problems such as thermoelasticity and electric-mechanical problems. The conclusions from this research are summarized in this chapter. Recommendations and outlook for future research are also provided in the last part of the chapter.

9.1. SUMMARY OF PRESENT RESEARCH

9.1.1. Macroscale modeling of materials by HFS-FEM

In this work a novel hybrid finite element formulation based on fundamental solutions (HFS-FEM) has been developed to provide a simple but accurate approach for analyzing general elastic materials in 2D and 3D, including both isotropic and anisotropic materials. In this approach, two independent displacements fields are employed, one being the intra-element displacement approximations defined in the element domain, and the other being the element frame displacement fields defined along the element boundary. General fundamental solutions are used for the interpolation of inter-element displacement and traditional shape functions as used in FEM are employed for frame field interpolation. For general anisotropic materials, Green's functions derived from Stroh formalism are employed to approximate the intra-element displacement field of the elements, and polynomial shape functions as used in traditional FEM are utilized to interpolate the frame field.

The method of particular solution and radial basis function approximation are applied to treat elastic problems involving body forces. The homogeneous solution is obtained by the HFS-FEM and the particular solution by the approach of radial basis function. Accuracy and convergence are verified through comparison with exact or numerical solutions given in the literature or by ABAQUS. The standard tests reveal that the new method with linear 8-node and quadratic 20-node brick elements can successfully pass the patch tests and that the HFS-HEX8 element exhibits shear locking phenomenon and cannot pass the trapezoidal and parallelogram beam test, although it is not very sensitive to the mesh distortion. It is also demonstrated that the convergence of the new method is usually superior to that of traditional FEM and it can be used in problems with nearly incompressible materials without volumetric locking. This new method seems to be promising to deal with problems involving complex geometry, stress concentration and multi-materials. Numerical results show that the proposed method is accurate and efficient in modeling anisotropic composite, and can easily be further extended to analyze composite laminates.

9.1.2. Microscale modeling of composites by HFS-FEM

In order to characterize the microstructures of heterogeneous composites, the new HFS-FEM and the HT-FEM are combined with homogenization techniques to perform micromechanical analysis of fiber-reinforced composite materials. The homogenization technique is implemented to determine the equivalent macroscale material properties of heterogeneous composites, using the concept of the RVE. For elasticity problems, two kinds of fiber reinforced composites are analyzed, including isotropic and orthotropic materials. Numerical results show that the solutions obtained by HT-FEM and HFS-FEM coincide with the results calculated by ABAQUS with fine and high order elements. HT-FEM and HFS-FEM are insensitive to mesh density and irregular element geometry, and give more accurate results than ABAQUS when using the same meshes. It is concluded that linear elements of HTFEM and HFS-FEM can achieve the same accuracy as achieved by ABAQUS using quadratic order elements with same element density.

The influence of microstructure parameters, such as the shape of fibers, on the effective parameters are investigated in this chapter. It is found that for both isotropic and orthotropic fiber-reinforced composites, all the effective stiffness parameters increase with an increase in FVF although the rates of increase of these parameters differ over the investigated range. Further, for isotropic fiber-reinforced composites, it is observed that effective transversal Young's modulus increases with the reinforced fiber volume fraction whereas the effective Poisson's ratio decreases with the reinforced fiber volume fraction. The results also reveals that an elliptical inclusion can dramatically increase the stiffness of a reinforced composite in its major axis direction while not significantly decreasing the other three stiffness parameters simultaneously. It is also demonstrated that a triangular shaped inclusion has good reinforcement performance, as composites thus reinforced have greater effective stiffness than composite counterparts with a circle inclusion.

For problems of heat transfer in heterogeneous composites, using the special fundamental solution, a type of special element with an inclusion involved is proposed for mesh reduction in analyzing the composites. The effective thermal conductivity of composites is evaluated through RVEs with single or multiple fibers, using the homogenization technique. The effects of fiber volume fraction and of the mismatch ratio of fiber and matrix in the composites are investigated by this method. It is shown that the numerical solutions obtained by HFS-FEM coincide with the results calculated by ABAQUS with a fine element mesh. It is also found that the effective thermal conductivity increases with an increase in fiber volume fraction. The usage of a special inclusion element can significantly reduce model meshing effort and computing cost, and simultaneously avoid mesh regeneration when the fiber volume fraction changes slightly. It can be concluded that the proposed micromechanical models based on HFS-FEM, especially with special elements, have the potential to model fiber-reinforced composites and to be further developed for considering defects such as cracks and pore voids in microstructures and for multi-scale simulation in future work.

9.1.3. HFS-FEM for multifield materials

A new solution procedure based on HFS-FEM is proposed to solve 2D and 3D thermoelastic problems with arbitrary body forces and temperature changes in this thesis. The body force and temperature change are treated by the method of particular solution, in which the homogeneous solution is obtained using the HFS-FEM with elastic fundamental solutions and the particular solution is approximated by the radial basis function. Comparison of different strategies shows that treating body force and temperature change as a whole is superior to approximating them separately. The numerical examples in this chapter show that the proposed method is able to predict the thermoelastic response of 2D and 3D thermoelasticity problems with complex geometry, arbitrary body force and arbitrary temperature changes. It is a promising methodology for mesh reduction, which is capable of obtaining satisfactory results with much coarser meshes than the traditional FEM. It is also possible to improve the results by increasing only the interpolation points while maintaining the mesh at a lower density, which will be investigated in further research.

Further, the HFS-FEM is developed to model the coupling behaviors of plane piezoelectric materials. This thesis develops two different series of formulations based respectively on foundational solutions derived from Lekhnitskii formalism and Stroh formalism. On the basis of special fundamental solutions derived from Stroh formalism, a special hybrid finite element with high efficiency for HFS-FEM is also developed for modeling plane piezoelectric materials with cracks or elliptical holes. The performance of the new method is verified and assessed using various numerical examples. It is found that the HFS-FEM has good performance in the analysis of the coupling behavior of piezoelectric materials under various different loading conditions. It is also found that the electromechanical coupling effect on the SCF is dependent on the loading direction. Compared with pure elastic materials, stress concentration in piezoelectric materials is lower when loaded in the poling direction but higher when loaded at the direction perpendicular to the poling direction. Numerical results show that the special element is able to capture the strong stress/electric displacement concentration around an elliptical hole and can obtain accurate SIFs for cracks while simultaneously eliminating the need for very fine meshing around such defects.

9.2. RECOMMENDATIONS FOR FUTURE RESEARCH

As stated initially, the goal of the present research is to extend the newly proposed HFS-FEM to elasticity problems (2D and 3D) and multifield materials, and to demonstrate its capability and performance in predicting the behaviors of heterogeneous composite materials at micro and macro scales. Due to time limitation, however, some interesting problems are left for further enhancement and future applications of the hybrid finite element method as listed here:

- In the examples of the thesis, all the meshes employed for numerical calculation are partially facilitated by the ABAQUS CAE, a GUI facilitating model building. For the general elements in the model, it is easier to use ABAQUS to generate the in-house code for preparing the input data file, however, when certain special elements are involved in the analysis, mesh generation work becomes a very challenging problem and much effort is required to partition the model and write the input file. It is of practical interest, therefore, to develop a preprocessing tool like the CAE/ABAQUS for the current code to facilitate creation of the meshing domains and preparation of the input files. If this is done, it will be much more convenient for potential users to employ this method and its code as a tool for design and analysis.
- One of the great merits of the new method is that an arbitrarily shaped element and certain special elements for local defects or singularity loads can easily be employed and implemented in the framework in order to reduce the number of elements and simultaneously improve accuracy. In the present work, only a few

special elements are proposed: a special element with a central hole for heat transfer and eleaticity, special element with a central inclusion for heat transfer, special elements with an elliptical hole for elasticity, and a special element with a point/line concentrated load for elasticity and piezoelasticity. It is interesting and important in further research to develop new special elements based on the Stroh formalism of multifield materials with defects and concentrated loads.

- In the current work, micromechanical modeling is conducted based on the averaged or homogenization technique. The cohesive zone model for interface failure will in future be employed to enrich the micro-scale model with the ability to simulate crack propagation. It will be of interest and beneficial in the future to develop a concurrent multiscale framework for modeling heterogeneous composite materials. The new multiscale methodology can be established based on the heterogeneous multiscale method.
- In this thesis thermoelasticity and piezoelectric problems are considered. Considering the importance of multifield materials in smart structures design and analysis, it will be beneficial to extend this method to be capable of modeling thermal-electric-mechanical and thermal-electric-magnetic-mechanical materials in future.
- It is also noted that all the problems considered in the thesis belong to the class of static problems. It will be a major development and improvement to extend the method to dynamic problems such as vibration, moving load, etc. In addition, it is interesting to develop this method with the capability to treating contact and friction problems.
- Finally, it is possible to extend the current method to nonlinear problems by treating nonlinear terms as a generalized body force and developing a convergent iterative algorithm.

Bibliography

A.H.-D, C. (2000). "Particular solutions of Laplacian, Helmholtz-type, and polyharmonic operators involving higher order radial basis functions." Engineering Analysis with Boundary Elements **24**(7-8): 531-538.

Aboudi, J. (1991). Mechanics of composite materials : a unified micromechanical approach. Amsterdam ; New York, Elsevier.

Abrate, S. (1994). "Optimal design of laminated plates and shells." Composite Structures **29**(3): 269-286.

Aghdam, M., S. Falahatgar, et al. (2008). "Micromechanical consideration of interface damage in fiber reinforced Ti-alloy under various combined loading conditions." Composites Science and Technology **68**(15-16): 3406-3411.

Andelfinger, U. and E. Ramm (1993). "EAS-elements for two-dimensional, three-dimensional, plate and shell structures and their equivalence to HR-elements." International Journal for Numerical Methods in Engineering **36**(8): 1311-1337.

Areias, P. M. A., J. M. A. César de Sá, et al. (2003). "Analysis of 3D problems using a new enhanced strain hexahedral element." International Journal for Numerical Methods in Engineering **58**(11): 1637-1682.

Argyris, J. H., P. Dunne, et al. (1974). "Large natural strains and some special difficulties due to non-linearity and incompressibility in finite elements." Computer Methods in Applied Mechanics and Engineering **4**(2): 219-278.

Aubry, D., D. Lucas, et al. (1999). "Adaptive strategy for transient/coupled problems applications to thermoelasticity and elastodynamics." Computer Methods in Applied Mechanics and Engineering **176**(1-4): 41-50.

Bahtui, A. and M. R. Eslami "Coupled thermoelasticity of functionally graded cylindrical shells." Mechanics Research Communications **34**(1): 1-18.

Barnett, D. M. and J. Lothe (1975). "Dislocations and line charges in anisotropic piezoelectric insulators." physica status solidi (b) **67**(1): 105-111.

Barsoum, R. G. S. (1997). "Active materials and adaptive structures." Smart materials and structures **6**: 117.

Béchet, E., M. Scherzer, et al. (2009). "Application of the XFEM to the fracture of piezoelectric materials." International Journal for Numerical Methods in Engineering **77**(11): 1535-1565.

Bensoussan, A., J. L. Lions, et al. (1978). Asymptotic analysis for periodic structures, North Holland.

Benveniste, Y. (1987). "A new approach to the application of Mori-Tanaka's theory in composite materials." Mechanics of Materials **6**(2): 147-157.

Brennan, K. P. and D. E. Walrath (2009). "A Self-contained Module for Predicting Micro-scale Material Properties during Fiber-reinforced Polymer Processing." Journal of Thermoplastic Composite Materials **22**(6): 727-751.

Brucker, K. A. and J. Majdalani (2005). "Effective thermal conductivity of common geometric shapes." International Journal of Heat and Mass Transfer **48**(23): 4779-4796.

Cao, C., Q.-H. Qin, et al. (2012a). "A new hybrid finite element approach for three-dimensional elastic problems." Archives of Mechanics **64**(3): 261–292.

Cao, C., Q.-H. Qin, et al. (2012b). "Hybrid fundamental-solution-based FEM for piezoelectric materials." Computational Mechanics **50**(4): 397-412.

Cao, C., A. Yu, et al. (2012c). "Evaluation of Effective Thermal Conductivity of Fiber-Reinforced Composites." International Journal of Architecture, Engineering and Construction **1**(1): 14-29.

Cao, C., Q.-H. Qin, A. Yu (2012d). "A Novel Boundary-Integral Based Finite Element Method for 2D and 3D Thermo-Elasticity Problems." Journal of Thermal Stresses **35**(10): 849-876.

Cao, C., A. Yu, et al. (2013a). "A novel hybrid finite element model for modeling anisotropic composites." Finite Elements in Analysis and Design **64**: 36-47.

Cao, C., Q.-H. Qin, et al. (2013b). "Micromechanical analysis of heterogeneous composites using Hybrid Trefftz FEM and Hybrid Fundamental Solution based FEM." Journal of Mechanics **In press**.

Cao, C., A. Yu, et al. (2013c). "A new hybrid finite element approach for plane piezoelectricity with defects." Acta Mechanica **224**(1): 41-61.

Cao, Y. P., N. Hu, et al. (2002). "A 3D brick element based on Hu–Washizu variational principle for mesh distortion." International Journal for Numerical Methods in Engineering **53**(11): 2529-2548.

Caporale, A., R. Luciano, et al. (2006). "Micromechanical analysis of interfacial debonding in unidirectional fiber-reinforced composites." Computers & Structures **84**(31-32): 2200-2211.

Carrazedo, R. and H. B. Coda (2010). "Alternative positional FEM applied to thermomechanical impact of truss structures." Finite Elements in Analysis and Design **46**(11): 1008-1016.

Chao, C. and M. Shen (1997). "On bonded circular inclusions in plane thermoelasticity." Journal of applied mechanics **64**: 1000.

Chattopadhyay, A. and C. E. Seeley (1997). "A higher order theory for modeling composite laminates with induced strain actuators." Composites Part B: Engineering **28**(3): 243-252.

Chaudouet, A. (1987). "Three-dimensional transient thermo-elastic analyses by the BIE method." International Journal for Numerical Methods in Engineering **24**(1): 25-45.

Chawla, N., V. V. Ganesh, et al. (2004). "Three-dimensional (3D) microstructure visualization and finite element modeling of the mechanical behavior of SiC particle reinforced aluminum composites." Scripta Materialia **51**(2): 161-165.

Chawla, N., R. S. Sidhu, et al. (2006). "Three-dimensional visualization and microstructure-based modeling of deformation in particle-reinforced composites." Acta Materialia **54**(6): 1541-1548.

Chen, C. and S. Cheng (1967). "Mechanical properties of fiber reinforced composites." Journal of Composite Materials **1**(1): 30-41.

Chen, C. S. and C. A. Brebbia (1998). "The dual reciprocity method for Helmholtz-type operators." Boundary Elements Xx **4**: 495-504.

Chen, X. and T. Papathanasiou (2004). "Interface stress distributions in transversely loaded continuous fiber composites: parallel computation in multi-fiber RVEs using the boundary element method." Composites science and technology **64**(9): 1101-1114.

Cheng, A. H. D., C. S. Chen, et al. (2001). "BEM for theomoelasticity and elasticity with body force -- a revisit." Engineering Analysis with Boundary Elements **25**(4-5): 377-387.

Chern, S. M. and M. E. Tuttle (2000). "On Displacement Fields in Orthotropic Laminates Containing an Elliptical Hole." Journal of Applied Mechanics **67**(3): 527-539.

Cheung, Y., W. Jin, et al. (1991). "Solution of Helmholtz equation by Trefftz method." International journal for numerical methods in engineering **32**(1): 63-78.

Cheung, Y., W. G. Jin, et al. (1989). "Direct solution procedure for solution of harmonic problems using complete, non - singular, Trefftz functions." Communications in applied numerical methods **5**(3): 159-169.

Chung, D. D. L. (1994). Carbon fiber composites. Newton, MA, Butterworth-Heinemann.

Chung, M. Y. and T. C. T. Ting (1996). "Piezoelectric solid with an elliptic inclusion or hole." International Journal of Solids and Structures **33**(23): 3343-3361.

Dai, L., W. Guo, et al. (2006). "Stress concentration at an elliptic hole in transversely isotropic piezoelectric solids." International Journal of Solids and Structures **43**(6): 1818-1831.

De Freitas, J. (1997). "Hybrid-Trefftz displacement and stress elements for elastodynamic analysis in the frequency domain." Comput Assis Mech Eng Sci **4**(3): 345-368.

de Freitas, J. and I. Moldovan (2011). "Hybrid - Trefftz stress element for bounded and unbounded poroelastic media." International journal for numerical methods in engineering **85**(10): 1280-1305.

de Freitas, J. and M. Toma (2009). "Hybrid-Trefftz stress and displacement elements for axisymmetric incompressible biphasic media." Computer Methods in Applied Mechanics and Engineering **198**(30-32): 2368-2390.

de Freitas, J. A. T. (2003a). "Time integration and the Trefftz Method Part I-First-order and parabolic problems." Computer Assisted Mechanics and Engineering Sciences **10**(4): 453-464.

de Freitas, J. A. T. (2003b). "Time integration and the Trefftz Method Part II-Second-order and hyperbolic problems." Computer Assisted Mechanics and Engineering Sciences **10**(4): 465-478.

de Freitas, J. A. T. and F. L. S. Bussamra (2000). "Three-dimensional hybrid-Trefftz stress elements." International Journal for Numerical Methods in Engineering **47**(5): 927-950.

de Freitas, J. A. T. and I. D. Moldovan (2011). "Hybrid-Trefftz stress element for bounded and unbounded poroelastic media." International Journal for Numerical Methods in Engineering **85**(10): 1280-1305.

de Freitas, J. A. T. and M. Toma (2009). "Hybrid-Trefftz stress elements for incompressible biphasic media." International Journal for Numerical Methods in Engineering **79**(2): 205-238.

de Medeiros, G. C., P. W. Partridge, et al. (2004). "The method of fundamental solutions with dual reciprocity for some problems in elasticity." Engineering Analysis with Boundary Elements **28**(5): 453-461.

Denda, M. and I. Kosaka (1997). "Dislocation and point-force-based approach to the special Green's function BEM for elliptic hole and crack problems in two dimensions." International Journal for Numerical Methods in Engineering **40**(15): 2857-2889.

Denda, M. and C. Y. Wang (2009). "3D BEM for the general piezoelectric solids." Computer Methods in Applied Mechanics and Engineering **198**(37-40): 2950-2963.

Deng, Q. and Z. Wang (2002). "Analysis of piezoelectric materials with an elliptical hole." Acta Mech. Sinica **34**(1): 109-114.

Dhanasekar, M., J. Han, et al. (2006). "A hybrid-Trefftz element containing an elliptic hole." Finite Elem. Anal. Des. **42**(14): 1314-1323.

Dhanasekar, M., J. J. Han, et al. (2006). "A hybrid-Trefftz element containing an elliptic hole." Finite Elements in Analysis and Design **42**(14-15): 1314-1323.

Ding, H., G. Wang, et al. (1998). "A boundary integral formulation and 2D fundamental solutions for piezoelectric media." Computer Methods in Applied Mechanics and Engineering **158**(1-2): 65-80.

Ding, H., G. Wang, et al. (1996). "General and fundamental solutions of plane piezoelectroelastic problem." Acta Mechanica Sinica (Chinese Edition) **28**: 441-448.

Dunn, M. L. and M. Taya (1993). "Micromechanics predictions of the effective electroelastic moduli of piezoelectric composites." International Journal of Solids and Structures **30**(2): 161-175.

Dvorak, G. J. and J. Zhang (2001). "Transformation field analysis of damage evolution in composite materials." Journal of the Mechanics and Physics of Solids **49**(11): 2517-2541.

Eshelby, J. D. (1957). "The Determination of the Elastic Field of an Ellipsoidal Inclusion, and Related Problems." Proceedings of the Royal Society of London. Series A. Mathematical and Physical Sciences **241**(1226): 376-396.

Fam, G. S. A. and Y. F. Rashed (2005). "The Method of Fundamental Solutions applied to 3D structures with body forces using particular solutions." Computational Mechanics **36**(4): 245-254.

Farooqi, J. K. and M. A. Sheikh (2006). "Finite element modelling of thermal transport in ceramic matrix composites." Computational Materials Science **37**(3): 361-373.

Feng, X. Q., Y. W. Mai, et al. (2003). "A micromechanical model for interpenetrating multiphase composites." Computational Materials Science **28**(3-4): 486-493.

Fish, J., Q. Yu, et al. (1999). "Computational damage mechanics for composite materials based on mathematical homogenization." International journal for numerical methods in engineering **45**(11): 1657-1679.

Folias, E. S. and J. J. Wang (1990). "On the three-dimensional stress field around a circular hole in a plate of arbitrary thickness." Computational Mechanics **6**(5): 379-391.

Freitas, J. (1999). "Hybrid finite element formulations for elastodynamic analysis in the frequency domain." International Journal of Solids and Structures **36**(13): 1883-1923.

Fu, S. Y., X. Q. Feng, et al. (2008). "Effects of particle size, particle/matrix interface adhesion and particle loading on mechanical properties of particulate–polymer composites." Composites Part B: Engineering **39**(6): 933-961.

Gao, S. W., Y. S. Wang, et al. (2005). "Dual reciprocity boundary element method for flexural waves in thin plate with cutout." Applied Mathematics and Mechanics-English Edition **26**(12): 1564-1573.

Gao, X. W. and T. G. Davies (2002). Boundary element programming in mechanics, Cambridge Univ Pr.

García-Sánchez, F., C. Zhang, et al. (2008). "2-D transient dynamic analysis of cracked piezoelectric solids by a time-domain BEM." Computer Methods in Applied Mechanics and Engineering **197**(33-40): 3108-3121.

Ghosh, A. and P. Sinha (2004). "Dynamic and impact response of damaged laminated composite plates." Aircraft Engineering and Aerospace Technology: An International Journal **76**(1): 29-37.

Ghosh, S., J. Bai, et al. (2009). "Homogenization-based continuum plasticity-damage model for ductile failure of materials containing heterogeneities." Journal of the Mechanics and Physics of Solids **57**(7): 1017-1044.

Ghosh, S., K. Lee, et al. (2001). "A multi-level computational model for multi-scale damage analysis in composite and porous materials." International Journal of Solids and Structures **38**(14): 2335-2385.

Ghosh, S., Z. Nowak, et al. (1997). "Quantitative characterization and modeling of composite microstructures by Voronoi cells." Acta Materialia **45**(6): 2215-2234.

Golberg, M. A., C. S. Chen, et al. (1999). "Some recent results and proposals for the use of radial basis functions in the BEM." Engineering Analysis with Boundary Elements **23**(4): 285-296.

Golecki, J. J. (1995). "On stress concentration around circular holes." International Journal of Fracture **73**(1): R15-R17.

Harari, I., P. Barai, et al. (1999). "Numerical and spectral investigations of Trefftz infinite elements." International journal for numerical methods in engineering **46**(4): 553-577.

Harari, I., P. Barai, et al. (2001). "Three-dimensional infinite elements based on a Trefftz formulation." Journal of Computational Acoustics **9**(2): 381-394.

Harari, I. and R. Djellouli (2004). "Analytical study of the effect of wave number on the performance of local absorbing boundary conditions for acoustic scattering." Applied Numerical Mathematics **50**(1): 15-47.

Hashin, Z. (1979). "Analysis of properties of fiber composites with anisotropic constituents." Journal of Applied Mechanics-Transactions of the Asme **46**(3): 543-550.

Hashin, Z. (1983). "Analysis of composite materials." J. appl. Mech **50**(2): 481-505.

Hazanov, S. and C. Huet (1994). "Order relationships for boundary conditions effect in heterogeneous bodies smaller than the representative volume." Journal of the Mechanics and Physics of Solids **42**(12): 1995-2011.

Henry, D., F. Ma, et al. (2007). "Steady state thermoelastic analysis of 3D solids with fiber inclusions by boundary element method." Computer Methods in Applied Mechanics and Engineering **197**(1-4): 294-307.

Henry, D. P. and P. K. Banerjee (1988). "A new boundary element formulation for two- and three-dimensional thermoelasticity using particular integrals." International Journal for Numerical Methods in Engineering **26**(9): 2061-2077.

Herrera, I. (1980). "Boundary methods: A criterion for completeness." Proceedings of the National Academy of Sciences **77**(8): 4395.

Hill, R. (1963). "Elastic properties of reinforced solids: Some theoretical principles." Journal of the Mechanics and Physics of Solids **11**(5): 357-372.

Hill, R. (1965). "Theory of mechanical properties of fibre-strengthened materials .3. self-consistent model." Journal of the Mechanics and Physics of Solids **13**(4): 189-198.

Huang, Y., K. X. Hu, et al. (1994). "Several variations of the generalized self-consistent method for hybrid composites." Composites Science and Technology **52**(1): 19-27.

Huet, C. (1990). "Application of variational concepts to size effects in elastic heterogeneous bodies." Journal of the Mechanics and Physics of Solids **38**(6): 813-841.

Hui, W. and Q. Qinghua (2007). "Some problems with the method of fundamental solution using radial basis functions." Acta Mechanica Solida Sinica **20**(1): 21-29.

Hwu, C. (2010). Anisotropic elastic plates, Springer.

Hwu, C. and W. J. Yen (1991). "Green's functions of two-dimensional anisotropic plates containing an elliptic hole." Int. J. Solids Struct **27**(13): 1705-1719.

Islam, M. R. and A. Pramila (1999). "Thermal Conductivity of Fiber Reinforced Composites by the FEM." Journal of Composite Materials **33**(18): 1699-1715.

Jański, Ł., M. Scherzer, et al. (2010). "Adaptive finite element computation of dielectric and mechanical intensity factors in piezoelectrics with impermeable cracks." International Journal for Numerical Methods in Engineering **81**(12): 1492-1513.

Jin, W. and Y. Cheung (1995). "Trefftz direct method." Advances in Engineering Software **24**(1-3): 65-69.

Jin, W. G., N. Sheng, et al. (2005). "Trefftz indirect methods for plane piezoelectricity." International Journal for Numerical Methods in Engineering **63**(1): 139-158.

Jirousek, J. (1978). "Basis for development of large finite elements locally satisfying all field equations." Computer Methods in Applied Mechanics and Engineering **14**(1): 65-92.

Jirousek, J. (1987). "Hybrid - Trefftz plate bending elements with p - method capabilities." International journal for numerical methods in engineering **24**(7): 1367-1393.

Jirousek, J. and L. Guex (1986). "The Hybrid-Trefftz Finite-Element Model and Its Application to Plate Bending." International Journal for Numerical Methods in Engineering **23**(4): 651-693.

Jirousek, J. and N. Leon (1977). "A powerful finite element for plate bending." Computer Methods in Applied Mechanics and Engineering **12**(1): 77-96.

Jirousek, J. and M. N'Diaye (1990). "Solution of orthotropic plates based on p-extension of the hybrid-Trefftz finite element model." Computers & Structures **34**(1): 51-62.

Jirousek, J. and Q. H. Qin (1995). "Application of Hybrid-Trefftz Element Approach to Transient Heat-Conduction Analysis." Computers & Structures **58**(1): 195-201.

Jirousek, J. and P. Teodorescu (1982). "Large finite elements method for the solution of problems in the theory of elasticity." Computers & Structures **15**(5): 575-587.

Jirousek, J. and A. Venkatesh (1989). "Implementation of curvilinear geometry into p ‐ version HT plate elements." International journal for numerical methods in engineering **28**(2): 431-443.

Jirousek, J. and A. Wroblewski (1996). "T-elements: State of the art and future trends." Archives of Computational Methods in Engineering **3**(4): 323-434.

Jirousek, J., A. Wroblewski, et al. (1995). "A Family of Quadrilateral Hybrid-Trefftz P-Elements for Thick Plate Analysis." Computer Methods in Applied Mechanics and Engineering **127**(1-4): 315-344.

Jirousek, J., A. Wróblewski, et al. (1995). "A new 12 DOF quadrilateral element for analysis of thick and thin plates." International journal for numerical methods in engineering **38**(15): 2619-2638.

Kachanov, M. and I. Sevostianov (2005). "On quantitative characterization of microstructures and effective properties." International Journal of Solids and Structures **42**(2): 309-336.

Kant, T. (1993). "A critical review and some results of recently developed refined theories of fiber-reinforced laminated composites and sandwiches." Composite Structures **23**(4): 293-312.

Korelc, J. and P. Wriggers (1996). "An efficient 3D enhanced strain element with Taylor expansion of the shape functions." Computational Mechanics **19**(2): 30-40.

Korelc, J. and P. Wriggers (1997). "Improved enhanced strain four-node element with Taylor expansion of the shape functions." International Journal for Numerical Methods in Engineering **40**(3): 407-421.

Kouznetsova, V., W. Brekelmans, et al. (2001). "An approach to micro-macro modeling of heterogeneous materials." Computational Mechanics **27**(1): 37-48.

Kumar, S., B. N. Rao, et al. (2007). "Effect of impactor parameters and laminate characteristics on impact response and damage in curved composite laminates." Journal of Reinforced Plastics and Composites **26**(13): 1273-1290.

Kumar, S. and R. Singh (1997). "Energy release rate and crack propagation in piezoelectric materials. Part I: mechanical/electrical load." Acta Materialia **45**(2): 849-857.

Kushch, V. I., S. V. Shmegera, et al. (2011). "Explicit modeling the progressive interface damage in fibrous composite: Analytical vs. numerical approach." Composites Science and Technology **71**(7): 989-997.

Landis, C. M., I. J. Beyerlein, et al. (2000). "Micromechanical simulation of the failure of fiber reinforced composites." Journal of the Mechanics and Physics of Solids **48**(3): 621-648.

Lee, J. S. and L. Z. Jiang (1994). "A boundary integral formulation and 2D fundamental solution for piezoelastic media." Mechanics Research Communications(21): 47-54.

Lekhnitskii, S. G. (1968). Anisotropic Plates. New York., Gordon and Breach, Science Publishers.

Lekhnitskii, S. G. (1981). Theory of elasticity of an anisotropic body. Moscow, Mir Publishers.

Li, H., S. Li, et al. (2011). "Prediction of effective thermal conductivities of woven fabric composites using unit cells at multiple length scales." Journal of Materials Research **26**(03): 384-394.

Li, Z. C., T. T. Lu, et al. (2008). Trefftz and collocation methods, WIT Press.

Liu, Y. J., N. Nishimura, et al. (2008). "A boundary element method for the analysis of CNT/polymer composites with a cohesive interface model based on molecular dynamics." Engineering Analysis with Boundary Elements **32**(4): 299-308.

Lu, P. and F. Williams (1998). "Green functions of piezoelectric material with an elliptic hole or inclusion." International Journal of Solids and Structures **35**(7): 651-664.

Ma, F., J. Chatterjee, et al. (2008). "Transient heat conduction analysis of 3D solids with fiber inclusions using the boundary element method." International Journal for Numerical Methods in Engineering **73**(8): 1113-1136.

Macneal, R. H. and R. L. Harder (1985). "A proposed standard set of problems to test finite element accuracy." Finite Elements in Analysis and Design **1**(1): 3-20.

Maligno, A., N. Warrior, et al. (2009). "Effects of inter-fibre spacing on damage evolution in unidirectional (UD) fibre-reinforced composites." European Journal of Mechanics-A/Solids **28**(4): 768-776.

Mauge, C. and M. Kachanov (1994). "Effective elastic properties of an anisotropic material with arbitrarily oriented interacting cracks." Journal of the Mechanics and Physics of Solids **42**(4): 561-584.

MERIC, R. and S. Saigal (1990). Shape sensitivity analysis of piezoelectric structures by the adjoint variable method.

Miehe, C. (2003). "Computational micro-to-macro transitions for discretized micro-structures of heterogeneous materials at finite strains based on the minimization of averaged incremental energy." Computer Methods in Applied Mechanics and Engineering **192**(5-6): 559-591.

Miehe, C. and A. Koch (2002). "Computational micro-to-macro transitions of discretized microstructures undergoing small strains." Archive of Applied Mechanics **72**(4-5): 300-317.

Minoru, T. (1999). "Micromechanics modeling of smart composites." Composites Part A: Applied Science and Manufacturing **30**(4): 531-536.

Moldovan, I. and J. Freitas (2008). "Hybrid-Trefftz stress and displacement elements for dynamic analysis of bounded and unbounded saturated porous media." Computer Assisted Mechanics and Engineering Sciences **15**(3/4): 289-303.

Mori, T. and K. Tanaka (1973). "Average stress in matrix and average elastic energy of materials with misfitting inclusions." Acta Metallurgica **21**(5): 571-574.

Mueller-Hoeppe, D. S., S. Loehnert, et al. (2009). "A finite deformation brick element with inhomogeneous mode enhancement." International Journal for Numerical Methods in Engineering **78**(10): 1164-1187.

Mura, T. (1987). Micromechanics of Defects in Solids. The Netherlands, Martinus Nijhoff.

Nemat-Nasser, S. and H. Hori (1999). Micromechanics: Overall Properties of Heterogeneous Materials, Elsevier Science.

Özdemir, I., W. Brekelmans, et al. (2008). "FE2 computational homogenization for the thermo-mechanical analysis of heterogeneous solids." Computer methods in applied mechanics and engineering **198**(3-4): 602-613.

Pan, E. (1999). "A BEM analysis of fracture mechanics in 2D anisotropic piezoelectric solids." Engineering Analysis with Boundary Elements **23**(1): 67-76.

Park, S., S. Park, et al. (1998). "Measuring strain distribution during mesoscopic domain reorientation in a ferroelectric material." Journal of engineering materials and technology **120**: 1.

Park, S. and C.-T. Sun (1995). "Fracture Criteria for Piezoelectric Ceramics." Journal of the American Ceramic Society **78**(6): 1475-1480.

Parton, V. Z. and B. A. Kudryavtsev (1988). Electromagnetoelasticity: piezoelectrics and electrically conductive solids, Routledge.

Patterson, C. and M. Sheikh (1982). "On the use of fundamental solutions in Trefftz method for potential and elasticity problems." Boundary element methods in engineering: 43-57.

Pian, T. H. H. and P. Tong (1986). "Relations between incompatible displacement model and hybrid stress model." International Journal for Numerical Methods in Engineering **22**(1): 173-181.

Piltner, R. (1985). "Special finite elements with holes and internal cracks." International Journal for Numerical Methods in Engineering **21**(8): 1471-1485.

Piltner, R. (1987). "The use of complex valued functions for the solution of three-dimensional elasticity problems." Journal of elasticity **18**(3): 191-225.

Piltner, R. (1992). "The derivation of a thick and thin plate formulation without ad hoc assumptions." Journal of Elasticity **29**(2): 133-173.

Piltner, R. (1992). "A quadrilateral hybrid - Trefftz plate bending element for the inclusion of warping based on a three - dimensional plate formulation." International journal for numerical methods in engineering **33**(2): 387-408.

Qin, Q. (1996). "Nonlinear analysis of thick plates by HT FE approach." Computers & Structures **61**(2): 271-281.

Qin, Q. (2000). The Trefftz finite and boundary element method. Southampton WIT Press.

Qin, Q. and S. Diao (1996). "Nonlinear analysis of thick plates on an elastic foundation by HT FE with p-extension capabilities." International Journal of Solids and Structures **33**(30): 4583-4604.

Qin, Q. and H. Wang (2008). Matlab and C programming for Trefftz finite element methods. New York, CRC Press.

Qin, Q. H. (1994). "Hybrid Trefftz Finite-Element Approach for Plate-Bending on an Elastic-Foundation." Applied Mathematical Modelling **18**(6): 334-339.

Qin, Q. H. (1995a). "Hybrid-Trefftz Finite-Element Method for Reissner Plates on an Elastic-Foundation." Computer Methods in Applied Mechanics and Engineering **122**(3-4): 379-392.

Qin, Q. H. (1995b). "Postbuckling analysis of thin plates by a hybrid Trefftz finite element method." Computer Methods in Applied Mechanics and Engineering **128**(1-2): 123-136.

Qin, Q. H. (1996). "Transient plate bending analysis by hybrid Trefftz element approach." Communications in Numerical Methods in Engineering **12**(10): 609-616.

Qin, Q. H. (2000). The Trefftz finite and boundary element method. Southampton WIT Press.

Qin, Q. H. (2003). "Solving anti-plane problems of piezoelectric materials by the Trefftz finite element approach." Computational Mechanics **31**(6): 461-468.

Qin, Q. H. (2003). "Variational formulations for TFEM of piezoelectricity." International Journal of Solids and Structures **40**(23): 6335-6346.

Qin, Q. H. (2004). "Micromechanics-BE solution for properties of piezoelectric materials with defects." Engineering Analysis with Boundary Elements **28**(7): 809-814.

Qin, Q. H. (2005). "Formulation of hybrid Trefftz finite element method for elastoplasticity." Applied Mathematical Modelling **29**(3): 235-252.

Qin, Q. H., Y. W. Mai, et al. (1998). "Effective moduli for thermopiezoelectric materials with microcracks." International Journal of Fracture **91**(4): 359-371.

Qin, Q. H. and M. V. Swain (2004). "A micro-mechanics model of dentin mechanical properties." Biomaterials **25**(20): 5081-5090.

Qin, Q. H. and H. Wang (2008). Matlab and C programming for Trefftz finite element methods. New York, CRC Press.

Qin, Q. H. and Q. S. Yang (2008). Macro-micro theory on multifield behaviour of heterogeneous materials. Beijing, Higher Education Press & Springer.

Qin, Q. H. and S. W. Yu (1997). "An arbitrarily-oriented plane crack terminating at the interface between dissimilar piezoelectric materials." International Journal of Solids and Structures **34**(5): 581-590.

Qin, Q. H. and S. W. Yu (1998). "Effective moduli of piezoelectric material with microcavities." International Journal of Solids and Structures **35**(36): 5085-5095.

Qu, J. and M. Cherkaoui (2006). Fundamentals of Micromechanics of Solids. Hoboken, NJ, Wiley.

R.J, Y. (1993). "Shape design sensitivity analysis of thermoelasticity problems." Computer Methods in Applied Mechanics and Engineering **102**(1): 41-60.

Rajesh, K. and B. Rao (2010). "Two-dimensional analysis of anisotropic crack problems using coupled meshless and fractal finite element method." International Journal of Fracture **164**(2): 285-318.

Reddy, J. N. (2004). Mechanics of laminated composite plates and shells: theory and analysis, CRC.

Reutskiy, S. Y. (2004). "A Trefftz type method for time-dependent problems." Engineering Analysis with Boundary Elements **28**(1): 13-21.

Ribeiro, D. B. and J. B. Paiva (2009). "An alternative multi-region BEM technique for three-dimensional elastic problems." Engineering Analysis with Boundary Elements **33**(4): 499-507.

Rizzo, F. J. and D. J. Shippy (1970). "A Method for Stress Determination in Plane Anisotropic Elastic Bodies." Journal of Composite Materials **4**(1): 36-61.

S. Nemat-Nasser, M. H. (1999). Micromechanics: Overall Properties of Heterogeneous Materials, Elsevier Science.

Sánchez-Palencia, E. (1980). Non-homogeneous media and vibration theory.

Sauter, S. A. and C. Schwab (2010). Boundary Element Methods, Springer.

Savin, G. N. (1961). Stress concentration around holes. New York, Pergamon Press.

Seidel, G. D. and D. C. Lagoudas (2006). "Micromechanical analysis of the effective elastic properties of carbon nanotube reinforced composites." Mechanics of Materials **38**(8-10): 884-907.

Sen, F. and K. Aldas (2009). "Elastic-plastic thermal stress analysis in a thermoplastic composite disc applied linear temperature loads via FEM." Advances in Engineering Software **40**(9): 813-819.

Sheng, N., K. Y. Sze, et al. (2006). "Trefftz solutions for piezoelectricity by Lekhnitskii's formalism and boundary-collocation method." International Journal for Numerical Methods in Engineering **65**(13): 2113-2138.

Shiah, Y. C. and Y. J. Lin (2003). "Multiple reciprocity boundary element analysis of two-dimensional anisotropic thermoelasticity involving an internal arbitrary non-uniform volume heat source." International Journal of Solids and Structures **40**(24): 6593-6612.

Shokrieh, M. M. and L. B. Lessard (2000). "Progressive fatigue damage modeling of composite materials, Part I: Modeling." Journal of Composite Materials **34**(13): 1056.

Simo, J. C. and M. Rifai (1990). "A class of mixed assumed strain methods and the method of incompatible modes." International Journal for Numerical Methods in Engineering **29**(8): 1595-1638.

Simpson, H. C. and S. J. Spector (1987). "On the positivity of the second variation in finite elasticity." Archive for Rational Mechanics and Analysis **98**(1): 1-30.

Sládek, V. and J. Sládek (1984). "Boundary integral equation method in two-dimensional thermoelasticity." Engineering Analysis **1**(3): 135-148.

Solin, P., J. Cerveny, et al. (2010). "Monolithic discretization of linear thermoelasticity problems via adaptive multimesh -FEM." Journal of Computational and Applied Mathematics **234**(7): 2350-2357.

Sosa, H. (1991). "Plane problems in piezoelectric media with defects." International Journal of Solids and Structures **28**(4): 491-505.

Stojek, M. (1998). "Least - squares Trefftz - type elements for the Helmholtz equation." International journal for numerical methods in engineering **41**(5): 831-849.

Stroh, A. N. (1958). "Dislocations and cracks in anisotropic elasticity." Philosophical Magazine **3**(30): 625-646.

Suleman, A. and V. Venkayya (1995). "A simple finite element formulation for a laminated composite plate with piezoelectric layers." Journal of intelligent material systems and structures **6**(6): 776.

Suo, C. M. (1992). "Fracture mechanics for piezoelectric ceramics." Journal of the Mechanics and Physics of Solids **40**(4): 739-765.

Sze, K., H. T. Wang, et al. (2001). "A finite element approach for computing edge singularities in piezoelectric materials." International Journal of Solids and Structures **38**(50): 9233-9252.

Sze, K., X. M. Yang, et al. (2004). "Electric assumptions for piezoelectric laminate analysis." International Journal of Solids and Structures **41**(9-10): 2363-2382.

Sze, K. Y. and G. H. Liu (2010). "Hybrid-Trefftz six-node triangular finite element models for Helmholtz problem." Computational Mechanics **46**(3): 455-470.

Teixeira de Freitas, J. (2002). "Mixed finite element formulation for the solution of parabolic problems." Computer Methods in Applied Mechanics and Engineering **191**(32): 3425-3457.

Teixeira de Freitas, J. and C. Cismaşiu (2003). "Hybrid-Trefftz displacement element for spectral analysis of bounded and unbounded media." International Journal of Solids and Structures **40**(3): 671-699.

Teixeira de Freitas, J. and Z. Wang (2001). "Elastodynamic analysis with hybrid stress finite elements." Computers & Structures **79**(19): 1753-1767.

Teixeira de Freitas, J. and Z. Wang (2002). "Elastoplastic dynamic analysis with hybrid stress elements." International journal for numerical methods in engineering **53**(3): 515-537.

Temizer, I. and P. Wriggers (2010). "A micromechanically motivated higher - order continuum formulation of linear thermal conduction." ZAMM - Journal of Applied Mathematics and Mechanics/Zeitschrift für Angewandte Mathematik und Mechanik **90**(10 - 11): 768-782.

Temizer, İ. and P. Wriggers (2007). "An adaptive method for homogenization in orthotropic nonlinear elasticity." Computer Methods in Applied Mechanics and Engineering **196**(35–36): 3409-3423.

Tenek, L. and J. Argyris (1997). "Computational aspects of the natural - mode finite element method." Communications in Numerical Methods in Engineering **13**(9): 705-713.

Terada, K. and N. Kikuchi (2001). "A class of general algorithms for multi-scale analyses of heterogeneous media." Computer methods in applied mechanics and engineering **190**(40-41): 5427-5464.

Timoshenko, S. and J. Goodier (1970). Theory of Elasticity. New York, McGraw-Hill.

Ting, K., K. Chen, et al. (1999). "Boundary element alternating method applied to analyze the stress concentration problems of multiple elliptical holes in an infinite domain." Nuclear engineering and design **187**(3): 303-313.

Ting, T. and C. Hwu (1988). "Sextic formalism in anisotropic elasticity for almost non-semisimple matrix N." International Journal of Solids and Structures **24**(1): 65-76.

Ting, T. C. T. (1996). Anisotropic Elasticity: Theory and Applications NewYork, Oxford Science Publications.

Toma, M. (2007). Modelling of hydrated soft tissues using hybrid-Trefftz finite elements, Universidade Técnica de Lisboa.

Tsai, C. (2009). "The method of fundamental solutions with dual reciprocity for three-dimensional thermoelasticity under arbitrary body forces." Engineering Computations **26**(3): 229-244.

Tsukrov, I. (2000). "Elastic Moduli of Composites with Rigid Elliptical Inclusions." International Journal of Fracture **101**(4): 29-34.

Tsukrov, I. and J. Novak (2002). "Effective elastic properties of solids with defects of irregular shapes." International Journal of Solids and Structures **39**(6): 1539-1555.

Tyrus, J. M., M. Gosz, et al. (2007). "A local finite element implementation for imposing periodic boundary conditions on composite micromechanical models." International Journal of Solids and Structures **44**(9): 2972-2989.

Van Paepegem, W. and J. Degrieck (2003). "Modelling damage and permanent strain in fibre-reinforced composites under in-plane fatigue loading." Composites Science and Technology **63**(5): 677-694.

Varelis, D. and D. A. Saravanos (2008). "Non-linear coupled multi-field mechanics and finite element for active multi-stable thermal piezoelectric shells." International journal for numerical methods in engineering **76**(1): 84-107.

Vasiliev, V. V. and E. V. Morozov (2007). Advanced mechanics of composite materials, Elsevier Science.

Voros, G. (1991). "Application of the hybrid-Trefftz finite element model to thin shell analysis." Periodica Polytechnica Mechanical Engineering **35**: 23-40.

Wang, G., S. Li, et al. (2005). "A circular inclusion in a finite domain II. The Neumann-Eshelby problem." Acta Mechanica **179**(1): 91-110.

Wang, H. and Q.-H. Qin (2011). "Fundamental-solution-based hybrid FEM for plane elasticity with special elements." Computational Mechanics **48**(5): 515-528.

Wang, H., Q. Qin, et al. (2006). "A meshless model for transient heat conduction in functionally graded materials." Computational Mechanics **38**(1): 51-60.

Wang, H. and Q. H. Qin (2009). "Hybrid FEM with fundamental solutions as trial functions for heat conduction simulation." Acta Mechanica Solida Sinica **22**(5): 487-498.

Wang, H. and Q. H. Qin (2010a). "FE approach with green's function as internal trial function for simulating bioheat transfer in the human eye." Archives of Mechanics **62**(6): 493-510.

Wang, H. and Q. H. Qin (2010b). "Fundamental-solution-based finite element model for plane orthotropic elastic bodies." European Journal of Mechanics, A/Solids **29**(5): 801-809.

Wang, H. and Q. H. Qin (2011a). "Boundary Integral Based Graded Element For Elastic Analysis of 2D Functionally Graded Plates." European Journal of Mechanics-A/Solids.

Wang, H. and Q. H. Qin (2011b). "Special fiber elements for analyzing thermal behavior and effective properties of fiber-reinforced composites." Engineering Computations **28**(8): 1079 - 1097.

Wang, H., Q. H. Qin, et al. (2007). "Application of hybrid Trefftz finite element method to non-linear problems of minimal surface." International Journal for Numerical Methods in Engineering **69**(6): 1262-1277.

Wang, H., K. Sze, et al. (2006). "Analysis of electromechanical stress singularity in piezoelectrics by computed eigensolutions and hybrid-trefftz finite element models." Computational Mechanics **38**(6): 551-564.

Wang, J., S. G. Mogilevskaya, et al. (2003). "A numerical procedure for multiple circular holes and elastic inclusions in a finite domain with a circular boundary." Computational mechanics **32**(4): 250-258.

Wang, M. and N. Pan (2008). "Modeling and prediction of the effective thermal conductivity of random open-cell porous foams." International Journal of Heat and Mass Transfer **51**(5-6): 1325-1331.

Weissman, S. L. (1996). "High-accuracy low-order three-dimensional brick elements." International Journal for Numerical Methods in Engineering **39**(14): 2337-2361.

Weissman, S. L. and R. L. Taylor (1992). "A unified approach to mixed finite element methods: Application to in-plane problems." Computer Methods in Applied Mechanics and Engineering **98**(1): 127-151.

Wriggers, P. and M. Hain (2007). Micro-Meso-Macro Modelling of Composite Materials. Computational Plasticity, Springer.

Xu, X. L. and R. K. N. D. Rajapakse (1999). "Analytical solution for an arbitrarily oriented void/crack and fracture of piezoceramics." Acta Materialia **47**(6): 1735-1747.

Xu, X. L. and R. K. N. D. Rajapakse (2001). "On a plane crack in piezoelectric solids." International Journal of Solids and Structures **38**(42-43): 7643-7658.

Yang, Q.-S. and Q.-H. Qin (2003). "Modelling the effective elasto-plastic properties of unidirectional composites reinforced by fibre bundles under transverse tension and shear loading." Materials Science and Engineering A **344**(1-2): 140-145.

Yang, Q.-S. and Q.-H. Qin (2004). "Micro-mechanical analysis of composite materials by BEM." Engineering Analysis with Boundary Elements **28**(8): 919-926.

Yao, W. and H. Wang (2005). "Virtual boundary element integral method for 2-D piezoelectric media." Finite elements in analysis and design **41**(9-10): 875-891.

Ye, Q. and P. Chen (2011). "Prediction of the cohesive strength for numerically simulating composite delamination via CZM-based FEM." Composites Part B: Engineering.

Yu, P., W. Guo, et al. (2008). "The influence of Poisson's ratio on thickness-dependent stress concentration at elliptic holes in elastic plates." International Journal of Fatigue **30**(1): 165-171.

Yuan, Z. and J. Fish (2009). "Multiple scale eigendeformation-based reduced order homogenization." Computer methods in applied mechanics and engineering **198**(21-26): 2016-2038.

Zeng, X. and S. Li (2010). "A multiscale cohesive zone model and simulations of fractures." Computer methods in applied mechanics and engineering **199**(9-12): 547-556.

Zhao, G. and C. Cho (2004). "On impact damage of composite shells by a low-velocity projectile." Journal of Composite Materials **38**(14): 1231.

Zhao, P., Y. Cao, et al. (2011). "Nonlinear electromechanical coupling behavior of 1–3 piezoelectric composites." Acta materialia **59**(14): 5534-5543.

Zielinski, A. and O. Zienkiewicz (1985). "Generalized finite element analysis with T - complete boundary solution functions." International journal for numerical methods in engineering **21**(3): 509-528.

Zienkiewicz, O., R. Taylor, et al. (2005). The Finite Element Method–Its Basis and Fundamentals, volume 1, Elsevier Butterworth-Heinemann, Amsterdam, London.

Zohdi, T. I. and P. Wriggers (2008). An introduction to computational micromechanics, Springer Verlag.

List of Publications

Journal paper

- Changyong Cao, Honfai Chan, Jianfeng Zang, Kam W. Leong and Xuanhe Zhao. Harnessing localized ridges for high-aspect-ratio hierarchical patterns with dynamic tunability and multifunctionality. Advanced Materials, DOI: 10.1002/adma. 201304589, 2013.
- Changyong Cao, Xuanhe Zhao. Tunable stiffness of electrorheological elastomers by designing mesostructures. Applied Physics Letter, 103, 041901, 2013.
- Changyong Cao, Aibing Yu, Qinghua Qin. A new efficient hybrid finite element approach for plane piezoelectricity with defects. Acta Mechanica, 224:41-61, 2013.
- Changyong Cao, Aibing Yu, Qinghua Qin. A novel hybrid approach for modeling anisotropic composites. Finite Elements in Analysis and Design, 64:36-47, 2013.
- Changyong Cao, Qinghua Qin, Aibing Yu. Hybrid Fundamental-Solution-based FEM for Piezoelectric Materials. Computational Mechanics, 50(4): 397-412, 2012.
- Changyong Cao, Qinghua Qin, Aibing Yu. A novel Boundary-Integral based finite element method for 2D and 3D thermo-elasticity problems. Journal of Thermal Stresses, 35:849-876, 2012.
- Changyong Cao, Qinghua Qin, Aibing Yu. New hybrid finite element approach for three-dimensional elastic problems. Archive of Mechanics, 64(3):261-292, 2012.
- Changyong Cao, Qinghua Qin, Aibing Yu. Micromechanical analysis of heterogeneous composites by HT-FEM and HFS-FEM. Journal of Mechanics, in Press, 2013.
- Changyong Cao, Aibing Yu, Qinghua Qin. Evaluation of effective thermal conductivity of fiber-reinforced composites. International Journal of Architecture, Engineering and Construction, 1(1):14-29, 2012.

Conference paper/talks

- Changyong Cao, Aibing Yu, Qinghua Qin. Mesh reduction strategy: Special element for modeling anisotropic materials with defects. Proceedings of the 36th International Conference on Boundary Elements and Other Mesh Reduction Methods, 22-24 October, 2013, Dalian, China.
- Changyong Cao, Xuanhe Zhao, Qinghua Qin. Hierarchical nano-micro-structures with tunability by harnessing localized instabilities. SES 50th Annual Technical Meeting and ASME-AMD Annual Summer Meeting, Brown University, Providence, USA, July 28-31, 2013.
- Changyong Cao, Xuanhe Zhao. Tunable Stiffness of Electrorheological Elastomers by Designing Mesostructures. The 12th U.S. National Congress on Computational Mechanics (USNCCM12), Rayleigh, USA, July 22-25, 2013.
- Changyong Cao, Aibing Yu, Qinghua Qin. A novel hybrid approach for modeling piezoelectric materials. The 15th International Conference on Advances in Materials & Processing Technologies Conference (AMPT 2012). Wollongong, NSW, Australia, September 23-26, 2012.
- Changyong Cao, Qinghua Qin, Aibing Yu. Modeling of anisotropic composite materials by newly developed HFS-FEM. The 23rd International Congress of Theoretical and Applied Mechanics (ICTAM2012). Beijing, August 19-24, 2012.